Acoustic Formulations for Aeronautical and Naval Rotorcraft Noise Prediction Based on the Ffowcs Williams and Hawkings Equation

Scuola Dottorale in Ingegneria

Sez. Ingegneria Meccanica e Industriale

Ciclo XX

Università degli Studi di ROMA TRE

Dipartimento di Ingegneria Meccanica e Industriale

Dottorando

Ing. Claudio Testa

Docente Guida

Prof. M. Gennaretti

Coordinatore

Prof. E. Bemporad

Summary

Noise requirements will be key design drivers in the development of the new generations of propeller-driven aircraft, helicopters and ships. Therefore aeroacoustics and hydroacoustics become increasingly important scientific branches since accurate acoustic predictions are an essential tool for the required Design for Reduced Noise Generation. Generally speaking, the prediction of aerodynamically and hydrodynamically generated noise can be considered as an aerodynamic/hydrodynamic analysis followed by an acoustic one.

The present thesis focuses on the development of acoustic formulations based on the Ffowcs Williams and Hawkings equation (FWHE), to describe the structure of the noise field induced by propeller driven aeronautical and naval craft, both in the unbounded space and in the presence of scattering bodies, like a fuselage or hull. The reason why the FWHE is at the basis of the developed acoustic formulations is its proven capability of providing physically consistent aeroacoustic predictions. Literature shows that, in the aeronautical context, the FWHE is a very efficient aeroacoustic tool allowing the prediction of the fluctuating pressure field induced by rotors and propellers, both for subsonic and transonic flight conditions. Although the modelling of noise generation and propagation in the naval context is as complicated as in aeronautics, most of the hydroacoustics analysis of non-cavitating and cavitating propellers is based on the unsteady Bernoulli equation. For this thesis, therefore, it was decided to first apply the FWHE for the prediction of noise generated by naval propellers in unbounded space. A comparison between the FWH-based and the Bernoulli-based approach has been carried out using potential flow assumptions. A novel formulation based on the porous form of the FWHE has been developed to predict the sound radiated by a cavitating propeller subjected to non-uniform inflow. The comparison has been performed both theoretically and numerically. A non-cavitating naval propeller, subjected to a uniform onset flow, has been analyzed. Observing that typical naval operating conditions are such that non-linear terms may be coherently neglected in both formulations, no hydrodynamic input concerning the flow-field around the propeller is required. The Laplace equation for the velocity potential has been solved through a boundary integral formulation and a zero-order boundary integral method (BEM) has been applied as discretization strategy. Using the velocity potential and pressure field on the propeller surface, numerical hydroacoustics investigations showed that the assumed shape of the potential wake has a large influence on the pressure disturbance evaluated by means of the Bernoulli equation. The results obtained with the FWHE, however, are not affected by the assumed wake because here the wake contributes to the noise field only through its indirect effects on the loading noise term. The introduction of free wake modelling resolves the discrepancies in the hydroacoustics results from a theoretical point of view, but introduces numerical problems because the introduction of a free wake leads to a very low rate of convergence in the evaluation of the velocity field compared to the analysis with a prescribed wake model. Because of the apparent high potential of the FWHE a novel formulation of this FWHE was developed aiming at the evaluation of noise generated by cavitation, especially sheet cavitation. This specific type occurs in real operating conditions with a propeller working in the wake of the hull, and governs the low-frequency range of the spectrum of cavitation noise. In this range, a significant contribution to the far field noise is associated with frequencies proportional to the blade

passage frequency (the tonal spectrum). The evaluation of the noise due to the cyclic growth and collapse of the cavity on the surface of the propeller in a non-uniform onset flow has been performed through a coupled approach involving the permeable form of the FWHE and a suitable hydrodynamic model describing the unsteady cavitation pattern. This model, called Transpiration Velocity Model (TVM) simulates the presence and the acoustic behaviour of the bubble through the difference between the normal component of the body velocity and the fluid velocity wherever cavitation occurs. This way of treating the impulsive noise radiation far away from cavitating propellers is consistent with the physics of the phenomenon and does not introduce approximations incompatible with a formulation derived under the assumption of rigid surfaces. Numerical results provided by the TVM compared satisfactorily with those provided by the Equivalent Blade Modeling (EBM) which is also based on the FWHE written for impermeable surfaces and that, nowadays, represents the single application, presented in literature, of the acoustic analogy to cavitation noise. The discrepancies in noise prediction arise from the different sensibility of the two approaches to the hydrodynamic data describing the cavitation pattern. Numerical investigations outline that the TVM is more sensitive to the accuracy of the hydrodynamic input because of the need to compute time derivatives of the function describing the cavity thickness distribution on the blade surface. For highly impulsive signals, the computation of time derivatives up to the second order may become a very difficult task. Contrarily, the EBM approach based on a step-by step strategy in computing the acoustic effect associated with the vapour cavity dynamics needs only the knowledge of the time-history of the cavity volume on the blade, but exhibits a limited capability to correctly describe rapidly changing flow conditions.

In this context, it is worth noting that both TVM and EBM model have been used here with hydrodynamic input from a surface tracking approach to describe the liquid–vapour interface as a regular surface defined over cavitating propeller blades. However, from a general standpoint, the FWHE may be coupled to more general two-phase flow solvers through a different use of the porous formulation. In fact, by coupling the hydrodynamics input on a suitable surface, enclosing the two-phase region, with the FWHE used as a *Kirchoff formulation* , it is possible to model noise sources located in the flow–field and associated with distributed vapour pockets. This fact highlights the generality of the FWHE approach.

In the described hydroacoustics investigations dealing with noise radiation from an acoustic source (the propeller) the boundary integral solution of the FWHE has always been used as an integral representation, exploiting the knowledge of the hydrodynamic quantities appearing in the kernel of the thickness noise and loading noise terms. The nature of the integral solution of the FWHE changes when the emphasis is on the scattering effects caused by the presence of bodies in the path of the travelling acoustic waves emitted from the propeller or rotor. In order to appreciate the sound field change when solid surfaces are present in the flow field and to allow the prediction of the noise produced by those aeronautical and naval configurations where one single body may be identified as the main noise source (assuming the pressure on the body independent of the presence of the other bodies), the problem of scattering has been investigated through a novel integral formulation based on the FWHE.

A scattering model allows studying the acoustic behaviour of configurations like fuselage–propeller (aircraft), fuselage–main/tail–rotor (helicopters) and hull–propeller (ships), without invoking the interactive aero–hydro–dynamics to calculate the scattered pressure field on the boundary of the scatterer. Differently from noise radiation problems where the FWHE is used as an integral representation, in this problem the integral solution of the FWHE is used as an integral equation to determine the scattered pressure distribution upon the scattering body. The proposed FWH formulation may be applied to those aeronautical or naval multi–body configurations where the sources of noise may be considered aerodynamically or hydrodynamically independent on the presence of the rest of the configuration. For some operating conditions, propeller–driven aircraft, rotorcrafts and ships fall in this category. The evaluation of the sound field produced by the im-

pingement of the pressure disturbance(s) on the scatterer(s) requires a prior analysis of the isolated source(s), to identify the incident pressure field(s). The formulation herein proposed is flexible in that it allows to study scattering problems concerning rigid as well as elastic bodies both moving and at rest. Numerical results show that, for stationary rigid or vibrating scattering bodies, the proposed methodology yields excellent results when simple configurations (for which analytical solutions exist) are investigated. Dealing with moving scatterers, the problem of the quadrupole term must be pointed out because the assumption to ignore the quadrupole term in the FWHE may become too restrictive. Permission to neglect the quadrupole term depends on the advance speed of the scatterer and on its shape. Hence, the analysis of moving scatterers has to be addressed carefully because the Lighthill tensor could give rise to perturbation terms which might become relevant when the integral formulation is used as an integral equation. The importance of the quadrupole contribution in the FWHE must be stressed also for the previous described radiation cases. It should be noted that numerical investigations performed throughout the thesis have been carried out neglecting the quadrupole contribution in the FWHE. The quadrupole contribution is, in principle, important for several reasons. First, it fully describes the acoustic effect of the potential wake. In order to compare the FWHE and the Bernoulli approach exactly, non-linear terms should be included in both formulations. The non-linearities in both methods *are not equivalent* , that is, some non-linear effects described by the Lighthill tensor in the FWHE are not accounted for by the non-linear terms in the Bernoulli method. Furthermore, the inclusion of the quadrupole term would account for acoustic effects related to cavitating phenomena occurring in the flow–field, like cavitating tip vortices and hub vortices, and bubble cavitation. However, even with neglecting quadrupole terms, numerical results show that the FWHE is an efficient mathematical model for the study of acoustic problems concerning acoustic radiation and scattering for a wide range of applications. A conjecture has been made and motivated that some of the discrepancies between FWHE and other formulations may be justified invoking the presence of the quadrupole term. Hence, for further development and improvement of the present work, a careful investigation of mathematical and computational aspects related to evaluating quadrupole contributions should be considered. In addition, the application of the present methodology to more realistic configurations could require the use of aero/hydrodynamic solvers able to take into account viscous–flow effects.

Contents

List of Figures

Chapter 1

Introduction

A brief introduction to the problem of the aerodynamically or hydrodynamically generated noise by rotating propulsive systems, as aeronautical or marine propellers or helicopter rotors, moving (throughout the fluid medium) in arbitrary motion is presented. The most common types of sources of noise are presented and the problem of radiated noise both in free field and in the presence of moving solid boundaries is addressed. The state of the art on the theoretical approaches used for modelling sound radiation is also given. The motivation of the present work is presented and the chapter ends with an outline of the current thesis.

1.1   Main Sources of Noise for Rotorcraft

In the last 80 years, the scientific community has devoted considerable effort toward the understanding of the physical mechanisms governing the noise generation in rotating propulsive systems and toward the development of computational methods able to predict the acoustic field. An accurate prediction of the noise field is essential to control or modify noise features so as to achieve noise reduction and comply with noise regulations. Propeller and helicopter rotor noise theory has been developed starting from 1940's; the importance of the role of unsteady loading in acoustics of moving bodies was recognized in the 1960's, and this yielded a great deal of progress in the development of theoretical modeling and noise prediction codes. In this context, a milestone is undoubtedly represented by the publication, in 1969, of the Ffowcs Williams and Hawkings (FWH) equation [1] representing the governing equation to describe the sound generated and propagated by a body moving in a fluid; however, the lack of computational power and difficulties in the prediction of unsteady loads have strongly limited the capability of supplying good qualitative and quantitative results up to 1980. In the last twenty years, with the increase of available computational power and the higher accuracy of aerodynamics prediction tools, numerical techniques for the aerodynamically generated noise evaluation have become more and more appealing; nowadays, different solvers, based on efficient and robust prediction tools, allow to solve efficiently a lot of problems related to noise emission and propagation. In spite of this scenario, the maturity level in rotating blades noise prediction is deeply different between the aeronautical and naval context; to distinguish the two fields, terms aeroacoustics and hydroacoustics are used throughout the present thesis to refer, respectively, to aeronautical and marine applications. Those theoretical approaches that may be considered as standard techniques for aeronautical applications are quite *unconventional* for the naval community that widely addresses hydroacoustics studies using *pseudo-acoustic* models often provided in the frequency domain. Despite the outstanding importance that propeller–induced noise analysis has for a wide class of naval applications, the lack of theoretical models addressing the problem under a rigorous approach is widely recognized, as mentioned, for instance, in many reports of the 23rd International Towing Tank Conference. Thus, challenges for present and future research are completely different for aeroacoustics and hy-

droacoustics; in the first case an accurate noise prediction for whole rotorcraft configurations and advanced–designed proprotor vehicles (including scattering effects) is of increasing importance, whereas the use of effective prediction models is one of the main goal for a physically-consistent computation of the hydroacoustic field induced by surface and underwater seacraft propellers. By keeping in mind the above considerations, in the following, for helicopters, propelled-aircraft and vessels, the most important (and common) sources of noise are outlined. The aim is to describe briefly the main aspects of noise generation and emission by rotating blades to identify those physical mechanisms governing the fluid–dynamically generated noise.

1.1.1 Helicopter Rotor Noise

For helicopter configurations, several distinct mechanisms are involved into the sound field generation; nowadays, they are object of extensive theoretical and experimental research because of the extremely annoying and undesired effects leading to a strong resistance to the widespread operation of helicopters in densely populated areas. Generally speaking, helicopter rotor noise tends to be concentrated at harmonics of the blade passage frequency (BPF) because of the periodic nature of the rotor loads as seen in the nonrotating frame. Thus, the acoustic pressure signal is basically periodic in time, with sharp impulses due to localized aerodynamic phenomena such as compressibility effects and vortex–induced loads. For the sake of clarity, the contributions to helicopter rotor noise may be conventionally split into broadband noise, rotational noise and blade slap noise, in order to focus, separately, on different aspects.

Broadband noise

Known earlier as vortex noise, it is a high frequency swishing sound produced by the rotor and modulated in frequency and amplitude at the BPF. Broadband noise is principally produced by the random lift fluctuations (especially by random blade loads induced by tip vortices) resulting from operation of the blade in the turbulent wake. The resulting sound is a random signal whose energy is distributed over a wide portion of the spectrum, in the audible range. Typically, for main rotors, it is extended from about 150 Hz to 1000 Hz, with a peak around 300-400 Hz. Other sources of broadband noise are the forces acting upon the blade due to vortex shedding from trailing edge, turbulence in free stream and boundary layer turbulence and separation. A complete definition of the origin of helicopter rotor broadband noise, as well as the development of efficient tools to predict it, are still subjects of extensive research.

Rotational noise

Rotational noise is related to the body's geometry and motion and the pressure loads acting upon the blade surface. The first contribution, due to the displacement of the fluid particles in the flow–field, is known as *thickness noise* term whereas the second one, caused by the loads experienced by the blade during a revolution, is known as *loading noise* term. Rotational noise is a thumping sound at the BPF (or at multiples of it if the fundamental is inaudible); as the higher harmonic content increases, the thumps sharpen into bangs, and eventually into blade slap. Being a purely periodic noise signal, its spectrum consists of discrete lines at harmonics of the BPF, deeply affected by rotor geometry and operating condition. Rotational noise dominates the helicopter rotor sound spectrum from below audible frequencies to about 150 Hz. The fundamental frequency is typically 10 to 20 Hz for a main rotor, so the fundamental and perhaps also the first or second harmonic will be below the threshold of hearing. For propellers or a tail rotor the fundamental frequency is much higher, typically around 100 Hz, thus increasing the importance of the rotational noise.

Blade slap

Blade slap is a periodic, impulsive sound pressure disturbance that may be reasonably considered as an extreme case of rotational noise; it occurs in such manoeuvres as flare to landing, shallow descents, decelerating steep turns and at high forward flight speeds. In these conditions, it represents undoubtedly the dominant rotor noise source. In fact, its impulsive character results in a substantial increase of the sound level over the entire spectrum (covering a range of about 20 to 1000 Hz for a main rotor). Its feature is a sharp cracking, popping or slapping sound occurring at the BPF and its annoying effect is so much high that the rotorcraft community has devoted considerable efforts towards alleviating it. Its genesis depends on any aerodynamic phenomenon causing rapidly changing loading on the blade, such as compressibility and thickness effects at the tip, blade–vortex interactions and probably also blade stall. Such phenomena induce large, localized transient loads upon the blade, which result into impulsive sound radiation. When the cause of the noise is the interaction of the shed tip vortex with the following blade, blade slap noise is well known as blade–vortex interaction (BVI) noise; in this case, strong tip vortices dominating the rotor wake, impinge or pass closely to the rotor blades resulting in impulsive changes of the blade loads that produce, in turn, high noise and vibration level. It is well documented that BVI concerns mainly the descent flight at relatively low–speed. On the other hand, when the cause of noise is the high–speed forward flight, blade slap is known as high–speed impulsive (HSI) noise closely associated with the appearance of shocks and transonic flow around the advancing rotor blades.

The most annoying contribution in terms of main rotor noise is due to blade slap (when occurs), broadband noise and rotational noise, respectively. Rotational noise, containing the deterministic components of thickness and loading noise, is most intensive at very low frequency even if the first few harmonics may even be below the threshold of hearing. Thus, although rotational noise is the primary determinant of the overall sound pressure level, it is not the most important source of noise in terms of subjective annoyance. In fact, by accounting for frequency content, broadband noise dominates. Only when the level of the rotational noise increases at high frequencies, *i.e*, in cases approaching blade slap, rotational noise may become important. It is worth noting that the acoustic fatigue and vibration of helicopter structures may be deeply affected by rotational noise; moreover, by observing that low frequencies propagate best in air, the high frequencies being attenuated most with distance, at very large distance from helicopter the blade slap and rotational noise of the main rotor are most important. Whatever said about the main rotor noise may be applied to the tail rotor unit that, however, has a higher fundamental frequency (40 to 120 Hz).

1.1.2 Aeronautical and Naval Propellers as Sources of Noise

Propeller noise consists of two dominant components: 1) thickness noise and 2) loading noise. As previously described, the thickness term is governed by the blade geometry and kinematics whereas the loading noise contribution depends on the blade pressure distribution. Akin to helicopter rotor blades, the thickness noise component may be computed accurately while the loading noise computation strongly depends on the aerodynamic or hydrodynamic modeling used for the loads prediction. In the aeronautical context, computation of advanced propeller noise may be regarded as challenging; in fact, advanced high–speed propellers have many features that are quite different from those of conventional low–speed propellers. For instance, advanced propellers employ eight or ten highly loaded, low-aspect-ratio, thin and highly swept blades, producing significantly more noise than low–speed propellers. Indeed, being characterized by transonic tip Mach, *significant* sources of noise are present in the flow–field and, as a consequence, the prediction of the aerodynamic loads upon the blade surface is not more sufficient to account for the emitted noise because the flow–field conditions around the blade become determinant; as matter of fact,

3

high–speed propellers noise prediction require an accurate estimation of the aerodynamic field around the blade.

Propellers used for marine applications may be classified as low–speed propellers because of the fully subsonic operating conditions. Nonetheless, the hydroacoustic prediction of marine propellers is, nowadays, a challenging issue. This is due to the fact that a hydroacoustic analysis of realistic configurations does not only concern the kinematic and dynamic behaviour of the rotating blades but involves a lot of different and very complex phenomena. A marine propeller typically operates in the wake of a hull; thus, the incoming flow is spatially non–uniform and characterized by an enormous turbulence and vorticity content which largely affects both propeller–induced noise and the propagation phenomena. Furthermore, the closeness of the hull and, eventually, of the free surface to the propeller disk may cause notable scattering effects, with a direct influence on noise spectra and directivity. Furthermore, the possible occurrence of cavitation phenomena deeply affects the hydroacoustic field; the formation, growth and collapse of vapor bubbles may provide large pressure peaks propagating away from the blades and may increase the noise level up to two orders of magnitude with respect to the same propulsor operating in non–cavitating conditions. Moreover, for an accurate hydroacoustic prediction of cavitating propellers, advanced hydrodynamic modeling accounting for transient cavitation phenomena have to be used to provide the time depending pressure distribution upon the blades. Thus, for different reasons, the computation of noise generated both by aeronautical or marine propellers is not an easy task.

1.2   Acoustic Scattering From Aircraft and Vessels

A pressure wave generated by a source of noise in presence of other bodies may be subject to scattering effects deeply modifying both the noise spectra and directivity. The effect of the scattering phenomenon on the noise field features depends on the ratio between the wavelength of the impinging wave and the physical dimensions of the scatterer. Only if comparable, acoustic scattering may modify the noise field with respect to a free-field computation. The evaluation of the scattered acoustic field is of interest both for the evaluation of the overall noise emitted by moving air/sea–craft and for the prediction of the fuselage and hull vibrations that, in turn, are a source of interior noise. The division of the noise field into incident and scattered components is physically consistent when, within the limits of the required accuracy, the source of the incident field may be considered fluid–dynamically independent of the presence of the scattering surfaces. Under such an assumption the incident pressure field may be determined through an aerodynamic–aeroacoustic analysis of the single main sources of noise, whereas the rest of the configuration may be included in the second step of the process, dealing with the scattering analysis. Such a way to face the problem is straightforward, not accounting for interactional aerodynamical effects between the noise source(s) and the scatterer. For aeronautical application, the prediction (and control) of interior noise is a crucial issue in providing a comfortable environment for aircraft passengers; although cabin noise sources include not only propellers, but also exhaust from turbofan engines, fuselage boundary layer, engine vibrations, etc., an accurate prediction of the interior noise level has to take into account aeroacoustoelasticity. For helicopter configurations, usually fuselage scattering effects are not taken into account for the evaluation of the acoustic field because the rotor blade passage frequency is generally low; hence, the wavelength of the noise signal is quite large compared to the physical dimensions of the fuselage cross-section and the influence of the body is minimal. Anyway, fuselage becomes a much more efficient scatterer when the spectra of the impinged acoustic noise exhibits a much higher frequency content, as in BVI or HSI conditions, or when the tail rotor, operating with BPF significantly higher than the main one, is included into the analysis. In these cases, the evaluation of the scattered acoustic field is of interest for the reasons above explained. For marine applications, realistic vessel configurations are such that the hull may be considered as a scattering body, deeply affecting the pressure distribution upon the

surface. When the wavelength of the underwater sound is comparable to hull dimensions, estimation of the distribution of fluctuating pressure over the whole hull surface is fundamental for a near–far field noise evaluation and to evaluate the fluctuating forces acting on the hull.

1.3   An Overview of Computational Methods for Aeroacoustics and Hydroacoustics

A brief discussion on computational methods currently used for the prediction of the acoustic field induced by moving bodies, is here addressed. The aim is to provide an overview on the capabilities and drawbacks of these approaches with respect to the problem to be faced, that is here recognized to be the noise generated by rotating blades; as a matter of fact, being the analysis of the radiated noise much more mature in the aeronautical field with respect to the naval context, the emphasis is here on the aeroacoustics.

The need to provide an efficient manner for computing aerodynamic noise has led to the emergence of a relatively new field: Computational AeroAcoustics (CAA).

CAA, as defined by Allan D. Pierce [2] *"implies the direct simulation of acoustic fields generated by flows and the direct simulation of the interaction of acoustic fields with flows starting from the time–dependent governing equations, without reliance on empirical results or heuristic conjectures"*; the full, time–dependent, compressible Navier–Stokes equations describe these phenomena. The development of CAA techniques is dependent largely upon the utilization of relatively mature Computational Fluid Dynamics (CFD); anyway, the direct extension of current CFD technology to CAA in not so straightforward because of the differences in the physics of acoustic noise propagation compared with aerodynamic flow field characteristics. In detail, for problems concerning noise due to moving surfaces (*i.e.,*helicopter rotor noise, propeller noise, fan noise, etc.), once the sound source is predicted through the use of Euler/Navier-Stokes or full potential models an obvious strategy is to extend the computational domain far enough to encompass the location where the sound is to be evaluated. Such a strategy attempts to solve the aerodynamic and acoustic fields in one step, using the same level of approximation, by unsteady methods such as DNS (Direct Numerical Simulation) or LES (Large Eddy Simulation). However, the problem of numerical prediction of the noise generated by realistic configurations (*i.e.,*wing section with deployed high lift devices) is still beyond the field of application of direct noise computation strategies. Furthermore, if the objective is to calculate the far–field noise, this direct approach would require prohibitive computer storage and would lead to unrealistic computational time. To overcome such limitations, hybrid CFD/CAA methods in which the near–field turbulent flow and the mid/far–field noise are computed separately, have to be used. The driving idea is to divide the physical space into several domains, in which specific physical mechanisms are simulated using the most efficient discretization strategy [3]. CFD techniques are first used to calculate the near–field unsteady flow to get an accurate prediction of the local unsteady noise sources. Available techniques include steady Reynolds-Averaged Navier-Stokes (RANS) computations, in combination with stochastic models of wavenumber–frequency spectrum of turbulence, unsteady RANS methods, LES and emerging techniques based on Navier-Stokes equations for perturbations over a mean flow (NLDE - Non Linear Disturbances Equations). This local flow solution has then to be coupled with an acoustic numerical technique for the prediction of mid–field and far–field noise. The most practical formulations are the integral methods based on the use of a free field acoustic Green function such as the Lighthill's analogy, the Boundary Element Methods (BEM) and the Kirchhoff integral. However, those integral methods assume that, beyond a given distance from the noise sources and body surface, the sound propagates in a medium at rest, or moving with uniform velocity. This assumption may become a strong limitation, especially when the radiated noise results from a surface integration on a control interface which is located near solid walls,

where velocity gradients are still significant. In that case, only the discretized Euler equations governing the acoustic propagation may account for the propagation in non–homogeneous flows. This is obtained at the price of a significant computational efforts since the propagation domain must be meshed with an adequate resolution with respect to the smallest acoustic wavelength, and also because finite difference high order schemes are needed to ensure numerical accuracy and low dispersion of the propagation of acoustic waves. Note that practically, the domain in which Euler equations must be used is strictly limited to regions where velocity gradients are significant; thus, an external boundary can be found, beyond which the flow can be assumed uniform. Integral methods can be so used for the noise prediction at very long distance from the airframe. Other theoretical approaches able to provide the noise field produced by moving bodies are represented by *volume integral methods* and *surface integral methods*. Undoubtedly, the first integral approach for acoustic propagation is the Lighthill Acoustic Analogy (1951) that solved the question of how to identify the real origins of sound wave [4]. In this model, the governing Navier–Stokes equations are rearranged into a wave equation that is exact in principle, and the far–field solution is given in terms of a volume integral over the domain containing the sound source. It is worth noting that by using the Lighthill's equation, the aerodynamic problem may be completely separated by the acoustic one. In fact, the aerodynamic analysis concerns only the identification of the sound source representing the forcing term of the Lighthill's equation. The extension of the Lighthill Acoustic Analogy is represented by the Ffowcs Williams Hawkings equation (FWH) that was introduced in 1969 to account for moving solid surfaces. The FWH equation allows to identify three source terms: two surface source terms and one volume source term. Hence, a volume integration, computationally expensive and difficult to be implemented is yet required for the prediction of the noise field. Anyway, for some operating conditions, the volume term source may be neglected. In these cases, the solution of the acoustic problem through the FWH equation involves only surface integrals instead of a volume integral as in the Lighthill Acoustic Analogy. This fact represents the powerful of the FWH approach. Among surface methods, Kirchhoff approach [5] assumes that the sound propagation is governed by an inhomogeneous wave equation in which the sources are distributed on a fictitious surface (Kirchhoff surface) which encloses all the nonlinear flow effects and noise sources. This formulation is very attractive because no volume integration is needed, allowing to overcome some of the difficulties associated with the traditional acoustic analogy approach. A drawback in using the Kirchhoff method is that the Kirchhoff surface must be chosen in the linear flow region such that the input surface pressure and its normal and time derivatives satisfy the homogeneous wave equation. By observing that for the prediction of the aerodynamic noise the knowledge of source strength information on the Kirchhoff surface is required, mature CFD codes are necessary. Anyway the location of the linear region is not well defined and is problem dependent; indeed, such a surface should be placed well away from source region but CFD solutions typically are not as well resolved or as accurate away from the body. Hence, the placement of the Kirchhoff surface is usually a compromise. To take advantages from an aeroacoustic formulation having the same flexibility of the Kirchoff approach, avoiding any problems due to the sensitivity of the formulation to the placement of the integration surface, the permeable (porous) FWH equation has to be used. In fact, because of the nature of the governing FWH equation, any physical acoustic sources enclosed by the integration surface contribute through surface–source terms whereas any physical sources of noise outside the surface contribute through the volume source term. Hence, if all physical sources of noise may be enclosed inside the integration surface, no contribution from volume source has to be computed and the acoustic effects computed by volume integration can be legitimately neglected. In other words, if the control porous surface (fictitious or physical) is suitably placed away from the body in order to include all sound sources, the overall noise prediction is achievable by the computation of surface integral only, in a similar fashion as the Kirchhoff method. In this case the location of the integration surface is only a matter of choice and convenience. Since the formulation combines aspect of both the FWH and

Kirchhoff approaches, it is referred as Kirchhoff-FWH formulation (KFWH). Many other details are found in Ref. [6]. As an example, Fig. 1.1 illustrates the possible hybrid strategy that can be used for the numerical simulation of airfoil aerodynamic noise.
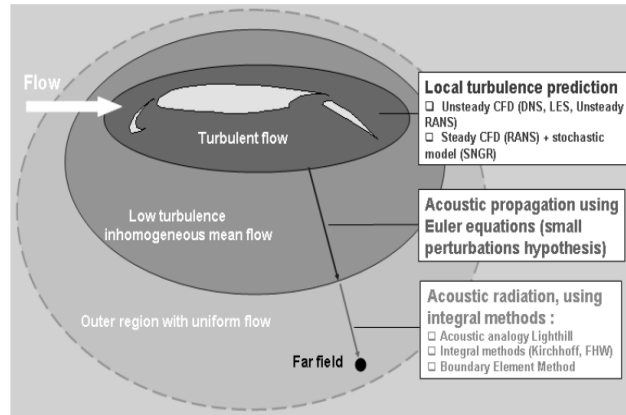
Figure 1.1: *Sketch of a possible strategies for noise computation in the near, mid and far field. (from Ref. [3]).*

Among surface methods for predicting the noise field produced by moving bodies, the use of the Bernoulli equation–based approach and the Helmholtz equation are notable, in particular for naval applications [7], [8]. In fact, except for the CAA approach that is widely used when realistic and complicated aeronautical or naval configurations have to be investigated, the evaluation of the pressure disturbance through the acoustic analogy–based methodologies (FWH, porous FWH, KFWH) is consolidated and mature only for aeronautical applications involving helicopter rotors and propelled aircraft; it remains unconventional, and nowadays, it is seen as too much complicated and challenging for the naval community that seems to be pervaded by a sort of *reverential fear* with respect to such fundamental equation-based approaches. In the framework of potential flows, the Bernoulli equation–based approach allows to calculate the noise field once the velocity potential problem has been solved; in this case the definition of the wake surface is required, affecting both the aero/hydro–dynamic and aero/hydro–acoustic solutions. About the Helmholtz equation, it represents the homogeneous wave equation transformed into the frequency domain; in this case appropriate boundary conditions must to be imposed (Dirichelet, Neumann or Robin boundary conditions in the case of scattering surfaces involved into the problem, or Sommerfeld condition for radiation problems) to close the problem.

1.4 Present Research

1.4.1 Motivation

Previous sections have shown that rotor noise prediction or propeller noise evaluation involves complex aspects both from theoretical and numerical standpoints; many different mechanisms are responsible of noise generation and radiation and separate treatment is required for each. Making reference to the aeronautical field, several prediction methods are available: among them, acoustic formulations and algorithms based on integral methods (Ffowcs Williams Hawkings equation, Kirchhoff formula) are widely used for rotating blade noise prediction and potentially useful for airframe noise, engine noise etc.; other approaches, whose feasibility is due to advances in CFD and computer technology allow direct computation of acoustics or the application of the KFWH approach. As a matter of fact, for rotors and propellers, the knowledge of aeroacoustics phenomena and their capability prediction is advanced; however, further efforts are required to improve

the analysis of particular problems as blade-vortex interaction noise, high–speed impulsive noise and broadband noise. Nowadays, the main goal of the aeroacoustic community is the prediction of noise generated by whole configurations as fuselage–main rotor–tail rotor for helicopters and fuselage–propeller for airplanes, to achieve a comprehensive aeroacoustic evaluation including aeroelastic couplings and scattering effects. Undoubtedly, to satisfy these challenges for future represents the most urgent need for aeroacousticians.

Unfortunately, the maturity level for marine propeller noise prediction is not advanced enough since the hydroacoustic computations are often based on semi-empirical predictions. The widely used hydroacoustic methodology consists of the Bernoulli equation that is applied under the erroneous hypothesis of incompressibility that in principle violates the concept of travelling pressure disturbance at the basis of any sound radiation. While some progress has been recently made in the noise prediction of non–cavitating propellers through the application of efficient tools widely used the aeronautics [9], enhancements are still required for the numerical analysis of cavitation noise. Therefore, the transfer of the aeroacoustics methodologies for rotors and propellers to the study of the noise generated by marine propellers is one of the most urgent need to satisfy.

1.4.2 Objective

The goal of this thesis is to present non–standard applications of the Ffowcs Williams and Hawkings equation for the evaluation of the far–field noise emitted by marine and aeronautical rotorcraft. In detail, the objective is threefold:

1) To provide a hydroacoustics methodology able to predict the hydrodynamically generated noise and to show its superiority with respect to the Bernoulli–based approach, currently adopted by hydroacousticians;

2) To apply such a methodology, in a suitable manner, to predict the impulsive noise caused by the dynamics of the vapor cavity occurring on the blade surface operating in cavitating conditions;

3) To apply the Ffowcs Williams and Hawkings equation to face problems of noise prediction in which the sound field is affected by the scattering of moving, deformable bodies.

Hence, the Ffowcs Williams and Hawkings equation represents the keypoint of the thesis; points 1) and 2) deal with the application of this fundamental equation to marine problems whereas point 3), dealing with scattering phenomenon, may be applied both to aeronautical and naval configurations for which the presence of fuselages or hulls may alter the noise prediction performed in free-field. Although it will be clarified later, here it is worth mentioning that the Ffowcs Williams and Hawkings equation is applied without including sound sources related to volume terms (quadrupole term); such a choice has a threefold motivation: 1) marine propellers are low–speed propeller, hence characterized by very low Mach tip number. In these conditions, previous studies have shown that the contribution of the volume terms is negligible for aeroacoustics predictions; 2) the application of the Ffowcs Williams and Hawkings equation to the study of cavitating propellers is non–conventional and innovative; hence, in the attempt to assess the methodology and derive guidelines for future developments, the inclusion of the non–linear terms is useless at this stage; 3) the application of Ffowcs Williams and Hawkings equation to the study of scattering problems involves the solution of the integral solution of the acoustic analogy on the scatterer surface. The presence of volume contributions in the structure of the solving integral equation requires the knowledge of the interactional aerodynamic field around the scattering body. In this way, the advantages from availability of a scattering modeling disappear and the scattered pressure field may be conveniently provided by the aerodynamic solver. Throughout the thesis, the

fluid-dynamic input for the acoustic solvers is based on subsonic compressible potential flow theory, solved by the boundary element method (BEM); all aerodynamics and hydrodynamics data are obtained by well assessed and validated codes developed at the Italian Ship Model Basin (IN-SEAN) and University of ROMA TRE (Department of Mechanical and Industrial Engineering).

1.4.3 Overview of Dissertation

The remaining chapters of this dissertation are organized as follows.

Chapter 2 presents a theoretical–numerical comparison between the Bernoulli–based approach and the Ffowcs Williams and Hawkings equation for the prediction of noise signature generated by marine skew propellers in steady, non–cavitating conditions. Chapter 3 focus on the capability of the acoustic analogy in predicting cavitation noise produced by sheet cavitation phenomenon for a marine propeller in hull-behind condition. Chapter 4 presents the application of the Ffowcs Williams and Hawkings equation for the evaluation of the scattered pressure fields by rigid or deformable moving bodies. Finally, conclusions and recommendations for future work are given in chapter 5.

Chapter 2

Models for Prediction of Noise Generated Aero–Hydrodynamically: The Ffowcs Williams Hawkings Equation and The Bernoulli Method

The aim of this chapter is to present two different acoustic formulations able to predict the aerodynamically generated noise by moving bodies. These formulations, based on the Ffowcs Williams Hawkings equation (FWHE) and the Bernoulli approach (BEA), are here compared theoretically and numerically to show their potentialities and drawbacks for solving sound radiation problems; rotating blade propulsors operating in fully subsonic regime are considered as acoustic sources of noise, with emphasis on ship/vessel propellers. Hence, the complex emission phenomena related to the high–speed operating conditions are not faced. In the following, the main aspects concerning FWHE and BEA approaches are shown; for the sake of clarity, mathematical manipulations and details are reported in appendix A. Numerical results are shown at the end of the chapter.

2.1   The Ffowcs Williams and Hawkings Equation

The Ffowcs Williams Hawkings equation [1] yields a physically-consistent wave propagation model for the analysis of noise emission due to the interactions between fluid and moving bodies. Derived from mass and momentum conservation principles, the FWHE represents an extension of the Lighthill's acoustic analogy to include the effects of surfaces in arbitrary motions. After decades of applications to aircraft rotors and propellers, the FWHE has been proven to be a very efficient acoustic solver for those problems where sound generated by fluid/solid body interactions plays a primary role.

Let $f(\mathbf{x}, t) = 0$ be a permeable surface moving with velocity $\mathbf{v}$, enclosing both the noise sources and solid surfaces such as the body surface; $f = 0$ is defined such that $\nabla f = \mathbf{n}$, where $\mathbf{n}$ is the outward unit normal vector, and $|\nabla f| = 1$. Furthermore, let us assume $f > 0$ outside the control surface and $f < 0$ inside.

The driving idea in deriving the FWHE is to embed the original bounded problem into unbounded space by extending the definition of the fluid properties (pressure, velocity, density, etc.) such that, inside the moving surface, the flow parameters have the same fluid state as the undisturbed medium; to this aim, the undisturbed medium properties are denoted with the subscript 0. Embedding the original bounded problem into unbounded space allows to derive a wave equation, valid everywhere in the field, that may be conveniently solved by using the Green's function of the wave equation in unbounded space. However, such an extension implies that the flow parameters
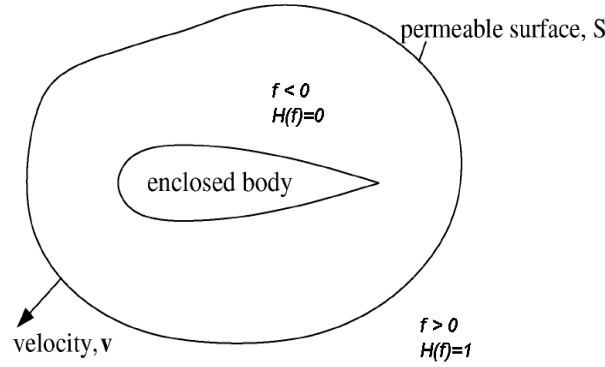
Figure 2.1: *Permeable control surface (from Ref. [10]).*

have artificial discontinuities across the moving surface and hence, all flow parameters must be interpreted as generalized functions [11]. To our purposes, let us assume that the fluid is compressible and undergoes transformations with negligible entropy changes; thus, flow parameters have no discontinuities other than those across the moving surface. As shown in appendix A.1 or, for instance, in Ref. [12], the FWHE may be obtained through an elegant manipulation of the Navier-Stokes equations written in terms of generalized derivatives; this yields the following inhomogeneous wave equation governing noise radiation phenomenon

$$
\begin{aligned}
\Box^2 p' \;=\;& \frac{\overline{\partial}}{\partial t}\left[\rho_0\,\mathbf{v}\cdot\nabla f\,\delta\left(f\right)\right] + \frac{\overline{\partial}}{\partial t}\left[\rho\left(\mathbf{u}-\mathbf{v}\right)\cdot\nabla f\,\delta\left(f\right)\right] \\
&-\;\overline{\nabla}\cdot\left[\mathbf{P}\,\nabla f\,\delta\left(f\right)\right] - \overline{\nabla}\cdot\left[\rho\,\mathbf{u}\otimes\left(\mathbf{u}-\mathbf{v}\right)\nabla f\,\delta\left(f\right)\right] \\
&+\;\overline{\nabla}\cdot\left\{\overline{\nabla}\cdot\left[\mathbf{T}\,H(f)\right]\right\} \quad \forall \mathbf{x}\in\Re^3
\end{aligned}
\tag{2.1}
$$

At the left hand side, p' is the acoustic disturbance defined by $p' = c_0{}^2\hat{\rho}$ with $\hat{\rho} = (\rho - \rho_0)$ representing the density perturbation (the jump in density at $f = 0$) and c_0 and ρ_0 denoting, respectively, the speed of sound and the density of the undisturbed medium. The bars denote generalized differential operators, $\Box^2 = (1/c_0^2)(\overline{\partial}^2/\overline{\partial}t^2) - \overline{\nabla}^2$ represents the generalized wave operator (D'Alembertian operator) whereas $H(f)$ and $\delta(f)$ are Heaviside and Dirac delta functions. In addition, $\mathbf{v}$ is the local velocity of the surface f, $\mathbf{u}$ the local fluid velocity, $\mathbf{P}$ the compressive stress tensor defined by $\mathbf{P} = [(p - p_0)\,\mathbf{I} + \mathbf{V}]$, with $\mathbf{V}$ representing the viscous stress tensor, and $\mathbf{T} = [\rho(\mathbf{u}\otimes\mathbf{u}) +$
$(p - p_0)\mathbf{I} - c_0^2(\rho - \rho_0)\mathbf{I} + \mathbf{V}]$ the Lighthill tensor. If the control surface is assumed to be impermeable and coincident with the body surface, the *transpiration velocity* term $(\mathbf{u} - \mathbf{v})$ becomes zero and the classical form of the FWH equation is obtained

$$
\begin{aligned}
\Box^2 p' \;=\;& \frac{\overline{\partial}}{\partial t}\left[\rho_0\,\mathbf{v}\cdot\nabla f\,\delta\left(f\right)\right] - \overline{\nabla}\cdot\left[\mathbf{P}\,\nabla f\,\delta\left(f\right)\right] + \\
&+\;\overline{\nabla}\cdot\left\{\overline{\nabla}\cdot\left[\mathbf{T}\,H(f)\right]\right\} \qquad\qquad \forall\mathbf{x}\in\Re^3
\end{aligned}
\tag{2.2}
$$

A unified version of the FWH equation may be derived by following the notation of Di Francescantonio [13]; by introducing the following variables

$$
\mathbf{w} = (1 - \frac{\rho}{\rho_0})\mathbf{v} + \frac{\rho}{\rho_0}\mathbf{u}
$$

$$
\mathbf{L} = \mathbf{P} + \rho\mathbf{u}\otimes(\mathbf{u} - \mathbf{v})
$$

$$
\tag{2.3}
$$

12

representing mass-like and momentum fluxes through $f = 0$, Eq. (2.1) may be conveniently re-written as

$$
\begin{aligned}
\Box^2 p' &= \frac{\overline{\partial}}{\overline{\partial t}} \left[\rho_0 \, \mathbf{w} \cdot \nabla f \, \delta \left(f \right) \right] - \overline{\nabla} \cdot \left[\mathbf{L} \, \nabla f \, \delta \left(f \right) \right] + \\
&+ \overline{\nabla} \cdot \left\{ \overline{\nabla} \cdot \left[\mathbf{T} \, H(f) \right] \right\} \qquad\qquad \forall \mathbf{x} \in \Re^3 \qquad (2.4)
\end{aligned}
$$

Equation (2.4) is the general form of the FWHE governing the aerodynamic noise propagation from bodies having general shapes and motions.

2.1.1 Interpretation

The presence of the Dirac and Heaviside functions points out the different nature of the noise source terms at the right side of Eq. (2.4): those having f as support of the Dirac function account for the contribution of the discontinuity surface $f(\mathbf{x}, t) = 0$ in the flow–field while that having f as support of the Heaviside accounts for all the sources outside the surface[1]. The first two terms at the right-side of Eq. (2.4) are called pseudo–thickness and pseudo–loading terms whereas the last one is the quadrupole source term. The pseudo–thickness term describes the contribution of the net mass flux through the surface f, while the pseudo–loading distribution is related to net momentum flux. The mathematical structure of the sources implies that pseudo–thickness and pseudo–loading terms correspond to monopole and dipole non–stationary surface distributions, respectively (whereas the quadrupole term corresponds to a quadrupole distribution). However, the directivity pattern, that is, the angular distribution of the sound field radiated by the sources, is different from those characterizing stationary monopole, dipole and quadrupole, because of the motion of the surface f.

When the surface $f = 0$ coincides with a solid surface (*i.e.*, the body surface), the application of the impermeability condition implies that the normal velocity of the fluid is equal to the normal velocity of the surface ($u_n = v_n$); in this case the monopole term $\dfrac{\partial \left[\rho_0 \, \mathbf{v} \cdot \nabla f \, \delta \left(f \right) \right]}{\partial t}$ accounts for the noise generated by the displacement of the fluid forced by the body passage whereas the dipole term $\overline{\nabla} \cdot \left[\mathbf{P} \, \nabla f \, \delta \left(f \right) \right]$ describes noise resulting from the pressure distribution upon the body surface. The sum of these two contributions provide accurate noise prediction when transonic flow conditions do not occur and the noise is not characterized by turbulence phenomena (see Refs. [14], [15] and [16]). Indeed, when pressure, density and velocity fields surrounding the source of noise are related to high–speed transonic operating conditions or to massive turbulence flow, the inclusion of the non–linear quadrupole volume term is needed.[2] For instance, dealing with rotorcraft in forward flight, the importance of the quadrupole term is well recognized to affect both the waveform shape and amplitude of high–speed impulsive (HSI) noise where the occurrence of shock delocalization and the requirement of accounting for multi–emissive supersonic sources make the noise computation a very difficult task [17], [18]. Now, some considerations on the choice of the more appropriate formulation to be used (permeable or rigid surface one) are pointed out. Apparently, there is no reason why a fictitious surface $f = 0$ not coincident with the boundary of the moving body, should be used. The convenience of using a porous non–deformable surface results by observing that the FWHE governs noise propagation phenomena outside the surface $f = 0$. Any source enclosed by $f = 0$ affects the noise field only through surface terms (thickness and loading) while sources of noise outside $f = 0$ are modeled through volume terms (quadrupole). Hence, by moving the control surface outwards, the effects coming from quadrupole sources surrounded by $f = 0$ can be accounted for by surface source terms. For rotorcraft applications, it has been proven that the noise generated by the volume quadrupole

---

[1]By assumption, $\mathbf{T} = 0$ inside the surface $f(\mathbf{x}, t) = 0$

[2]The nonlinearity is referred to the fact the knowledge of $\mathbf{u} \otimes \mathbf{u}$ is required.

distribution is significant only in regions of transonic flow; it is generated mainly at the shock surfaces but also near the leading edge toward the blade tip. Hence, if the control surface is placed to enclose the blade and all transonic (non linear) regions of flow, the volume outside it is fully subsonic and the noise contribution from quadrupole sources becomes negligible; thus, the permeable FWH formulation allows to not account for any volume contribution.[3] A similar result could be obtained by using the Kirchhoff method for moving bodies [5]; in fact, as shown in Refs. [6] and [12], the FWH and the Kirchhoff formulation are equivalent when the integration surface is place in the linear region of the flow (where the input data are compatible with the wave equation). However, when the linear region is far from the body, as for transonic helicopters rotor noise prediction, obtaining a CFD solution at the control surface is computationally too time consuming and could be not enough accurate. This problem may be overcame by noting that the most intense quadrupole sources (responsible for noise generation and distortion of the acoustic waveform) are in the vicinity of the blades; therefore, if the control surface is placed to enclose the volume of intense quadrupoles in the FWHE, the level of acoustic pressure may be accurately computed. The role of the weaker quadrupoles which are further away from the body is primarily to provide a small distortion to the acoustic waveform. Hence, even when the integration surface is fairly close to the noise generating surface, the external quadrupoles may be neglected. In comparison, the prediction of the acoustic pressure through the Kirchhoff formula might be substantially in error if the Kirchhoff surface is placed inside the nonlinear region: the nature and the order of magnitude of this error may be hard to estimate or even recognize [6].

On the contrary, for those problems dealing with fully subsonic flows where effects as turbulence, vorticity, vapor bubbles, viscosity, variation in the local sound speed, scattering effects etc., do not affect the noise the linear no porous FWH equation given by Eq. (2.2) remains a useful tool for describing sound propagation.

2.1.2 Integral Solution

Different integral solutions, suitable for numerical implementation, may be considered for the FWHE; among them, formulation 1A proposed by Farassat (see Refs. [19] and [20]) represents the most widely used integral representation for the acoustic disturbance. An exhaustive and useful review of the alternative FWH–based integral formulations is given in Ref. [21].

An equivalent integral formulation, proposed by Morino and Gennaretti for the combined analysis of the aerodynamics and aeroacoustics [22], [23] is here applied for the solution of the FWHE. The motivation in using this formulation is that it has been applied to the aerodynamic problem in order to obtain the aerodynamic input required by the aeroacoustic problem. Specifically, for a moving permeable surface S enclosing the noise sources (both on the body surface and, eventually, around it) in a volume $\mathcal{V}$, Eq. (2.1) or equivalently Eq. (A.19) governs the analysis of the aeroacoustic field in $\Re^3 \setminus \mathcal{V}$ moving in arbitrary motion with respect to the air space. As shown in appendix A.3 the solution of Eq. (2.1) is given by the following boundary integral formulation expressed in the space rigidly moving with the domain $\mathcal{V}$ (body–space, SRC)

$$
\begin{aligned}
p'(\mathbf{x}, t) = {} & \int_0^\infty \int_{\Re^3} \check{G}\, \chi d\mathcal{V} dt - \int_S \left\{ (\mathbf{Pn}) \cdot \nabla \hat{G} - (\dot{\mathbf{Pn}}) \cdot \nabla \vartheta\, \hat{G} \right\}_\vartheta \mathrm{d}S \\
& - \rho_0 \int_S \left\{ \mathbf{v} \cdot \mathbf{n}\, \mathbf{v} \cdot \nabla \hat{G} + [\mathbf{v} \cdot \mathbf{n}\, (1 - \mathbf{v} \cdot \nabla \theta)]^{\cdot}\, \hat{G} \right\}_\vartheta \mathrm{d}S \\
& - \int_S \left\{ \rho \mathbf{u}^- \cdot \mathbf{n}\, \mathbf{u}^+ \cdot \nabla \hat{G} + [\rho \mathbf{u}^- \cdot \mathbf{n}\, (1 - \mathbf{u}^+ \cdot \nabla \vartheta)]^{\cdot}\, \hat{G} \right\}_\vartheta \mathrm{d}S \qquad (2.5)
\end{aligned}
$$

where the suffix *y* appearing in appendix A.3, and denoting the images of vectors and tensors in SRC, has been omitted. In Eq. (2.5) ϑ represents the time delay required by an acoustic

---

[3]The permeable formulation based on the use of a porous control surface enclosing the fluid regions where the Lighthill's tensor is not negligible, is known as Kirchoff-Ffowcs Williams Hawkings formulation (KFWH).

disturbance released from a source in $\mathbf{y}$ to reach the observer point $\mathbf{x}$ at current time t; thus, $\{...\}_\vartheta$ denotes that the kernel of the integrals are evaluated at the emission time $\tau = t - \vartheta$. The first integral at the right hand side of Eq. (2.5) accounts for the noise contribution due to volume terms (see section A.3); $\mathbf{n}$ is the outward unit normal vector on the permeable surface S. Furthermore, $\hat{G}$ indicates the retarded Green function

$$\hat{G} = \left[-\frac{1}{4\pi\, r} \left(\frac{1}{1 - M_r} \right) \right]_\vartheta \tag{2.6}$$

where $r = |\mathbf{r}|$, with $\mathbf{r} = \mathbf{x}(t) - \mathbf{y}(\tau)$, and $M_r = \dfrac{\mathbf{v}}{c_0} \cdot \hat{\mathbf{r}}$ denotes the surface Mach number in the direction of radiation. In addition, the symbol $(\dot{\ })$ denotes time derivation whereas $\mathbf{u}^- = (\mathbf{u} - \mathbf{v})$ and $\mathbf{u}^+ = (\mathbf{u} + \mathbf{v})$.

Choosing the surface S to be coincident with the body surface, the impermeability condition implies that $\mathbf{u}^- = 0$; in addition, neglecting the quadrupole contribution to the radiated noise, the prediction of the noise field in may be expressed by the thickness and loading noise terms

$$p'(\mathbf{x}, t) \cong p_T{}'(\mathbf{x}, t) + p_L{}'(\mathbf{x}, t) \tag{2.7}$$

where

$$p_T{}'(\mathbf{x}, t) = -\rho_0 \int_S \left\{ \mathbf{v} \cdot \mathbf{n}\, \mathbf{v} \cdot \nabla \hat{G} + [\mathbf{v} \cdot \mathbf{n}\, (1 - \mathbf{v} \cdot \nabla \vartheta)]\dot{}\, \hat{G} \right\}_\vartheta \mathrm{d}S \tag{2.8}$$

and

$$p_L{}'(\mathbf{x}, t) = -\int_S \left\{ (\mathbf{P}\mathbf{n}) \cdot \nabla \hat{G} - (\dot{\mathbf{P}}\mathbf{n}) \cdot \nabla \vartheta\, \hat{G} \right\}_\vartheta \mathrm{d}S \tag{2.9}$$

The integral solution given by Eq. (2.5) allows the prediction of the acoustic disturbance outside the surface S by a linear superimposition of three noise contributions; they are interdependent and their physical basis provides valuable guidance to design quieter rotors and propellers. The separation of the source terms also is an advantage numerically because not all terms must be computed at all time if a particular source does not contribute to the sound field. In Eqs. (2.8), (2.9) the kernels of the solving integrals depend on geometry and kinematics of the moving surface S, as well as on the pressure distribution and velocity field upon it. It is notable that the proposed solving formulation is completely equivalent to the formulation 1A by Farassat; such equivalence is shown in appendix A.4. These aerodynamics quantities are assumed to be known, either from experimental data or from computational results. In the second case, the output of an aerodynamic code is the input for the aeroacoustic one. This provides a strong motivation for attempting an integration of aerodynamics and aeroacoustics.

2.2   The Bernoulli Equation–based Approach

The prediction of the pressure disturbance generated by moving bodies may be also achieved through a unified aerodynamic and aeroacoustic formulation. For aeronautical applications it has been introduced by Morino and Gennaretti [23] and is based on the assumption of compressible, potential flows. When flow separation phenomena do not occur, the influence of viscous effects on the pressure distribution upon the body surface may be neglected and hence the assumption of potential flow allows an accurate aerodynamic description.[4] Furthermore, the assumption of (compressible) inviscid flow is appropriate for aeroacoustics; in fact, it is well known that viscous effects are usually negligible in a sound field because the pressure represents a far greater stress field than that induced by viscosity at frequencies of most practical interest [24].

The first step of the unified aerodynamic-aeroacoustic solution procedure consists in determining the velocity potential on the body, by a boundary integral equation approach. Then, the integral representation for the potential yields the potential distribution in the field and the Bernoulli theorem gives the corresponding acoustic pressure. This methodology is here applied for the aerodynamic and aeroacoustic analysis of propellers; mathematical details are extensively outlined in appendix A.2.

2.2.1   Differential Formulation

In the absence of shock waves, an inviscid nonconducting fluid that is initially at rest remains isentropic and irrotational at all times (except for wake points). Under these assumptions, the velocity field $\mathbf{u}$ may be expressed in terms of a scalar potential ϕ, as $\mathbf{u} = \nabla\phi$. It may be shown (see, for instance, Ref. [23]) that in a frame of reference connected to the undisturbed medium the velocity potential is governed by the following differential equation

$$\nabla^2\phi - \frac{1}{c_0^2}\frac{\partial^2\phi}{\partial t^2} = \sigma \tag{2.10}$$

where σ accounts for all the non–linear terms that in aerodynamic applications are important in the transonic regime. The differential problem is closed by suitable boundary conditions. Three surfaces has to be considered: the surface at infinity, the body surface and the potential wake surface. At infinite distance from the body, the perturbation velocity is zero, hence $\mathbf{u} = 0$, *i.e.,* $\phi = 0$; then assuming that the body surface $\mathcal{S}$ is impermeable, it results that $\frac{\partial\phi}{\partial n} = \mathbf{v}\cdot\mathbf{n}$ where $\mathbf{v}$ is the local velocity of a point on the body surface and $\mathbf{n}$ the local outward unit normal vector. For lifting bodies, the vorticity generated on the body forms a surface on both sides of which the flow is necessarily potential; this surface represents the potential wake surface $\mathcal{S}_W$. The boundary conditions on the wake state the absence of penetration (the wake cannot be crossed by fluid particles) and of pressure discontinuity. These, in terms of velocity potential, yield (see appendix A.2)

$$\Delta\left(\frac{\partial\phi}{\partial n}\right) = 0 \tag{2.11}$$

$$\frac{D_W(\Delta\phi)}{Dt} = 0 \tag{2.12}$$

where $\frac{D_W(\Delta\phi)}{Dt} = \frac{\partial}{\partial t} + \mathbf{u}_W\cdot\nabla$, with $\mathbf{u}_W$ being the velocity of a point of a wake $\mathbf{x}_W$ (*i.e.,* the average of the velocity on the two side of the wake). Equation (2.12) is the evolution equation

---

[4]Note that the aerodynamic loads may be accurately described only by including friction effects.

for $\Delta\phi$ and states that it is constant in time following a wake point and equal to the value it had when $\mathbf{x}_W$ left the trailing edge. The value of $\Delta\phi$ at the trailing edge is obtained by using the Kutta condition hypothesis that no vortex filament exists at the trailing edge [25]; this implies that the value of $\Delta\phi$ on the wake and on the body are equal at the trailing edge, that is

$$\lim_{\mathbf{x}_W \to \mathbf{x}_{TE}} \Delta\phi(\mathbf{x}_W, t) = \phi_u(t) - \phi_l(t) \tag{2.13}$$

and

$$\Delta\phi(\mathbf{x}_W, t) = \Delta\phi(\mathbf{x}_{TE}, t - \tau_w) \tag{2.14}$$

where ϕ_u and ϕ_l are the potential at the upper and lower side of the wake, $\mathbf{x}_{TE}$ denotes a wake point located at the blade trailing edge and τ_w the convection time between wake points $\mathbf{x}_W$ and $\mathbf{x}_{TE}$.

2.2.2 Boundary Integral Solution

In order to solve the potential problem it is convenient to recast Eq. (2.10) into the following equivalent infinite–space differential equation (see appendix A.2)

$$
\begin{aligned}
-\Box^2\hat{\phi} &= \sigma\, H(f) + \nabla\phi\cdot\mathbf{n}\,\delta(f) + \nabla\cdot[\phi\,\mathbf{n}\,\delta(f)] + \\
&- \frac{1}{c_0^2}\left\{-\dot{\phi}\,\mathbf{v}\cdot\mathbf{n}\,\delta(f) + [-\phi\,\mathbf{v}\cdot\mathbf{n}\,\delta(f)]^{\cdot}\right\} \quad \forall\mathbf{x}\in\Re^3
\end{aligned}
\tag{2.15}
$$

where $\hat{\phi}(\mathbf{x}, t) = H(f)\phi(\mathbf{x}, t)$, and $\sigma = [(c^2 - c_0^2)\nabla^2\phi + 2\mathbf{u}\cdot\dot{\mathbf{u}} + \mathbf{u}\cdot\dfrac{\nabla u^2}{2}]/c^2$. Then, integrating Eq. (2.15) through the formulation proposed by Morino and Gennaretti and shown in appendix A.3, yields the following boundary integral representation for the potential ϕ

$$
\begin{aligned}
\phi(\mathbf{x}, t) &= \int_V \hat{G}\,[\sigma]_\vartheta\, dV + \int_S \left[\frac{\partial\phi}{\partial\tilde{n}}\hat{G} - \phi\frac{\partial\hat{G}}{\partial\tilde{n}}\right]_\vartheta\, \mathrm{d}S + \\
&+ \int_S \left[\hat{G}\frac{\partial\phi}{\partial t}\left(\frac{\partial\vartheta}{\partial\tilde{n}} + 2\frac{\mathbf{v}\cdot\mathbf{n}}{c_0^2}\right)\right]_\vartheta\, \mathrm{d}S \\
&+ \frac{1}{c_0^2}\int_S \left[\phi\,\hat{G}\frac{\partial}{\partial t}[\mathbf{v}\cdot\mathbf{n}\,(1-\mathbf{v}\cdot\nabla\vartheta)]\right]_\vartheta\, \mathrm{d}S
\end{aligned}
\tag{2.16}
$$

where the integrals are expressed in a frame of reference fixed to the body.

In the equation above the symbols maintain the same meaning as in Eq. (2.5), and in addition $\dfrac{\partial}{\partial\tilde{n}} = \dfrac{\partial}{\partial n} - \dfrac{1}{c_0^2}(\mathbf{v}\cdot\mathbf{n})(\mathbf{v}\cdot\nabla)$. For bodies without wake (non-lifting), Eq. (2.16) is an integral representation of ϕ anywhere in the field, in terms of the values of ϕ, $\dfrac{\partial\phi}{\partial\tilde{n}}$ and $\dfrac{\partial\phi}{\partial t}$ on $\mathcal{S}$, and of σ in $\mathcal{V}$. If $\mathbf{y}^*$ approaches $\mathcal{S}$, one obtains a compatibility condition between the above quantities. If $\sigma = 0$ this compatibility condition is an integral equation for the unknown ϕ, as $\dfrac{\partial\phi}{\partial n}$ is known from the boundary condition.

The extension of the formulation to lifting bodies requires to account for the presence of the potential wake surface; in the following, propellers are considered as lifting bodies. In this case, let us consider the presence of N disjoint, closed rigid surfaces S_i and S_i^W surrounding, respectively, the volume occupied by the i-th propeller blade and the volume occupied by a thin fluid region containing the corresponding i-th wake surface. It may be shown [22] that the integral representation for the solution of Eq. (2.10)) has the form

$$\phi(\mathbf{x}, t) = \sum_i^N \left(\mathcal{I}_i^S + \mathcal{I}_i^W\right) \tag{2.17}$$

Each integral contribution appearing in equation (2.17) may be evaluated in a different frame of reference. In the case of rigid surfaces, the most suitable frame of reference is attached to the surface where the integral is evaluated (*i.e.,* the frame where the integration domain does not depend on time). Thus, under the assumption of a prescribed, non–deforming wake shape and a propeller in axial flow, it is convenient to use a propeller-fixed frame of reference to evaluate both the blade and wake contributions to the velocity potential field.[5] In this frame, the most general expression for the blade surface contributions $\mathcal{I}_i^S$ is given by Eq. (2.16). The wake contribution $\mathcal{I}^W$ may be obtained by coupling Eq. (2.16) with the wake boundary conditions (note we have assumed the wake to be rigidly connected with the propeller blades). In steady-flow conditions, it has the form

$$\mathcal{I}_W(\mathbf{x}, t) = - \int_{\mathcal{S}_W} \left[\Delta\phi \, \frac{\partial \hat{G}}{\partial \tilde{n}} \right]_{\vartheta} \mathrm{d}S \qquad (2.18)$$

By positioning point $\mathbf{y}$ on the body surface, Eq. (2.17) is used as a *boundary integral equation* for ϕ. This step enables the evaluation of the velocity potential on the integration domain itself. Once ϕ is known on S, the same equation appears as an *integral representation* of the potential and can be used to determine such a variable at any point in the field. At this stage the pressure p can be determined through the Bernoulli theorem (written for compressible, isentropic flows)

$$\frac{\partial\phi}{\partial t} + \frac{1}{2}|\mathbf{u}|^2 + \frac{\kappa}{\hat{\gamma}}p^{\hat{\gamma}} = \frac{1}{\hat{\gamma}}\frac{p_0}{\rho_0} \qquad \text{where:} \qquad \hat{\gamma} = \frac{\gamma - 1}{\gamma} \quad ; \quad \kappa = \frac{p_0^{1/\gamma}}{\rho_0} \qquad (2.19)$$

where γ denotes the specific heat ratio.

2.3 Comparison Between the two Aeroacoustics Methodologies

In this section some commonalities and differences between the acoustic formulation based on the Ffowcs Williams Hawkings equation and the unified aerodynamic-aeroacoustic methodology, are outlined from a theoretical standpoint. Their potentialities and drawbacks are further shown by means of numerical results. Within the context of potential compressible aerodynamics and basing on sections 2.1 and 2.2, it comes out that there exists a symmetry in the way of computing the noise field through the FWHE and BEA. Both methods are governed by the same differential operator, that is an inhomogeneous wave equation, describing the propagation of the pressure disturbance and velocity potential in the flow–field, respectively. This implies that the corresponding integral solutions have the same mathematical structure. The FWHE directly computes the noise field by using the integral formulation as a representation for p' once the required aerodynamics input are provided, whereas BEA first requires the solution of an integral equation to determine ϕ on the body; then the Bernoulli equation allows the computation of the sound once the potential is evaluated everywhere in the field. To this aim, Eq. (2.17) is used as integral representation for ϕ. Hence, in the solution procedure of the unified aerodynamic-aeroacoustic approach, the step involving the use of the Bernoulli theorem represents the acoustic solver of the method; for the sake of clarity, Fig. 2.2 emphasizes the main aspects of the methodologies. As a matter of fact, both acoustic solvers are based on the same conservation laws and represents two fully equivalent approaches for dealing with aeroacoustics phenomena; as a consequence the same prediction of propeller noise is expected. The main difference between the two approaches is that the BEA is

---

[5]The same arguments are valid for a helicopter rotors in hovering. In forward flight condition, the formulation is more complicated because in the body space the wake surface is not time independent. However, in this case, the wake may be assumed to be time independent in the air space.
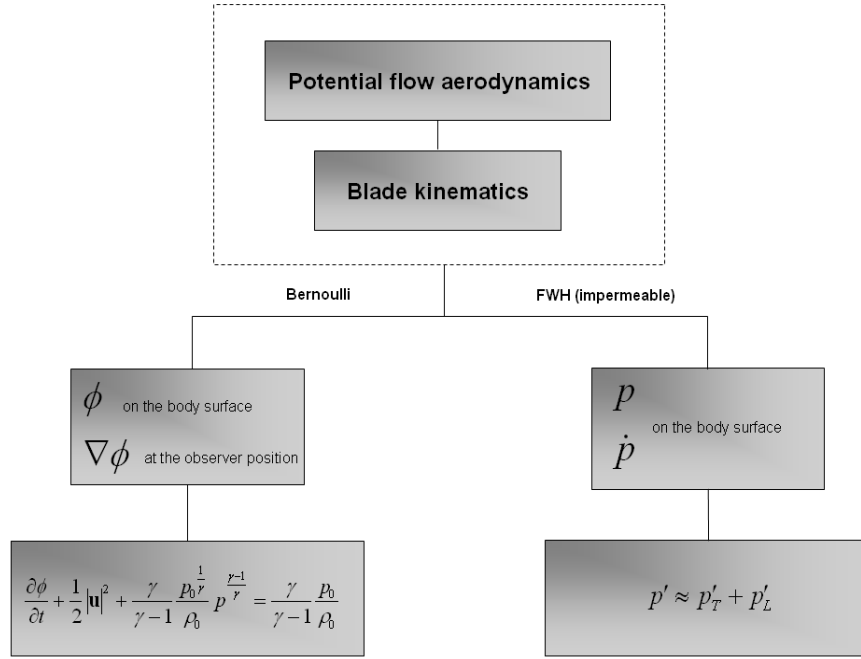
Figure 2.2: *Comparison between the FWHE and the Bernoulli methods: flow-chart.*

formulated in terms of velocity potential whereas the FWHE directly involves the main variable of the aeroacoustic problem, that is the acoustic disturbance p'. From a mathematical point of view, such a circumstance implies the introduction in the BEA of a discontinuity surface for ϕ represented by the wake surface that affects both steps of the solution procedure through the term (2.18). The FWHE has the advantage of not requiring information on the presence of the wake because the only discontinuity surface for the pressure is the boundary of the body, being the potential wake a zero–thickness surface across which the pressure is continuous; thus, it does not exist a noise contribution from the wake. It is worth noting that the loading noise term given by Eq. (2.9) indirectly accounts for the presence of the potential wake through its influence on the evaluation of the blade pressure distribution (*i.e.,* the computation of $\mathbf{P}$). Although the potential wake does not affect the thickness and loading noise contributions, its presence, in terms of noise, may be accounted for through the non–linear term $(\rho\mathbf{u}\otimes\mathbf{u})$ in the quadrupole contribution. Akin to the quadrupole noise contribution due to the body motion, the noise related to the presence of the potential wake may be reasonably neglected when the sources of noise are not related to high–speed operating conditions or massive turbulence flow, since $(\rho\mathbf{u}\otimes\mathbf{u})$ is negligible respect to the perturbation velocity field $\mathbf{u}$. Note that the KFWH formulation directly accounts for the presence of the potential wake through the velocity and pressure fields on the control surface. On the other hand, differently from the Bernoulli approach, the KFWH formulation could be used to predict the noise field induced by aerodynamic configurations where non–linear phenomena as turbulence, massive flow separation, non–homogeneity in the local sound speed, etc., are at the basis of the noise generation; in these cases, the potential flow theory falls and the required data input on the permeable surface of the KFWH method may be provided by CFD solvers (for instance, full-potential, RANSE). In any case, in the frame of aeroacoustics, these are aerodynamic issues rather than aeroacoustic one.

2.4   Underwater Propeller Noise: Marine Scenario

Despite the outstanding importance that propeller-induced noise analysis has for a wide class of marine applications, the lack of theoretical models addressing the problem under a rigorous, physically-consistent approach is widely recognized. Undoubtedly, the propulsor represents one of the main sources of noise generated both by surface and underwater seacraft. A hydroacoustic analysis of realistic configurations does not only concern the kinematic and dynamic behaviour of the rotating blades but involves a lot of different and very complex phenomena. A marine propeller operates in the wake of a hull: the incoming flow is characterized by an enormous turbulence and vorticity which largely affect both the propeller-induced noise and the propagation phenomena. The proximity of the hull and, eventually, of the free surface to the propeller can cause some notable scattering effects, with a direct influence on noise spectra and directivity. Moreover the possible occurrence of cavitation (i.e., vaporization occurring in fluid regions where pressure drops below vapor pressure value) completely changes the hydroacoustic behaviour of the body. The formation, growth and collapse of vapor bubbles can provide large pressure peaks propagating from the blades and increase the noise level of two orders of magnitude with respect to the same propulsor operating in non-cavitating conditions.

In spite of this very complex scenario, the numerical models presently used for the hydroacoustic analysis of marine propellers are rather poor. The propeller is often considered as a pointwise source with given intensity and the numerical solutions are often provided in the *filtering* frequency domain, where the acoustic pressure time history is usually reduced to a single, representative value. The physically–consistent hydroacoustic modelling widely used by the naval community is based on the unified approach previously considered; in fact, although conventional in the aeronautical context, the FWH equation represents a no standard solving approach for naval applications. In a recent paper [26] the authors cite the FWH equation as a not easy method and erroneously declare that the noise integrals must be determined on a retarded surface. Dealing with the Helmholtz equation and hull scattering effects, Spivack *et al.* [8] recognize in the FWH approach a complete solution to the combined hydrodynamic-acoustic analysis, but define the numerical problems difficult and challenging. Compared with the extensive amount of literature concerning the application of the FWHE to the prediction of aeronautical propeller noise, works concerning marine propellers noise are hard to find; among them, Seol *et al.* [9], investigate the non-cavitation noise of underwater propeller by coupling potential–based panel method with time–domain acoustic analogy to predict the noise generated by single and duct propellers in a non–uniform flow condition. As a matter of fact, the integration of the FWH equation yields to simple and powerful computing tools, which make the evaluation of the acoustic pressure in the far field a pure post-processing of the hydrodynamic data. Looking at the wide literature available for aeroacoustics, it is clear that the actual problems concerning the numerical solutions are mainly related to the quadrupole source terms whose contribution, however, becomes relevant only at a high blade rotational speed. In that case, the singular behaviour of sources rotating at transonic speed makes the evaluation of the acoustic pressure field a very complex problem [27]. Such operating conditions, however, never occur for a marine propeller. Differently from aeronautical propellers that usually operate in unperturbed incoming flow, marine propellers are subjected to an onset flow represented by the wake hull; therefore, it is non–uniform and characterized by turbulence and vorticity. These flow conditions largely affect the propeller-induced noise and propagation phenomena. Apart from the frame–noise associated to the development of the boundary layer around the hull surface and not accounting for the acoustic scattering effect given by the hull-plate, the presence of the hull may be modeled in the prediction of the propeller-induced noise, indirectly, by considering the propeller as an isolated body subjected to a spatially non-uniform onset flow [28].

Although the Bernoulli equation is at length used by the hydroacousticians to predict underwa-

ter propellers noise, it is worth observing that the incompressible flow assumption is generally adopted, thus neglecting *a priori* any propagation phenomena taking place in the flow field. At this stage, a fundamental aspect of the problem should be pointed out. Due to the nature of what we call *sound*, an actual noise prediction could not be performed by assuming a constant density field. Sound is a pressure disturbance which *propagates* at a finite speed in the flow field, and the propagation velocity (the speed of sound) is just given by $c^2 = dp/d\rho$. This implies that the pressure disturbances and the corresponding propagation phenomena are necessarily related to a density variation. Therefore, the use of a solver based on the incompressibility assumption violates the theoretical basis of any (hydro)acoustic analysis providing an evaluation of an *instantaneous* ($c \to \infty$) pressure field which, theoretically speaking, should not be in any case identified as an *acoustic* pressure. This is especially true in a naval context where, as previously noted, the noise propagation mechanisms can be heavily affected by the hull and/or free surface scattering and the presence of a non homogeneous flow. Fortunately, the requirement of a variable density for hydroacoustic purposes may be suitably combined with the incompressibility assumption adopted within any naval hydrodynamic code. In fact, in the so-called acoustic *hybrid* approaches the evaluation of the noise "source" terms and their subsequent "propagation" in the (acoustic) far field represent two distinct steps of the computing strategy. If no compressibility effect represents a source of sound on its own (like, for instance, the shock waves occurring on a high speed aeronautical propeller), this separate evaluation of the hydrodynamic and hydroacoustic aspects of the problem enables the achievement of a very accurate noise prediction despite the use of a constant density in the hydrodynamic solver. Thus, due to the low rotational Mach number at which a marine propeller usually operates, the noise generation is only related to the blade geometry/kinematics and to a hydrodynamic load which can be suitably determined through an incompressible solver. The subsequent noise propagation, however, should include the effects of the compressibility delays although in practice these values could be even negligible (depending on the relative source-observer distance). In detail, a correct estimation of the pressure disturbance should account for the following steps: i) Evaluation of the velocity potential ϕ upon the blade under the incompressibility assumption. In this case, the retarded time ϑ and M_r are zero, and Eq. (2.17) becomes

$$\phi(\mathbf{x}, t) \;=\; \int_S \left(\frac{\partial \phi}{\partial n} G - \phi \frac{\partial G}{\partial n} \right) \mathrm{d}S - \int_{\mathcal{S}_W} \Delta \phi \, \frac{\partial G}{\partial n} \mathrm{d}S \qquad (2.20)$$

where $G = -1/4\pi r$, thus yielding the potential field as induced by a superposition of sources over the body surface and of doublets over the body and wake surfaces. In addition, the Bernoulli theorem reads

$$\frac{\partial \phi}{\partial t} + \frac{1}{2}|\mathbf{u}|^2 + \frac{p}{\rho_0} \;=\; \frac{p_0}{\rho_0} \qquad (2.21)$$

Due to the low rotational speed, Eq. (2.20), used as integral equation, and Eq. (2.21) may be applied to determine the hydrodynamic load of a marine propeller. ii) Computation of the acoustic pressure field. At this stage, the velocity potential and consequentially, the pressure disturbance, have to be propagated into the field. To accomplish this, a theoretically correct estimation of the acoustic disturbance must necessarily account for Eqs. (2.16), (2.17) and (2.18) to determine ϕ *in the far field*, disregarding the incompressibility assumption. Then, the use of Eq. (2.19) close the hydroacoustic problem.

Unfortunately, in naval applications the hydrodynamic and hydroacoustic problems are usually not treated in a separate way, and the incompressibility assumption is erroneously applied to both the solutions without exception. In this thesis, an alternative strategy to compute marine propellers noise is proposed: it consists in using the FWHE as hydroacoustic solver once the step i) of the unified approach has been performed. In this way the incompressible potential flow theory,

correctly governs the evaluation of the hydrodynamic loads on propeller blades whereas the hydroacoustic problem is directly modeled through the wave equation for the pressure disturbance. In order to show capabilities and drawbacks of the proposed approach respect to the widely used Bernoulli method, the two solving strategies are compared numerically in the following section.

2.5 Numerical Results

In view of the suggested application of the FWHE to marine propellers noise, here it is presented a numerical comparison of noise predictions provided by the FWHE and the unified, Bernoulli–based methodology, concerning both an aeronautical and a marine propeller. Keeping in mind the theoretical basis of a hydroacoustic analysis, the unified approach outlined in the previous section will be used under the assumption of an incompressible flow. Such choice seems to be inconsistent with the considerations given in section 2.4; however it has a triple justification. First, the use of Eqs. (2.20) and (2.21) is much simpler with respect to the compressible potential formulation and allows a notable reduction of the computational effort. In this way, an analysis on the influence of different numerical parameters can be reasonably carried out. Second, the acoustic pressure determined through the incompressible Bernoulli theorem should not exhibit any appreciable discrepancy with respect to the FWH solutions, provided that the compressibility delays are limited to some negligible value. Hence, by accounting for observers very close to the propeller disc such a numerical comparison does make sense. Third, it will be shown that the numerical differences between the hydroacoustic formulations are primarily related to the wake modeling; thus, they concern both the compressible and incompressible flow analysis. For this reason, it is somehow useless at this stage to focus the attention on the complex Eqs. (2.16), (2.17) and (2.18) since the differences between the two approaches can be conveniently pointed out by limiting the analysis to the incompressible formulation. In the following, a validation analysis of the (impermeable) FWH prediction tool used in this work is presented; the emphasis is on the acoustic analogy approach because an extensive validation of the combined methodology used to provide BEA numerical predictions is presented, for instance, in Refs. [29], [30], [31]. Then, after the analysis of the influence of the wake model on the aero–hydroacoustic prediction, the approximations related to the incompressibility assumption for the evaluation of the far field pressure will be investigated through the use of the FWH formulation, re-written in an incompressible form. First, the numerical algorithm applied to obtain the discrete form of the integral formulations is present.

Discretization Strategy

The numerical investigation is performed by applying a zero-th order boundary element method (BEM) for the discretization of the boundary integral formulation given by Eq. (2.7), for the FWHE, and Eq. (2.17) for the unified approach. First, let us consider the FWHE; the discretization is obtained by dividing the moving body surface S into quadrilateral panels and assuming p' to be piecewise constant. Then, the integral equation is solved by requiring that the equation be satisfied at the center of each body element (collocation method). Specifically, discretizing S into M panels S_j, at the center of k-th element Eq. (2.7) yields

$$p'_k(t) = \sum_{j=1}^{M} C_{kj}\, p'_j(t - \vartheta_{kj}) + \sum_{j=1}^{M} D_{kj}\, \dot{p}'_j(t - \vartheta_{kj}) + \sum_{j=1}^{M} T_{kj} + \sum_{j=1}^{M} R_{kj} \qquad (2.22)$$

The function $f(t - \vartheta_{kj})$ indicates that f must be evaluated at the emission time $(t - \vartheta)$ whereas the coefficients are defined in the following way

$$
\begin{aligned}
C_{kj} &= -\int_{S_j} \left\{ \nabla \hat{G}_{kj} \cdot \mathbf{n} \right\}_{\vartheta_{kj}} \mathrm{d}S \\[4pt]
D_{kj} &= \int_{S_j} \left\{ \nabla \hat{\vartheta} \cdot \mathbf{n}\, \hat{G}_{kj} \right\}_{\vartheta_{kj}} \mathrm{d}S \\[4pt]
T_{kj} &= -\rho_0 \int_{S_j} \left\{ \mathbf{v} \cdot\, \mathbf{n} \mathbf{v} \cdot \nabla \hat{G}_{kj} \right\}_{\vartheta_{kj}} \mathrm{d}S \qquad (2.23) \\[4pt]
R_{kj} &= -\rho_0 \int_{S_j} \left\{ [\mathbf{v} \cdot \mathbf{n}(1 - \mathbf{v} \cdot \nabla \theta)]\dot{}\, \hat{G}_{kj} \right\}_{\vartheta_{kj}} \mathrm{d}S
\end{aligned}
$$

where $\hat{G}_{kj} = \hat{G}(\mathbf{x}_k, \mathbf{x})$. The core of the algorithm is the evaluation of the emission time that represents a typical root-finding problem for equation

$$\frac{|\mathbf{x}(t) - \mathbf{y}(t - \vartheta)|}{c_0} - \vartheta = 0 \tag{2.24}$$

Because of the blade rotational motion, an iterative procedure must be used. Starting from the initial delay $\vartheta = 0$ and the corresponding positive root $|\mathbf{r}|/c_0$, the search for the root proceeds backwards with a prescribed time step up to the first sign inversion. Thus, the emission time is captured through the usual bisection method, until a specified error condition is satisfied. The subsonic speed of the source point assures the existence of a single root for Eq. (2.24).

Similarly, the discretization of Eq. (2.17) is obtained by dividing into M panels the body surface S and into N panels the potential wake $\mathcal{S}_W$. This operation yields the following discretized integral representation

$$
\begin{aligned}
\phi_k(t) \;=\; & \sum_{j=1}^{M} B_{kj}\,\psi_j(t - \vartheta_{kj}) + \sum_{j=1}^{M} C_{kj}\,\phi_j'(t - \vartheta_{kj}) \\
& + \sum_{j=1}^{M} D_{kj}\,\dot{\phi}_j'(t - \vartheta_{kj}) + \sum_{l=1}^{N} F_{kl}\,\Delta\phi_l^{TE}(t - \pi_{kl})
\end{aligned}
\tag{2.25}
$$

where ψ_j denotes $\left.\dfrac{\partial\phi}{\partial\tilde{n}}\right|_{\mathbf{y}_j}$ and $\Delta\phi_l^{TE}$ represents the value of $\Delta\phi^{TE}$ at the trailing edge point from which $\mathbf{x}_W$ left the trailing edge; in addition, π_{kl} is the time delay given by the sum of compressibility effects and the time of convection of wake points.

The coefficients are indeed defined as

$$
\begin{aligned}
B_{kj} \;=\; & \int_{S_j} \left\{ \hat{G}_{kj} \right\}_{\vartheta_{kj}} \mathrm{d}S \\
C_{kj} \;=\; & \int_{S_j} \left\{ -\frac{\partial \hat{G}_{kj}}{\partial \tilde{n}} + \frac{1}{c_0^2}\,\hat{G}_{kj}\,\frac{\partial}{\partial t}[\mathbf{v}\!\cdot\!\mathbf{n}(1 - \mathbf{v}\!\cdot\!\nabla\vartheta)] \right\}_{\vartheta_{kj}} \mathrm{d}S \\
D_{kj} \;=\; & \int_{S_j} \left\{ \hat{G}_{kj} \left(\frac{\partial \vartheta}{\partial \tilde{n}} + 2\frac{\mathbf{v}\cdot\mathbf{n}}{c_0^2} \right) \right\}_{\vartheta_{kj}} \mathrm{d}S \\
F_{kl} \;=\; & -\int_{S_l} \left\{ \frac{\partial \hat{G}_{kj}}{\partial \tilde{n}} \right\}_{\vartheta_{kj}} \mathrm{d}S
\end{aligned}
\tag{2.26}
$$

Validation Results

Four test cases have been considered and the aeroacoustic predictions (in terms of pressure disturbance) have been compared with the numerical results provided by the validated and well-assessed FWH HERNOP code [32]. Test cases herein considered make reference to helicopter rotor noise; they are well known in literature and they are suitable for the validation of numerical codes. In particular, test cases consider a $1/4 - scale$ UH-1 baseline main rotor having two rectangular blades 1.83m long, with linear twist distribution and NACA 0012 airfoil sections. Geometrical details of the main rotor, blade controls for the trimmed flight condition and the observers location, can be found in Ref. [33]. Test case 1 considers a helicopter in forward flight with an advance speed of 100 Knots, a shaft angle[6] of 8.85°, a rotational speed of

---

[6]It describes the angle between the rotor shaft and the vertical.

$1296 RPM$ and the co–moving observer position, with respect to the observer coordinate system [7] [33], given by $(3.21m, -2.16m, -0.3m)$; test case 2 considers a forward flight condition with an advance speed of 60 Knots, a shaft angle of $8°$ and co–moving observer position, given by $(0.41m, -0.68m, -0.72m)$; test case 3 differs from test case 2 only for the co–moving observer position given by $(0, -3m, 0)$; finally test case 4 deals with a BVI condition for a main rotor whose geometry and flight conditions are documented inside the 1333 case of the Helinoise european project [34]; in this case the noise signals are evaluated for a co–moving observer position, given by $(0, 3m, 0)$. The aerodynamic loads for all test–cases are obtained through a BEM compressible analysis; as expected, Fig. 2.3 and Fig. 2.4 show that thickness and loading noise dominate the overall noise, respectively. Numerical results show that the agreement with the predictions by HERNOP code is very good. The prediction capabilities of the implemented code are confirmed also by Figs. 2.5 and 2.6.
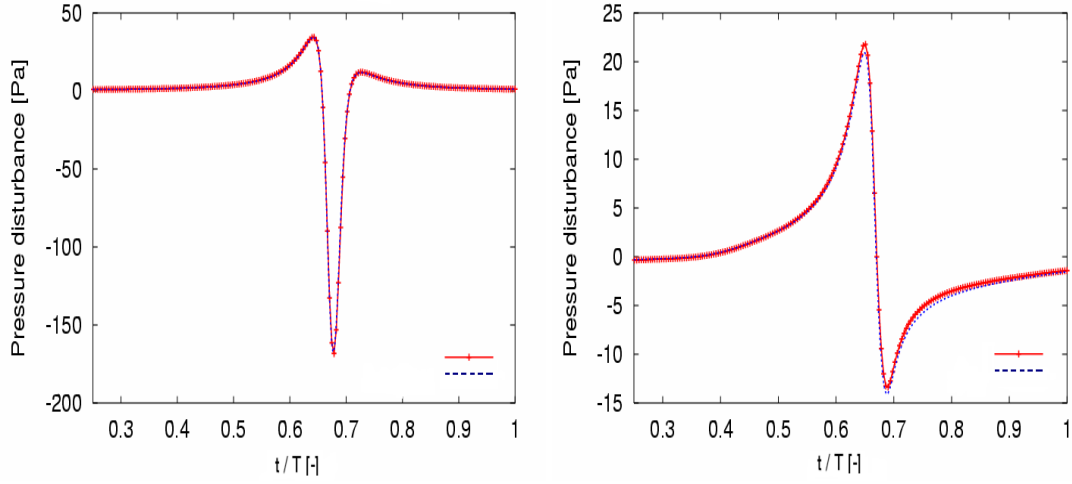
Figure 2.3: *Test case 1 – Comparison between literature data (HERNOP, red line with points +) and implemented FWH code (blue dotted line). Thickness noise signature (left) and loading noise signature (right).*

The Influence of Wake Model

As shown in section 2.2, in the frame of potential flows for lifting bodies, the presence of the potential wake affects the evaluation of the potential ϕ, on the body and in the field. In the following, the influence of the potential wake modelling on the aeroacoustic prediction performed through BEA and FWHE is investigated through numerical comparisons. In particular, the numerical study concerns a comparison between a high aspect ratio blade (rather typical for helicopter rotors) and a highly twisted and skewed blade with a very small span to chord ratio (usual for vessels). A low-order boundary element method is used to determine the blade hydrodynamic solution to be applied in both hydroacoustic formulations. Body and wake surfaces are discretized into hyperboloidal quadrilateral elements and flow quantities are supposed to be piecewise constant on each element. Thus, Eq. (2.20) gives rise to a linear system of equations where the unknowns represent the velocity potential at the panels centroids. The computational grids are characterized by the

---

[7] It is defined as follows: the x,y plane is parallel to the ground and the z–axis points upward, forming a right–hand coordinate system. The x–axis points in the direction of the wind. The origin of this coordinate system is the center of the rotor hub at time equal to zero, then this frame moves with the helicopter but retains its original attitude, without rotation, with its origin fixed to the center of the rotor hub.
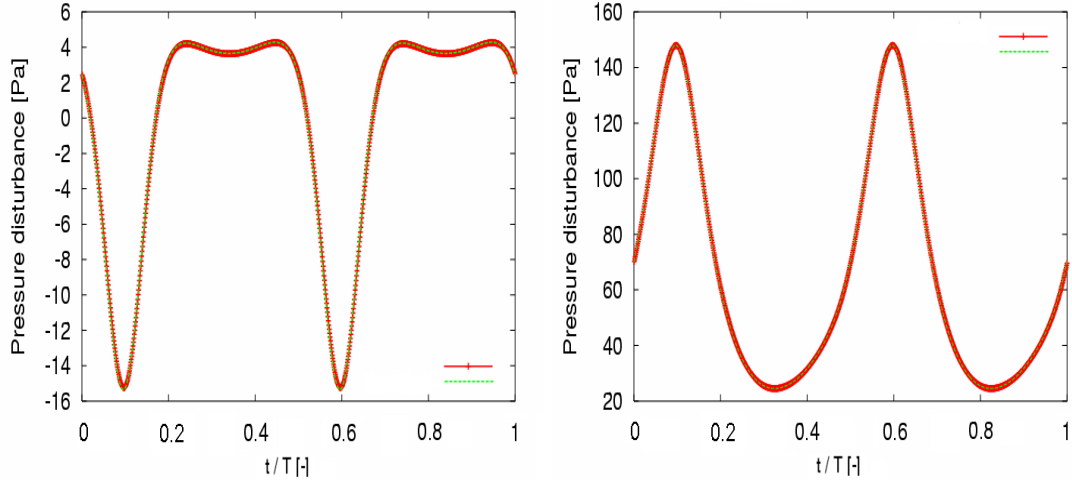
Figure 2.4: *Test case 2 – Comparison between literature data (HERNOP, red line with points +) and implemented FWH code (green dotted line). Thickness noise signature (left) and loading noise signature (right).*
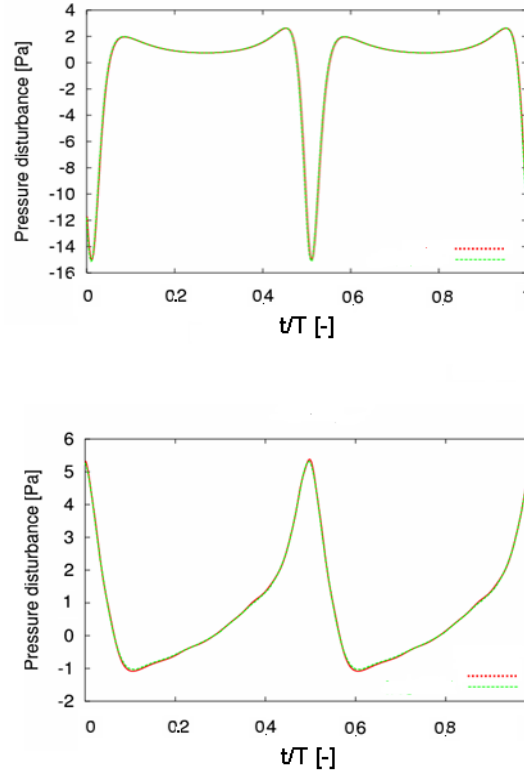
Figure 2.5: *Test case 3 – Comparison between literature data (HERNOP, green points) and implemented FWH code (red points). Thickness noise signature (top) and loading noise signature (bottom).*

number of blade elements along chord (M_B) and along span (N_B), and the number of elements along each wake turn, both streamwise (M_W) and in radial direction (N_W). A preliminary analy-
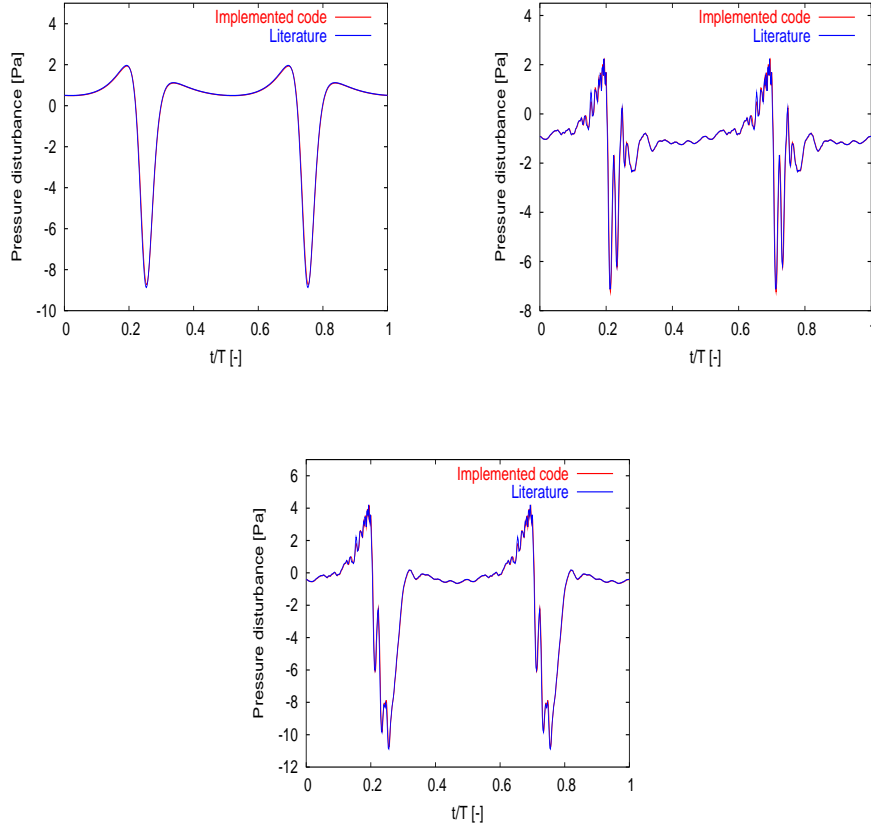
Figure 2.6: *Test case 4 – Comparison between validated data (HERNOP) and implemented FWH code. Thickness noise signature (left), loading noise signature (right) and overall noise (bottom).*

sis (not reported) has been performed to evaluate the effect of these parameters on the numerical solution of Eq. (2.20). Among the many grids considered, the values which seem to minimize the discretization uncertainty are $M_B=N_B$=20 and M_W=90. Moreover, the value $N_W=N_B$ has been adopted. All the calculations refer to a single-bladed propeller in a uniform flow.

The first configuration concerns a non-lifting blade having a uniform spanwise distribution of a NACA 0012 profile, with diameter $D = 2m$, constant chord $c = 0.1m$ and a root cut-off equal to $0.2m$. Both the advance velocity U_∞ and the local angle of attack are equal to zero (hovering condition), while the rotational speed is set to $\Omega = 286RPM$ ($n = 4.77rev/s$), corresponding to a tip rotational Mach number $M = 0.02$. The noise prediction refers to an observer placed in the rotor disk plane, at a distance of only $2m$ from the blade tip. Despite the aeronautical blade configuration, the computations are performed in water, where the speed of sound is $c_0 = 1520m/s$. This way, the closeness of the observer to the rotating blade should reasonably give rise to negligible compressibility delays. A sketch of the discretized blade and relative blade-observer position is reported in Fig. 2.7 while Fig. 2.8 shows the comparison between the noise predictions provided by the two hydroacoustic solving approaches. At the proposed operating conditions, the excellent agreement of these two signatures confirms the numerical equivalence of the *pseudo-acoustic* pressure provided by the incompressible Bernoulli–based approach and the noise signal determined through the FWH equation.

Such a satisfactory comparison deteriorates by accounting for the presence of the wake (lifting configuration). For the same observer position, first, let us focus our attention on a moderately
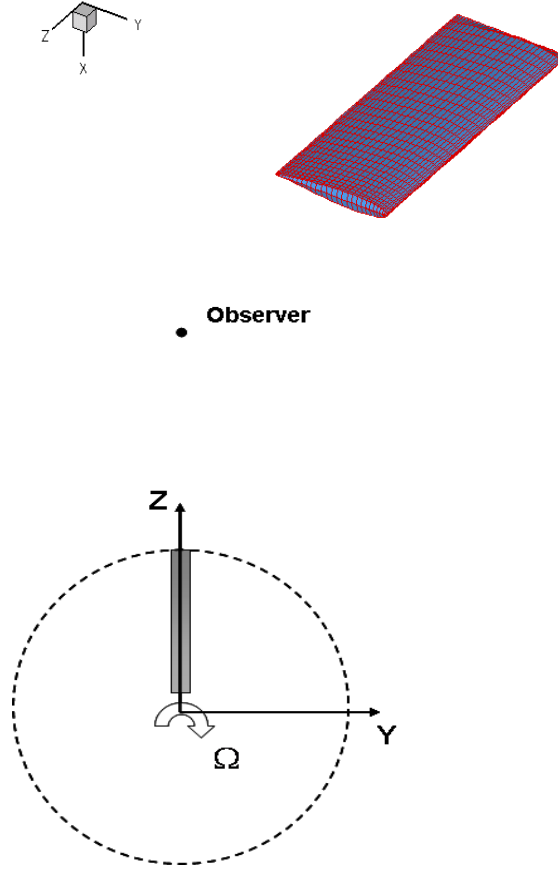
Figure 2.7: *A sketch of the NACA 0012 blade (top) and the rotor disk observer location (bottom) used for the non–lifting test case.*
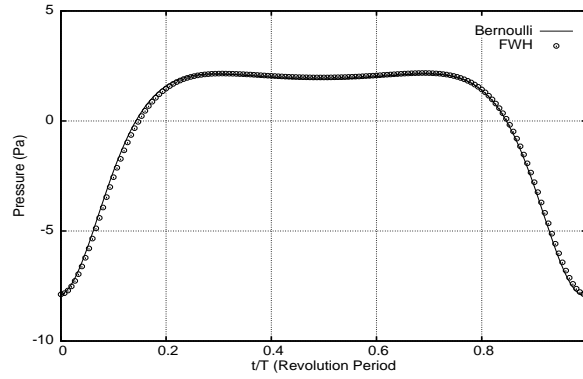
Figure 2.8: *Noise signals under non–lifting operating condition.*

loaded blade, by imposing a linear twist of $\Delta\theta$=33.6° between the blade root and tip (see Fig. 2.10) and considering two different values for the advance ratio $J = U_\infty/nD$ (namely J=0.75 and J=0.5), corresponding to thrust coefficient $K_T = 2T/\rho n^2 D^4$ values equal to 0.02653 and 0.04484, respectively. In the unified approach, both the velocity potential and the pressure on the

body and in the field depend on the wake considered in the numerical solution of Eq. (2.20). Thus it is necessary a preliminary assessment of the wake length by checking the numerical solutions while truncating the wake to different numbers of spirals. Generally speaking, a limited wake portion attached to the body affects the numerical results upon the body (hydrodynamic solution), whereas a very long wake must be taken into account to correctly capture its effects in the field, far from the body (hydroacoustic solution). For instance, for J=0.75 and by considering a prescribed helical–shape wake, three wake turns (corresponding to a wake length L_W=2.3D) yield a converged blade pressure distribution. Nevertheless, a higher number of wake spirals (at least L_W=20D) are necessary to achieve a converged acoustic pressure in the far field. This result
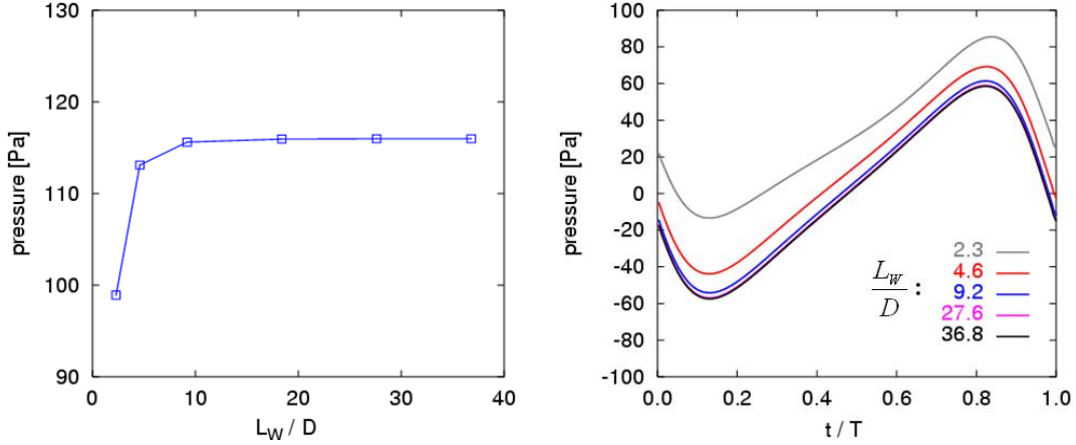
Figure 2.9: *Assessment of the wake surface length for the NACA 0012 blade in lifting conditions at J=0.75. On the left the peak-to-peak pressure intensity is reported as a function of L_W/D ratio, while the right figure shows the corresponding noise predictions achieved by the Bernoulli–based approach.*

is clearly shown in Fig. 2.9, where the convergence of the numerical solution for p is reported through a peak-to-peak pressure intensity versus wake length curve (on the left) and the noise signatures determined by increasing the value of the L_W/D ratio (right figure). The notable increase of the wake length needed to get a converged potential and/or pressure evaluation in the field depends on the fact that the wake doublet influence (related to the solid angle through which it is seen by the observer) slowly tend to zero for observers placed far from the blade.

Previous considerations on the unified approach outline that, for a given observer position, the presence of the potential wake requires an initial assessment on the wake length needed to get a converged solution. In the following, the hydroacoustic analysis of the NACA 0012 lifting blade shown in Fig. 2.10 is performed by taking into account three different observer locations as shown in Fig. 2.11. Still, observer 1 is located in the propeller plane while observers named 2 and 3 are placed downstream and upstream (with respect to the disk plane) for both values of the advance ratio, J. The observer coordinates, non dimensional with respect to the propeller diameter, are: MIC1→($\hat{x}$=0.0, $\hat{y}$=1.0, $\hat{z}$=0.0), MIC2→($\hat{x}$=1.0, $\hat{y}$=0.75, $\hat{z}$=0.0), MIC3→($\hat{x}$=-1.0, $\hat{y}$=0.75, $\hat{z}$=0.0), with $\hat{x}_i$=x_i/D. The hydrodynamic input data is determined by means of Eq. (2.20) with a prescribed wake model. In particular, the wake shed at the blade trailing edge is supposed to be a simple helical surface with a fixed pitch equal to the distance travelled by the rotor during one revolution (see Fig. 2.12). A preliminary analysis outlines that a converged hydrodynamic solution is obtained using three wake spirals, whereas a wake length of $L_W = 30D$ ensures a converged hydroacoustic solution for the above observer positions. Figures 2.13, 2.14, 2.15 show comparisons between the pressure time histories determined through the FWH and the Bernoulli equations at the two aforementioned advance ratios. The two pressure signature predictions
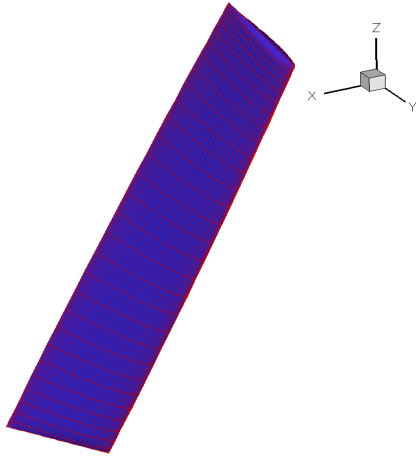
Figure 2.10: *3D pre–twisted blade.*
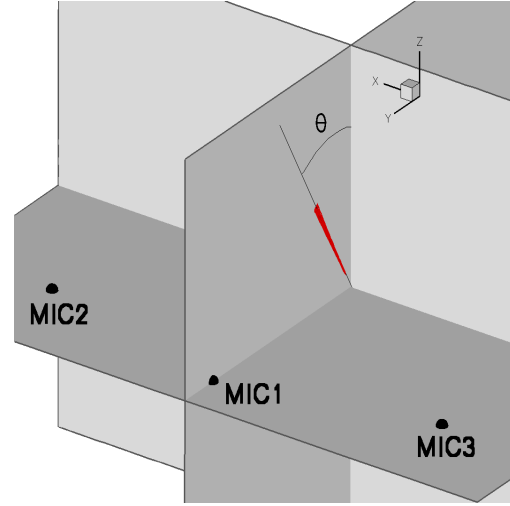
Figure 2.11: *Microphones locations.*
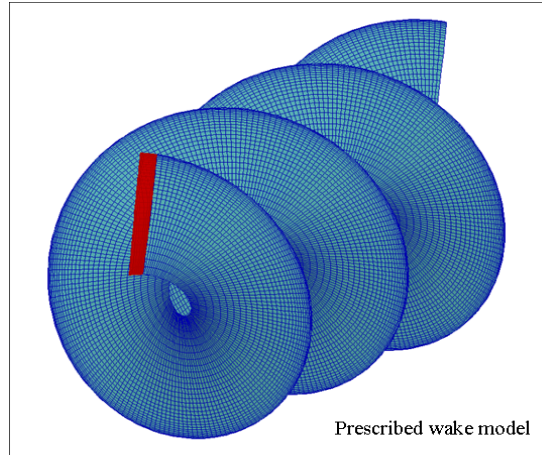
Figure 2.12: *Sketch of prescribed wake modeling for the NACA0012 helicopter blade.*

are very similar, although slight differences appear at all the observer locations. Furthermore, the discrepancies increase at the lower advance ratio, which corresponds to a wake closer to the propeller and a higher blade hydrodynamic load. In order to better understand the role played by the wake modeling, let us move the attention to a marine propeller. In this case, the more complex geometry (the blades are usually characterized by large values of the skew and twist angles) and the heavier loading conditions suggest a notable wake–shape influence. The analysis will be focused on the INSEAN E779A scaled model. A sketch of such a four-bladed hubbed-propeller, with diameter $D = 22.727cm$, is reported in Fig. 2.16, although the computations always refer to a single blade. On the right picture of Fig. 2.16 the four different observer locations, placed in the XY-plane used in noise predictions, are depicted. The operating conditions still refer to a rotational velocity of $\Omega = 286RPM$ and an advance speed $U_\infty = 8.395m/s$, so that J is now equal to 0.88 and the blade is heavily loaded (K_T=0.16). A parametric analysis is performed in order to assess the wake influence on noise prediction without applying any wake radial contraction. Then, a variation of the wake surface can be carried out by changing the pitch distribution of
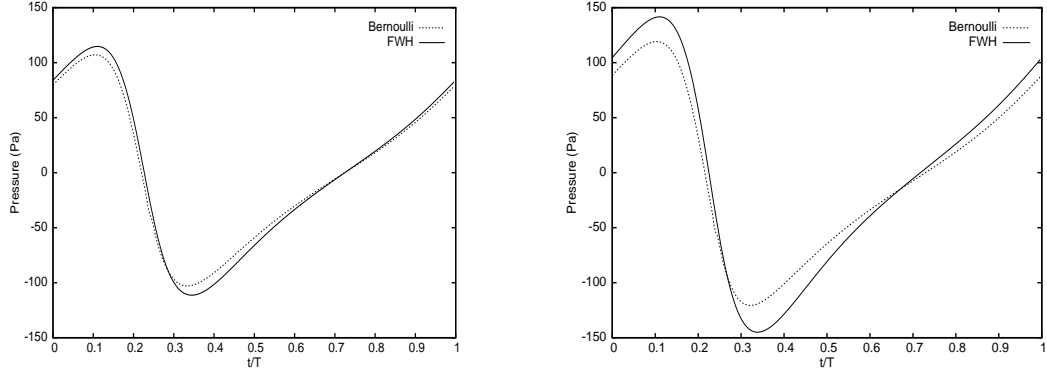
Figure 2.13: *NACA 0012 lifting blade at J=0.75 (K_T=0.026-left figure) and at J=0.5 (K_T=0.045-right figure). MIC1: $\hat{x}$=0.0, $\hat{y}$=1.0, $\hat{z}$=0.0*
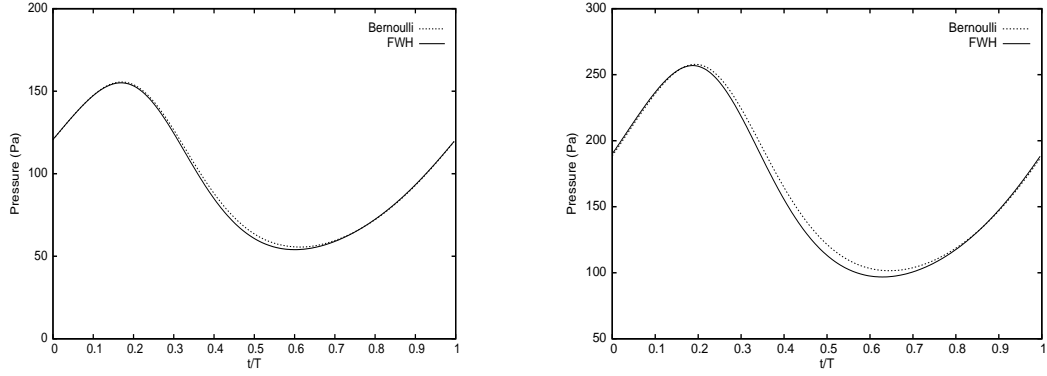
Figure 2.14: *NACA 0012 lifting blade at J=0.75 (left figure) and at J=0.5 (right figure). MIC2: $\hat{x}$=1.0, $\hat{y}$=0.75, $\hat{z}$=0.0*
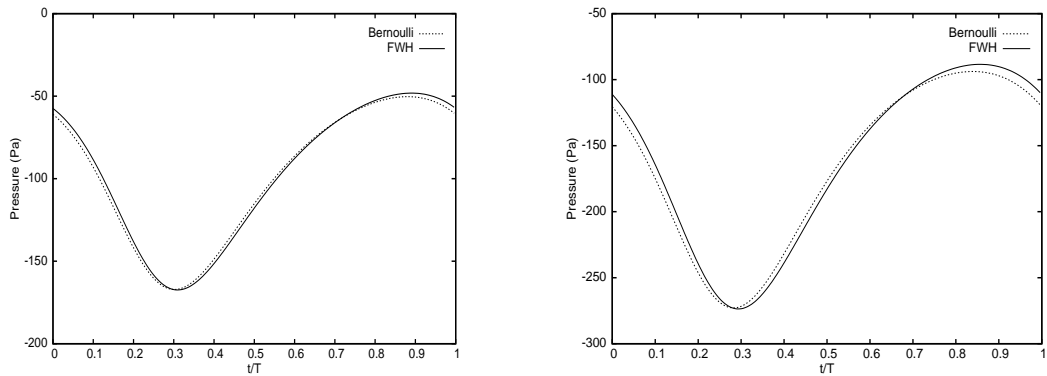
Figure 2.15: *NACA 0012 lifting blade at J=0.75 (left figure) and at J=0.5 (right figure). MIC3: $\hat{x}$=-1.0, $\hat{y}$=0.75, $\hat{z}$=0.0*

the prescribed model. To this aim, the wake surface appearing into the integral equation for the velocity potential is divided into two subsequent patches: a *near wake* extending for a prescribed number Λ of revolutions (starting from the blade trailing edge) and a *far wake* extended further
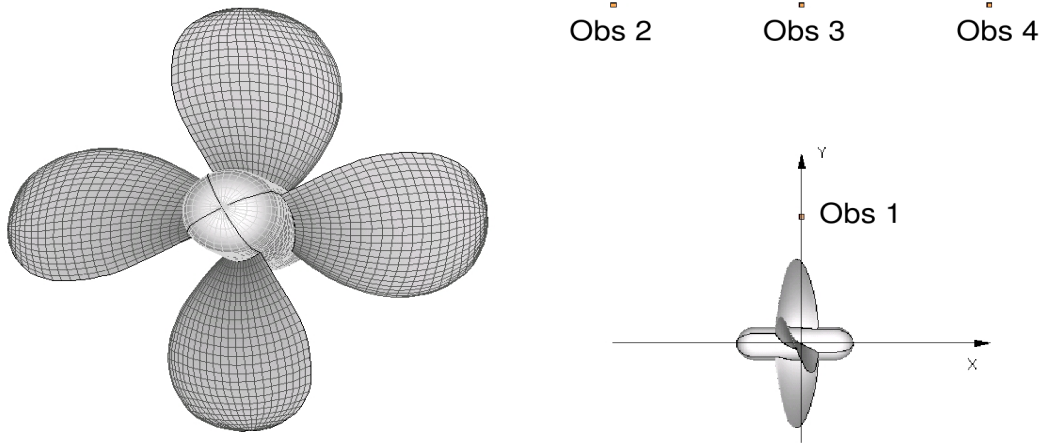
Figure 2.16: *A 3D view of INSEAN E779A propeller model is depicted on the left. The right figure shows the four observers placed in the XY-plane and used for noise predictions.*

downstream. The far wake pitch is defined as

$$\beta_{FW} = \alpha\beta_I + (1 - \alpha)\beta_B$$

where β_B represents the blade mean pitch, β_I denotes the inflow pitch and α is a weight factor which can be set between 0 and 1. Similarly, for the near wake

$$\beta_{NW} = \xi\beta_{FW} + (1 - \xi)\beta_{TE}$$

where β_{TE} is the blade pitch at trailing edge and ξ indicates a nondimensional streamwise arclength (with ξ=0 at trailing edge and ξ=1 at the downstream end of the near wake). Note that the β_{TE} value is selected in order to have a wake tangent to the section mean lines at the blade trailing edge. The pitch wake distribution can be modified by acting on both Λ and α parameters. Figure 2.17 depicts a 3D sketch of the two separate wake–patches, while Fig. 2.18 shows the noise signatures at the observer 4 corresponding to different values of the Λ and α parameters.

It is rather clear that the adopted wake model plays a significant role in the Bernoulli–based
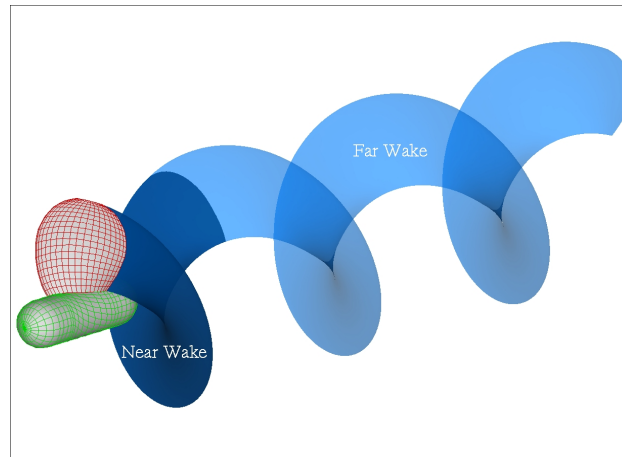
Figure 2.17: *Three–dimensional sketch of the near and far wake patches.*

noise evaluation. Despite a general similarity of all waveforms, the discrepancies of the acoustic pressure absolute values can be relevant. Many tests have been performed by using other values
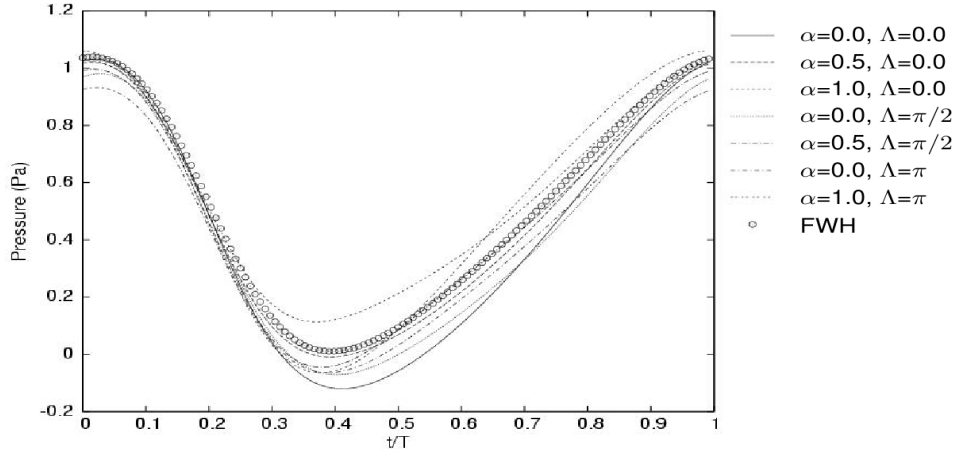
Figure 2.18: *Effect of the wake shape on the waveform of the overall signal.*

for Λ and α, substantially obtaining very similar results. In practice, in the Bernoulli approach an *ad hoc* choice of the wake shape is essential to approach the numerical solution provided by the FWH equation. On the other hand, the shape of S_W has a very weak influence on the blade hydrodynamic loads (as well as on the computed thrust coefficient), so that the noise prediction provided by the FWH equation does not change with it. Looking at Fig. 2.18, the couple of values $\Lambda=0$ and $\alpha=0.5$ seems to be the *best* choice for the wake shape in terms of similarity with FWH results. Then, Figs. 2.19 and 2.20 show the comparison between the FWH and Bernoulli acoustic pressure time histories at the four aforementioned observer locations, corresponding to such optimized wake model. Actually, the differences are rather small and a satisfactory agreement is
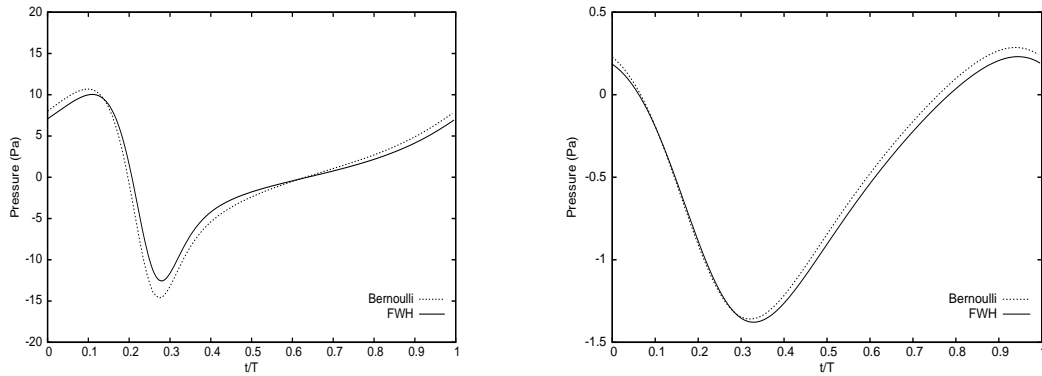
Figure 2.19: *Comparison between the pressure time histories provided by the FWHE and BEA. Obs 1:$\hat{x}$=0.0, $\hat{y}$=0.75, $\hat{z}$=0.0 (left), Obs 2: $\hat{x}$=-1.0, $\hat{y}$=2.0, $\hat{z}$=0.0 (right).*

achieved from both a qualitative and a quantitative point of view. Nevertheless, it can not be assured that changing, for instance, the blade loading conditions, the adopted wake remains the best choice. A possible explanation of the observed wake influence on noise predictions could concern the not respected continuity condition for pressure on the wake panels. In fact, a prescribed surface is a simple approximation of an actual potential wake and, in general, does not match the
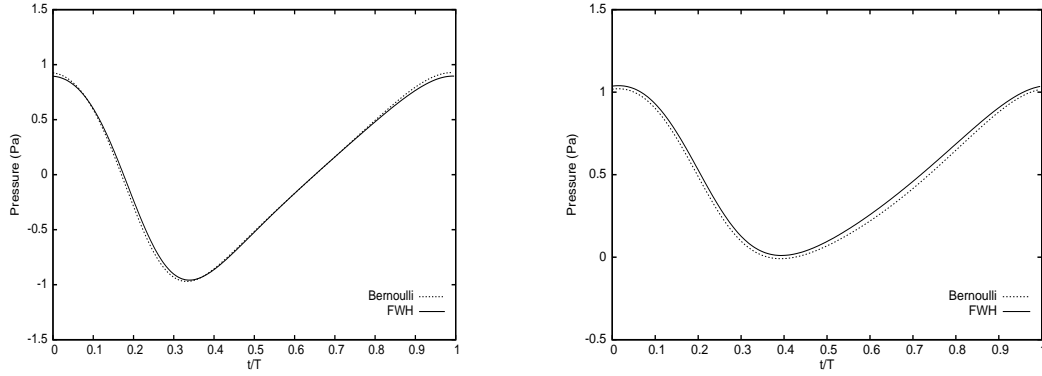
Figure 2.20: *Comparison between the pressure time histories provided by the FWHE and BEA. Obs 3: $\hat{x}=0.0$, $\hat{y}=2.0$, $\hat{z}=0.0$ (left), Obs 4: $\hat{x}=1.0$, $\hat{y}=2.0$, $\hat{z}=0.0$ (right).*

theoretical boundary condition Δp equals zero across the wake.[8] Then, the wake behaves as a sort of an additional, zero-thickness source, generating a fictitious loading noise component of numerical nature. This conjecture has been numerically investigated by taking into account a free–wake model, where the field velocity is determined through a boundary integral representation of the potential gradient and the wake points are moved in order to be aligned to the local flowfield (*wake alignment technique*). Hydrodynamic numerical results provided by such a free–wake algorithm have been validated by comparison with experimental data concerning the E779A propeller model [35]. Unfortunately, the use of this more sophisticated wake model has not provided the expected improvements on noise predictions. Figures 2.21 and 2.22 show a comparison of the acoustic pressure time histories obtained through the prescribed and free wake models depicted in Fig. 2.23. At observer 1 (placed very close to the propeller) the noise signature computed by the free–wake model seems to be closer to the FWH solution with respect to the prescribed wake surface (left picture in Fig. 2.21). However as the observer moves far away from the blade, this tendency is inverted. For instance, at observer location 4 the agreement between the FWH and the free–wake model becomes notably worse (right picture in Fig. 2.22). Such negative behaviour involves all the observers placed far from the body and even seems to generate a higher level of uncertainty with respect to the results of the right Fig. 2.18.

The numerical solution of the non–linear potential flow problem with free–wake algorithm is inherently affected by inaccuracies; in particular, a Δp not equal to zero still affects the wake at the blade trailing edge and can occur at some critical regions such as in the wake tip region where the vortical surface tends to roll-up under the effect of the induced velocity, as shown at the right side of Fig. 2.23. Furthermore, as shown in Ref. [35], the grid refinement deeply affects the flow–aligned wake shape and a large number of discretization elements in the spanwise direction is required to capture the wake roll-up at tip, where most of the trailing vorticity concentrates. Hence, wake discretization plays a fundamental role in determining both the magnitude and position of the wake singularities. This fact implies that the rate of convergence in the evaluation of the flow–field velocity through the free-wake modeling is expected to be significantly slower with respect to that obtained through a prescribed wake model in which the shape of the wake is fixed and does not depend on the flow–field solution. Therefore, in order to achieve the *same* converged solution provided by a prescribed wake a too much fine grid should be used, with a not acceptable

---

[8]This condition is intimately related to the fact that the wake surface is a material surface, and hence it is aligned to the local flowfield.

34

requirement of CPU time and storage capacity. This is especially true by increasing the blade-observer distance since the larger this distance is, the greater is the wake portion affecting the far field pressure estimation. At this stage, whatever the numerical reasons for the free–wake model failure could be, a fundamental result is carried out. The proven influence of the wake modeling
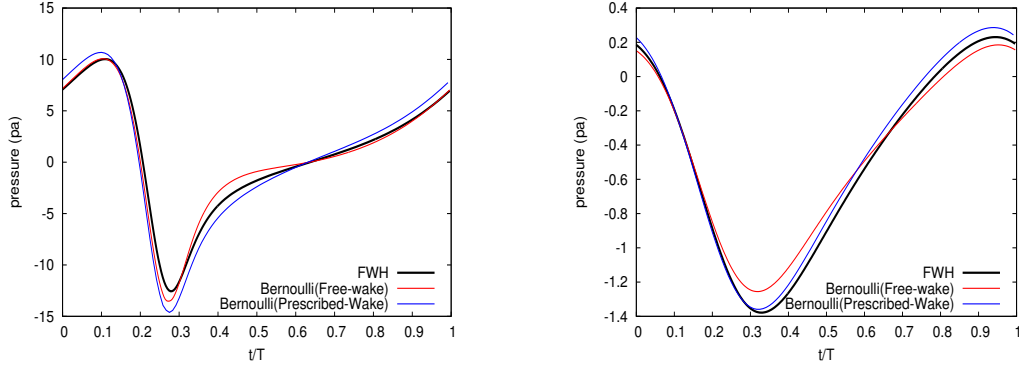
Figure 2.21: *Comparison between the noise predictions provided by the FWH-based solver and the Bernoulli approach through the best prescribed–wake and the free–wake model, at the observers 1 (left) and 2 (right).*
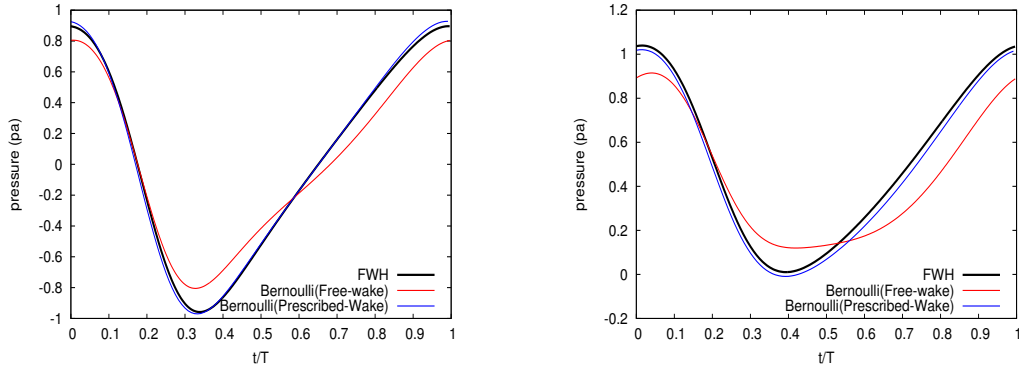
Figure 2.22: *Comparison between the noise predictions provided by the FWH-based solver and the Bernoulli approach through the best prescribed–wake and the free–wake model, at the observers 3 (left) and 4 (right).*

on the acoustic pressure demonstrates that the reliability and the robustness of the acoustic analogy approach is unquestionably superior with respect to the Bernoulli–based methodology. Since the requirement for the wake modeling concerns both the simpler (and, hydroacoustically speaking, erroneous) incompressible form of the Bernoulli theorem and the more complex and CPU demanding compressible formulation, the advantages offered by the FWH equation are evident. This equation by–passes the insidious influence of the wake on noise prediction by only using the pressure distribution upon the blade as the source term in the loading noise component. At this stage, it is also worth noting that the computational effort associated to the FWHE is very limited and the evaluation of thickness and loading terms usually requires a handful of CPU seconds (depending on the mesh resolution).
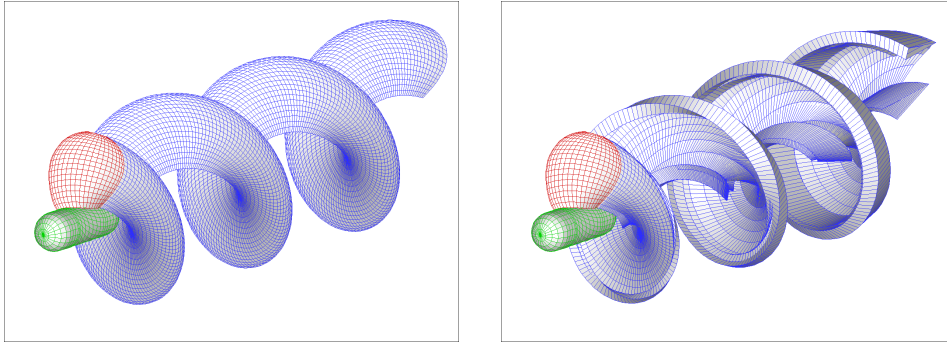
Figure 2.23: *Trailing wake behind the INSEAN E779A marine propeller, $J = 0.88$. Prescribed wake model (left) and flow–aligned wake (right).*

Sound Propagation Effects

This section examines the effects of the compressibility delays when the distance between the source and the observer increases, in order to assess the inaccuracies in the evaluation of the acoustic pressure far field due to the the assumption of incompressible flow. In order not to ascribe the influence of the compressibility delays to any other *collateral* numerical effect (such as the wake model influence discussed in the previous section for the BEA methodology), the investigation will be carried out by comparing the numerical solutions of the FWHE given by Eq. (2.2) with those obtained from a simplified form of the FWHE, derived under the incompressibility assumption. Figure 2.24 shows the contour plots of noise level in dB, determined on a squared area with the center at the propulsor hub, having side equal to $5D$. The map is plotted by accounting for 100 microphones, moving with the advancing propeller and located on the XY–plane depicted in the right Fig. 2.16. The footprint on the left refers to the noise predictions provided by the incompressible FWH formulation while the right one concerns those given by Eq. (2.2). As expected, the noise maps are almost identical. However, widening the microphone map this qualitative equivalence tends to disappear. Figure 2.25 shows a map with a side length of $50D$ (where, for the sake of clarity, the previous smaller propulsor–centered map is also reported) traced on a mesh of 900 different microphones. Although an overall similarity of the directivity patterns is shown, the compressible solution (on the right hand side) exhibits a rather higher noise level with respect to the numerical results achieved under the incompressibility assumption (left hand side figure). Furthermore, the two main noise lobes seem to be larger thus providing a more uniform distribution of the dB level around the propeller. These qualitative differences are highlighted by looking at the acoustic pressure time histories reported in Figs. 2.26, 2.27, 2.28 and corresponding to the six microphones selected on the map (see Fig. 2.25). At locations quite close to the propulsor (observers 435 and 466) the discrepancies between the two noise predictions are negligible. On the contrary, by moving far away from the propeller, the effect of the compressibility delays becomes relevant and the noise signatures notably differ each other, both in the acoustic pressure amplitude and phase. These results confirm that the propagation effects are essential to predict accurately the acoustic pressure in the far field and the use of an incompressible hydroacoustic solver would provide significant inaccuracies in noise predictions.
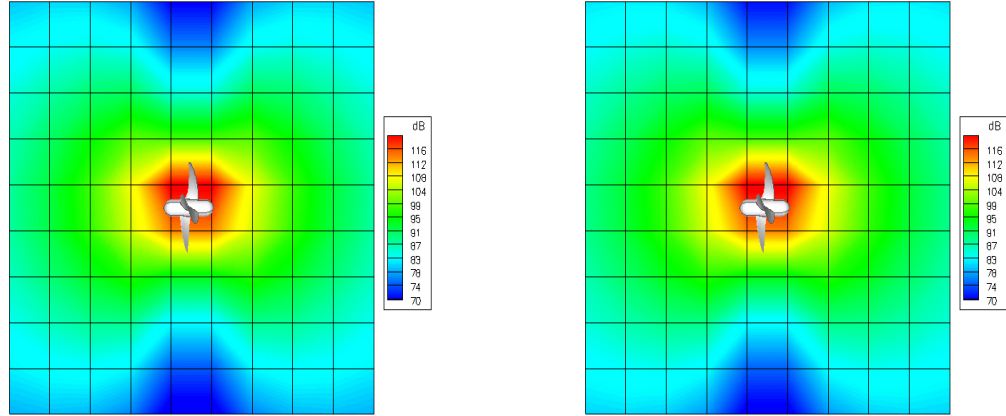
Figure 2.24: *Noise dB level contour plot determined through the incompressible (left figure) and compressible (right figure) FWH equation, up to* $10R$.
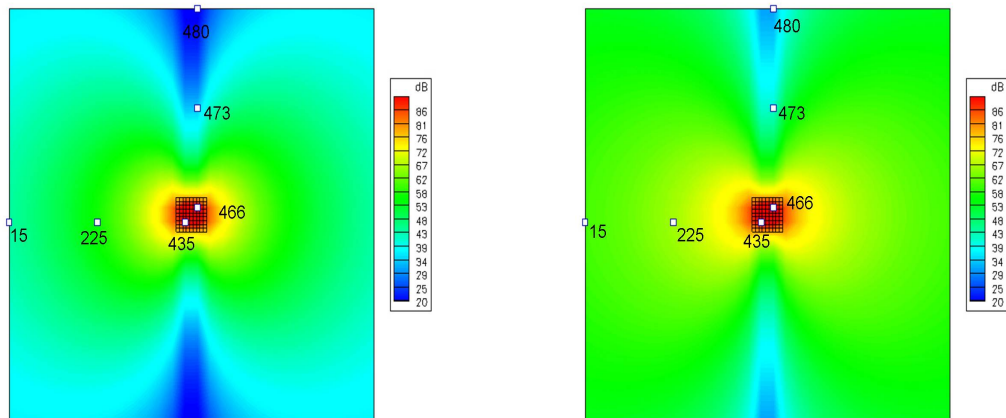
Figure 2.25: *Noise dB level contour plot for a map side up to* $100R$.
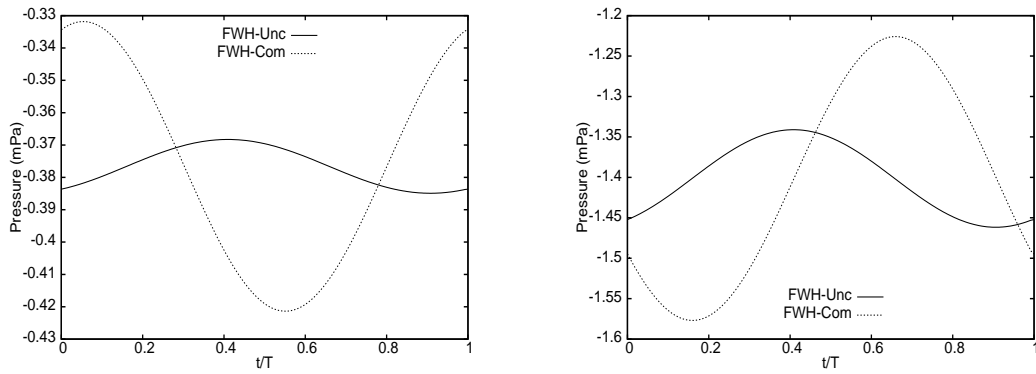
Figure 2.26: *Comparison between the pressure time histories provided by the incompressible (Unc) and compressible (Com) FWH formulations. Obs. No.15 and Obs. No.225.*
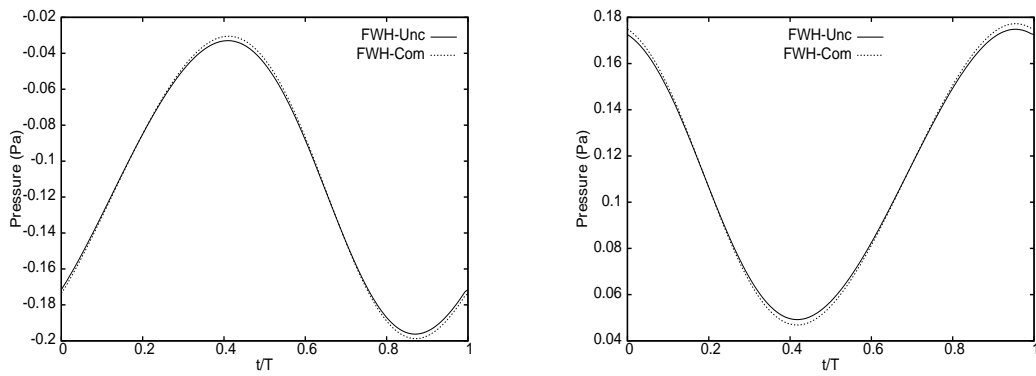
Figure 2.27: *Comparison between the pressure time histories provided by the incompressible (Unc) and compressible (Com) FWH formulations. Obs. No.435 and Obs. No.466.*
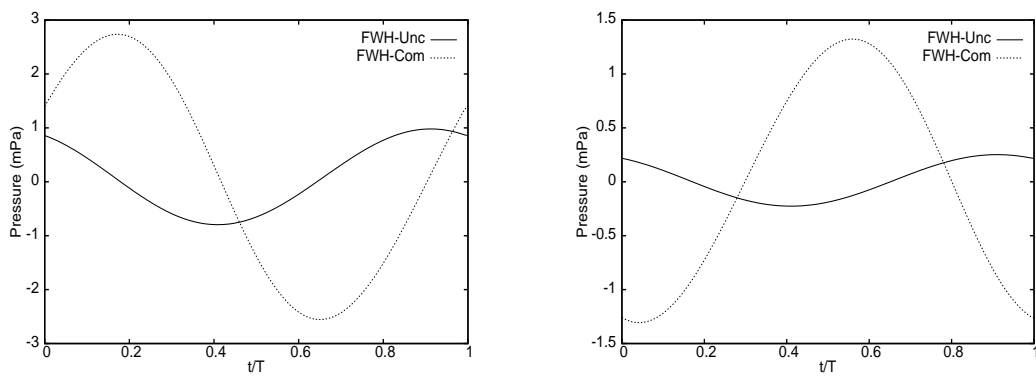
Figure 2.28: *Comparison between the pressure time histories provided by the incompressible (Unc) and compressible (Com) FWH formulations. Obs. No.473 and Obs. No.480.*

Chapter 3

Hydroacoustics of Cavitating Propellers

The emphasis of chapter 2 has concerned the noise field radiated by non–cavitating propellers; it has been proven that the rotational noise may be successfully predicted by Ffowcs Williams and Hawkings equation or, in the framework of potential flow theory, by the Bernoulli method after a preliminary assessment of the wake contribution. However, the main source of noise generated by marine propellers in realistic operating conditions is due to cavitation. It affects underwater communications, sonar systems and acoustic signature. Therefore, for military applications, low radiated noise levels are a crucial requirement for a good propeller design; for passenger ship, low inboard noise level are desirable for the passengers comfort. Undoubtedly, cavitation occurrence is a source of undesirable effects as radiated noise, structural vibrations, erosion and loss of efficiency. Propeller–induced noise and vibrations are primarily related to the fluctuating volume of the cavity; the growth and implosion of the cavity deeply modifies the frequency content of the noise signal with respect to the non–cavitating case. Typically, the spectrum of the radiated pressure disturbance exhibits a much higher frequency content and the first harmonics amplitude may be up to ten times greater (or more) than in the non–cavitating case [36]. Through the impinging pressure on the hull–plate, the cavitation affects also the structural response of the hull that, in turn, is a source of interior noise. All these reasons make accurate cavitation effects predictions essential in order to give designers tools to make them satisfy strict noise and vibration requirements. To this purpose, the development of numerical tools able to predict the cavitation pattern and the emitted noise is fundamental. The aim of this chapter is to present a method for evaluating the noise induced by cavitating marine screw propellers. Specifically a coupled hydrodynamic-hydroacoustic modeling based on potential flow hydrodynamics and the Ffowcs Williams and Hawkings equation able to predict the noise generated by a propeller when cavitation occurs, is presented. The main goal is to investigate the (spatial and temporal) correlations between the cavitation pattern and the radiated noise of a propeller in a non–uniform flowfield. Transient sheet cavitation is taken into account and the problem of cavitation noise is faced through a suitable application of the FWHE. In view of the fact that nowadays the use of the acoustic analogy in the naval context is seen as challenging and the few applications to hydroacoustic purposes are limited to non–cavitating blades, the proposed modeling is quite innovative in the framework of propeller cavitation acoustics. The results obtained by this approach are compared with those predicted by using the FWHE as suggested by Salvatore and Ianniello [37], that first applied the acoustic analogy to the naval context.

3.1   General Aspects on Cavitation

Cavitation is a very complicated phenomenon involving phase change, surface tension, turbulence, non–equilibrium thermodynamic effects, etc.; it is unsteady in nature and occurs over a wide range of time and length scales. Quoting Franc and Michel from their recent book on Fundamentals of

Cavitation [38], "*Cavitation can be defined as the breakdown of a liquid medium under very low pressure* ".

In hydrodynamics of propellers are of interest high–speed flow phenomena where vaporization is associated to regions where pressure drops below vapor pressure; in this condition, liquid changes phase to vapor, resulting in a visible vapor region called *bubble* or *cavity* . This change occurs approximately at constant temperature, which distinguishes cavitation from boiling.[1] On a lifting hydrofoil cavitation can take a variety of forms as discussed in the following; growth of a cavity occurs at a slow rate when dissolved gas diffuses into the cavity or when the liquid temperature rises or drops. On the contrary, the growth of the cavity is *explosive* if it is primarily the result of vaporization into the cavity [39]. Whenever cavitation induced by high–speed flows occurs, the bubbles or cavities grow and travel until a high pressure region is reached; the vapor condense into liquid at a very high rate, higher than the growing rate, and ultimately collapses and disappears. Such *implosive* reverse process, can be very violent, which results into many detrimental effects in marine systems. In particular when the implosion takes place near a solid surface, being it a propeller, hydrofoil, strut, rudder, hub or hull, erosion may occur. In some cases, this can be catastrophic even after a short operation time. The sudden collapse of the cavities also radiates noise which is highly undesirable for naval applications; the emitted noise is a consequence of the momentary large pressure that is generated when the content of the bubbles is highly compressed, and affects underwater communications, sonar systems and acoustic signature. Also associated to the occurrence of cavitation on propellers is the increase in hull pressure fluctuations; these may cause severe vibrations of the ship hull resulting in discomfort for passengers situated near the stern of the ship. Furthermore the performance of the propeller may also be affected when cavitation occurs; large cavitation zones may lead to thrust breakdown and consequent loss of efficiency.

There are three basic conditions for cavitation occurrence (see Ref, [40]):

The presence of a Low Pressure

Pressure should be lower than a critical value given by the vapor pressure p_v. The non–dimensional parameter to scale this low pressure is represented by the cavitation number σ defined as

$$\sigma = \frac{p_\infty - p_v}{\frac{1}{2}\rho u^2{}_\infty} \tag{3.1}$$

where p_∞ is the static pressure of the inflow, p_v is the vapor pressure, ρ the fluid density and u_∞ is a reference flow velocity. The cavitation number measures the vulnerability of the flow to cavitation. The higher the cavitation number, the less likely cavitation occurs.

The presence of Nuclei

Water is typically characterized by the presence of tiny bubbles of microscopic size filled with vapor or gases from microorganisms or some other sources from the nature. Nuclei are measured in nuclei population spectrum (N/cm^3) or by nuclei number density spectrum [41] based on nuclei sizes. Nuclei are always needed for cavitation since "pure water" can withstand very high tension, representing a macroscopic manifestation of the intermolecular forces that tend to hold molecules together [42]; cavitation never occurs in this kind of water. Gaseous nuclei form the impurity in the liquid that reduce the tensile strength of the liquid. Different tensile strengths in different cavitation test facilities gives different cavitation inception results for the same test.

---

[1]Boiling also involves phase change when the liquid temperature is raised to the *boiling–point* at constant pressure conditions.

Duration of Exposure to Low Pressure

The duration of time during which the nuclei are exposed to the low pressure is an important factor to be considered; enough duration of exposure to low pressure enables the nuclei to grow up to visible sizes.

The typology of cavitation phenomenon strongly depends on the three conditions mentioned above. This is one of the essences of "scale effects". Other influences are turbulence, viscous effects diffusion, etc. Cavitation occurs in a broad variety of forms. It can be fixed to body or fixed to the fluid; it occurs in the fluid or at the surface of immersed bodies; it can shape as a group of perfect spheres (bubbles) or as a single sheet. The surface of a sheet cavity can be very smooth and transparent, or very frothy and opaque.

According to Carlton [43], the cavitation patterns which most commonly occur on marine propellers are referred to as sheet cavitation, bubble cavitation, cloud cavitation, tip and hub vortex cavitation. Some features are hereafter outlined (see Ref, [44]):

- Bubble cavitation

It occurs when low pressure areas are present in the mid–chord region of the blade section. Usually, the pressure gradient is not large in these areas and therefore bubble cavitation tends to occur in non–separated flows. It appears as individual bubbles, growing sometimes to large sizes and contracting rapidly when moving over the blade surface, travelling into high–pressure region. This kind of cavitation has a relatively less influence on hydrodynamic forces and efficiency of propellers, but generates strong noise emission and erosion when it is close to the surface of the propeller blades.

Figure 3.1: *Photo of a lifting surface that exhibits a fairly clean "sheet" cavity; near the end of the cavity bubble cavitation occurs. Photograph courtesy of S.A Kinnas, MIT's Variable Pressure Water Tunnel (1996).*

- Sheet cavitation

Sheet (fixed or attached) cavitation is fixed to the body; it starts close to the leading edge of propeller blades on the suction surface and appears when large suction peaks build up near the leading edge of the blades. With the increase of the angle of incidence or the decrease of ambient pressure, the extent of the cavity over the blade grows usually in chordwise and spanwise directions. It normally has the appearance of a thin and smooth transparent film as long as laminar flow exists. Over the entire length of the sheet cavity, the *pocket of vapor* is always concave towards the
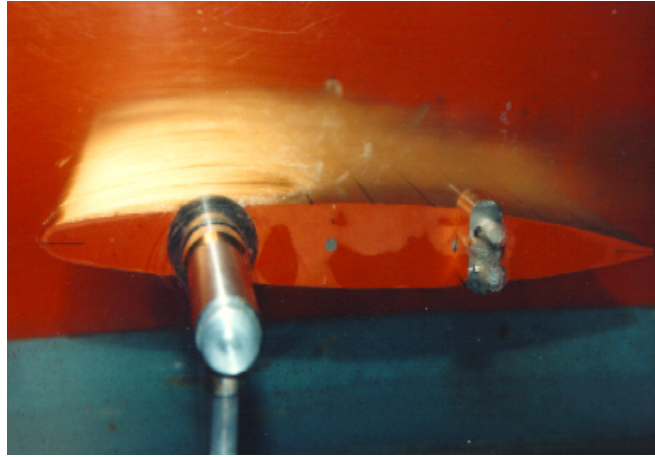
Figure 3.2: *Sheet cavitation on a lifting surface. Photograph courtesy of S.A Kinnas, MIT's Variable Pressure Water Tunnel (1996).*

blade surface [45]. Because of this, the cavity must close on the blade surface (partial cavity) or close somewhere downstream with other cavity surfaces (super cavity). The end of the sheet cavity is normally unsteady. It either breaks into a lot of small bubbles, which is very local and non–periodic, or it induces large–scale cavity shedding periodically. Both of these different processes eventually form cloud cavitation further downstream (see below). It is worthwhile noting that sheet cavity closure controls the behavior of the sheet cavitation; the sheet remains smooth and transparent if the flow reattaches the blade surface as *laminar reattachment*. It becomes frothy if the cavity surface flow becomes turbulent. This is called *turbulent reattachment* .

- Cloud cavitation

Often, sheet cavitation seems steady at first sight; however, observations by De Lange [46] show that the complex behaviour of the flow in the vicinity of the cavity closure may produce the shedding of a major part of the cavity. Such phenomenon is mainly due to the appearance of a *reentrant jet* that flows into the cavity from the closure region. In fact, because of the high

Figure 3.3: *Photograph of a hydrofoil exhibiting cloud cavitation. Photograph courtesy of S.A Kinnas, MIT's Variable Pressure Water Tunnel (1996).*

pressure level at the end of the cavity, the flow moves upstream as a reverse flow (with a speed as high as the free stream velocity at the cavity surface [47]) between the underside of the cavity and

the blade surface. The presence of this reentrant jet causes the detachment of the sheet cavity; as a consequence, it breaks and large portion of it is shed and forms a large–scale cloud cavity. This cavitation is highly periodic as shown by De Lange [46].

- Tip and hub vortex cavitation

Vortex cavitation often occurs in the low–pressure core of the vortices trailing from the propeller hub and blade tips. It happens when nuclei are trapped into the core of the vortex and grow into longitudinal bubbles. When these bubbles merge with each other, they form a hollow long spiral tube, which can extend stably over a considerable distance downstream. A vortex cavity finally collapses when the vortex is diffused by viscosity and therefore the pressure in the core is no longer low enough. This collapse could be also violent and generate very strong noise emission, but not erosive because it normally occurs far downstream of the propeller blades. However it is possible that erosion damage occurs on rudders. In detail, the *hub vortex* results from the vortices
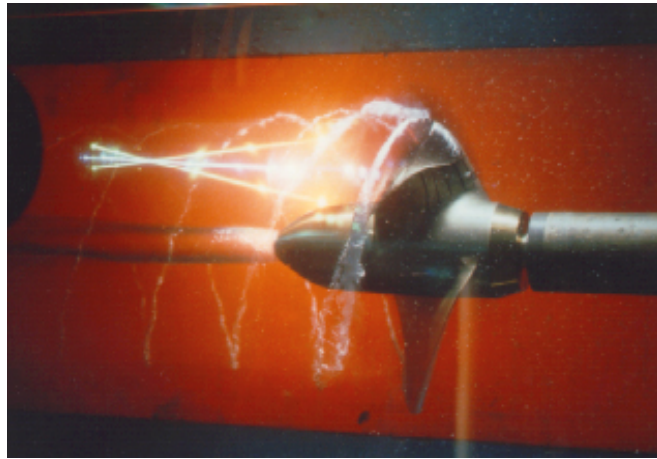
Figure 3.4: *Photograph of a cavitating propeller in presence of tip-vortex cavities and hub-vortex originating from the tip and the hub of the propulsor. Photograph courtesy of S.A Kinnas, MIT's Variable Pressure Water Tunnel (1996).*

shed from the blade roots which give rise to a strong axial vortex under the influence of the converging hub cone. Cavitation may occur in the core of such strong vortex. *Tip vortex cavitation* is either observed at some distance behind the tips of the propeller blades or attached to the blade. Also the coexistence of tip vortex and sheet cavitation is common, leading to the usual situation for propellers: a partial sheet cavity growing into a tip vortex cavity. For high skew propellers, the detachment point of the tip vortex may move along the leading edge to smaller radii, leading to the formation of *leading edge vortex cavitation.*

Marine screw propellers operate in a flow perturbated by the presence of the hull, which generally causes the upstream flow to decelerate in a limited region of the hull wake where the levels of turbulence are also significantly increased. The non–uniformity of the incoming flow into the propeller disc causes a periodic variation of the blade loading and of the hydrostatic pressure. Apart from the varying thrust developed by the propeller, this situation creates the necessary set of conditions for the occurrence of unsteady cavitation on the propeller blades for some time during a propeller blade revolution. Unsteady cavitation generates strong pressure fluctuations radiating to the far–field or to the submerged part of the hull structure through the water medium; the broadband frequency content of the noise generated by cavitation makes it the major source of noise and vibrations on a ship, hence contributing to crew discomfort on a passenger vessel, interfering with onboard instrumentation, etc..
Modern ships and vessels have cruise speed such that cavitation occurrence can not be avoided
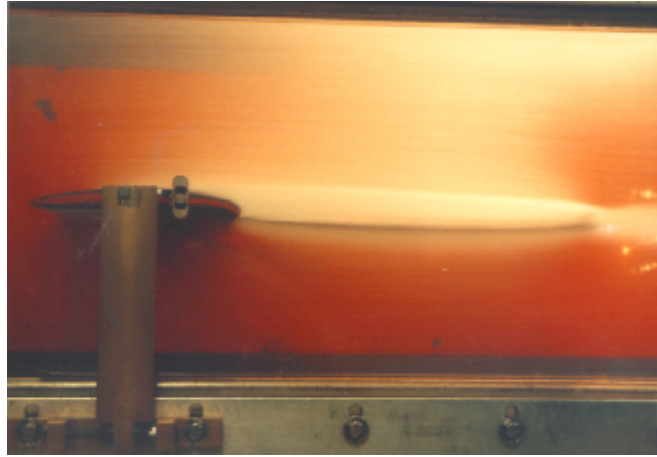
Figure 3.5: *Supercavitating hydrofoil. Photograph courtesy of S.A Kinnas, MIT's Variable Pressure Water Tunnel (1996).*

during the operating conditions; in these cases the capability to control the detrimental induced–noise effects due to the dynamics of the cavity represents a crucial point for the design of the propulsors. Therefore, the availability of effective, fast and reliable computational tools for the analysis of cavitation noise is nowadays one of the most urgent designer's needs.
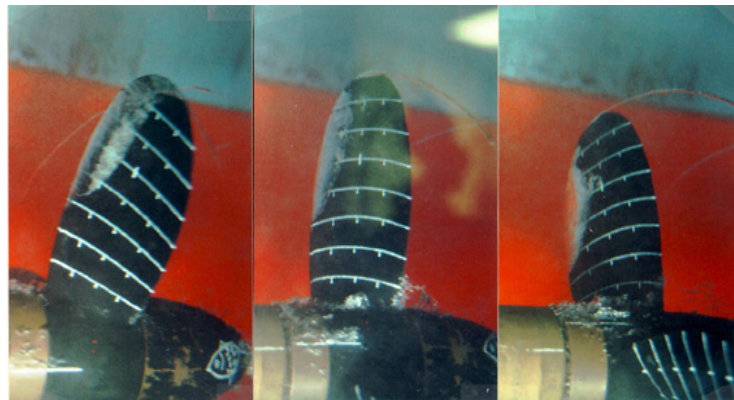
Figure 3.6: *Naval propeller under cavitating conditions. Photograph courtesy of S.A Kinnas, MIT's Variable Pressure Water Tunnel (1996).*

For these reasons, the following sections are devoted to the analysis of cavitation noise induced by unsteady cavitation; in particular, the emphasis is on the noise radiated by the occurrence of transient sheet cavitation that is very common in practice.

3.2 Cavitation Noise

The growth and violent catastrophic collapse of large transient vapor cavities on ship propeller blades occurring as they pass in the region of low inflow in the wake abaft the hull, result in the generation of noise and material damage to nearby solid surfaces. As a prelude to the mathematical model proposed in section 3.2.1 for the prediction of the cavitation noise and in order to identify the relationships between noise and dynamics of bubble growth and collapse, the behaviour of a single bubble in an infinite domain of liquid at rest with uniform temperature far from the bubble, is first examined. This is a simple case that, however, reveals some important correlations useful for further analysis. Let us consider a spherical bubble of radius $R(t)$ (t is time) located in a
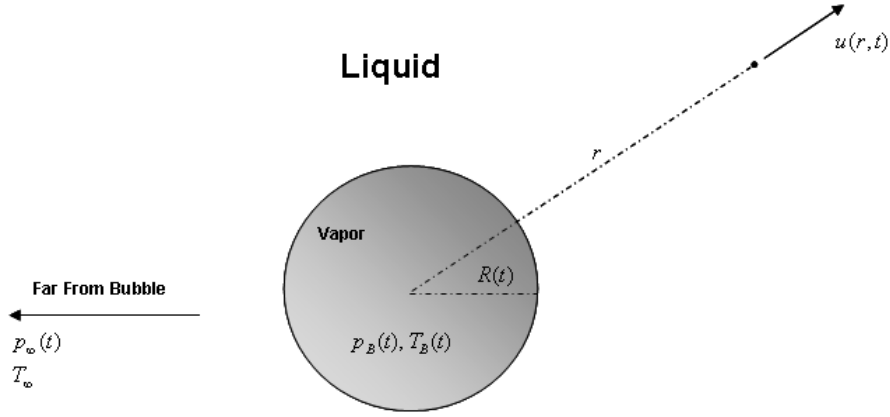
Figure 3.7: *Pulsating spherical bubble in an infinite liquid.*

infinite domain of liquid having temperature and pressure far from the bubble T_∞ and $p_\infty(t)^2$ respectively; furthermore let the temperature and pressure $T_B(t)$ and $p_B(t)$ within the bubble be always uniform. Denoting with r the radial position from the center of the bubble within the liquid, the conservation of mass requires that

$$u(r,t) = \frac{F(t)}{r^2} \tag{3.2}$$

where $u(r,t)$ is the radial outward fluid velocity and the function $F(t)$ is related to $R(t)$ by a kinematic boundary condition at the bubble surface. In the idealized case of zero mass transport across this interface

$$u(R,t) = \frac{dR}{dt} \tag{3.3}$$

and hence

$$F(t) = R^2 \frac{dR}{dt} \tag{3.4}$$

This is often a good approximation even when evaporization or condensation is occurring at the interface [48]. The Euler equation in r direction, using Eq. (3.2) yields

$$-\frac{1}{\rho_0}\frac{\partial p}{\partial r} = \frac{1}{r^2}\frac{dF}{dt} - \frac{2F^2}{r^5} \tag{3.5}$$

---

[2]The pressure is assumed to be a known–controlled input which regulates the growth and collapse of the bubble.

that once integrated gives

$$\frac{p - p_\infty}{\rho_0} = \frac{1}{r}\frac{dF}{dt} - \frac{1}{2}\frac{F^2}{r^4} \tag{3.6}$$

after application of the condition $p \to p_\infty$ as $r \to \infty$.

Although compressibility of the liquid can be important in the context of bubble collapse, here it is assumed that the fluid density ρ_0 is constant: hence, Eq. (3.6) may yield information only on the pseudo–acoustic disturbance caused by the dynamic behavior of the bubble.

Considering the flow in the liquid caused by the volume displacement of a growing or collapsing cavity, it results that in the far–field the flow approaches that of a simple source and the term $O(\frac{1}{r})$ decays more slowly with r than the term $O(\frac{1}{r^4})$. If the time–varying volume of the cavity is denoted by $V(t)$, one obtains that the time-varying component of the pseudo–acoustic pressure is given by:

$$p - p_\infty = \frac{\rho_0}{4\pi\,r}\frac{d^2 V}{dt^2} \tag{3.7}$$

Hence, far–field noise generated by a pulsating spherical cavity is directly proportional to the second derivative of the volume with respect to time and the crackling noise that is related to cavitation is due to the (very large and) positive values of $\frac{d^2 V}{dt^2}$ when the bubble is close to its minimum size.

Obviously, on propeller blades, the cavities are far from being spherical. However, such a model gives a useful link between the incremental pressure at a given distance from the expanding cavity and the acceleration of the cavity volume. Previous work by Pereira *et al.* [49] shows that on bidimensional hydrofoils the height of the leading edge cavity is linearly related to its length; these authors also show experimentally that the vapor structures generated by unsteady sheet cavitation may be represented by a characteristic length $l_c = \sqrt{E_c}$ where E_c indicates the cavity extension. More recently, experimental observations and calculations of cavitating propeller flows performed in Ref. [50] have brought new evidence that the cavity thickness on a propeller blade have a similar behavior. Therefore, by making the hypothesis that the cavity volume V_c is proportional to l_c, Eq. (3.7) can be also written using the expression:

$$\frac{d^2 V}{dt^2} = \left[6l_c (\frac{dl_c}{dt})^2 + 3l_c^2 \frac{d^2 l_c}{dt^2} \right] \tag{3.8}$$

that allows the calculation of the volume acceleration once the cavity extension is known, numerically or experimentally.

For marine screw propellers, the prediction of the pressure fluctuations due to unsteady cavitation requires a comprehensive insight into the correlations between the cavitation pattern and the radiated noise; to this aim, the hydrodynamic solver has to provide a detailed prediction of the cavitation pattern on the propeller surface whereas the hydroacoustic tool has to be able of accounting for the source of noise due to the growth or collapse of the cavity. In principle, the hydroacoustic analysis might be performed through the Bernoulli equation. However, as shown in chapter 2, this kind of approach is inherently affected by the problem of the potential wake modeling because of its sensitivity to the shape of the wake that affects the hydroacoustics of rotors and propellers. Hence, in the attempt to describe the behaviour of cavitating propellers, and assuming the occurrence of the sheet cavitation phenomenon, the Ffowcs Williams and Hawkings equation is proposed and applied to include the dynamics of the fluctuating vapor cavity occurring during the blade revolution. In the framework of cavitation noise, this methodology is an extension of that proposed by Salvatore and Ianniello [37] that represents an early attempt to apply the FWH

concept to the analysis of the hydroacoustics of cavitating propellers in non–uniform flow. This novel formulation, hereafter presented, is referred as Transpiration Velocity Modeling (TVM) to emphasize the presence of a flow velocity due to the dynamics of the cavity; indeed, the approach suggested in Ref. [37] is referred to as Equivalent Blade Modeling (EBM) to emphasize that the key point of that methodology is the definition of an equivalent blade. All these concepts are explained and discussed in the following. In particular, section 3.2.1 deals with the TVM that is discussed by emphasizing the way to include the unsteady behaviour of the cavity as source of noise; in order to highlight the differences with the model proposed in Ref. [37], section 3.2.2 outlines the main features of the latter. Finally, in section 3.3 the numerical predictions given by these two methodologies are compared. At this stage it is worth observing that the TVM and EBM differ only in the computation of cavitation noise; in the absence of cavity, the two methodologies yield the same results because the governing equations become the FWH equation for impermeable surfaces.

3.2.1   Approach 1: The Transpiration Velocity Modeling (TVM)

Let us consider the occurrence of transient sheet cavitation on marine propeller blades. Let θ represent the angular position of the reference blade, with $\theta = 0$ corresponding to the blade in the twelve o'clock position. For an azimuthal position $\theta = \hat{\theta}$, Fig. 3.8 depicts a section of the cavitating blade; in particular, the boundary of the cavity, its thickness and the projection $\mathcal{S}_{C_B}$ onto the blade surface are shown.
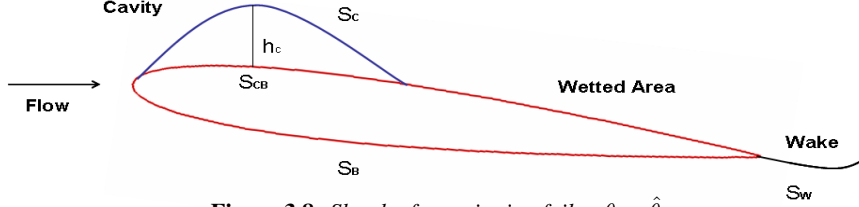
Figure 3.8: *Sketch of a cavitating foil at $\theta = \hat{\theta}$.*

Dealing with sheet cavitation, let us assume the cavity thickness h_c is very thin compared to the hydrofoil chord such that the cavity outer edge $\mathcal{S}_C$ may be assumed to be coincident with the cavitating portion of the body surface, *i.e.,* with its projection $\mathcal{S}_{C_B}$ (see Fig. 3.8). Then, for $f = 0$ identifying the points of a porous surface S enclosing the propeller blade and rigidly moving with it, the permeable FWHE, Eq. (2.1), reads

$$
\begin{aligned}
\Box^2 p' \;=\; & \frac{\overline{\partial}}{\overline{\partial}t}\left[\rho_0\, \mathbf{v}\cdot\nabla f\,\delta\left(f\right)\right] + \frac{\overline{\partial}}{\overline{\partial}t}\left[\rho\left(\mathbf{u}-\mathbf{v}\right)\cdot\nabla f\,\delta\left(f\right)\right] \\
& -\; \overline{\nabla}\cdot\left[\mathbf{P}\,\nabla f\,\delta\left(f\right)\right] - \overline{\nabla}\cdot\left[\rho\,\mathbf{u}\otimes\left(\mathbf{u}-\mathbf{v}\right)\nabla f\,\delta\left(f\right)\right] \\
& +\; \overline{\nabla}\cdot\left\{\overline{\nabla}\cdot\left[\mathbf{T}\,H(f)\right]\right\} \quad \forall \mathbf{x}\in\Re^3
\end{aligned}
\tag{3.9}
$$

and, following the integral formulation in appendix A.3 the corresponding boundary integral representation of the acoustic field may be written as the superposition of the following three terms

$$
p'(\mathbf{x},t) \;\cong\; \mathcal{I}_1 \,+\, \mathcal{I}_2 \,+\, \mathcal{I}_3
\tag{3.10}
$$

with

$$\mathcal{I}_1 = -\int_S \rho_0 \Big[\mathbf{v}\cdot\mathbf{n}\, \mathbf{v}\cdot\nabla\hat{G} + \big[\mathbf{v}\cdot\mathbf{n}\,(1 - \mathbf{v}\cdot\nabla\vartheta) \big]^{\displaystyle\cdot}\, \hat{G} \Big]_\vartheta \mathrm{d}S$$

$$\mathcal{I}_2 = -\int_S \Big[(\mathbf{P}\,\mathbf{n})\cdot\nabla\hat{G} - (\dot{\mathbf{P}}\,\mathbf{n})\cdot\nabla\vartheta\,\hat{G} \Big]_\vartheta \mathrm{d}S$$

$$\mathcal{I}_3 = -\int_S \Big[\rho\,\mathbf{u}^-\cdot\mathbf{n}\,\mathbf{u}^+\cdot\nabla\hat{G} + \big[\rho\,\mathbf{u}^-\cdot\mathbf{n}\,(1 - \mathbf{u}^+\cdot\nabla\vartheta) \big]^{\displaystyle\cdot}\, \hat{G} \Big]_\vartheta \mathrm{d}S$$

The quantities above are expressed in a frame of reference rigidly connected to the non–deformable, permeable, emitting surface S moving through the fluid with velocity $\mathbf{v}$. Moreover, $\mathbf{u}$ denotes the fluid velocity, $\mathbf{u}^- = (\mathbf{u} - \mathbf{v})$, $\mathbf{u}^+ = (\mathbf{u} + \mathbf{v})$ whereas the symbol $(\dot{\ })$ denotes time derivation and subscript ϑ indicates that quantities must be evaluated at the emission time, $(t - \vartheta)$. The term $\mathcal{I}_1$ describes the contribution to the overall pressure disturbance due to the kinematics of the moving surface S whereas $\mathcal{I}_2$ accounts for the pressure distribution p and $\dot{p}$ on S; they would coincide with the thickness and loading noise terms if S were impermeable. Indeed, $\mathcal{I}_3$ is related to the porosity of S and accounts for the velocity field distribution upon S; it would be equal to zero if S were impermeable.

   Cavitation noise generated by unsteady sheet cavitation may be predicted through the integral representation (3.10) by assuming the surface S to be coincident with the blade surface $\mathcal{S}_B$ with porosity contributions from those blade regions, $\mathcal{S}_{CB}$, where transient sheet cavitation occurs, in order to take into account for the presence of the cavity (as source of noise). Indeed, the fluctuating cavity volume produces a difference between the normal components of the rigid–body velocity, $\mathbf{v}$, and of the fluid velocity, $\mathbf{u}$, that, in the body frame of reference, corresponds to

$$(\mathbf{u} - \mathbf{v})\cdot\mathbf{n} = \frac{dh_c}{dt} \tag{3.11}$$

Such term, defined as *cavitating transpiration velocity* , is the term through which, in Eq. (3.10), the effect of the dynamics of the bubble is included without arbitrarily introducing effects related to (not compatible, in the integral formulation for rigid surfaces applied) surface deformations due to the growth and collapse of the cavity. Decomposing the fluid density as

$$\rho = \rho_0 + \rho' \tag{3.12}$$

where ρ' indicates the (small) density perturbation with respect the density of the undisturbed medium, and assuming $\rho' << \rho_0$, the $\mathcal{I}_3$ term may be re-written as

$$\mathcal{I}_3 = -\rho_0 \int_{S_{CB}} \Big[\frac{dh_c}{dt}\,\mathbf{u}^+\cdot\nabla\hat{G} + \frac{d^2 h_c}{dt^2}\,(1 - \mathbf{u}^+\cdot\nabla\vartheta)\hat{G} - \frac{dh_c}{dt}\,(\dot{\mathbf{u}^+})\cdot\nabla\vartheta \Big]_\vartheta \mathrm{d}S$$

Cavitation noise is described by the porous term $\mathcal{I}_3$ and is due to the mass and momentum flux through the cavitating region of the blade surface $\mathcal{S}_{CB}$ while on the non–cavitating portion of the blade, $\mathcal{S}_{WB}$, $\mathbf{u}^-\cdot\mathbf{n} = 0$ and its contribution to noise is associated to the thickness and loading terms $\mathcal{I}_1$ and $\mathcal{I}_2$, respectively.

Thus, the terms appearing in Eq. (3.10) may be re-written as

$$\mathcal{I}_1 = -\rho_0 \int_{S_{WB}\bigcup S_{CB}} \Big[\mathbf{v}\cdot\mathbf{n}\,\mathbf{v}\cdot\nabla\hat{G} + \big[\mathbf{v}\cdot\mathbf{n}\,(1 - \mathbf{v}\cdot\nabla\vartheta) \big]^{\displaystyle\cdot}\,\hat{G} \Big]_\vartheta \mathrm{d}S$$

$$\mathcal{I}_2 = -\int_{S_{WB}\bigcup S_{CB}} \Big[(\mathbf{P}\,\mathbf{n})\cdot\nabla\hat{G} - (\dot{\mathbf{P}}\,\mathbf{n})\cdot\nabla\vartheta\,\hat{G} \Big]_\vartheta \mathrm{d}S \tag{3.13}$$

$$\mathcal{I}_3 = -\rho_0 \int_{S_{CB}} \Big[\frac{dh_c}{dt}\,\mathbf{u}^+\cdot\nabla\hat{G} \Big]_\vartheta \mathrm{d}S - \rho_0 \int_{S_{CB}} \Big\{ \big[\frac{dh_c}{dt}\,(1 - \mathbf{u}^+\cdot\nabla\vartheta) \big]^{\displaystyle\cdot}\,\hat{G} \Big\}_\vartheta \mathrm{d}S$$

48

where, the porous term

$$\mathcal{I}_{3_v} = -\rho_0 \int_{S_{CB}} \left[\frac{dh_c}{dt}\, \mathbf{u}^+ \cdot \nabla \hat{G} \right]_\vartheta dS \tag{3.14}$$

is defined as velocity term and that

$$\mathcal{I}_{3_a} = -\rho_0 \int_{S_{CB}} \left\{ \left[\frac{dh_c}{dt} \left(1 - \mathbf{u}^+ \cdot \nabla \vartheta \right) \right]^{\cdot} \hat{G} \right\}_\vartheta dS \tag{3.15}$$

is defined as acceleration term. Note that this physically consistent way of predicting noise from cavitating blades is obtained at the price of a significant computational efforts because of the need to compute first and second order time derivatives of the cavity thickness combined with the high impulsive character of the cavitation. From the above discussion it comes out that the TVM accounts for cavitation noise induced by the dynamics of the sheet cavity through the term $\mathcal{I}_3$. Such a way to apply the FWHE is based on the main assumption that cavity thickness may be thought thin with respect to a characteristic length of the blade section, as reasonable when dealing with sheet cavitation phenomenon. Hence, the TVM fails when noise is generated by other types of cavitating phenomena. Akin to the problem of non–cavitating propellers, the quadrupole term has been neglected in Eq. (3.10) since the presence of the *small* thickness, attached cavity does not induce perturbations velocity in the flow field such that the quadrupole noise term may be relevant. It is important to highlight that the occurrence of cavitation causes the presence of two–phase flow in flow field such that the speed of sound and density are characterized by local spatial gradients; within the limit of the accuracy required, perturbations with respect to the values of the undisturbed medium may be considered negligible. Obviously, this approximation in the noise evaluation might be overcome through the Kirchhoff-Ffowcs Williams Hawkings approach. Indeed, placing the control porous surface S suitably away from the cavitating blades such to include all sound sources, a two–phase CFD code might provide the pressure and velocity distribution on the surface S accounting for the aforementioned spatial gradients. However, this requires the knowledge of CFD solution in the field and is beyond the scope of the present work.

3.2.2 Approach 2: The Equivalent Blade Modeling (EBM)

This approach has been suggested by Salvatore and Ianniello [37] to study the hydroacoustics of cavitating propellers in non–uniform flow by using the Eq. (3.9) for a non–permeable surface S. Specifically, an *equivalent* blade shape $S_B \bigcup S_C$ surrounding the blade surface and the fluctuating cavity surface is considered as the emitting surface.
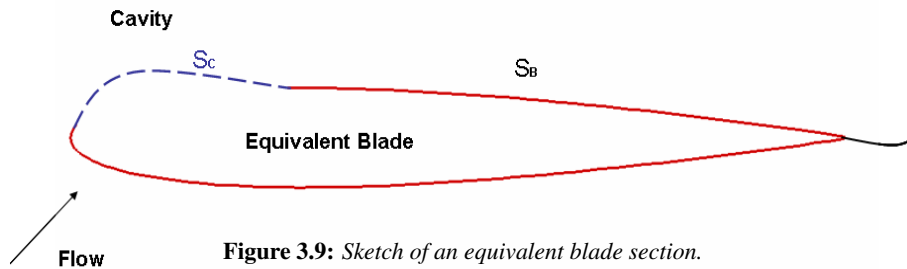
Figure 3.9: *Sketch of an equivalent blade section.*

During the blade revolution, thickness noise contribution may be computed by a step-by-step procedure where the equivalent blade surface $S_B \bigcup S_C$ is *updated* at each azimuthal position to account for the transient cavitation phenomenon, whereas the loading noise term may be evaluated once the pressure load fluctuations, due to the growth and collapse of the bubbles, are known on $S_B \bigcup S_C$.

This way of computing the effect of cavity dynamics is motivated from a numerical standpoint to avoid those theoretical and numerical problems related to the need of introducing a boundary integral formulation for deformable surfaces. Indeed, under cavitating conditions the time-varying shape of the cavity makes $S_B \bigcup S_C$ a deformable surface, and hence a suitable formulation should be used for solving the FWH equation. As a matter of fact, the above step-by-step approach attempts to solve the far–field noise prediction through a sequence of *quasi–steady* states characterized by a certain cavity shape and blade pressure distribution.

3.3   Numerical Results

The approaches 1 and 2 previously described are here applied to study the hydroacoustics of an isolated cavitating propeller in non–uniform onset flow. The aim is to investigate the capability of the TVM to describe propellers induced noise with emphasis on unsteady cavitation as the primary source of noise. The INSEAN E779A four–bladed model is considered; propeller diameter, advance speed and rotational speed are, respectively, $D_p = 22.727cm$, $U_\infty = 6.24m/s$, $n = 30.5\,rps$ and hence the corresponding advance coefficient is $J = U_\infty/(nD_P) = 0.9$. In order to simulate the presence of a hull, an onset flow with given velocity distribution representative of the boundary layer of a single–screw ship is considered. The velocity distribution is depicted in Fig. 3.10, taken from Ref. [51].
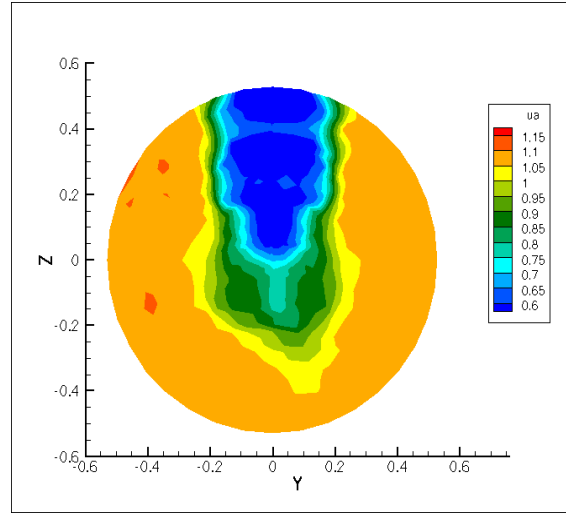
Figure 3.10: *Non uniform inflow to propeller: axial velocity distribution u_a on a transversal plane upstream a representative single screw configuration.*

The numerical hydrodynamic formulation, outlined in appendix B.1, is used here to study the isolated propeller operating in an unbounded fluid with spatially varying flow field generated by the ship, having the axial velocity distribution $u_a = u/U_\infty$ shown in Fig. 3.10. The numerical investigations are performed by discretizing each blade surface in 36 elements in chordwise direction (from leading edge to trailing edge) and 18 elements in spanwise direction, whereas 140 elements are used in the streamwise direction on each wake turn, and 1000 elements are used on the hub surface. A prescribed wake modeling is used; wake and blade spanwise discretizations are identical. The trailing wake surface is approximately extended three diameters downstream the propeller. Discretization node are not uniformly distributed on the blade in order to cluster elements in those regions where strongest gradients of flow quantities are expected, *i.e.,* leading and trailing edge, blade tip. The resulting computational grid on propeller and wake surfaces is depicted in Fig. 3.11. As shown in Ref. [31] such a spatial discretization is a good compromise between the need to obtain negligible discretization errors and reasonable computational efforts. Time discretization is related to spatial discretization of the propeller wake: the number of time steps dividing the propeller revolution period equals the number of wake elements per turn. This allows to prevent numerical instabilities while computing potential discontinuity convection along the wake [see Eq. (B.47)]. In the present hydrodynamic calculations, the unsteady flow under non–uniform inflow conditions is analyzed by discretizing each propeller revolution into 140 time steps. Although a larger number of time steps might provide a more detailed description of the bubble as a function of the time, the number of time steps is the result of a compromise between accuracy of hydrodynamic data and the need to prevent numerical instabilities. Details
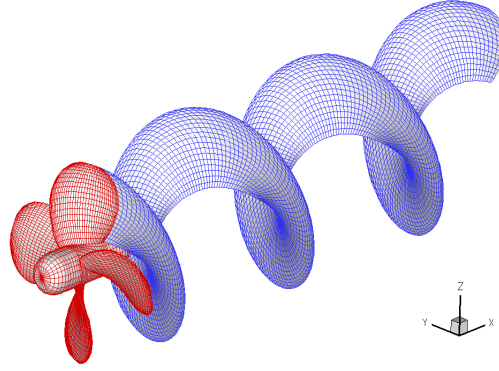
Figure 3.11: *Computational grid used to discretize propeller and trailing wake surfaces. For clarity, a helicoidal wake emanating from only one blade is represented.*

of these hydrodynamic aspects related to numerical scheme verification are given in Refs. [31] and [52]. In order to correlate propeller noise to blade loads fluctuations and cavitation pattern, first some significant results performed by the hydrodynamic modeling are shown, starting with the numerical predictions of propeller loads in terms of thrust and torque coefficients, respectively $K_T = T/\rho n^2 D_P^4$ and $K_Q = Q/\rho n^2 D_P^5$. Figures 3.12, 3.13, 3.14 show the propeller thrust and torque coefficient over a blade revolution period when the propulsor is operating in non–uniform wake (behind–hull condition). As an example, the non–cavitating condition is compared with three cavitating cases characterized by $\sigma = 2(p_\infty - p_v)/\rho\, n\, D_P^2$ equal to 2.835, 3.240, 4.455. The abscissa θ represents the angular position of the reference blade, with $\theta = 0°$ corresponding to the blade in the twelve o'clock position. When $\theta \cong -45°$ the reference blade enters into the hull wake and, as a consequence, blade loads increase and cavitation areas extend. The blade experiences this hydrodynamic environment up to $\theta \cong 30°$ when the blade exits form the wake hull. For the same flow conditions, Fig. 3.15 shows time history of the cavity in terms of dimensionless volume and area; cavity area is presented as a fraction of a blade reference area A_0 defined as the area of blade face portion for $r/D_p > 0.18$ ($A_0 = 1.115\, D_P^2$). As expected, cavity inception and collapse, as well as the increase of the cavity, are largely influenced by flow pressure; the common trend at different σ_n values is that the cavity collapse phase, concentrated in a limited azimuthal range (approximately, $15° < \theta < 40°$ at $\sigma_n = 2.835$), is generally faster than the growth phase (approximately, $-50° < \theta < 0°$ at $\sigma_n = 2.835$) and that the maximum values of the volume cavity occurs at positive θ. In these conditions an increase of both thrust and torque, due to a blade thickening effect related to sheet cavitation, is observed.
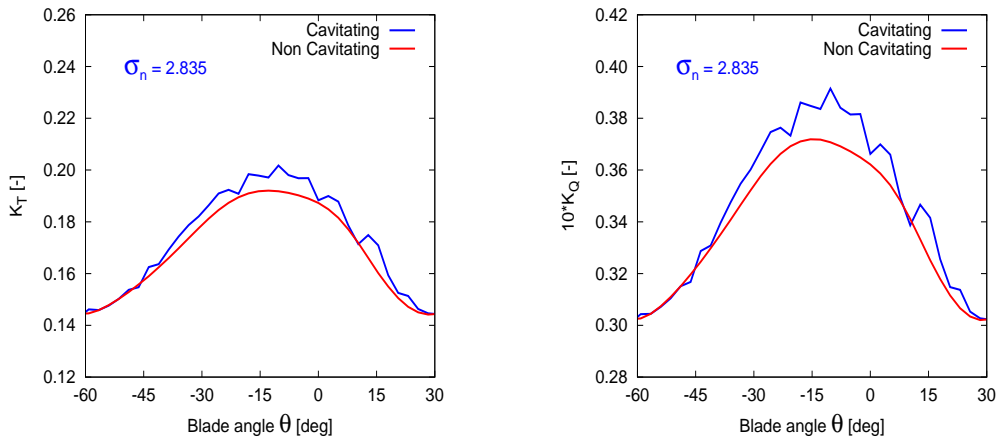
Figure 3.12: *Thrust and torque coefficient in cavitating and non cavitating conditions: $\sigma_n = 2.835$*
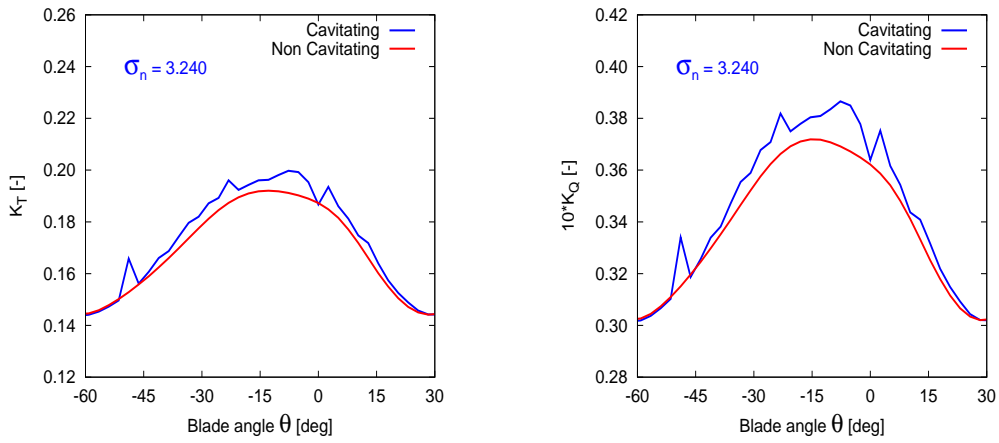
Figure 3.13: *Thrust and torque coefficient in cavitating and non cavitating conditions: $\sigma_n = 3.240$*
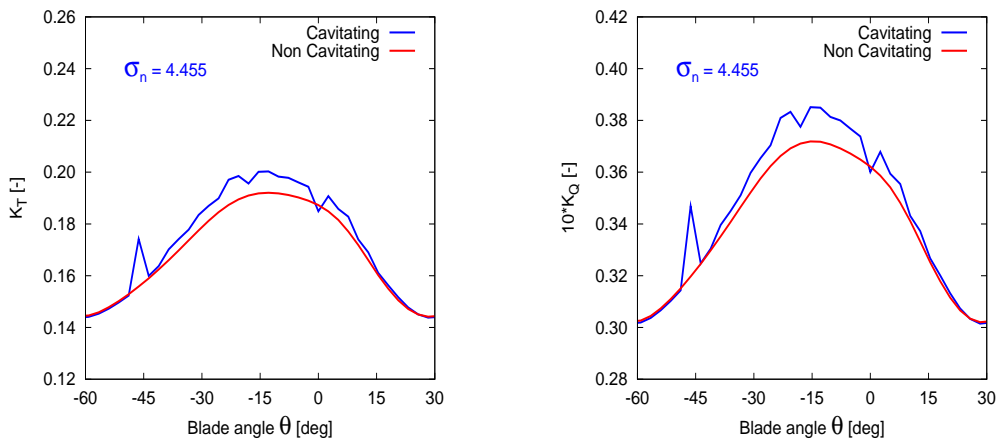
Figure 3.14: *Thrust and torque coefficient in cavitating and non cavitating conditions: $\sigma_n = 4.455$*
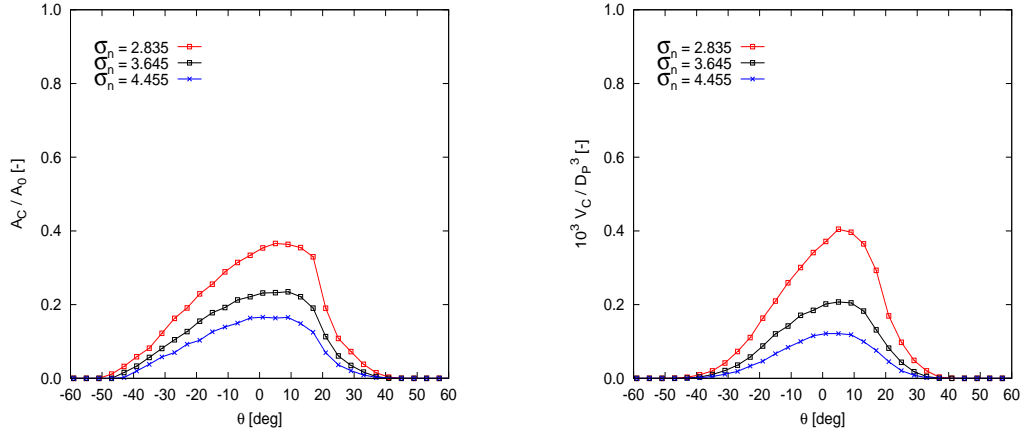
Figure 3.15: *Time histories of cavity area A_c (left) and volume V_c (right), as a function of blade angular position θ.*

Figures 3.16 and 3.17 show the cavity pattern during the growing phase ($\theta < 0°$), at the maximal extension ($\theta = 0$) and in the successive collapsing phase ($\theta > 0°$).

Hydroph	x/D_p	y/D_P	z/D_P
P2	0.0	0.0	1.32
H4	0.5	0.0	-0.88
H5	-0.5	0.0	-0.88
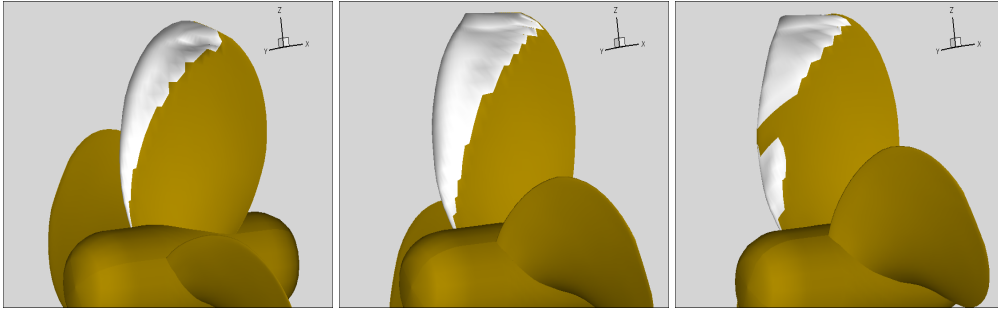
Figure 3.16: *Cavity pattern at different blade angular positions:σ_n = 2.835. From left to right: $\theta = -22°$, $0°$, $11°$, approximately.*

The hydrodynamic solution described above yields the input for the hydroacoustic analysis discussed hereafter. Three hydrophones are considered in and out of the propeller plane, to analyze some features of noise predictions by EBM and TVM. The hydrophone P2 is located in the propeller plane whereas hydrophones H4 and H5 are positioned downstream and upstream the propeller disc plane, respectively. Coordinates of the three observer locations are given in the previous table while propeller and hydrophones location are depicted in Fig.3.18. To better understand the influence of sheet cavitation on the resulting noise waveform and to highlight the main differences between the two strategies in the prediction of the cavitation noise, the acoustic
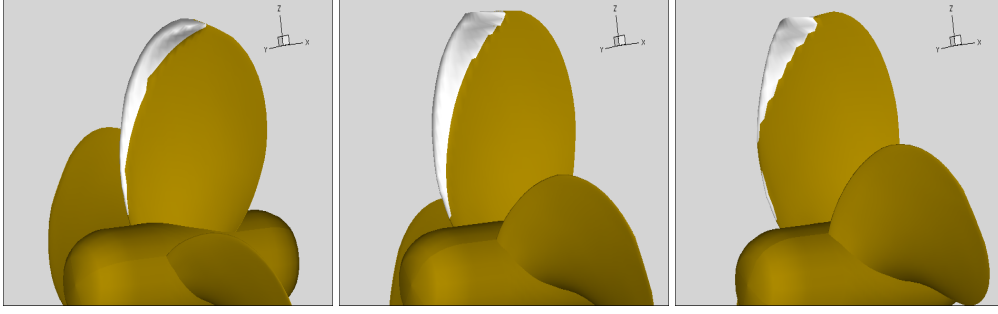
Figure 3.17: *Cavity pattern at different blade angular positions:σ_n = 4.455. From left to right: θ = $-22°$, $0°$, $11°$, approximately.*

Figure 3.18: *A 3D view of the propeller model (left) and hydrophones location (right).*

pressure signatures are first computed by considering perturbation only from one single blade. Figures 3.19, 3.20, 3.21 show noise time history predicted by the Equivalent Blade modeling at the three hydrophones, for $\sigma_n = 3.240$. Noise amplitude is plotted as a function of θ; at each location, the comparison between cavitating and non–cavitating flow condition is presented. For the non–cavitating conditions, at hydrophone P2, very close to the propeller blade tip, the thickness noise component is dominant whereas at hydrophones H4 and H5, the loading noise term is predominant with respect to the thickness noise contribution. Due to the symmetrical location of these hydrophones with respect to the propeller plane, the loading noise term rightly exhibits the sign inversion due to pressure values on face and back sides of the thrusting blade. The most relevant differences at cavitating conditions arise from the monopole (thickness) term that exhibits a more impulsive character in the waveform, governing the overall pressure signature. On the contrary the dipole (loading) term is not much altered by vaporization although a little increase in the pressure disturbance, at the angular positions affected by cavitation, appears. Such a behaviour is common for all the observers (P2, H4, H5) and may be explained by observing that the Equivalent Blade Approach accounts for the growth and collapse of the cavity by a step-by-step procedure where the blade shape is updated at each angular position. As a consequence, the equivalent body, composed of the blade plus the vapor sheet, is characterized by a geometry and (in particular) a normal velocity distribution $\mathbf{v} \cdot \mathbf{n}$ to the body surface that rapidly change during the revolution period, thus explaining the impulsive character of the resulting noise signatures [see Eq. (3.10),
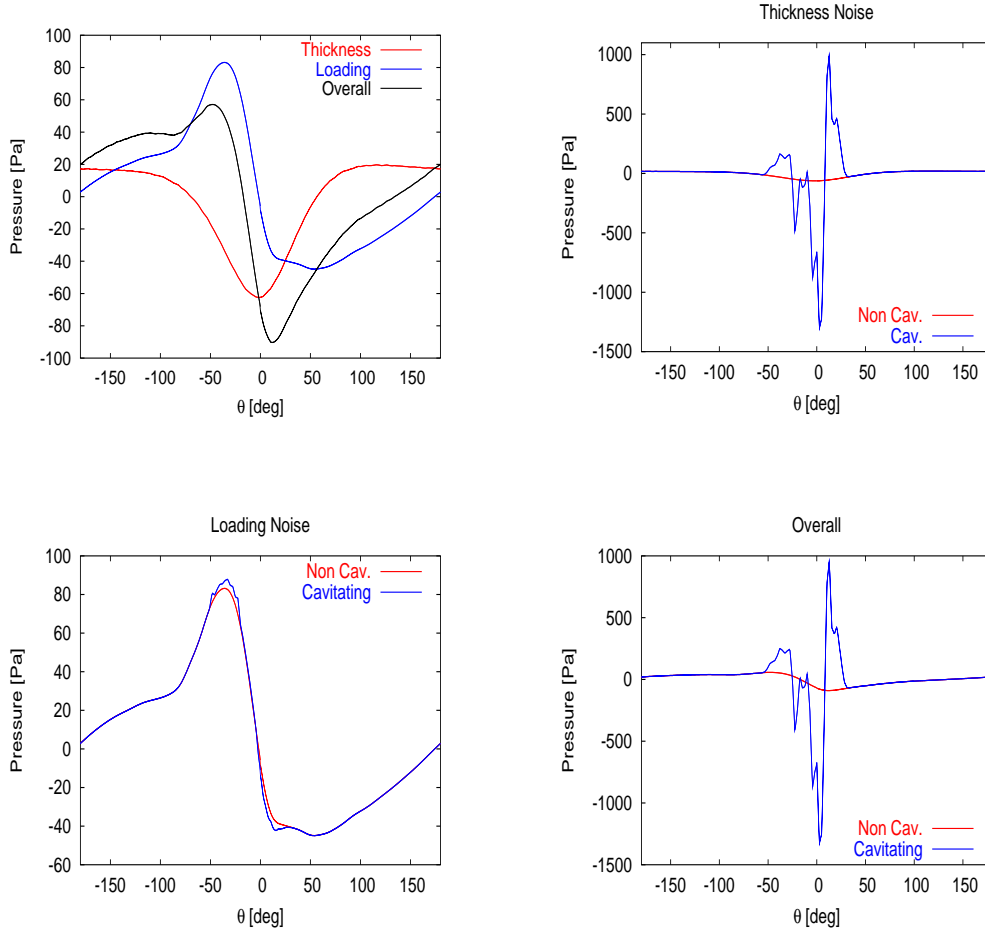
Figure 3.19: *Equivalent Blade Approach: acoustic pressure signatures at hydrophone P2. Non cavitating condition (top–left). Comparison between cavitating and non–cavitating conditions for thickness (top–right), loading (bottom–left) and overall (bottom–right) noise predictions.*

term $\mathcal{I}_1$]. On the contrary, the influence of the sheet bubble on the loading noise component $\mathcal{I}_2$ is negligible since the blade pressure time histories is not heavily affected by the presence of the cavity. As an example, sectional pressure distribution corresponding to the case $\sigma_n = 4.455$ is shown in Fig. 3.22 and Fig. 3.23 at two representative radial section, $r/R = 0.70$ and $r/R = 0.90$, and compared with the non–cavitating conditions at different time step. Major differences appear at the leading edge suction side region while the presence of the cavity slightly modifies the solution anywhere else. This behaviour is responsible for the global hydrodynamic loads (thrust–torque) shown in Figs. 3.12, 3.13, 3.14 and induces small variations in the loading noise signal. Note that at hydrophones H4 and H5, the resulting cavitating thickness noise waveforms are very similar eventhough the presence of the vapor sheet is limited to the upper side of the blade surface (suction side). Such a circumstance points out the monopole behaviour of the bubble which acts as a pulsating sphere with a 3D homogeneous influence around the body.

For the same observer positions and operating conditions, Figs. 3.24, 3.25, 3.26 show noise time histories predicted by the Transpiration Velocity Modeling. In this approach the dynamics of the sheet cavity is described by the porous term $\mathcal{I}_3$ of Eq. (3.10), which requires the knowledge of the flow–velocity distribution, **u**, upon the basic blade and the values of velocity and acceleration
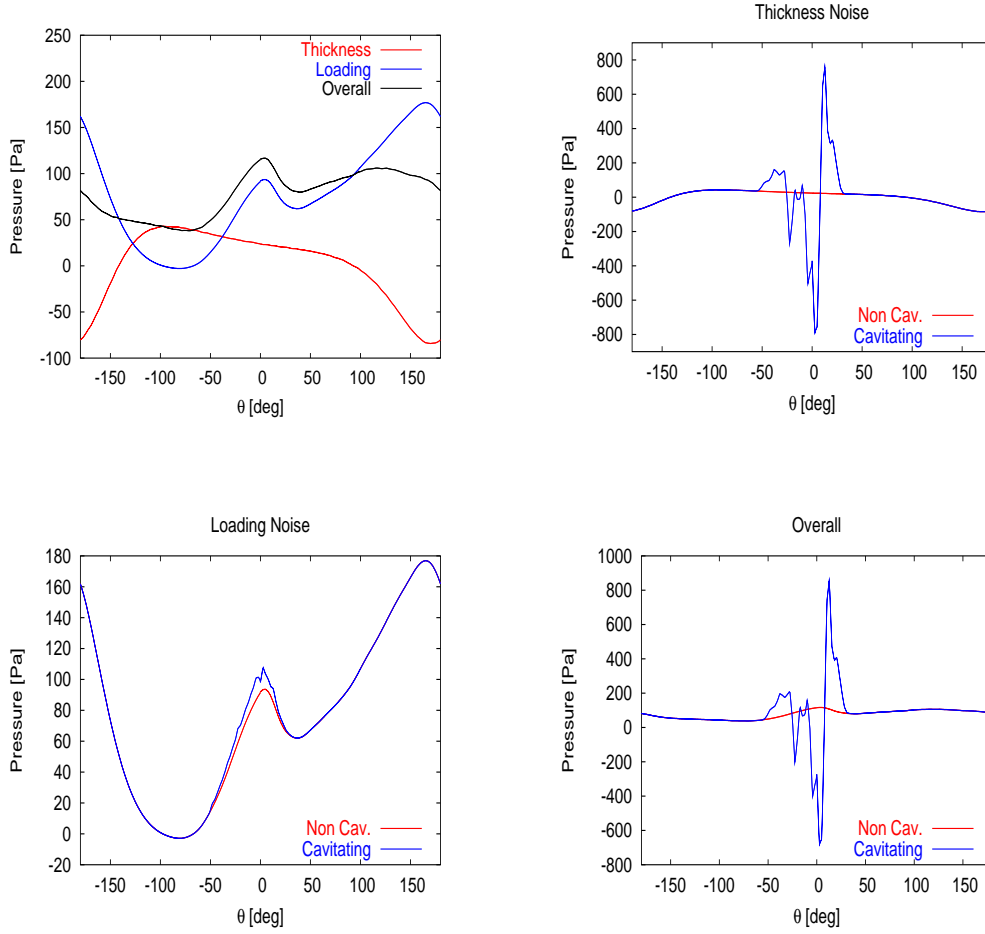
Figure 3.20: *Equivalent Blade Approach: acoustic pressure signatures at hydrophone H4. Non cavitating condition (top–left). Comparison between cavitating and non–cavitating conditions for thickness (top–right), loading (bottom–left) and overall (bottom–right) noise predictions.*

at each point of the cavitating region during the blade revolution. At each hydrophone location, the thickness noise term $\mathcal{I}_1$ does not change from non–cavitating to cavitating condition because the integration surface does not change during the revolution period. Similarly to what observed in the loading noise prediction by the Equivalent Blade Approach, numerical results show that the dipole term $\mathcal{I}_2$ is slightly affected by the transient cavity because of the negligible dependence of the blade loads on the cavitation occurrence. The evaluation of cavitation noise computed by the proposed model depends on the velocity term $\mathcal{I}_{3_v}$ and the acceleration term $\mathcal{I}_{3_a}$ defined in section 3.2.1: in agreement with Eq. (3.7), numerical results show that the major contribution to the impulsive noise comes from the term containing the acceleration time history of the vapor pocket attached to the blade surface, while the velocity term noise component is negligible.

Specifically, observing that observers P2, H4 and H5 are fully within the range of 5 diameters from the propeller plane and recalling that this value is a limit up to which the compressibility delays effects, and hence $\nabla\vartheta$, may be neglected (see section 2.5), the major noise contribution derives from the pseudo–thickness term $\left[\rho_0 \dfrac{d^2 h_c}{dt^2}\, \hat{G}\right]_\vartheta$. For distances from the disc greater than 5 diameters, the terms containing $\nabla\vartheta$ in the acceleration term are in general not negligible, affecting the acoustic pressure amplitude and phase. However, when the aim of the analysis is to evaluate
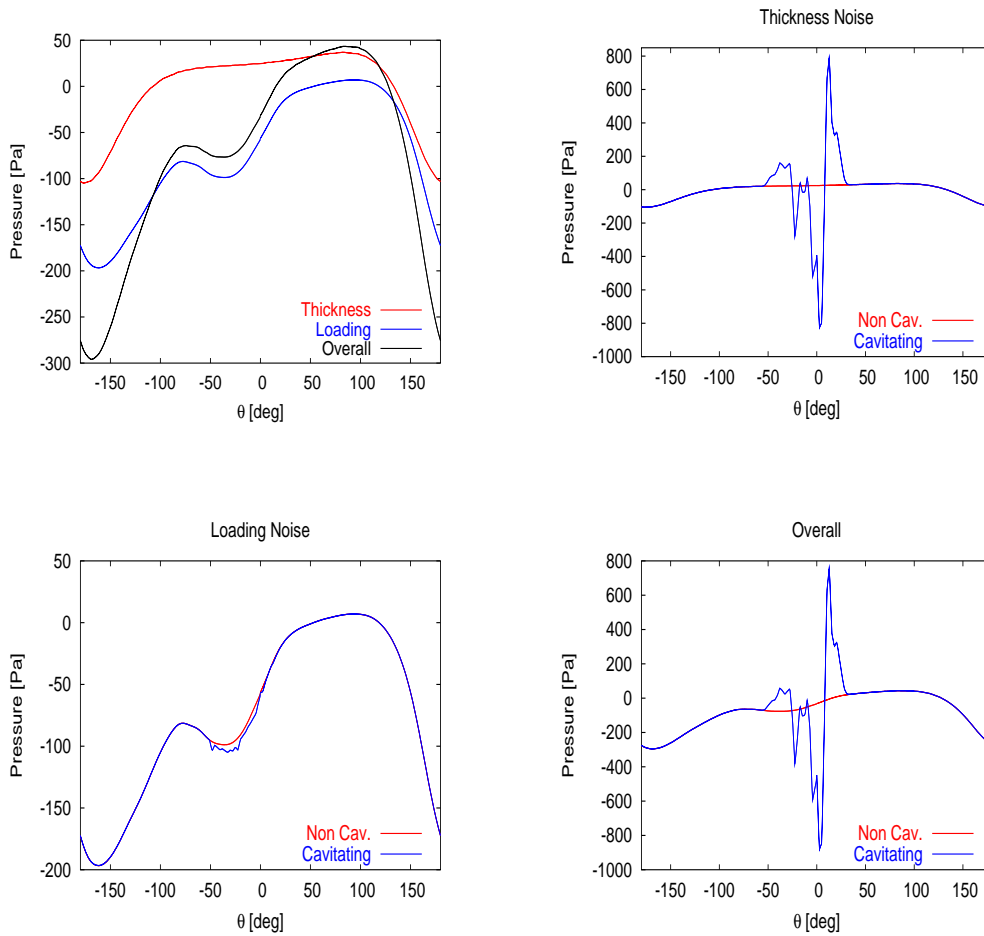
Figure 3.21: *Equivalent Blade Approach: acoustic pressure signatures at hydrophone H5. Non cavitating condition (top–left). Comparison between cavitating and non–cavitating conditions for thickness (top–right), loading (bottom–left) and overall (bottom–right) noise predictions.*

the effect of the impulsive cavitation noise on the hull–plate[3], the distances involved in the hydroacoustic computation are fully within the range of 5 diameters and hence, the dominant noise effect is mainly due to the inertial term $\dfrac{d^2 h_c}{dt^2}$.

The comparison between the acoustic predictions obtained by the Equivalent Blade Model and the Transpiration Velocity Model is shown in Figs. 3.27, 3.28, 3.29 and 3.30 for a four–bladed propeller and for the hydrophones P2, H4, H5 at different cavitation numbers. Numerical results point out that the agreement between the two hydroacoustic models is good: the resulting noise signatures, induced by the four–bladed propeller model, are very similar in shape and order of magnitude at any observer and for any cavitating condition, thus providing substantially the same evaluation of the sheet cavitation influence on the overall noise. However, discrepancies between the two numerical results are present in the peak values and become more evident by decreasing the cavitation number. The reasons of such a behaviour are in the different way to account for the dynamics of the vapor cavity. Peak–values are principally related to the time history of the bubble; in the Transpiration Velocity Model, the accuracy in computing both the velocity and

---

[3]Civil ships configuration fall within this case.
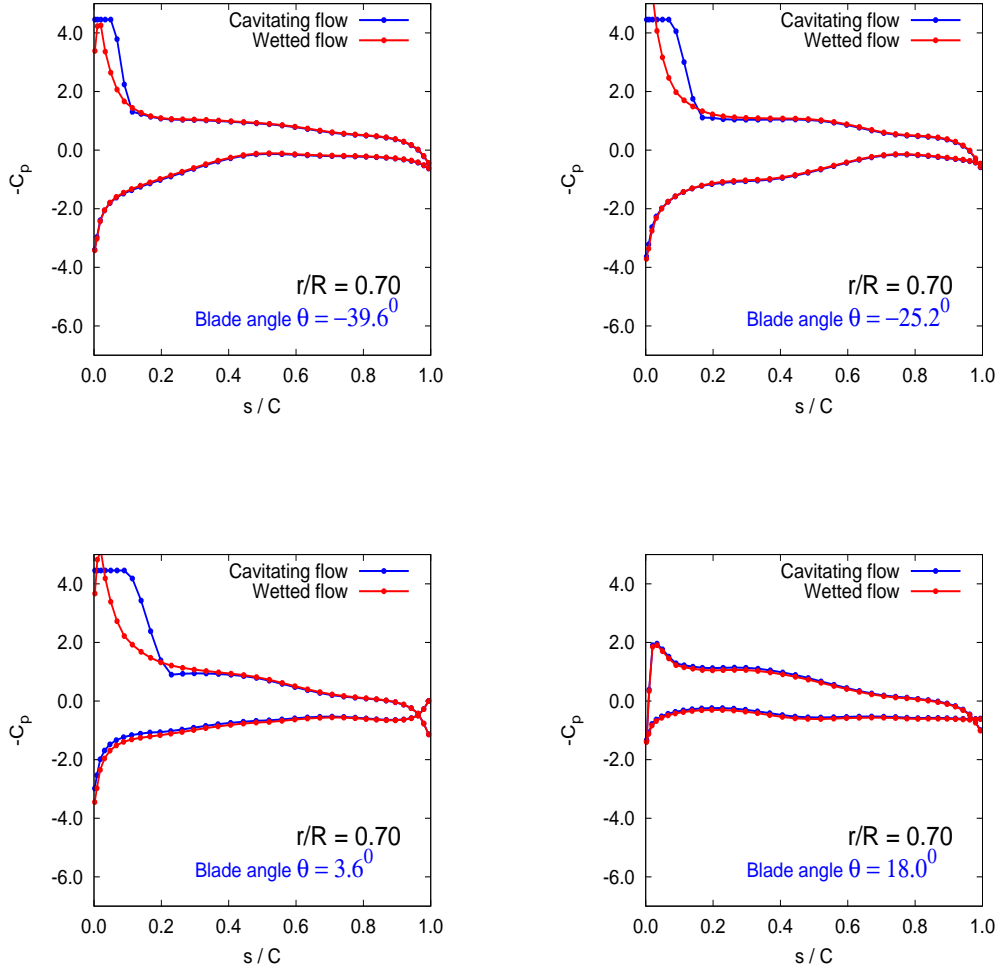
Figure 3.22: *Pressure coefficient distribution at blade section $r/R_P = 0.7$ and $\sigma_n = 4.455$. Blade angular position between $\theta = -39.6°$ and $\theta = 18°$.*

the acceleration of the cavity (at the cavitating panels) strongly depends on the quality of the hydrodynamic data. Dealing with impulsive functions, the higher is the time resolution, the more is the accuracy of computing the time derivatives. In the present calculations, the time steps used to discretize each propeller revolution are equal to 140, representing a compromise between the need of a detailed description of the growth and implosion of the cavity and reduced computational efforts. On the contrary, the Equivalent Blade Approach does not involves explicitly the time derivatives of the cavity, hence is less accurate in describing the shape of the bubble during the propeller revolution does not affect the hydroacoustic prediction as in the Transpiration Velocity Model. Such a behaviour in the noise prediction is well shown in Fig. 3.31: it is evident that both models have the same sensibility with respect to the cavitation number but the decrease of the peak value by increasing σ_n is more evident in the signals predicted by the Equivalent Blade Approach. The capabilities of the two approaches in describing the field-noise radiation at different observer locations is shown in Figure 3.32 which reveals that the two models have the same sensibility with respect to the noise directivity.

The comparison in the frequency domain is shown in Figs. 3.33, 3.34, 3.35 and 3.36 where
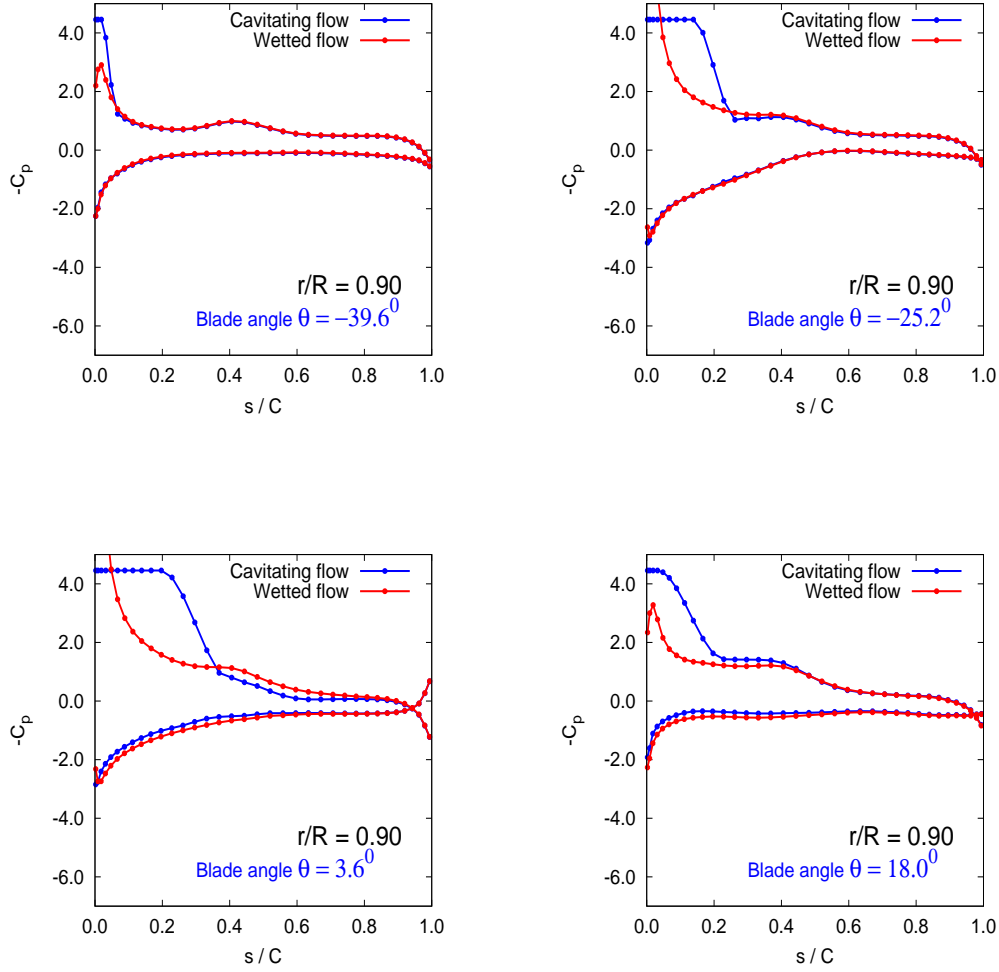
Figure 3.23: *Pressure coefficient distribution at blade section $r/R_P = 0.9$ and $\sigma_n = 4.455$. Blade angular position between $\theta = -39.6°$ and $\theta = 18°$.*

the noise components are plotted as a function of the Fourier harmonics. The intensity of the components is given as $A_k = \sqrt{c_k^2 + s_k^2}$ where c_k and s_k are, respectively, cosine and sine terms of the Fourier series. The pressure spectra show that the differences in the noise signatures are spread over the examined frequency range; more discrepancies appear at harmonics greater than 8, corresponding to multiples of blade passing frequency (BPF) greater than 2, although the good agreement at the first two BPF worsens at low cavitation number (see Fig. 3.36). Finally, Fig. 3.37 shows the difference in the pressure spectra computed by the Transpiration Velocity Modeling for $\sigma = 3.240$ between cavitating and the non–cavitating condition. In the cavitating case the amplitude of the pressure disturbance at the fundamental frequency (1 BPF) is 5 or 6 times greater than that related to the non–cavitating case while, as expected, at higher frequencies the frequency content of the rotational noise (the only existing for non–cavitating propellers) is negligible.
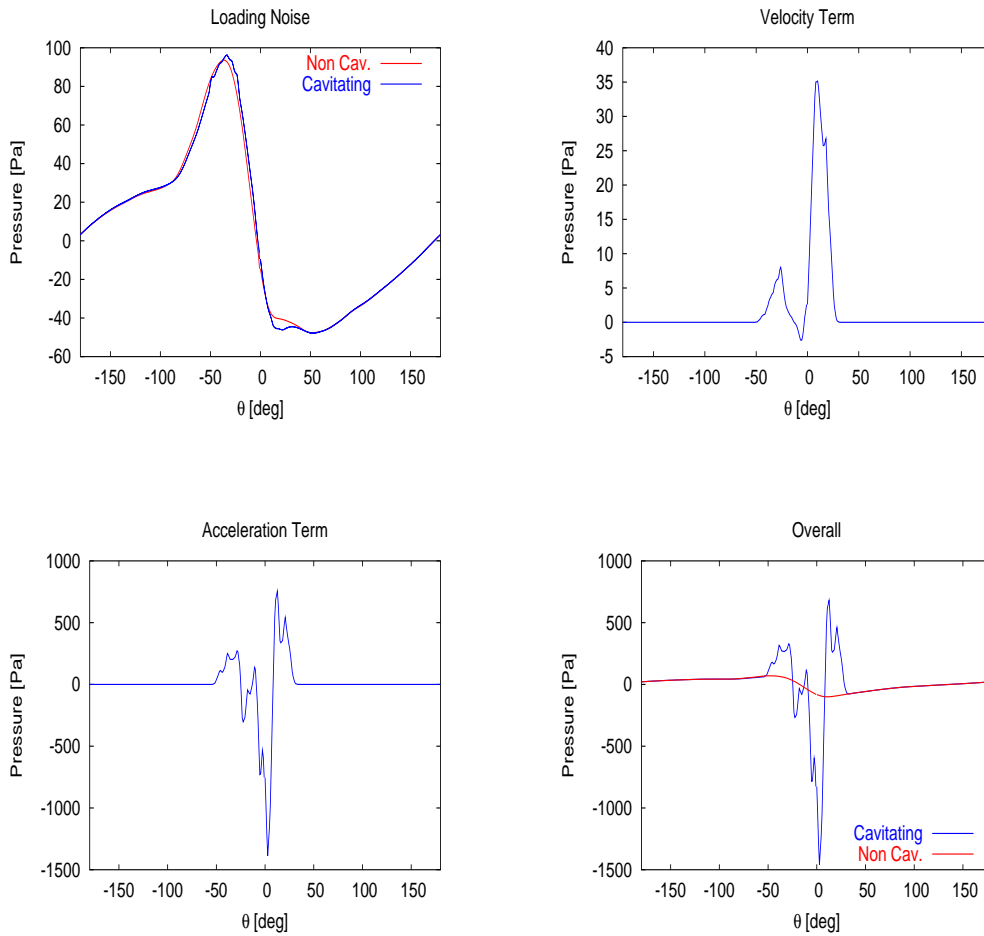
Figure 3.24: *Transpiration Velocity Modeling: acoustic pressure signatures at hydrophone P2. Comparison between cavitating and non–cavitating conditions for loading (top–left) and overall (bottom–right) noise predictions. Pressure disturbance due to the velocity term (top–right) and acceleration term (bottom–left).*

Summary and Discussion

The two methodologies aimed at the prediction of the noise induced by sheet–cavitation phenomenon on propeller blades examined here, are based on different strategies to compute the effects of growth and implosion of the cavity. The Transpiration Velocity Modeling includes the presence of the fluctuating cavity into the hydroacoustic solver through porosity terms directly associated to the velocity and acceleration of the cavity. No further assumption is made except that concerning the small thickness of the cavity, enabling to identify the cavity with its projection $\mathcal{S}_{CB}$ onto the body surface. On the contrary, in the algorithm proposed by Salvatore and Ianniello (EBM), no porosity terms are introduced and the dynamics of the cavity is modelled by a step-by-step procedure where the blade surface is *updated* at each azimuthal position to account for the cavity shape, as it were an equivalent rigid blade; hence, the lower the frequency of the cavitating phenomenon, the better the noise prediction is. Numerical comparison between approaches 1 and 2 confirms their capabilities to capture the main influence of the sheet cavitation dynamics on the overall noise signature. The different strategies in computing the acoustic effects of the time evolution of the cavity does not affect the the waveform of the overall noise signal but rather the

61
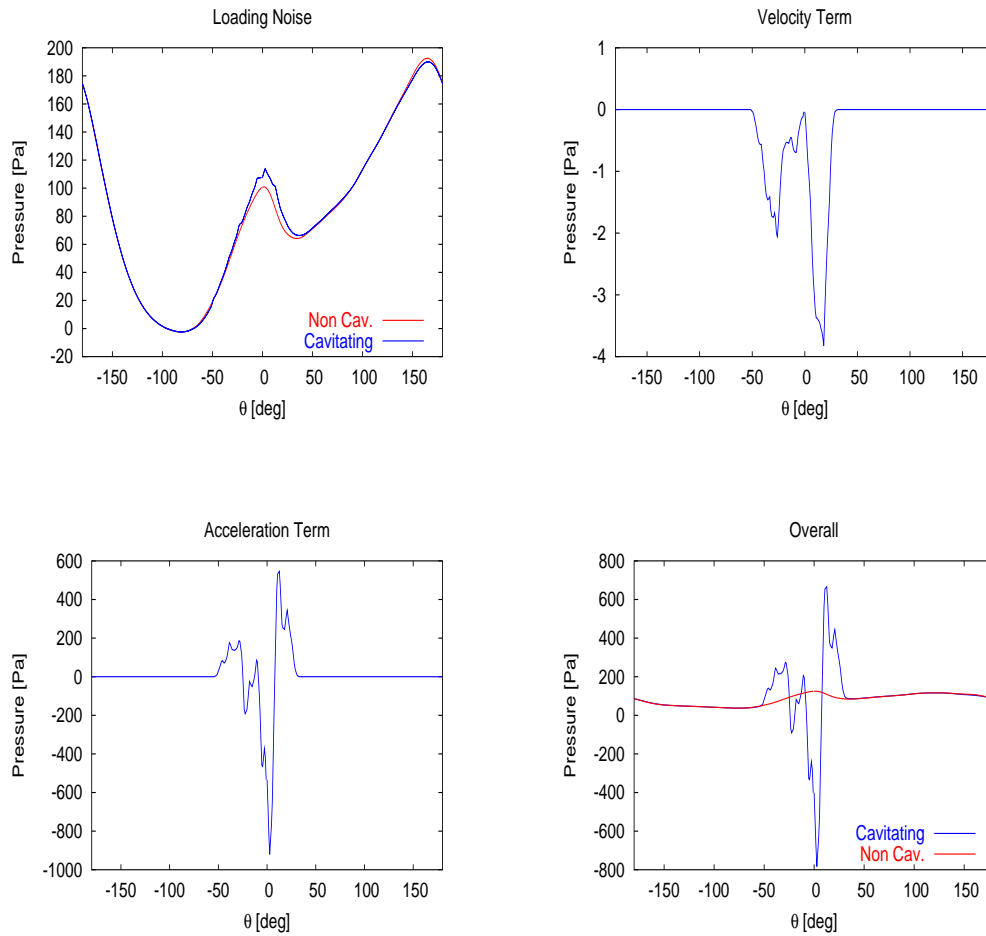
Figure 3.25: *Transpiration Velocity Modeling: acoustic pressure signatures at hydrophone H4. Comparison between cavitating and non–cavitating conditions for loading (top–left) and overall (bottom–right) noise predictions. Pressure disturbance due to the velocity term (top–right) and acceleration term (bottom–left).*

higher frequency content of its spectrum. From a computational point of view, an advantage in using the Transpiration Velocity Modeling is that the integration surface does not change during the blade revolution, while the Equivalent Blade Approach requires an integration process over a time–depending surface. Nonetheless, a drawback of the proposed methodology is its sensitivity with respect to the accuracy of the evaluation of the time–history of the bubble shape.
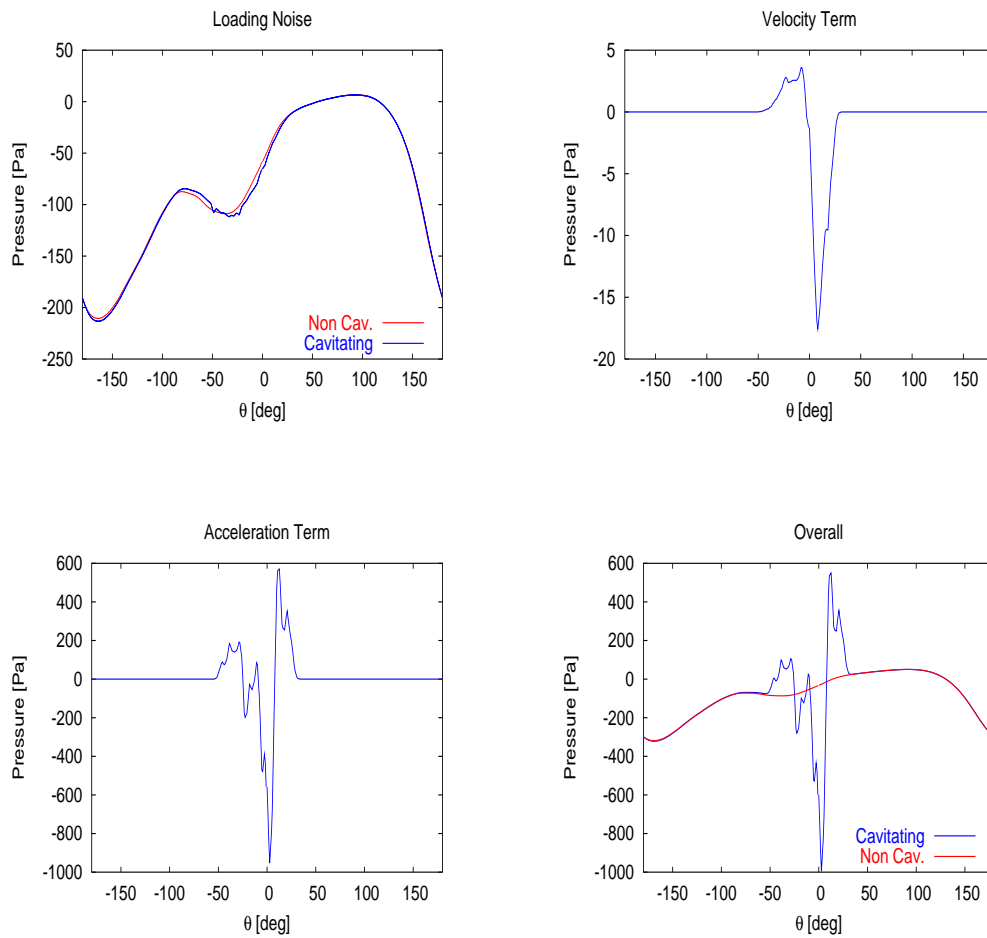
Figure 3.26: *Transpiration Velocity Modeling: acoustic pressure signatures at hydrophone H5. Comparison between cavitating and non–cavitating conditions for loading (top–left) and overall (bottom–right) noise predictions. Pressure disturbance due to the velocity term (top–right) and acceleration term (bottom–left).*
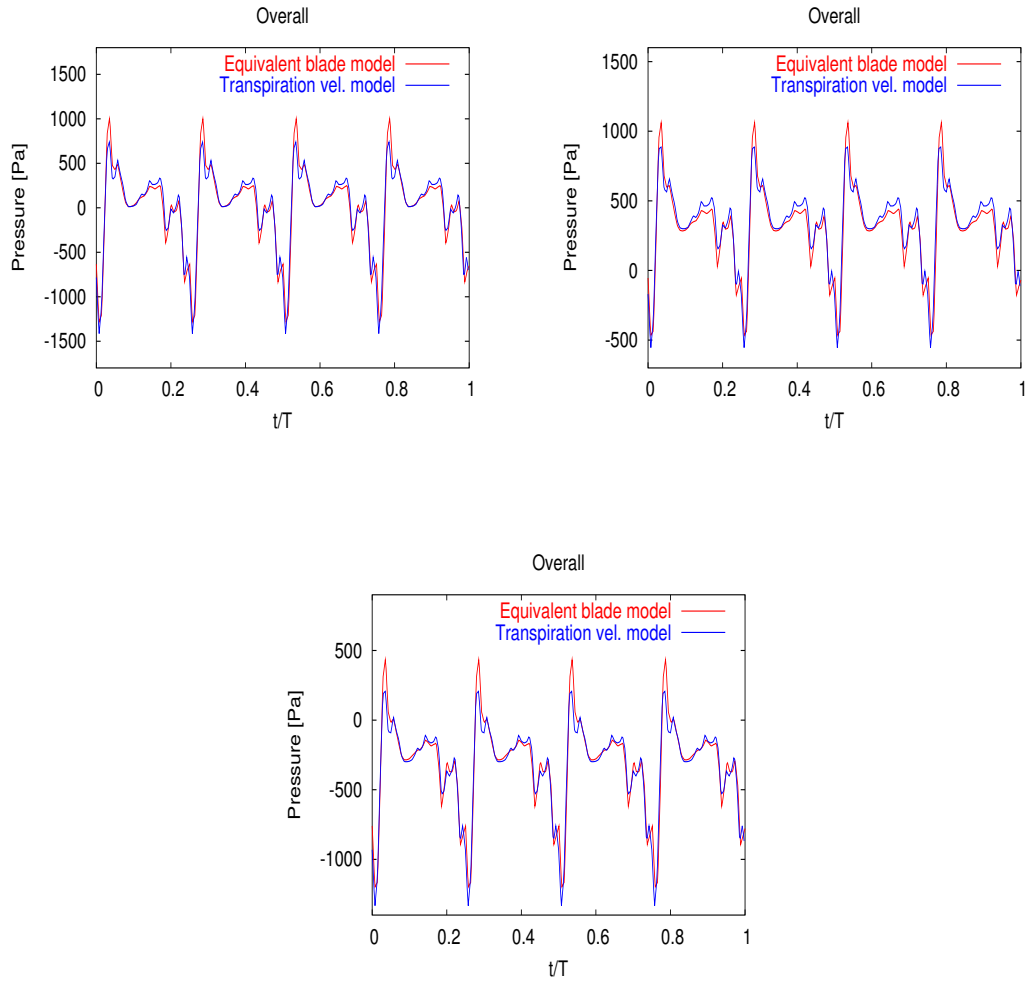
Figure 3.27: *Comparison between the Equiv. blade model and the Trans. velocity model at observer P2 (top-left), H4 (top–right) and H5 (bottom) at $\sigma_n = 3.240$*
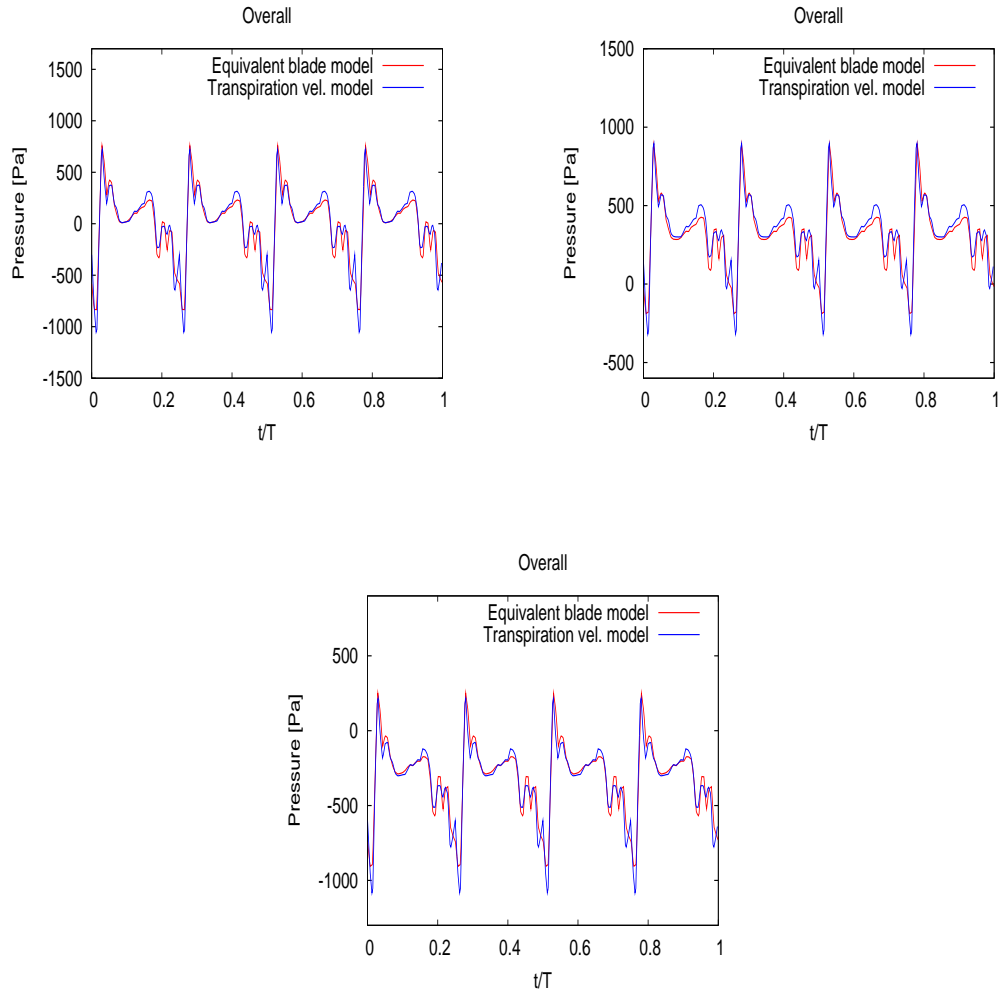
Figure 3.28: *Comparison between the Equiv. blade model and the Trans. velocity model at observer P2 (top-left), H4 (top–right) and H5 (bottom) at $\sigma_n = 3.645$*
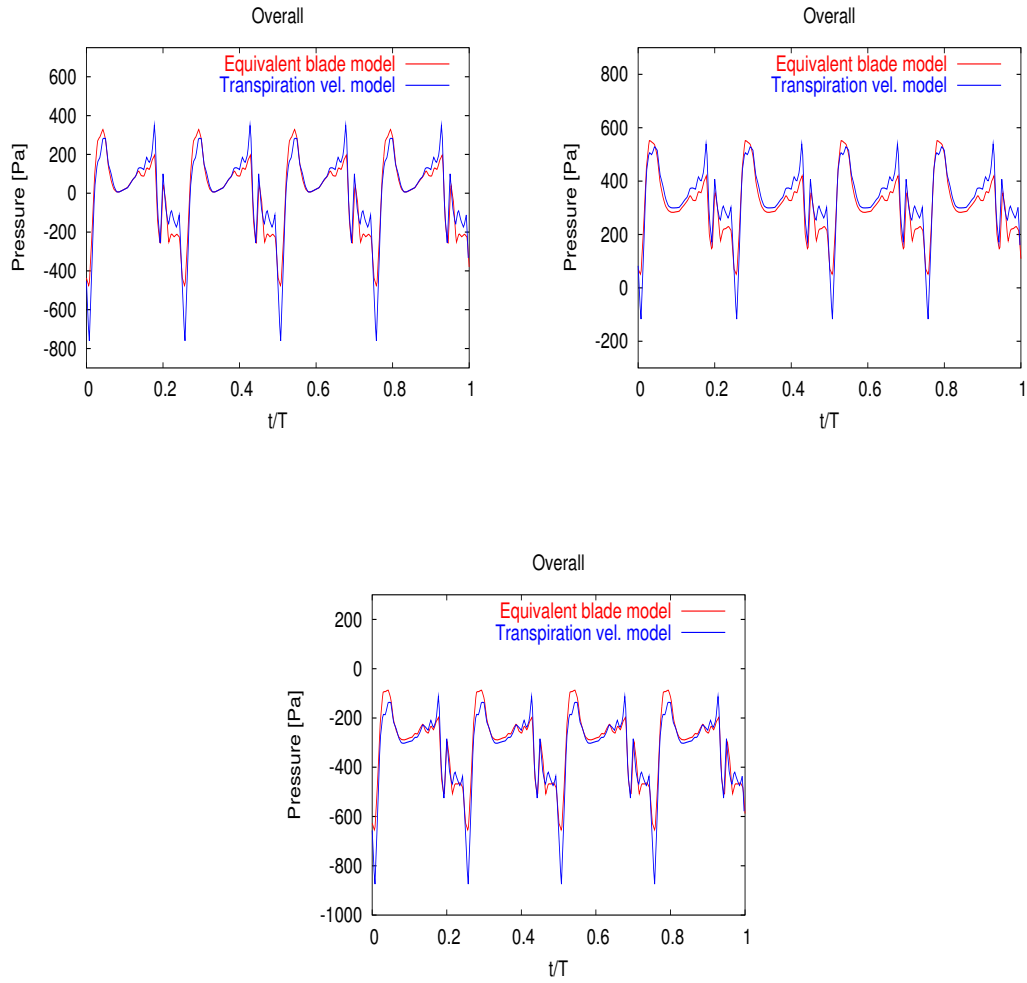
Figure 3.29: *Comparison between the Equiv. blade model and the Trans. velocity model at observer P2 (top-left), H4 (top–right) and H5 (bottom) at $\sigma_n = 4.455$*
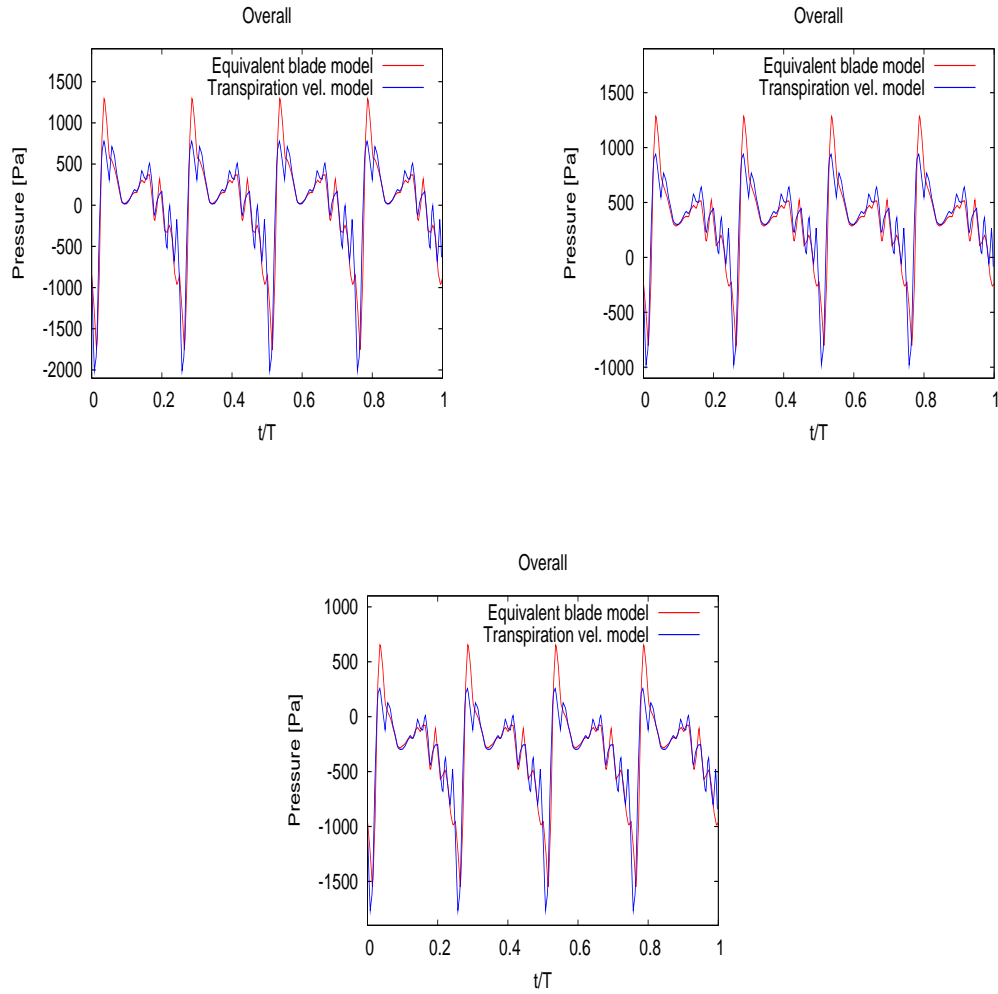
Figure 3.30: *Comparison between the Equiv. blade model and the Trans. velocity model at observer P2 (top-left), H4 (top–right) and H5 (bottom) at $\sigma_n = 2.835$*
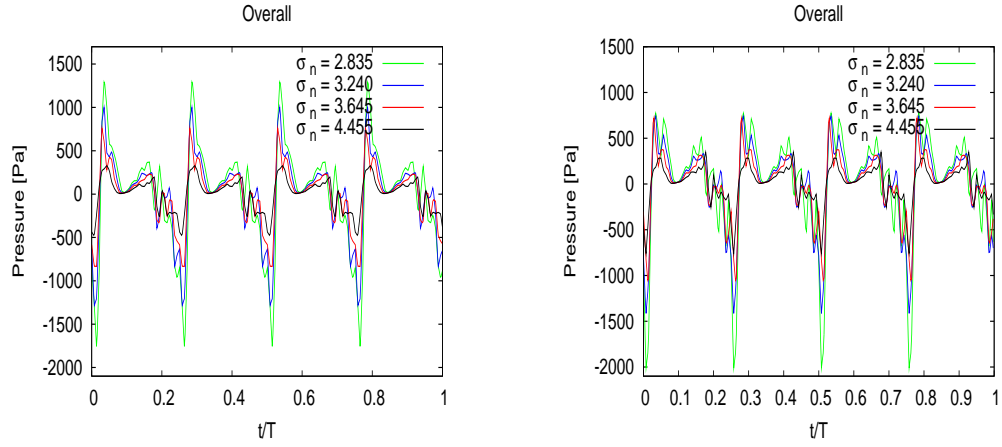
Figure 3.31: *Noise signature predicted by the Equiv. blade model (left) and the Trans. velocity model (right) at P2 for different cavitation numbers.*
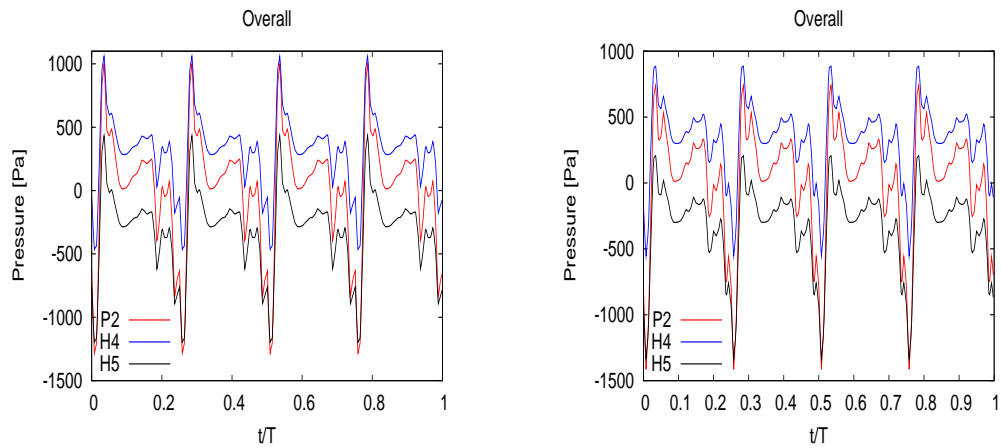
Figure 3.32: *Noise signature predicted by the Equiv. blade model (left) and the Trans. velocity model (right) at P2, H4 and H5. Cavitation number: $\sigma_n = 3.240$*
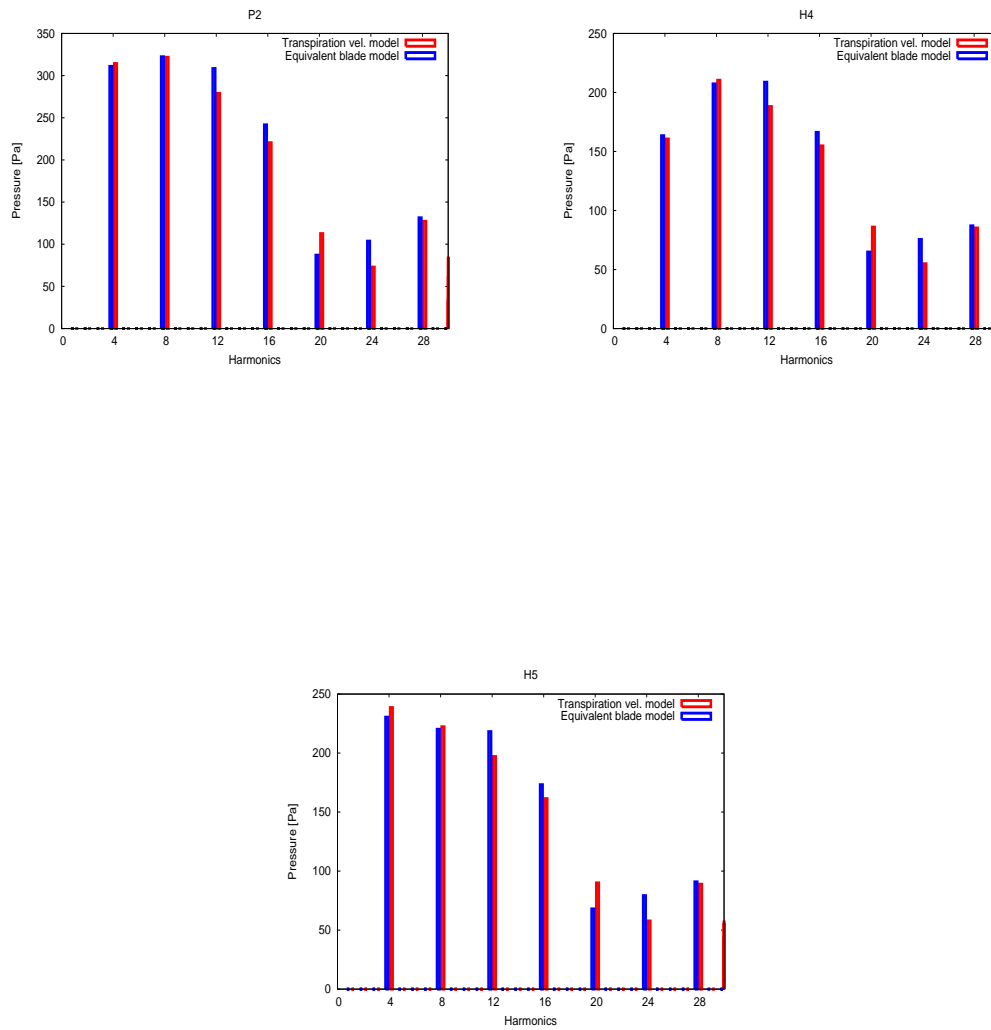
Figure 3.33: *Acoustic pressure spectra as a function of blade passing frequency multiplies. Comparison between the Equiv. blade model and the Trans. velocity model at observer P2 (top-left), H4 (top–right) and H5 (bottom) at $\sigma_n = 3.240$*
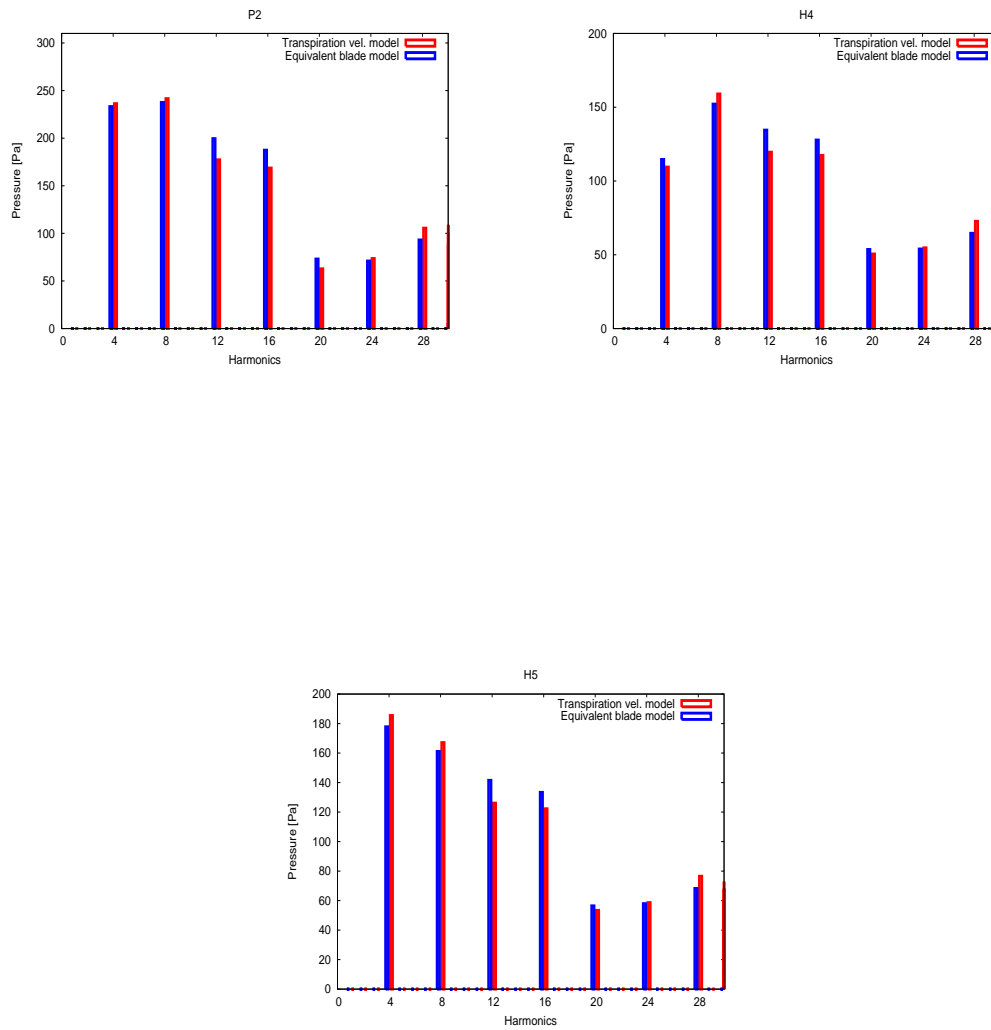
Figure 3.34: *Acoustic pressure spectra as a function of blade passing frequency multiplies. Comparison between the Equiv. blade model and the Trans. velocity model at observer P2 (top-left), H4 (top–right) and H5 (bottom) at* $\sigma_n = 3.645$
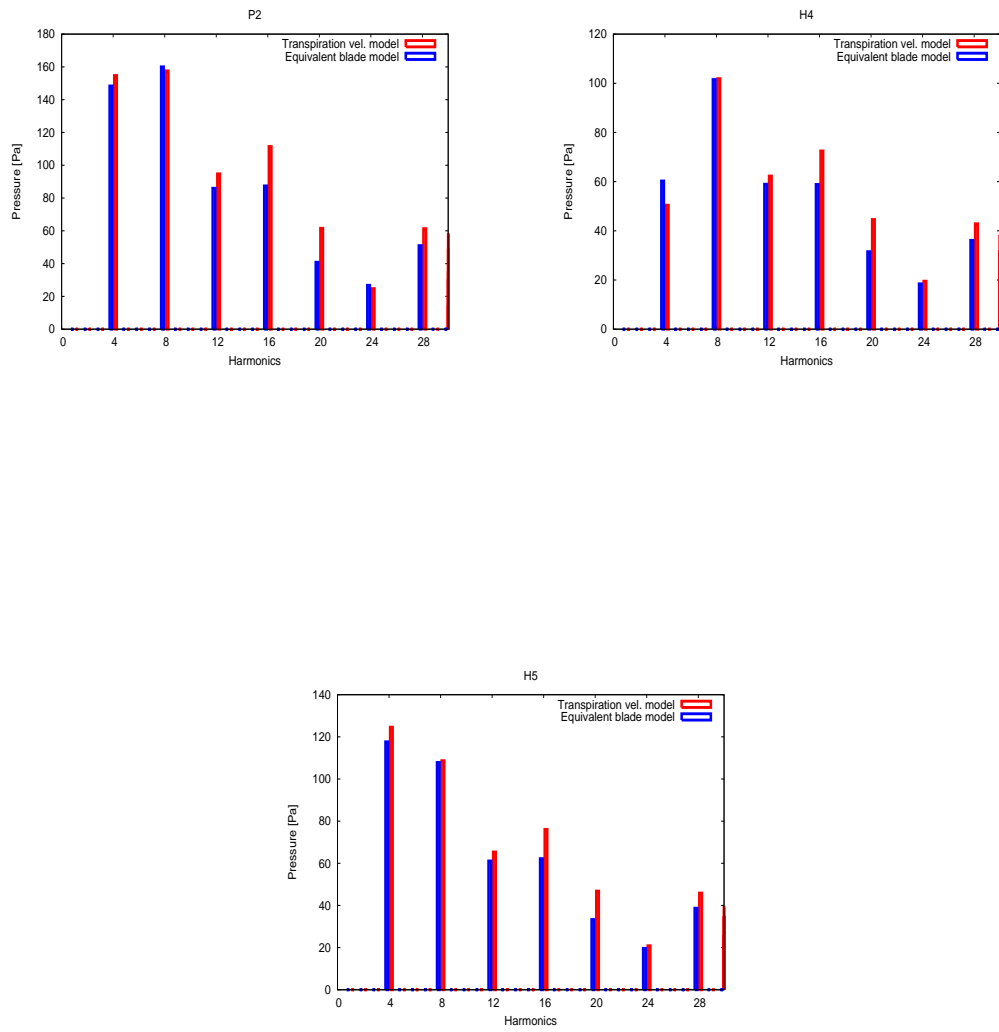
Figure 3.35: *Acoustic pressure spectra as a function of blade passing frequency multiplies. Comparison between the Equiv. blade model and the Trans. velocity model at observer P2 (top-left), H4 (top–right) and H5 (bottom) at $\sigma_n = 4.455$*
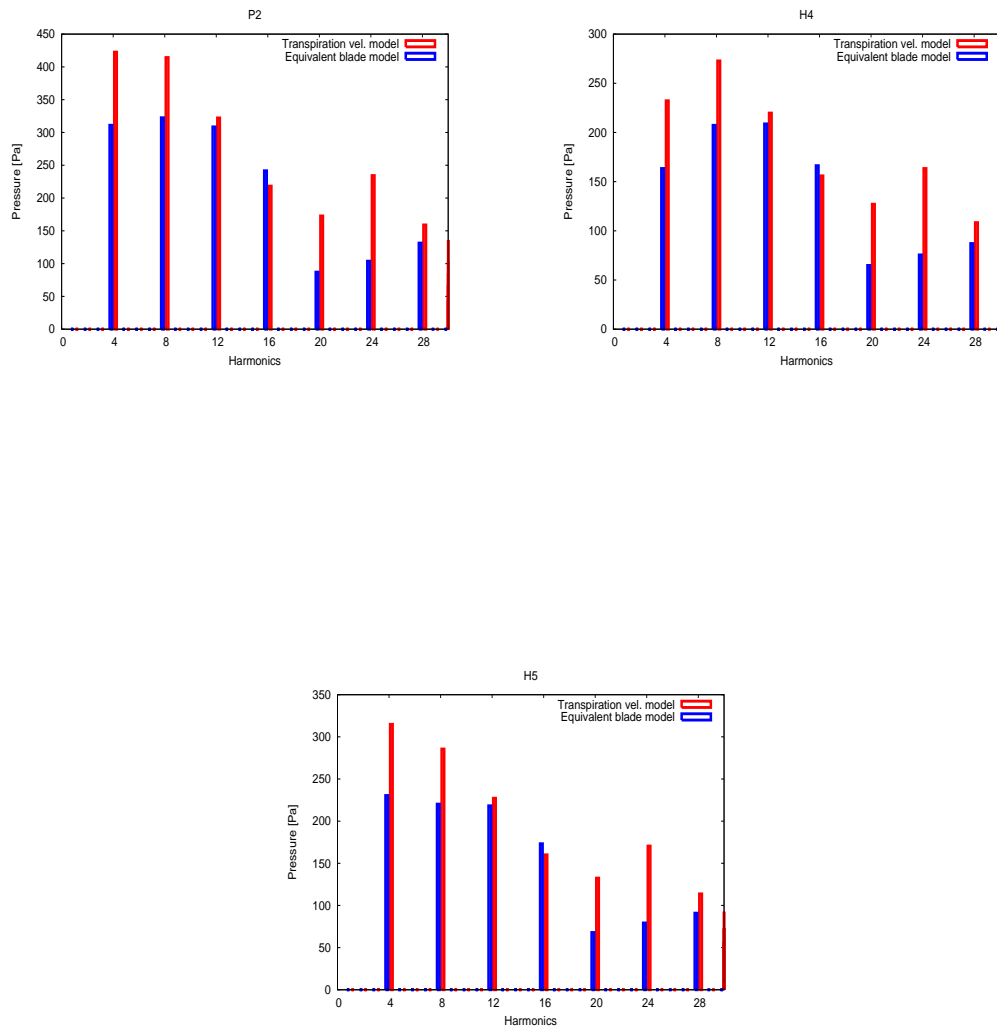
Figure 3.36: *Acoustic pressure spectra as a function of blade passing frequency multiplies. Comparison between the Equiv. blade model and the Trans. velocity model at observer P2 (top-left), H4 (top–right) and H5 (bottom) at $\sigma_n = 2.835$*
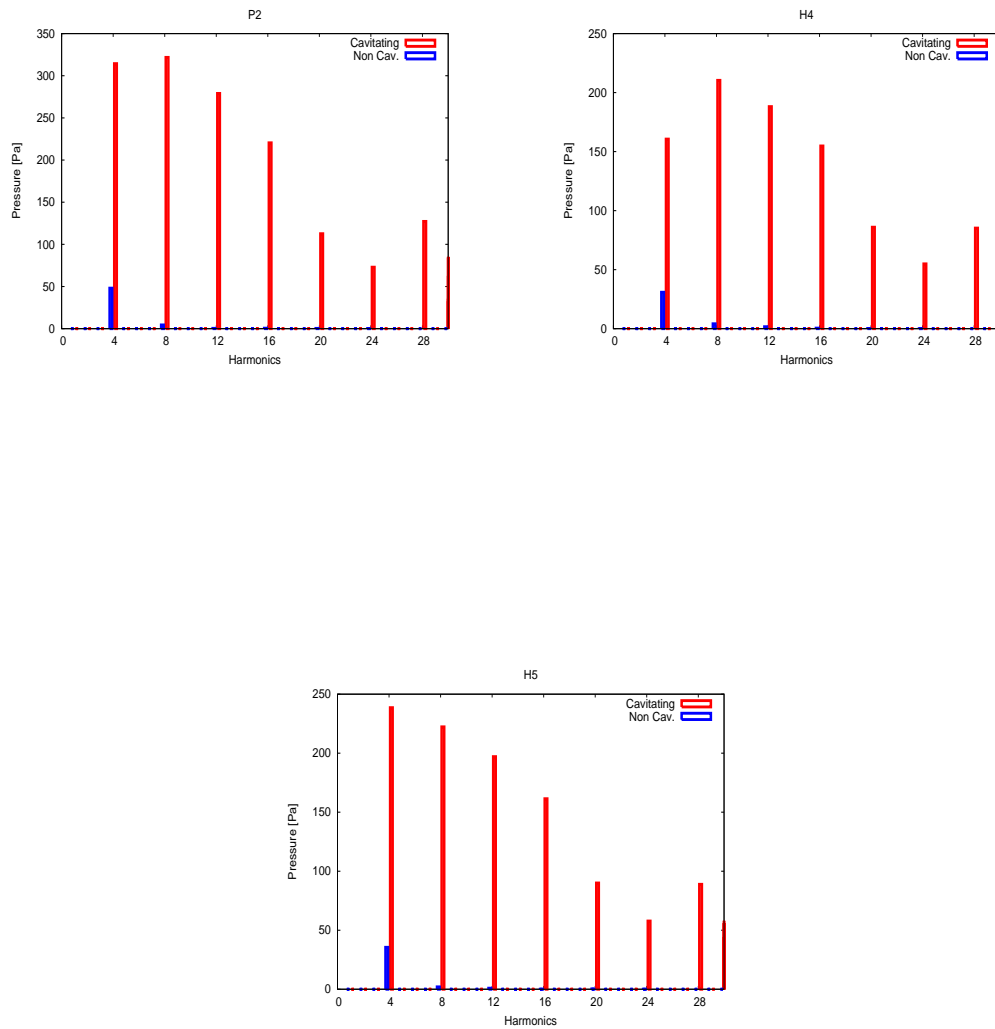
Figure 3.37: *Acoustic pressure spectra as a function of blade passing frequency multiplies. Comparison between non cavitating and cavitating conditions at $\sigma_n = 3.240$, performed by TVM.*

Concluding Remarks

An important aspect must be pointed out about the numerical investigation that has been performed. The numerical results concern the INSEAN E779A propeller subject to a non–uniform onset flow. Cavitating propeller flow reference data are obtained from measurements performed

Figure 3.38: *Tunnel flow visualization of the INSEAN E779A propeller model during experimental investigation.*

at the Italian Navy Cavitation Tunnel (CEIMM) (see Fig. 3.39); a detailed description of the experimental investigation and of the techniques used is presented in Ref. [31], for the propeller operating in uniform flow condition, and in Ref. [51] for the extension to non uniform inflow condition; further details are found also in Ref. [53]. As a matter of fact, the two–phase data described in Refs. [31], [51] and [53] represent part of an experimental dataset collecting propeller hydrodynamics and hydroacoustics investigations performed at INSEAN during the last decade. The locations of hydrophones P2 and H4 used for the numerical analysis correspond exactly two of the pressure measurement points used in the experimental campaign; in detail P2 corresponds to the pressure transducers located in the propeller disk plane on the tunnel wall, whereas H4 corresponds to the hydrophone located in the radial plane at distance of about one radius downstream of the propeller plane at about $200mm$ far from the propeller axis. The availability of experimental data would suggest a numerical–experimental comparison to test the capabilities of the TVM modeling with respect to the prediction of the cavitation noise. Unfortunately, this necessary comparison has not been addressed for the following reasons:

1) The experiment has been performed in a cavitation tunnel and hence the presence of the walls is important and affects the noise signatures for both hydrophones P2 and H4. This problem is amplified by the dimensions of the test section: the propeller model, having a diameter $D_p = 22.727cm$ long, is installed inside the $200cm$ long tunnel with a $60X60cm$ test section. No noise data related to free-field noise are available.

2) Even if experimental data of the isolated propeller in unbounded space were available, the flow reference data are such that sheet cavitation is not the unique cavitation phenomenon appearing on the blades, as well shown in Fig. 3.38 other complex cavitation structures appear. In particular, it is worth noting the presence of the tip–vortex and presence of a separated cavity region composed of many bubbles. Such structures of vapor can not be modelled through the coupled hydrodynamic–hydroacoustic algorithm herein presented. Their implosion induce further noise

74

Figure 3.39: *INSEAN E779A propeller model inside the cavitation tunnel.*

that in any case can not be modeled through the TVM or EBM approach. There is no possibility of quantifying the sheet cavitation noise contribution with respect to those induced by other type of cavitation.

3) To the author's knowledge there are no other test-cases for cavitating propeller available in literature to address a comparison between numerical results (TVM or EBM) and experimental data; this assertion is supported by the fact that the experimental dataset indicated as *INSEAN E779A Dataset* and partially described in Refs. [31], [51] and [53], has been recognized as benchmark by partners of the FP6 Project Virtue "The Virtual Tank Utility in Europe".

Chapter 4

Sound Scattering from Moving Vibrating Surfaces

In this chapter a nonstandard application of the Ffowcs Williams and Hawkings equation is presented. A novel integral formulation devoted to the study of the noise signal scattered by moving vibrating bodies impinged by acoustic waves is proposed, and its potentialities are discussed. Capabilities and drawbacks of the proposed sound scattering methodology are proven through the analysis of different test cases. In aeronautical or marine rotorcraft, a scattering formulation allows both the analysis of the effects of fuselage or hull on the sound radiated by the rotor (the main source of noise), and the corresponding vibrating loads acting on their surfaces. Here, the scattering formulation is applied to the analysis of noise emitted by a helicopter in descent flight.

4.1 The Problem

An obstacle or inhomogeneity in the path of a sound wave causes scattering if secondary sound spreads out from it in a variety of directions. This phenomenon may be relevant when the wavelength of the impinging acoustic wave is comparable with a characteristic dimension of the scatterer (solid bodies, interfaces among different media, etc.); as a consequence of the wave-scatterer interaction, the features of the resulting pressure field (in terms of magnitude, waveform, directivity and frequency content) may be very different from the structure of the noise field in unbounded space. The problem of sound scattering is present in a wide range of engineering applications dealing with steady and moving objects; the presence of solid boundaries, as fuselage or hull, may cause the sound field emitted by rotors to change greatly. In aeronautics, for instance, the evaluation of scattered acoustic fields is of interest both for the evaluation of overall noise emitted by moving aircraft and for the prediction of fuselage wall vibrations that, in turn, are a source of cabin noise (aeroacoustoelastic application). The same phenomena are of interests for marine applications; increasing emphasis on prediction of hull vibration due to propeller sources stems from the need to meet demanding requirements for passenger comfort. Broadband random vibration can be particularly obtrusive as well as single frequency components at multiples of propeller blade passing frequency. Satisfactory vibration prediction requires estimation of the distribution of fluctuating pressure over the whole hull surface.

The decomposition of the noise field into incident and scattered components is useful when, within the limits of the required accuracy, the source of the incident field may be considered independent of the presence of the scattering surface. Indeed, in aeronautical applications where the main source of noise is an aircraft component that may be assumed to be aerodynamically independent, first the incident pressure field may be determined through an aerodynamic/aeroacoustic analysis of it, and then the rest of the aircraft configuration (the scattering portion) may be taken into account in the second step of the process dealing with the scattered field. For instance, this

approach is applicable in the analysis of propeller-driven aircraft where the noise emitted by the propellers is scattered by the fuselage (see Refs. [54], [55]). However, a similar acoustic analysis may be applied also to those rotorcraft configurations where the rotating blades are the main source of noise, with the major contribution of the fuselage to the noise field being represented by its scattering effect (some helicopter flight configurations fall within this category). For ships and vessels, the main source of noise is undoubtedly the (cavitating) propeller operating in hull–behind condition; the coupling between the propeller and the hull flow is generally considered sufficiently weak to permit separation of the two problems [28]. In particular, this configuration may be successfully studied through a simplified model where hull–propeller hydrodynamic interactions are limited to consider the hull wake flow incoming to an isolated propeller in unbounded fluid domain. Therefore, once the spatially non–uniform onset flow due to the wake of the ship is known numerically or experimentally, the assumption of hydrodynamic independence of the hull is applicable.

The analysis of noise scattering involves pressure waves impinging both on non-moving and on moving surfaces. A wide literature is available on this subject (see, for instance, Refs. [56], [57]). Here, a boundary integral formulation based on the Ffowcs Williams and Hawkings (FWH) equation [58] for the analysis of the pressure field scattered by an elastic moving body is presented. This formulation yields a unified solver that is not only able to radiate the sound, but can also be used to evaluate the acoustic disturbance over moving, vibrating surfaces. It may be conveniently applied to acoustoelastic problems where body elastic vibrations interact with the exterior pressure field and generate noise within its cavity (if any). Although sound radiation prediction tools derived from the FWH equation have been proven to be very efficient, the analysis of wave scattering is not a standard field of application of the FWH equation and its potentiality is investigated in the following.

4.2   Theoretical Modeling for Sound Scattering Analysis

The FWH equation is applied for the development of a methodology aimed at the analysis of sound scattered by elastic moving surfaces; such approach is based on the boundary integral formulation solver described in appendix A.3.

4.2.1   Background

In this section, for the sake of completeness, the FWHE and some main aspects concerning its integral solution are re–called; it may be useful in deriving the governing equations at the basis of the scattering formulation.

Let us assume that the fluid is compressible and undergoes transformations with negligible entropy changes. If N bodies move in the fluid, each having velocity $\mathbf{v}_j$ and surface S_j defined by those points that satisfy $f_j(\mathbf{x}, t) = 0$, and if the boundary surfaces are assumed to be permeable (porous), the following form of the FWH equation can be written (see also Eq. (2.1))

$$
\begin{aligned}
\Box^2 p' &= \sum_j^N \frac{\overline{\partial}}{\partial t} \left[\rho_0\, \mathbf{v}_j \cdot \nabla f_j\, \delta\left(f_j\right) \right] + \frac{\overline{\partial}}{\partial t} \left[\rho\left(\mathbf{u} - \mathbf{v}_j\right) \cdot \nabla f_j\, \delta\left(f_j\right) \right] \\
&\quad - \sum_j^N \overline{\nabla} \cdot \left[\mathbf{P}\, \nabla f_j\, \delta\left(f_j\right) \right] - \sum_j^N \overline{\nabla} \cdot \left[\rho\, \mathbf{u}\left(\mathbf{u} - \mathbf{v}_j\right) \cdot \nabla f_j\, \delta\left(f_j\right) \right] \\
&\quad + \overline{\nabla} \cdot \left\{ \overline{\nabla} \cdot \left[\mathbf{T} \prod_j^N H(f_j) \right] \right\} \quad \forall \mathbf{x} \in \Re^3
\end{aligned}
\tag{4.1}
$$

where $p' = c_0{}^2 \hat{\rho}$ is the acoustic disturbance, with $\hat{\rho} = (\rho - \rho_0)$ representing the density perturbation and c and ρ_0 denote, respectively, the speed of sound and the density of the undisturbed medium. The bars denote generalized differential operators and $\Box^2 = (1/c_0^2)(\overline{\partial}^2/\partial t^2) - \overline{\nabla}^2$ is

the generalized wave operator (D'Alembertian operator) whereas $H(f)$ and $\delta(f)$ are Heaviside and Dirac delta functions. In addition, $\mathbf{v}$ is the local velocity of the surface f, $\mathbf{u}$ the local fluid velocity, $\mathbf{P}$ the compressive stress tensor defined by $\mathbf{P} = [(p - p_0)\mathbf{I} + \mathbf{V}]$, with $\mathbf{V}$ representing the viscous stress tensor, and $\mathbf{T} = [\rho(\mathbf{u} \otimes \mathbf{u}) + (p - p_0)\mathbf{I} - c_0^2(\rho - \rho_0)\mathbf{I} + \mathbf{V}]$ the Lighthill tensor. Assuming the nonlinear perturbation field terms to be negligible and the body surfaces to be undeformable, for f_j such that $|\nabla f_j| = 1$, the boundary integral representation of the acoustic field governed by Eq. (4.1) is given by (see Eq. (2.5))

$$
\begin{aligned}
p'(\mathbf{x}, t) = & -\sum_j^N \int_{S_j} \rho_0 \Big[\mathbf{v}\!\cdot\!\mathbf{n}\, \mathbf{v}\!\cdot\!\nabla\hat{G} + [\mathbf{v}\!\cdot\!\mathbf{n}\,(1 - \mathbf{v}\!\cdot\!\nabla\vartheta)]^{\displaystyle\cdot}\, \hat{G} \Big]_\vartheta \, \mathrm{d}S(\mathbf{y}) \\
& - \sum_j^N \int_{S_j} \Big[(\mathbf{P}\,\mathbf{n})\cdot\nabla\hat{G} - (\dot{\mathbf{P}}\,\mathbf{n})\cdot\nabla\vartheta\,\hat{G} \Big]_\vartheta \, \mathrm{d}S(\mathbf{y}) \qquad\qquad (4.2) \\
& - \sum_j^N \int_{S_j} \Big[\rho\,\mathbf{u}^-\!\cdot\!\mathbf{n}\, \mathbf{u}^+\!\cdot\!\nabla\hat{G} + [\rho\,\mathbf{u}^-\!\cdot\!\mathbf{n}\,(1 - \mathbf{u}^+\!\cdot\!\nabla\vartheta)]^{\displaystyle\cdot}\, \hat{G} \Big]_\vartheta \, \mathrm{d}S(\mathbf{y})
\end{aligned}
$$

where each moving surface is defined in a Lagrangean frame fixed to the surface (i.e., the integrations are performed over time-independent surfaces).

In the equation above, $\mathbf{u}^- = (\mathbf{u} - \mathbf{v})$, $\mathbf{u}^+ = (\mathbf{u} + \mathbf{v})$, $\mathbf{n}$ denotes the outward unit normal on S_j, whereas

$$
\hat{G}(\mathbf{x}, \mathbf{y}, t) = \frac{-1}{4\,\pi} \left[\frac{1}{r\,(1 - M_r)} \right]_\vartheta
$$

where, for $\mathbf{x}(t)$ representing the observer position at the observer time, t, and $\mathbf{y}(\tau)$ representing the source position at the emission time, τ, $r = |\mathbf{r}|$ with $\mathbf{r} = \mathbf{x}(t) - \mathbf{y}(\tau)$, while $(1 - M_r)$ is the Doppler factor, with $M_r = \mathbf{v} \cdot (\mathbf{r}/r)/c$ denoting the surface velocity Mach number in the direction of radiation. In addition, the symbol $(\dot{\ })$ denotes the time derivative, whereas the symbol $[\,]_\vartheta$ indicates that the quantities must be evaluated at the retarded emission time, $\tau = t - \vartheta$, where ϑ is the time taken by an acoustic disturbance released from $\mathbf{y}$ to reach the observer location, $\mathbf{x}$, at current time, t. The time delay, ϑ, is evaluated as root of the equation $|\mathbf{x}(t) - \mathbf{y}(t - \vartheta)|/c - \vartheta = 0$. Note that the integrands appearing in Eq. (4.2) have to be interpreted carefully. In particular, attention has to be paid on the identification of the variables $\hat{G}$ and θ depend on when carrying out their analytical gradients for computational purposes.

4.2.2 Acoustic Disturbance in the Presence of Impinging Pressure Waves

The analysis of the noise radiated by bodies that are impinged by pressure waves concerns acoustic configurations where a noise source distribution radiates a pressure disturbance (incident) field that, interacting with moving or stationary bodies, is subject to modifications in directivity and intensity (scattering effects). An essential feature of this kind of problems is that the noise source is assumed to be independent from the presence of the scatterers. In order to analyze the problem through the FWH formulation, let us assume that two surfaces are present in the domain of interest: one, S_B, is the boundary of an arbitrarily moving scattering body, whereas the second, S_I, is a closed surface that surrounds the sources of an incident acoustic disturbance. The limitation of the analysis to one single body is for the sake of simplicity, and does not affect the generality of the formulation that will be developed. The surface S_I is a virtual, arbitrarily shaped surface, that is perfectly permeable and does not alter the flow field. The only constraint in its choice is that it must be close enough to the source of the pressure disturbances (moving with them, if necessary) in such a way that the flow field over it is unaffected by the presence of the scattering body.

Under these assumptions, noting that acoustic disturbance and pressure perturbation coincide under the hypothesis of small perturbation fields, the incident pressure distribution, p'_I, may be expressed by the following integral representation for $\mathbf{x}$ outside S_I (Eq. (4.2) written for "frozen"

noise sources)

$$
\begin{aligned}
p'_I(\mathbf{x},t) = & -\int_{S_I} \rho_0 \Big[\mathbf{v}\cdot\mathbf{n}\,\mathbf{v}\cdot\nabla\hat{G} + [\mathbf{v}\cdot\mathbf{n}\,(1 - \mathbf{v}\cdot\nabla\vartheta)]^{\cdot}\,\hat{G}\Big]_\vartheta \mathrm{d}S(\mathbf{y}) \\
& -\int_{S_I} \Big[p'_I\mathbf{n}\cdot\nabla\hat{G} - \dot{p}'_I\,\mathbf{n}\cdot\nabla\vartheta\,\hat{G}\Big]_\vartheta \mathrm{d}S(\mathbf{y}) \\
& -\int_{S_I} \Big[\rho\,\mathbf{u}_I^-\cdot\mathbf{n}\,\mathbf{u}_I^+\cdot\nabla\hat{G} + [\rho\,\mathbf{u}_I^-\cdot\mathbf{n}\,(1 - \mathbf{u}_I^+\cdot\nabla\vartheta)]^{\cdot}\,\hat{G}\Big]_\vartheta \mathrm{d}S(\mathbf{y})
\end{aligned}
\tag{4.3}
$$

where $\mathbf{u}_I^-$ and $\mathbf{u}_I^+$ are porosity effects due to the velocity field related to the incident pressure. The total acoustic disturbance field may be decomposed into an incident component and a component, p'_B due to the body presence

$$
p' = p'_B + p'_I
\tag{4.4}
$$

From the above pressure field decomposition, considering Eq. (4.3) for the incident pressure field, and by applying Eq. (4.2) for $\mathbf{x}\in S_B$, a boundary integral equation for the acoustic disturbance generated by the body impinged by the incident pressure wave may be derived. Taking into account the singularities of the kernel functions $\hat{G}$ and $\nabla\hat{G}$ arising when $\mathbf{x}$, approach the surface, S_B, the boundary integral equation for p'_B reads (see Ref. [59] for details and Ref. [60] for an alternative derivation of the regularized integrals)

$$
\begin{aligned}
[1 - \lambda(\mathbf{x},t)]\,p'_B\,(\mathbf{x},t) = & \,\lambda(\mathbf{x},t)\,[\rho_0 v_n^2(\mathbf{x},t) + p'_I(\mathbf{x},t) + \rho\,u_n^-(\mathbf{x},t)\,u_n^+(\mathbf{x},t)] \\
& -\int_{S_B} \rho_0\Big[\mathbf{v}\cdot\mathbf{n}\,\mathbf{v}\cdot\nabla\hat{G} + [\mathbf{v}\cdot\mathbf{n}\,(1 - \mathbf{v}\cdot\nabla\vartheta)]^{\cdot}\,\hat{G}\Big]_\vartheta \mathrm{d}S(\mathbf{y}) \\
& -\int_{S_B} \Big[p'_B\,\mathbf{n}\cdot\nabla\hat{G} - \dot{p}'_B\,\mathbf{n}\cdot\nabla\vartheta\,\hat{G}\Big]_\vartheta \mathrm{d}S(\mathbf{y}) \\
& -\int_{S_B} \Big[p'_I\,\mathbf{n}\cdot\nabla\hat{G} - \dot{p}'_I\,\mathbf{n}\cdot\nabla\vartheta\,\hat{G}\Big]_\vartheta \mathrm{d}S(\mathbf{y}) \\
& -\int_{S_B} \Big[\rho\,\mathbf{u}^-\cdot\mathbf{n}\,\mathbf{u}^+\cdot\nabla\hat{G} + [\rho\,\mathbf{u}^-\cdot\mathbf{n}\,(1 - \mathbf{u}^+\cdot\nabla\vartheta)]^{\cdot}\,\hat{G}\Big]_\vartheta \mathrm{d}S(\mathbf{y})
\end{aligned}
\tag{4.5}
$$

where $\lambda = 0.5/(1 - M_n^2)$, with $M_n = v_n/c_0$, $v_n = \mathbf{v}\cdot\mathbf{n}$, $u_n^- = \mathbf{u}^-\cdot\mathbf{n}$, $u_n^+ = \mathbf{u}^+\cdot\mathbf{n}$ and the kernel singularity have to be assumed removed from the integral terms [59]. The boundary integral equation given by Eq. (4.5) allows the computation of p'_B on S_B from the knowledge of incident pressure field, motion of the body and porosity effects. Once p'_B is evaluated over the body surface, the following boundary integral representation (obtained combining Eq. (4.2) with Eq. (4.3) for $\mathbf{x}$ outside S_B), may be applied to determine the noise radiated by the body

$$
\begin{aligned}
p'_B(\mathbf{x},t) = & -\int_{S_B} \rho_0\Big[\mathbf{v}\cdot\mathbf{n}\,\mathbf{v}\cdot\nabla\hat{G} + [\mathbf{v}\cdot\mathbf{n}\,(1 - \mathbf{v}\cdot\nabla\vartheta)]^{\cdot}\hat{G}\Big]_\vartheta \mathrm{d}S(\mathbf{y}) \\
& -\int_{S_B} \Big[p'_B\,\mathbf{n}\cdot\nabla\hat{G} - \dot{p}'_B\,\mathbf{n}\cdot\nabla\vartheta\,\hat{G}\Big]_\vartheta \mathrm{d}S(\mathbf{y}) \\
& -\int_{S_B} \Big[p'_I\,\mathbf{n}\cdot\nabla\hat{G} - \dot{p}'_I\,\mathbf{n}\cdot\nabla\vartheta\,\hat{G}\Big]_\vartheta \mathrm{d}S(\mathbf{y}) \\
& -\int_{S_B} \Big[\rho\,\mathbf{u}^-\cdot\mathbf{n}\,\mathbf{u}^+\cdot\nabla\hat{G} + [\rho\,\mathbf{u}^-\cdot\mathbf{n}\,(1 - \mathbf{u}^+\cdot\nabla\vartheta)]^{\cdot}\,\hat{G}\Big]_\vartheta \mathrm{d}S(\mathbf{y})
\end{aligned}
\tag{4.6}
$$

The sum of Eqs. (4.6) and (4.3) yields the total acoustic field. In standard acoustics applications, Eq. (4.6) is used to obtain the sound radiated by the body once a prior aerodynamic analysis has

solved the flow field around the body and has made the total pressure, p', available over its surface. On the other hand, the acoustic formulation represented by Eqs. (4.5) and (4.6) yields the sound radiated by the body with the only requirement of knowing the incident pressure field and the nature of porosity contributions (usually of small-perturbation type and related to body surface characteristics). In the presence of multiple bodies, this formulation extended to the whole set of bodies is able to capture also the interactional effects. An acoustics approach of this type could be of interest, for instance, in the prediction of the noise produced by those multibody configurations where, within the limits of the required accuracy, it is possible to identify one single body as the main noise source, with the pressure on it approximately independent on the presence of the other bodies. Indeed, in this case, the only fluid-dynamic input required would be that related to the pressure solution on the isolated noise source body to be used in Eq. (4.3) for the determination of the incident pressure field.

Observing Eqs. (4.5) and (4.6), it is evident that the pressure field over an arbitrarily moving body, along with the noise it radiates, is the result of the action of three forcing terms: one is related to the rigid-body motion, one is related to the impinging pressure wave and one is related to the surface porosity. The formulation presented above is not intended for the prediction of pressure perturbation generated by rigid-body motion (neither for lifting nor for non-lifting configurations). Indeed, it is usually related to the arise of regions where velocity perturbation are not small, and thus an accurate evaluation of the corresponding surface pressure would require the inclusion of the contribution from the Lighthill tensor in Eq. (4.1) (see, for instance, Refs. [61] and [62] for the inclusion of the quadrupole terms). This problem does not occur in the standard aeroacoustics since the pressure over the surface is obtained from an aerodynamic solver and the inaccuracy mentioned above vanishes when the acoustic disturbance is evaluated at points that are far from the emitting surface (see the quadrupole expression in Refs. [61] and [62]). In addition, note that in many applications of interest for scattering problems, the rigid-body motion is a uniform translation that yields a constant pressure field over the body surface that, in turn, does not produce any noise disturbance at points located in a frame of reference fixed with it.

4.2.3 Wall Vibration Effects: Sound Radiated by Scattering Elastic Surfaces

The formulation derived in section 4.2.2 is aimed at the prediction of the acoustic disturbances generated by elastic shells when impinged by pressure waves, i.e., due to pressure perturbations from scattering and surface vibration effects. Surface vibration effects may be simulated as surface porosity contributions. Indeed, surface vibrations produce a difference between the normal component of the rigid-body velocity and that of the fluid flow, and it corresponds exactly to the "elastic transpiration velocity" term $\chi = \mathbf{u}^- \cdot \mathbf{n} \equiv (\mathbf{u} - \mathbf{v}) \cdot \mathbf{n}$ which represents surface porosity effects in Eqs. (4.1), (4.5) and (4.6). Note that this is the only way to include theoretically the influence of wall vibrations in an integral formulation that has been derived under the assumption of undeformable surfaces, without arbitrarily introducing approximated effects related to (not compatible) surface deformations.

Then, let us decompose the pressure field perturbation into a component due to the rigid-body motion, p'_R, and a scattering component, p'_S, due to incident pressure and surface vibrations, such that

$$p'_B = p'_R + p'_S \tag{4.7}$$

Under the assumption of small perturbations, the fluid velocity $\mathbf{u}$ may be decomposed into a component over the unperturbed body due to the rigid-body translation and into a perturbation $\mathbf{u}'$ due to wall vibrations

$$\mathbf{u} = \mathbf{u}_0 + \mathbf{u}' \tag{4.8}$$

81

where in the unperturbed, nonvibrating, impermeable body configuration, $\mathbf{u}_0 \cdot \mathbf{n} = \mathbf{v} \cdot \mathbf{n}$. By introducing the normal and tangential component of the perturbation term, the porosity contribution $\rho\,\mathbf{u}^- \cdot \mathbf{n}\,\mathbf{u}^+$ may be re-written as

$$\rho\,\mathbf{u}^- \cdot \mathbf{n}\,\mathbf{u}^+ = \rho\,\chi\,(\mathbf{u}_0 + u_n'\mathbf{n} + u_t'\mathbf{t} + \mathbf{v}) \tag{4.9}$$

where $\mathbf{t}$ indicates the local unit vector tangential to S_{B} and $u_n'\mathbf{n}$ coincides with $\chi\mathbf{n}$. In addition expressing air density as $\rho = \rho_0 + \hat{\rho}$, where $\hat{\rho}$ indicates the (small) density perturbation with respect the density of the undisturbed medium, and assuming that the elastic transpiration velocity term is a small-perturbation term, discarding the second order perturbation terms yields the following first–order surface porosity contribution

$$\rho\,\mathbf{u}^- \cdot \mathbf{n}\,\mathbf{u}^+ \cong \rho_0\,\chi\,(\mathbf{u}_0 + \mathbf{v}) \tag{4.10}$$

Following the same procedure, the linearization of the other porosity terms gives

$$\rho\,\mathbf{u}^- \cdot \mathbf{n}\,(1 - \mathbf{u}^+ \cdot \nabla\vartheta) \cong \rho_0\,\chi\,[1 - (\mathbf{u}_0 + \mathbf{v}) \cdot \nabla\vartheta] \tag{4.11}$$

and

$$\rho\,u_n^-\,u_n^+ \cong 2\,\rho_0\,v_n\,\chi \tag{4.12}$$

Therefore, recalling the linearity of the integral operator, the boundary integral equation in Eq. (4.5) yields the following linearised boundary integral equation for the sound scattered by a moving, vibrating surface

$$
\begin{aligned}
[1 - \lambda(\mathbf{x}, t)]\,p'_{S}(\mathbf{x}, t) = {} & \lambda(\mathbf{x}, t)\,[p'_{I}(\mathbf{x}, t) + 2\rho_0\,v_n\,\chi(\mathbf{x}, t)] \\
& - \int_{S_B} \left[p'_S\,\mathbf{n} \cdot \nabla\hat{G} - \dot{p}'_S\,\mathbf{n} \cdot \nabla\vartheta\,\hat{G} \right]_\vartheta \mathrm{d}S(\mathbf{y}) \\
& - \int_{S_B} \left[p'_I\,\mathbf{n} \cdot \nabla\hat{G} - \dot{p}'_I\,\mathbf{n} \cdot \nabla\vartheta\,\hat{G} \right]_\vartheta \mathrm{d}S(\mathbf{y}) \\
& - \int_{S_B} \rho_0 \left[\chi(\mathbf{u}_0 + \mathbf{v}) \cdot \nabla\hat{G} + \left[\chi(1 - (\mathbf{u}_0 + \mathbf{v}) \cdot \nabla\vartheta) \right]^{\cdot}\hat{G} \right]_\vartheta \mathrm{d}S(\mathbf{y})
\end{aligned} \tag{4.13}
$$

This boundary integral equation yields the scattered pressure from the knowledge of the incident pressure over the surface and of the surface elastic vibrations. Note that, although the rigid-body motion pressure term, p'_{R}, is not present in this formulation (as motivated above), the effects of rigid-body small oscillations (if any) can always be taken into account through the transpiration velocity term.

The inclusion of the vibrational effects allows the application of the acoustic formulation presented in acoustoelastic problems where wall vibrations transmit exterior pressure disturbances within the cavity bounded by the deforming wall (typical aircraft cabin noise production mechanism). The acoustic formulation presented is a simplification with respect to the widely-used scattering formulations based on the Kirchhoff integral operator that require the knowledge of the normal derivative of the incident pressure over the scattering surface. Indeed, whenever the incident pressure field is the result of complex acoustic radiation processes (like, for instance, those occurring in aeronautical problems involving helicopter rotors and propellers), the numerical evaluation of the pressure gradient may become computationally expensive in terms of run time and memory use and introduce further approximation in the algorithm of solution. Recently, some authors have developed a boundary integral formulation for the evaluation of the pressure gradient to be used in such kind of problems, starting from Farassat's Formulation 1A [63].

Scattering, vibroacoustic problems are usually analysed in the frequency domain, where the acoustic field is evaluated for each harmonic of the incident wave pressure and of the vibrating motion. Because of the linearity of Eq. (4.13), if the body velocity has constant components in a body-fixed frame of reference so that all terms are time independent (of course, with the exception of p'_I, p'_S and χ), then it is possible to transform it in the frequency domain. For $p'(\mathbf{x}, t) = \tilde{p}'(\mathbf{x}, \omega)\, e^{i\,\omega\,t}$ and $\chi(\mathbf{x}, t) = \tilde{\chi}(\mathbf{x}, \omega)\, e^{i\,\omega\,t}$ this yields

$$
[1 - \lambda(\mathbf{x})]\, \tilde{p}'_S\,(\mathbf{x}, k) = \lambda(\mathbf{x}) \left[\tilde{p}'_I(\mathbf{x}, k) + 2\,\rho_0\, c\, M_n\, \tilde{\chi}(\mathbf{x}, k)\right]
$$
$$
- \int_{S_B} \left[\mathbf{n} \cdot \nabla \hat{G} - i\,k\,\mathbf{n} \cdot \nabla \sigma\, \hat{G}\right] \tilde{p}'_S(\mathbf{y}, k)\, e^{-i\,k\,\sigma}\mathrm{d}S(\mathbf{y})
$$
$$
- \int_{S_B} \left[\mathbf{n} \cdot \nabla \hat{G} - i\,k\,\mathbf{n} \cdot \nabla \sigma\, \hat{G}\right] \tilde{p}'_I(\mathbf{y}, k)\, e^{-i\,k\,\sigma}\mathrm{d}S(\mathbf{y}) \qquad (4.14)
$$
$$
- \int_{S_B} \rho_0\, c \left[\hat{\mathbf{M}} \cdot \nabla \hat{G} + i\,k\,(1 - \hat{\mathbf{M}} \cdot \nabla \sigma)\, \hat{G}\right] \tilde{\chi}(\mathbf{y}, k)\, e^{-i\,k\,\sigma}\mathrm{d}S(\mathbf{y})
$$

where $k = \omega/c$ is the wave number, $\sigma = c\,\vartheta$, $M_n = v_n/c$, and $\hat{\mathbf{M}} = (\mathbf{u}_0 + \mathbf{v})/c$.

Once the pressure over the scattering, vibrating surface has been evaluated by Eq. (4.14), the following boundary integral representation gives the corresponding acoustic disturbance it radiates in the field

$$
\tilde{p}'_S(\mathbf{x}, k) = \; - \int_{S_B} \left[\mathbf{n} \cdot \nabla \hat{G} - i\,k\,\mathbf{n} \cdot \nabla \sigma\, \hat{G}\right] \tilde{p}'_S(\mathbf{y}, k)\, e^{-i\,k\,\sigma}\mathrm{d}S(\mathbf{y})
$$
$$
- \int_{S_B} \left[\mathbf{n} \cdot \nabla \hat{G} - i\,k\,\mathbf{n} \cdot \nabla \sigma\, \hat{G}\right] \tilde{p}'_I(\mathbf{y}, k)\, e^{-i\,k\,\sigma}\mathrm{d}S(\mathbf{y}) \qquad (4.15)
$$
$$
- \int_{S_B} \rho_0\, c \left[\hat{\mathbf{M}} \cdot \nabla \hat{G} + i\,k\,(1 - \hat{\mathbf{M}} \cdot \nabla \sigma)\, \hat{G}\right] \tilde{\chi}(\mathbf{y}, k)\, e^{-i\,k\,\sigma}\mathrm{d}S(\mathbf{y})
$$

Hence, the procedure proposed in this work to determine the frequency-domain acoustic field generated by a scattering, vibrating surface consists of the following three steps: first, the incident pressure is evaluated over the surface, then the integral equation Eq. (4.14) is applied to determine the pressure perturbation over the surface, and finally the integral representation Eq. (4.15) is used to evaluate the acoustic disturbance in the field.

A different way to account for the vibration of the scatterer(s) surface(s), without invoking porosity terms in the FWHE, is that to include the velocity vibration into the thickness noise term of the impermeable FWHE. In fact, under the small-perturbation assumption, the term $\mathbf{v} \cdot \mathbf{n}$ in Eq. (4.2) written for $N = 1$ without porosity terms may be expressed as the sum of the normal velocity of mean surface (due to the rigid translation) and the normal velocity of surface point vibration (see Ref. [64] for details). This approach leads to a boundary integral equation for the scattered pressure p'_S where the thickness noise term accounts for the elastic vibration. Strictly speaking, the introduction of the elastic vibration effect into the rigid body translation velocity may be not justifiable form a physical point of view but it is convenient from a numerical standpoint avoiding a prior aerodynamic analysis to determine the steady solution $\mathbf{u}_0$ over the undeformable body.

4.3   A Remark on the Scattering Formulation Presented

Let us consider a stationary virtual closed surface S within a fluid region where an arbitrary unsteady pressure field, p', is present without being perturbed by any physical surface (the stationarity of the surface is invoked for the sake of simplicity, but does not alter the generality of the results).

For a point $\mathbf{x}$ in the field and neglecting second order terms, Eq. (4.6) yields

$$0 = \int_S \left[\rho\, \dot{\mathbf{u}} \cdot \mathbf{n}\, \hat{G} \right]_\vartheta \mathrm{d}S(\mathbf{y}) + \int_S \left[p'\, \mathbf{n} \cdot \nabla \hat{G} - \dot{p}'\, \mathbf{n} \cdot \nabla\vartheta\, \hat{G} \right]_\vartheta \mathrm{d}S(\mathbf{y}) \qquad (4.16)$$

where $\mathbf{u}$ is the fluid velocity related to p' through the momentum equation. Equation (4.16) is the compatibility condition on a closed surface between the pressure field and the corresponding velocity field, in an unbounded fluid medium. Then, if $p' \equiv p'_I$, $\mathbf{u} \equiv \mathbf{u}_I$ and the shape of S coincides with that of S_B, the combination of Eq. (4.16) with Eq. (4.6) written for an impermeable surface yields the following alternative boundary integral representation for the pressure scattered by a stationary surface

$$4\pi\, p'_S(\mathbf{x}, t) = - \int_{S_B} \left[\frac{\rho\, \dot{\mathbf{u}}_I \cdot \mathbf{n}}{r} \right]_\vartheta \mathrm{d}S(\mathbf{y}) + \int_{S_B} \left[p'_S\, \frac{\mathbf{n} \cdot \mathbf{r}}{r^3} + \dot{p}'_S\, \frac{\mathbf{n} \cdot \mathbf{r}}{c\, r^2} \right]_\vartheta \mathrm{d}S(\mathbf{y}) \qquad (4.17)$$

(note that, for the stationary surface, $\hat{G} = -1/4\pi\, r$). Observing that the linearized momentum equation gives $\rho\, \dot{\mathbf{u}}_I \cdot \mathbf{n} = -\partial p'_I / \partial n$, and using this expression in the equation above, one obtains that Eq. (4.17) is similar to with the formulations based on the Kirchhoff approach where the incident pressure forces the scattered one through a term depending on its normal derivative on the scattering surface. This demonstrates the equivalence between the formulation presented here and the Kirchhoff ones, the difference lying on the way in which the incident field is related to the scattered field (in the present approach the scattered pressure is forced by the distribution of the incident pressure and its time derivative on the same surface. Incidentally, note that Eq. (4.17) coincides with Eq. (3) in Ref. [65] where $\cos\alpha = \mathbf{n} \cdot \mathbf{r}/r$). Finally, Eq. (4.16) shows also that the term forcing the scattered pressure in the formulation examined here is closely related to the forcing term in the scattering formulations based on the velocity potential, which is given by the velocity flow of the incident perturbation field.

4.4   Numerical Results

In order to validate the acoustic formulation presented, first, results concerning the pressure field generated by a plane wave impinging on a stationary rigid sphere are presented and compared with available analytical solutions. The problem of the appearance of spurious frequencies is examined, along with acoustically small sphere configurations. Then, the surface deformation effects on sound scattered are analysed by assuming that the sphere is a thin elastic shell subject to vibrations because of the impinging plane pressure wave. Also in this case, the numerical predictions are validated by comparison with analytical solutions. Next, the acoustic analysis of scattering and vibrating surfaces is performed also for bodies in uniform rectilinear motion, and the results are compared with those given by a formulation based on the velocity potential. Finally, the scattering formulation is applied in the analysis of fuselage effects in the sound emitted by a helicopter in descent flight. First, the numerical algorithm applied to obtain the discrete form of the integral formulation is presented.

Discretization Procedure

The numerical investigation is performed by applying a zero-th order boundary element method for the discretization of the boundary integral formulation. It consists of dividing the scattering and vibrating surface, S_B, into quadrilateral panels and assuming $\tilde{p}'_S$, $\tilde{p}'_I$ and $\tilde{\chi}$ to be piecewise constant. Then, the integral equation is solved by requiring that the equation be satisfied at the center of each body element (collocation method, see also Ref. [22]). Specifically, discretizing S_B

into M panels S_m^B, at the center of j-th element Eq. (4.14) yields, for a given value of k,

$$
\begin{aligned}
(1 - \lambda_j)\,\tilde{p}'_{S_j}(k) \;=\;& \sum_{m=1}^{M}(B_{jm} + i\,k\,C_{jm})\,\tilde{p}_m^S(k) \\
&+ \sum_{m=1}^{M}(\lambda_j\,\delta_{jm} + B_{jm} + i\,k\,C_{jm})\,\tilde{p}_m^I(k) \\
&+ \sum_{m=1}^{M}(2\,M_j^n\,\lambda_j\,\delta_{jm} + D_{jm} + i\,k\,F_{jm})\,\tilde{\chi}_m(k) \qquad (4.18)
\end{aligned}
$$

where, for $\mathbf{x}_m$ denoting the center of the m-th panel, $\tilde{p}_m^S(k) = \tilde{p}'_S(\mathbf{x}_m, k)$, $\tilde{p}_m^I(k) = \tilde{p}'_I(\mathbf{x}_m, k)$, $\tilde{\chi}_m(k) = \tilde{\chi}(\mathbf{x}_m, k)/\rho_0\,c$, $M_j^n = M_n(\mathbf{x}_j)$ and $\lambda_j = \lambda(\mathbf{x}_j)$. In addition, δ_{jm} is the Kronecker delta function, while the coefficients are defined in the following way

$$
\begin{aligned}
B_{jm}(k) &= -e^{-i\,k\,\sigma_{jm}}\int_{S_m^B}\mathbf{n}\cdot\nabla\hat{G}\,\mathrm{d}S \\
C_{jm}(k) &= e^{-i\,k\,\sigma_{jm}}\int_{S_m^B}\mathbf{n}\cdot\nabla\sigma\,\hat{G}\,\mathrm{d}S \\
D_{jm}(k) &= -e^{-i\,k\,\sigma_{jm}}\int_{S_m^B}\hat{\mathbf{M}}\cdot\nabla\hat{G}\,\mathrm{d}S \\
F_{jm}(k) &= -e^{-i\,k\,\sigma_{jm}}\int_{S_m^B}(1 - \hat{\mathbf{M}}\cdot\nabla\sigma)\,\hat{G}\,\mathrm{d}S
\end{aligned}
$$

with σ_{jm} denoting the time delay of the propagation of signals between the source point at $\mathbf{x}_m$ and the observer point at $\mathbf{x}_j$. Collecting scattered pressure, incident pressures and elastic transpiration velocities at the M panels respectively in the vectors p_S, p_I and x, and collecting the coefficients in the matrices $\mathsf{B}, \mathsf{C}, \mathsf{D}$ and F, the solution of Eq. (4.18) may be written in the following matrix form

$$
\tilde{\mathsf{p}}_S = \mathsf{E}_I(k)\,\tilde{\mathsf{p}}_I + \mathsf{E}_\chi(k)\,\tilde{\mathsf{x}} \qquad (4.19)
$$

where, for I denoting the unit matrix and Λ denoting the diagonal matrix collecting the λ_j's,

$$
\mathsf{E}_I(k) = [\mathsf{I} - \Lambda - \mathsf{B}(k) - i\,k\,\mathsf{C}(k)]^{-1}[\Lambda + \mathsf{B}(k) + i\,k\,\mathsf{C}(k)] \qquad (4.20)
$$

is the matrix of the transfer functions between incident and scattered pressures at panel centers while

$$
\mathsf{E}_\chi(k) = [\mathsf{I} - \Lambda - \mathsf{B}(k) - i\,k\,\mathsf{C}(k)]^{-1}[2\,\mathsf{M}\,\Lambda + \mathsf{D}(k) + i\,k\,\mathsf{F}(k)] \qquad (4.21)
$$

is the matrix of the transfer functions between elastic vibrations and pressure perturbations, with M denoting the vector of the normal Mach numbers M_m^n at the panel centers.

4.4.1   Plane Wave Scattered by a Stationary Rigid Sphere

The solution of the problem of a plane wave impinging on a stationary rigid sphere is obtained through the application of the boundary integral equation in Eq. (4.14), with $\mathbf{v} = 0$, $\tilde{\chi} = 0$, and $\tilde{p}'_I(x, k) = e^{-i\,k\,x}$ (the wave is assumed to propagate along the $x-$axis, see Fig. 4.1). As shown in section 4.3, the present boundary integral formulation for the scattered pressure becomes perfectly equivalent to that discussed in Ref. [65] for the same kind of problem. The formulation in Ref. [65] has been obtained starting from the FWH equation for the scattered pressure.

For a sphere of radius R, and an impinging wave with wave number such that $kR = 1$, Fig. 4.2 depicts the comparison between the analytical scattered pressure solution [66] and those
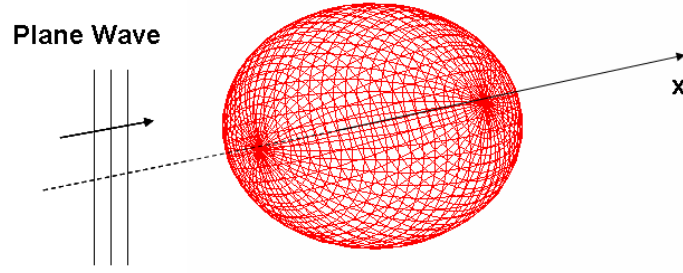
Figure 4.1: *Sketch of a plane wave impinging a stationary rigid sphere.*

obtained numerically using an increasing number of panels to discretize the sphere surface. The scattered signal is evaluated on a circle of radius $d/R = 5$ centered at the center of the sphere, N_m denotes the number of elements of discretization along its meridians and N_p denotes the number of elements of discretization along the parallel circles (the $x-$axis coincides with the polar axis). The result is given in terms of the angular dependence of the ratio $|\tilde{p}'_S|/|\tilde{p}'_I|$, for the impinging wave travelling from left to right, and sphere located at the origin of the coordinate system. The same will be done for all of the following figures, unless different definitions are specifically indicated. For $N_m = N_p = 32$ the numerical result may be assumed to be the converged one, and perfectly matches the analytical solution. However, the prediction appears to be quite accurate even for a coarse discretization (for instance, for $N_m = N_p = 16$ the numerical solution is fairly close to the analytical one).
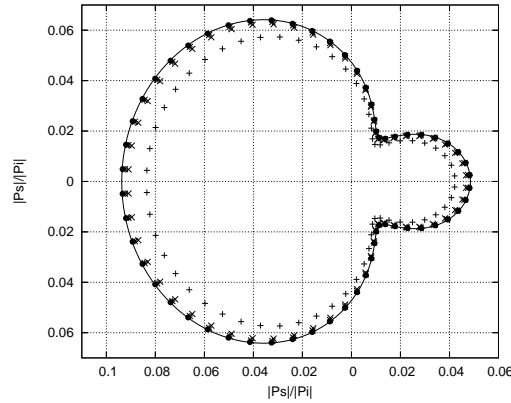
Figure 4.2: *Angular dependence of scattering for a plane wave impinging on a stationary sphere. Convergence analysis and comparison with the analytical solution for $kR = 1$ and $d/R = 5$. — analytical solution; $+$ $N_m = N_p = 8$; $\times$ $N_m = N_p = 16$; $*$ $N_m = N_p = 24$; $\bullet$ $N_m = N_p = 32$.*

Further comparisons between analytical solutions and converged numerical ones are given in Figs. 4.3 and 4.4, respectively for $kR = 2$ and $kR = 4$. In both cases the observers are placed at a distance $d/R = 5$, and the agreement between the two solutions is excellent. The numerical

results show a similar level of accuracy also in predicting the far field scattered pressure. This is demonstrated in Figs. 4.5, 4.6 and 4.7 where, respectively for $kR = 1, kR = 2$ and $kR = 4$, the directivity patterns of the intensity of scattered pressure predicted by the formulation presented here are compared with those obtained analytically [66].
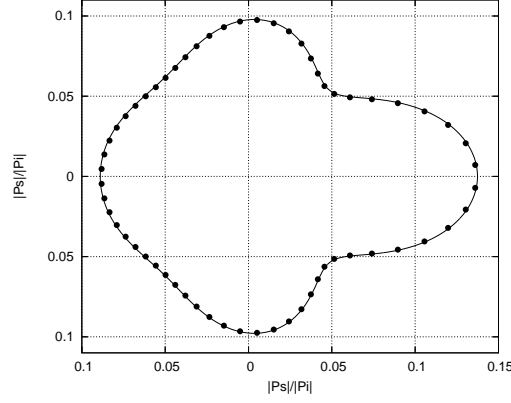
Figure 4.3: *Angular dependence of scattering for a plane wave impinging on a stationary sphere. $kR = 2$ and $d/R = 5$. — analytical solution; • numerical solution.*
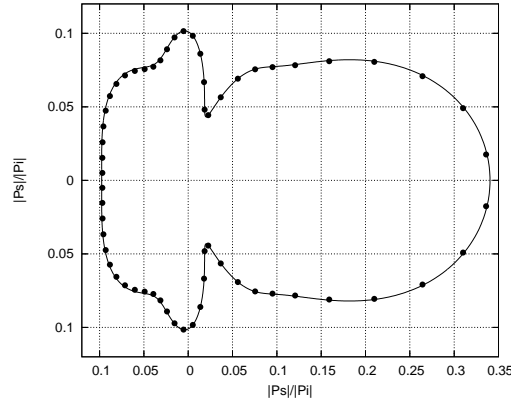
Figure 4.4: *Angular dependence of scattering for a plane wave impinging on a stationary sphere. $kR = 4$ and $d/R = 5$. — analytical solution; • numerical solution.*
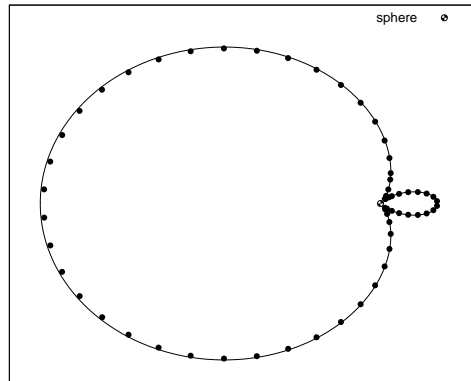
Figure 4.5: *Directivity patterns of scattered pressure intensity for a plane wave impinging on a stationary sphere. Far-field solution for $kR = 1$.   — analytical solution;   • numerical solution.*
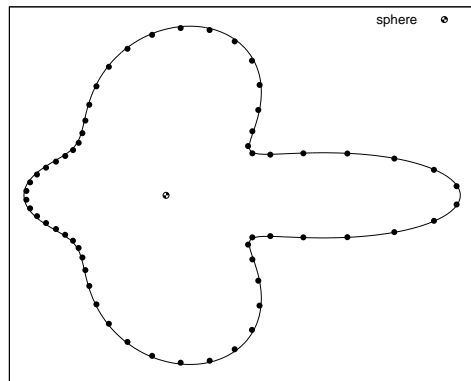
Figure 4.6: *Directivity patterns of scattered pressure intensity for a plane wave impinging on a stationary sphere. Far-field solution for $kR = 2$.   — analytical solution;   • numerical solution.*

Elimination of Spurious Frequencies

A drawback in using a boundary integral method in this type of analysis arises from the so-called "fictitious eigenvalues". These are non-physical resonances appearing in the numerical method that can completely destroy the integral operator [56],[67]. Spurious frequencies appear also in the formulation applied in this paper and correspond to the frequencies at which the matrix to be inverted in the numerical solution of the integral equation becomes singular [see Eqs. (4.20) and (4.21)]. In order to overcome this problem, here the CHIEF regularization technique introduced in Ref. [68] has been applied. This technique consists of augmenting the set of equations of the
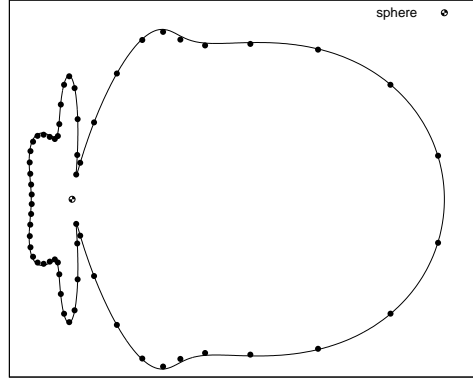
Figure 4.7: *Directivity patterns of scattered pressure intensity for a plane wave impinging on a stationary sphere. Far-field solution for $kR = 4$.   — analytical solution;   • numerical solution.*
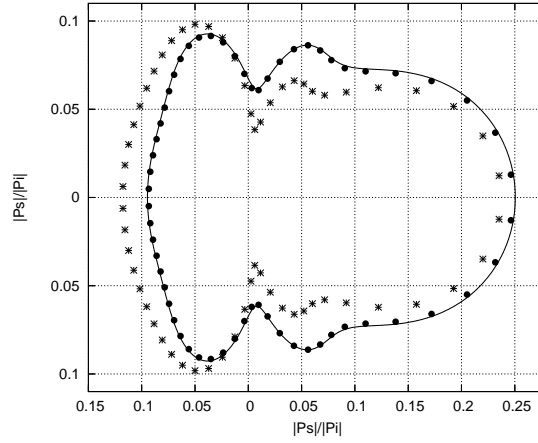
Figure 4.8: *Angular dependence of scattering for a plane wave impinging on a stationary sphere at the first spurious frequency. Non-regularized and regularized numerical predictions compared with the analytical solution for $kR = \pi$ and $d/R = 5$.   — analytical solution;   ∗ numerical solution without CHIEF regularization;   • numerical solution with CHIEF regularization.*

discrete form of the boundary-integral operator with homogeneous-condition equations at some points within the volume bounded by the scattering surface, followed by the application of a least-square technique for the computation of unknowns. For a spherical stationary scattering surface, the first fictitious eigenvalue appears at $kR = \pi$. For this wave number, at $d/R = 5$, Fig. 4.8 shows the comparison between the analytical solution, the non-regularized numerical one

and the numerical one obtained through application of the regularization technique. This result demonstrates that also for the formulation proposed here, the effects of the spurious frequencies can be efficiently eliminated by application of the CHIEF approach.

Acoustically Small Spheres

Next, we examine the sound scattered by an acoustically small sphere. This case is characterized by the condition $kR << 1$ or, in other words, by an impinging wave length much longer than the sphere radius. The analytical solution of the scattered field is given in Ref. [69] and has been used in Refs. [65] and [70] to discuss the applicability of the FWH equation in scattering problems. In Ref. [65] it is shown that the far-field solution given by a boundary integral formulation based on the FWH equation coincides with the analytical one. This is confirmed by Fig. 4.9 where, for $kR = 0.15$ and $d/R = 300$, the solution obtained through the approach presented here is in excellent agreement with the analytical one. Figure 4.10 depicts the comparison between the solution from the present approach and the analytical one for $kR = 0.015$ and $d/R = 1.4$. In contrast to what is claimed in Refs. [71] and [70], this near-field prediction, using the formulation based on the FWH equation, perfectly matches the analytical solution. However, it is apparent that the solution obtained in Ref. [70] from the Curle equation is incorrect. Indeed, it would predict a non-zero scattered field even at $k = 0$, while it is easy to show that in this case the Curle equation reduces to a distribution of stationary, uniform dipoles and that the signal emitted by such a distribution is equal to zero.
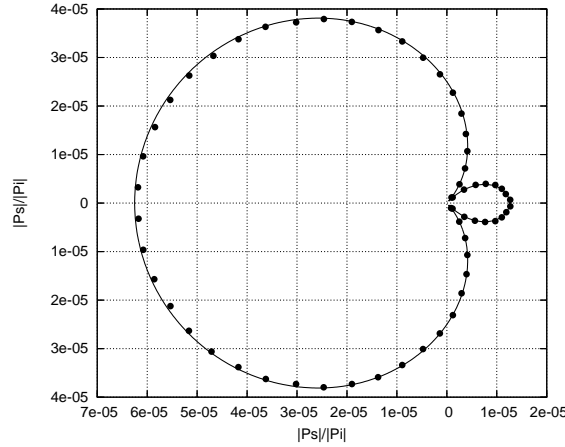
Figure 4.9: *Angular dependence of scattering for a plane wave impinging on a stationary acoustically small sphere. $kR = 0.15$ and $d/R = 300$. — analytical solution; • numerical solution.*
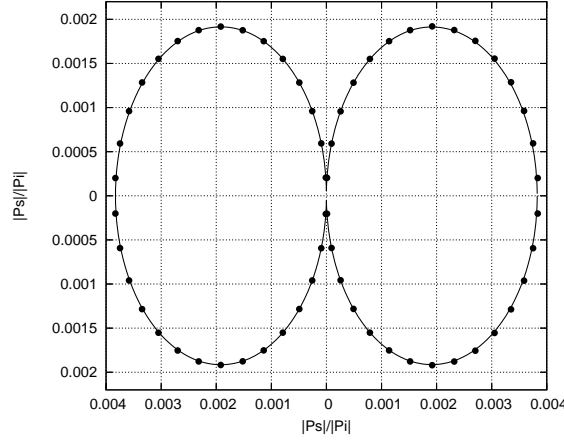
Figure 4.10: *Angular dependence of scattering for a plane wave impinging on a stationary acoustically small sphere.* $kR = 0.015$ *and* $d/R = 1.4.$ *— analytical solution;* • *numerical solution.*

4.4.2   Plane Wave Scattered by a Stationary Elastic Sphere

When a pressure wave impinges a thin elastic shell, the corresponding acoustic disturbance field is the result of an aeroelastic phenomenon where incident and scattered pressure produce wall vibrations that, in turn, modify the scattered pressure field. Here, this closed-loop aeroelastic mechanism is analysed for a plane wave impinging a spherical shell by coupling the sphere structural dynamics equations with the acoustics equations.

The discrete form of the equations of the shell structural dynamics are obtained by a modal approach based on the description of elastic deformations in terms of a linear combination of the modes of vibration given in Ref. [72]. For q denoting the vector of the corresponding Lagrangean variables, it yields the following form of the dynamics equations in the frequency domain

$$[-k^2 \mathsf{M}_s + \mathsf{K}_s]\,\tilde{\mathsf{q}} = \tilde{\mathsf{f}} \tag{4.22}$$

where M_s and K_s are, respectively, mass and stiffness matrices which depend on the geometrical (thickness, radius) and material (mass distribution, Young's modulus) properties of the shell, while f is the vector of the generalized loads that force the elastic degrees of freedom (projection of pressure onto the modes of vibration). From the knowledge of the modes used in the discretization of the structural dynamics equations, it is possible to relate the elastic deformation velocity to the shell Lagrangean variables through the expression $\tilde{\mathsf{x}} = \mathsf{E}_d(k)\,\tilde{\mathsf{q}}$, where the deformation matrix E_d depends on vibration frequency and shape of modes. Using this deformation matrix in Eq. (4.19), the acoustic formulation provides

$$\tilde{\mathsf{p}}_S = \mathsf{E}_I(k)\,\tilde{\mathsf{p}}_I + \mathsf{E}_q(k)\,\tilde{\mathsf{q}} \tag{4.23}$$

where $\mathsf{E}_q = \mathsf{E}_\chi\,\mathsf{E}_d$ is the matrix that takes into account the influence of wall vibrations on the scattered pressure over the surface. Then, defining the (projection) matrix, E_p, relating the shell surface pressure with the corresponding generalized forces [i.e., such that $\tilde{\mathsf{f}} = \mathsf{E}_p\,(\tilde{\mathsf{p}}_S + \tilde{\mathsf{p}}_I)$], the following acoustoelastic operator is obtained by coupling Eq. (4.23) with Eq. (4.22)

$$\tilde{\mathsf{q}} = [-k^2\,\mathsf{M}_s + \mathsf{K}_s - \mathsf{E}_p\mathsf{E}_q(k)]^{-1}[\mathsf{E}_p + \mathsf{E}_p\mathsf{E}_I(k)]\,\tilde{\mathsf{p}}_I \tag{4.24}$$

Equation (4.24) yields the shell elastic deformation from the knowledge of the impinging pressure, and takes into account both its direct action (through the matrix E_p) and also its indirect effects from the scattered pressure (through the matrix E_I). Once the Lagrangean variables of the elastic deformation are known from Eq. (4.24), the scattered pressure over the shell surface is obtained by Eq. (4.23) and then, the scattered pressure radiated in the field is obtained through the integral representation in Eq. (4.15). Note that the acoustoelastic procedure outlined above has a general validity, in that may be applied to elastic scatterers of arbitrary material and shape. Scatterers having different material and geometrical properties yield different mass and stiffness matrices in Eq. (4.22), while the shape of modes affects both matrix E_d and matrix E_p.

For an aluminium spherical shell having thickness $T = (3/1000)R$, Fig. 4.11 depicts the distribution of the amplitude of the radial elastic displacement, w, along a meridian circle induced by a unit impinging plane wave with wave number $kR = 11.16$, that coincides with the first natural frequency of vibration of the structure (note that the impinging wave travels along the sphere polar axis and, therefore, the solution is constant along parallel circles). Figure 4.11 presents three numerical results obtained using 30 modes for the description of the radial displacement: one is related to a surface discretization with $N_m = N_p = 40$, one is related to a surface discretization with $N_m = 40$ and $N_p = 72$, whereas the third one is the result provided by an extrapolation procedure based on numerical predictions with increasing number of elements of discretization. The numerical result obtained with the finer grid is in good agreement with the analytical solution [73], while the extrapolated result perfectly matches it. The angular dependence of the scattered acoustic disturbance that corresponds to the elastic deformation in Fig. 10 is shown in Fig. 4.12. It is evaluated at a distance $d/R = 5$, where the present numerical prediction using $N_m = 40$ and $N_p = 72$ is in very good agreement with the analytical solution [73]. This figure demonstrates also that the acoustic scattering of the elastic sphere significantly differs from that produced by the rigid body. Next, Fig. 4.13 depicts the pressure scattered at $d/R = 5$ by the elastic shell impinged by the plane wave with wave number $kR = 13.214$, that corresponds to the second natural frequency of vibration of the shell. Also in this case the numerical prediction obtained using $N_m = 40$ and $N_p = 72$ is in very good agreement with the analytical solution.

4.4.3 Scattering and Vibrating Moving Bodies

In the following, the effect of motion on the pressure perturbation field generated by scattering and vibrating surfaces is examined.

First, consider the rigid wing scattering problem analysed in Ref. [74]. It consists of a rectangular wing in uniform rectilinear translation at zero angle of attack, with the incident pressure field generated by a co-moving harmonic potential point source, located in its mid-span plane. The span of the wing is three times the chord length, c_w, while the cross sections have symmetric biconvex parabolic shape with thickness ratio $t_w/c_w = 0.1$. For $(\mathbf{x}_0, x, y, z)$ denoting a wing-fixed coordinate system (see Fig. 4.14 and 4.15), having chordwise x-axis, spanwise y-axis and origin, $\mathbf{x}_0$, at the center of the mid-span cross section, Figs. 4.16 and 4.17 depict directivity patterns of pressure scattered in the mid-span plane at radial distance $d/c_w = 52.5$ from $\mathbf{x}_0$ by the wing moving at $M = 0.5$ in the negative x-axis direction (from right to left in the picture). Specifically, for wave number $kc_w = 6$, Fig. 4.16 concerns the source point located above the leading edge at $\mathbf{x}_s^{LE} = (-5c_w, 0, 5c_w)$, while Fig. 4.17 concerns the source point located above the trailing edge at $\mathbf{x}_s^{TE} = (5c_w, 0, 5c_w)$. These figures compare the results given by the present formulation with those obtained through a linear velocity-potential approach based on the integral formulation described in Refs. [75] and [22], which is equivalent to that used in Ref. [74]. The results are presented in terms of the ratio between the scattered pressure and a reference pressure defined as $p_{ref} = 2\,d\,|\tilde{p}'_I(\mathbf{x}_0, k)|/c_w$ [74]. As expected, the results obtained from the potential approach are in perfect agreement with those presented in Ref. [74], but show significant discrepancies with re-
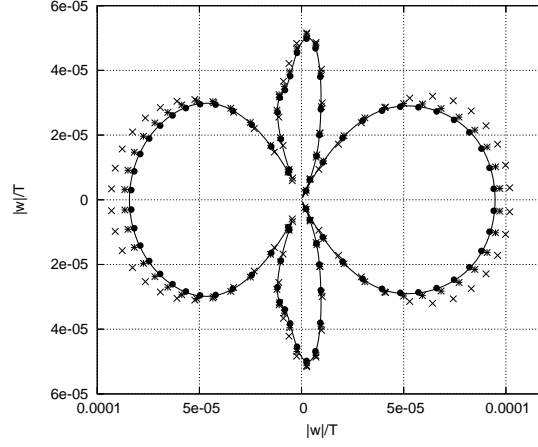
Figure 4.11: *Angular dependence of radial elastic displacement on the meridian circle of a sphere impinged by a plane wave with $kR = 11.16$.   — analytical solution; $\times\ N_m = 40, N_p = 40$; $*\ N_m = 40, N_p = 72$;   • extrapolated numerical solution.*
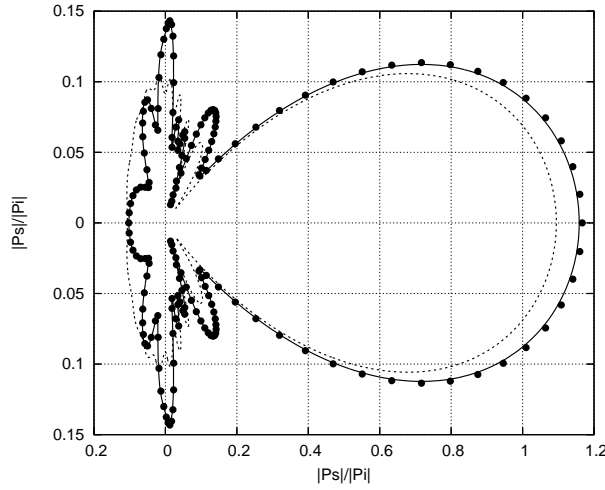
Figure 4.12: *Angular dependence of scattering for a plane wave impinging on a stationary elastic sphere. $kR = 11.16$ and $d/R = 5$.   — analytical solution;   • numerical solution;   - - - analytical solution (rigid sphere).*

spect to the prediction obtained through the formulation based on the FWH equation, especially in the region closer to the source (i.e., in front of the leading edge in Fig. 13 and in front of the trailing edge in Fig. 4.17). Such disagreement is quite unexpected and should be due to the different effect
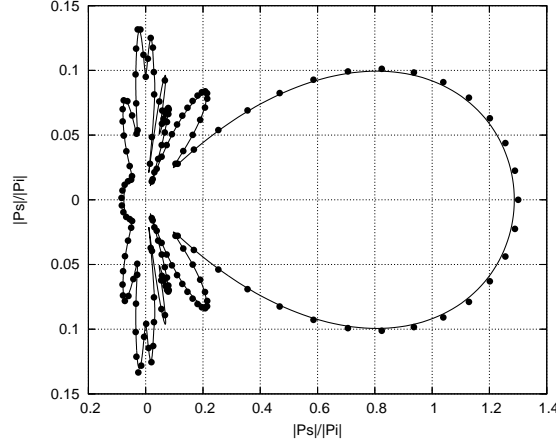
Figure 4.13: *Angular dependence of scattering for a plane wave impinging on a stationary elastic sphere.* $kR = 13.214$ *and* $d/R = 5$. *— analytical solution;* $\bullet$ *numerical solution.*
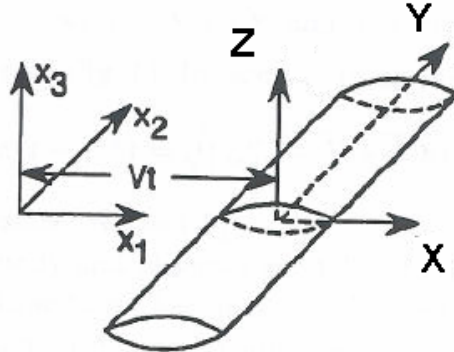
Figure 4.14: *Geometry of the translating wing used to analyze the scattering from moving rigid bodies. (Adapted from Ref. [74]).*

that the elimination of the nonlinear terms has on the two solutions. In the present approach, when subsonic configurations are examined, the quadrupole term vanishes in sound radiation (observer far from the body), but might become relevant when the integral formulation is used as an integral equation (observer on the body), unless the Lighthill tensor is very small. Note that the perturbed Lighthill tensor would give rise to linear perturbation terms which could become important as the body Mach number increases, in that proportional to the local unperturbed flow velocity on the body surface. Indeed, the scattered fields predicted by potential and FWH formulations are quite similar as the Mach number decreases to $M = 0.1$ (see Fig. 4.18, for $\mathbf{x}_s^{LE} = (-5c_w, 0, 5c_w)$), while become almost identical in the steady-wing case (see Fig. 4.19, for $\mathbf{x}_s^{LE} = (-5c_w, 0, 5c_w)$).
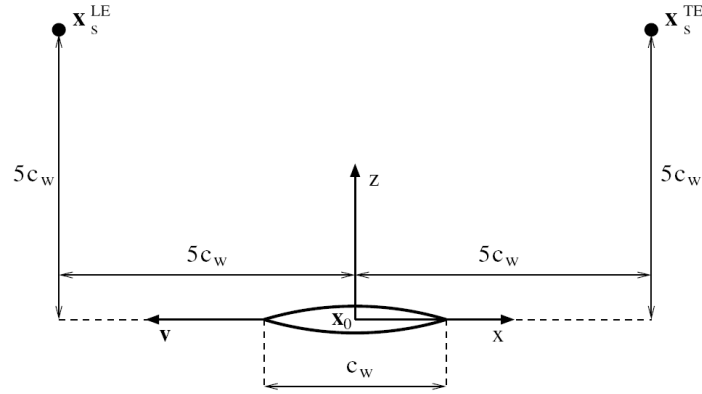
Figure 4.15: *Mid–plane of the scattering wing. Wing velocity and location of point sources.*

The importance of the nonlinear terms is analysed also in Fig. 4.20 that shows the steady pressure perturbation at distance $d/c_w = 5$ due to the wing uniform motion at $M = 0.5$. In this case the predictions from the two formulations are in good agreement for $t_w/c_w \leq 0.1$, while significant discrepancies start arising for $t_w/c_w = 0.2$, particularly at observer locations in front of the wing regions where the highest values of fluid flow velocity occur and the Lighthill tensor is greater (note that in this case $p_{ref} = 0.5\,\rho_0\,c^2\,M^2$).

Finally, a rigid vibrating sphere is examined. It is considered in uniform rectilinear translation, while oscillating back and forth along the direction of motion, with $kR = 1$. The results from the present formulation are compared with those from a linearized velocity potential approach in terms of the ratio $|\tilde{p}'|/p_{ref}$, where $p_{ref} = \rho_0\,c\,U$ with U denoting the magnitude of sphere oscillations. Figures 4.21 and 4.22 depict the acoustic disturbance distribution on a surface meridian circle parallel to the direction of motion, respectively for $M = 0.1$ and $M = 0.2$, in addition to that for $M = 0$. Akin to the wing scattering problem, the agreement between the two formulations is excellent for $M = 0$, but worsen as the Mach number increases, although remaining quite similar up to $M = 0.2$. The two approaches predict that, at both Mach numbers, the sphere motion induces an increase of the pressure disturbance in the front region, while in the rear part the pressure disturbance is slightly reduced at $M = 0.1$ and slightly increased at $M = 0.2$. Note that these results differ from those presented in Ref. [76] where the same problem has been analysed using a formulation very close to that presented here. In particular, the results presented in Ref. [76] are in worse agreement with respect to the results based on the potential formulation, in that overestimate the pressure perturbation in the front region, while underestimate it in the rear part.

4.4.4   A Case of Aeronautical Interest: the Effect of Fuselage on Noise Emitted by a Helicopter in Descent Flight

The extremely annoying noise generated by helicopters in many flight conditions is a critical issue for helicopters certification that deeply limits its widespread operation in populated areas. Typically, the evaluation of the acoustic field in forward flight conditions deals with the noise generated aerodynamically by the main rotor without including fuselage scattering effects. This is motivated by the fact that since the rotor blade passage frequency (BPF) is generally low, the wavelength of the noise signal is quite large compared to the physical dimensions of the fuselage cross-section and thus the acoustic influence of the body turns out to be minimal. However, in many cases the acoustically critical environment is caused by Blade Vortex Interactions (BVI) that occur at those helicopter flight conditions such that strong tip vortices impinge or pass closely to

95
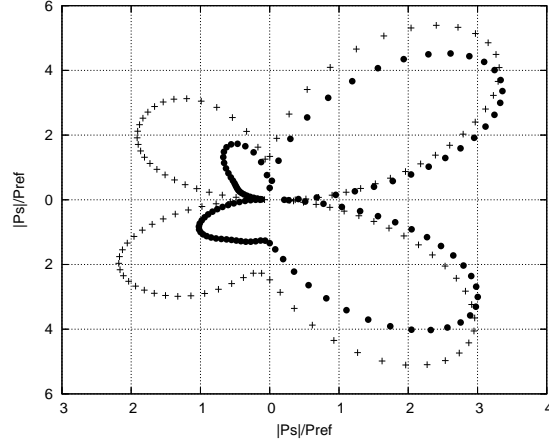
Figure 4.16: *Pressure scattered in mid-span plane by a wing in uniform rectilinear translation.* $\mathbf{x}_s^{LE} = (-5c_w, 0, 5c_w)$, $kc_w = 6$, $d/c_w = 52.5$, $M = 0.5$. $+$ *potential solution;* $\bullet$ *FWH solution.*
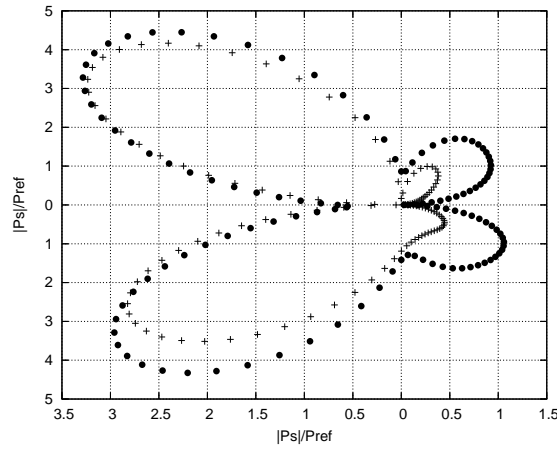
Figure 4.17: *Pressure scattered in mid-span plane by a wing in uniform rectilinear translation.* $\mathbf{x}_s^{TE} = (5c_w, 0, 5c_w)$, $kc_w = 6$, $d/c_w = 52.5$, $M = 0.5$. $+$ *potential solution;* $\bullet$ *FWH solution.*

the following rotor blade (slow descent is a typical example of them). The spectrum of resulting noise signal has a much higher frequency content and the fuselage may affect the distribution of the acoustic field in a significant way. Note that the fuselage turns out to be an efficient scatterer also for High-Speed Impulsive (HSI) noise and for the acoustic signal emitted by the tail rotor, that usually operates at BPF's higher than those of the main rotor.
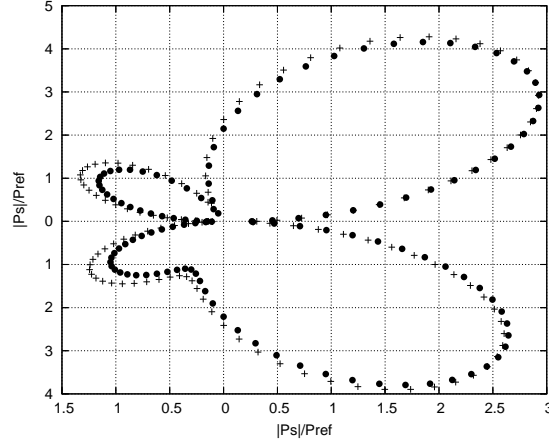
Figure 4.18: *Pressure scattered in mid-span plane by a wing in uniform rectilinear translation.* $\mathbf{x}_s^{LE} = (-5c_w, 0, 5c_w)$*,* $kc_w = 6$*,* $d/c_w = 52.5$*,* $M = 0.1$*.* $+$ *potential solution;* $\bullet$ *FWH solution.*
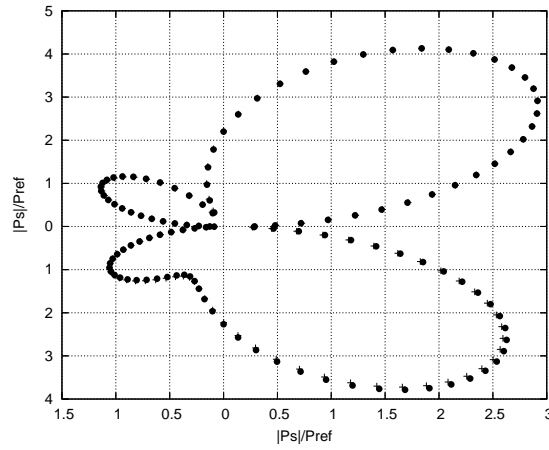
Figure 4.19: *Pressure scattered in mid-span plane by a wing in uniform rectilinear translation.* $\mathbf{x}_s^{LE} = (-5c_w, 0, 5c_w)$*,* $kc_w = 6$*,* $d/c_w = 52.5$*,* $M = 0$*.* $+$ *potential solution;* $\bullet$ *FWH solution.*

In several aeronautical configurations and flight conditions it is possible to assume that some aerodynamic interactional effects are negligible and hence that the contribution from a subset of surfaces is unaffected by the presence of the other bodies. This is, for instance, the case examined here that concerns a helicopter descent flight such that the wake shed by the main rotor does not impinge the fuselage. In this way, the source of the incident field (the main and tail rotor) may
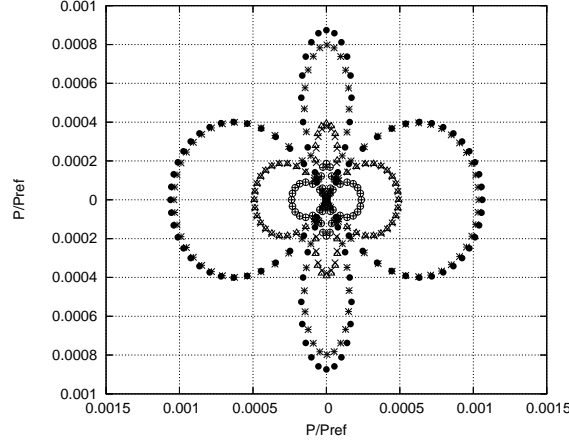
Figure 4.20: *Pressure steady perturbation in mid-span plane due a wing in uniform rectilinear translation at $M = 0.5$. $d/c_w = 5$. + potential solution, $t/c_w = 0.05$; ∘ FWH solution, $t/c_w = 0.05$; × potential solution, $t/c_w = 0.1$; △ FWH solution, $t/c_w = 0.1$; ∗ potential solution, $t/c_w = 0.2$; • FWH solution, $t/c_w = 0.2$.*
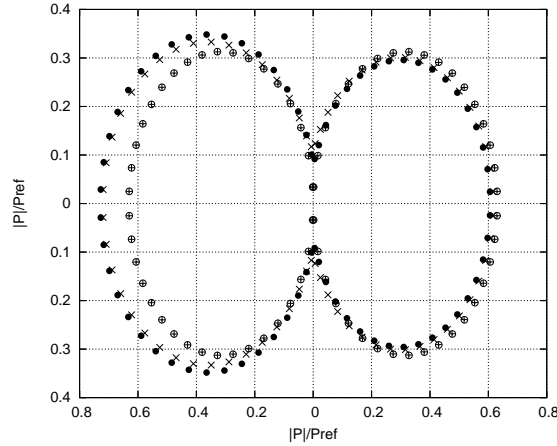
Figure 4.21: *Angular dependence of pressure perturbation on the surface of a rigid sphere in uniform rectilinear translation and oscillating back and forth along the direction of motion. $kR = 1$. + potential solution, $M = 0$; ∘ FWH solution, $M = 0$; × potential solution, $M = 0.1$; • FWH solution, $M = 0.1$.*

be considered aerodynamically independent on the presence of the scattering surfaces; thus, the incident pressure field may be determined through a prior combined aerodynamic-aeroacoustic analysis of main and tail rotors, whereas the rest of the configuration (the fuselage) is included only in the second step of the process, dealing with the scattering analysis.

98
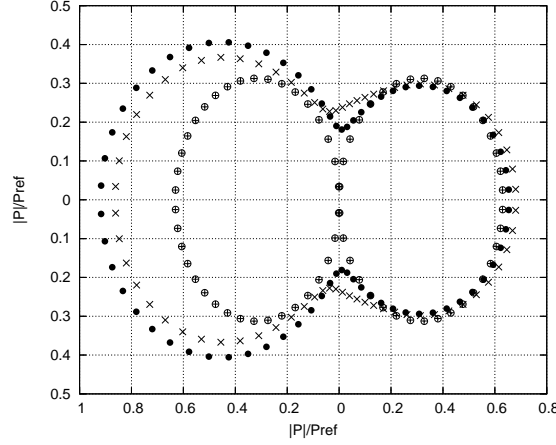
Figure 4.22: *Angular dependence of pressure perturbation on the surface of a rigid sphere in uniform rectilinear translation and oscillating back and forth along the direction of motion. $kR = 1$. $+$ potential solution, $M = 0$; $\circ$ FWH solution, $M = 0$; $\times$ potential solution, $M = 0.2$; $\bullet$ FWH solution, $M = 0.2$.*

Under these basic assumptions, the scattering effects induced by a realistic helicopter fuselage during a low-speed descent, are examined through the theoretical model presented in section 4.2.2. An alternative way to compute the fuselage influence on the helicopter noise consists of using an interactional aerodynamics solver applied to the main-rotor/tail unit–fuselage configuration, followed by the application of a conventional aeroacoustic tool for the radiation of the acoustic disturbance; however, this approach is more computationally expensive than the FWH-based scattering approach, in that requires the aerodynamic solution of a multibody configuration, instead of a sequence of single body solutions.

Limiting the analysis to a main-rotor/fuselage configuration for the sake of conciseness (the extension to a complete helicopter is straightforward), for $\mathcal{S}_F$ and $\mathcal{S}_R$ denoting fuselage and main rotor surface, respectively, Eq. (4.2) yields the overall acoustic disturbance. Assuming main rotor aerodynamics weakly influenced by the rest of the rotorcraft, Eq. (4.3) yields the (incident) acoustic disturbance p'_M generated by the main rotor once the blade pressure on $\mathcal{S}_R$ is evaluated by the isolated-body prior aerodynamic analysis.

Then, decomposing the total pressure disturbance field into a fuselage component, p'_F, and a main-rotor component, *i.e.*, $p' = p'_F + p'_M$, and following the procedure presented in section 4.2.2, Eq. (4.5) with $\mathbf{u}^- \cdot \mathbf{n} = 0$, $p'_I = p'_M$ and $p'_B = p'_F$ governs the scattered pressure field on $\mathcal{S}_F$. Considering observers fixed with the helicopter fuselage and discarding the stationary contribution generated aerodynamically by the motion of the fuselage surface [55], [77], Eq. (4.15) yields the scattered noise in the frequency domain. For the sake of simplicity, the tail unit is not considered as source of impinging pressure field. Note that the aerodynamic formulation used to examine the fluid flow around the isolated main rotor and to evaluate main-rotor/fuselage interactional aerodynamics (thus including fuselage scattering effects) is suited for the analysis of flight configurations where strong blade/wake interactions occur. It has been presented in Refs. [78] and [79] as a development of the boundary integral formulation for the velocity potential introduced in Ref. [80] and further

extended in Ref. [22]. Such a formulation for BVI analysis has been validated through correlation with experimental data [78],[79].
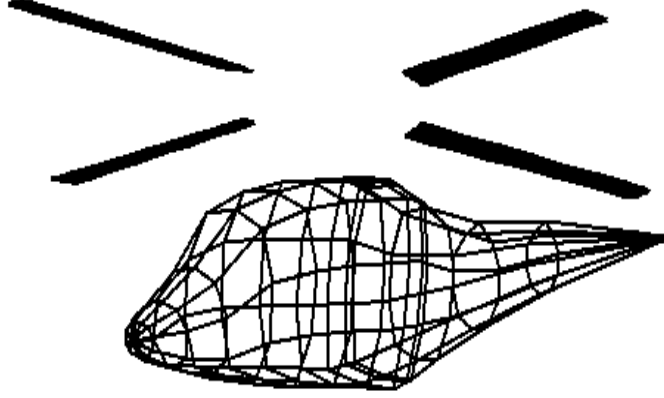
Figure 4.23: *Sketch of the paneled fuselage–main rotor configuration.*

The helicopter considered in this investigation has a four-bladed model main rotor of radius $R = 5$m, constant chord $c = 0.32$m, NACA 23012 airfoil sections and angular velocity $\Omega = 390$RPM. The fuselage is about 12m long and the characteristic dimension of the cabin cross section is equal to 1.8m. The descent flight path is such that the shaft angle is equal to $4°$, while the advance ratio is $\mu = 0.15$. All the results that will be presented concern the SPL (dB) of the noise calculated on a plane parallel to the ground, located 33m below the helicopter and travelling with it.
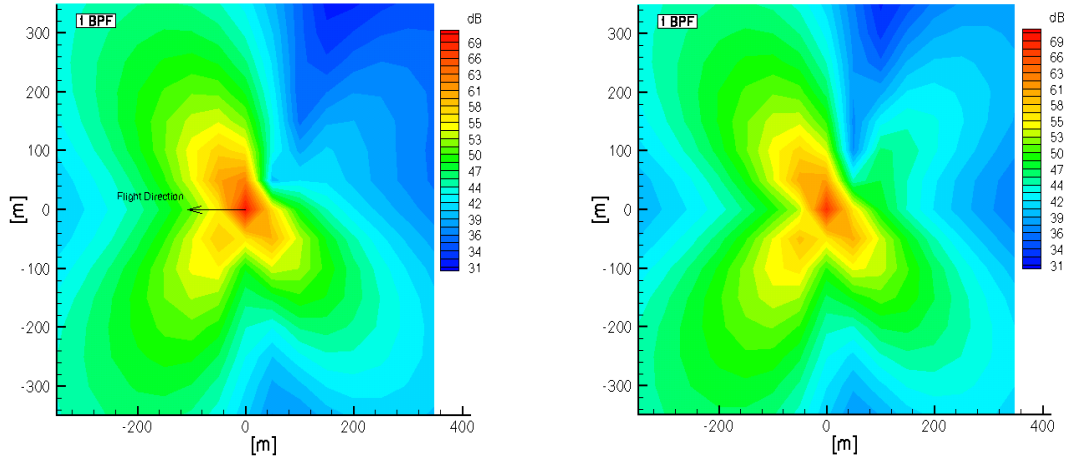
Figure 4.24: *SPL from aerodynamic formulation (left); SPL from scattering formulation (right).*

Before examining the results of the scattering analysis of the noise emitted by the rotor experiencing BVI, a preliminary conceptual study concerning the sound radiated by the fuselage with the main rotor in nonlifting conditions is presented. In particular, the noise predicted by the scattering formulation and that predicted by the aerodynamic solver in which the full aerodynamic coupling between rotor and fuselage is taken into account are compared. Being the fuselage in uniform translation, the sound it radiates comes from the interaction with the unsteady pressure

field generated by the main rotor: the scattering formulation evaluates the effects of the fuselage on the noise radiated by the main rotor considered as an isolated body, while the aerodynamic formulation takes into account also the effects of the fuselage on the rotor blade pressure distribution. Fig. 4.24 (left) shows the total noise contour levels predicted by the interactional aerodynamics,
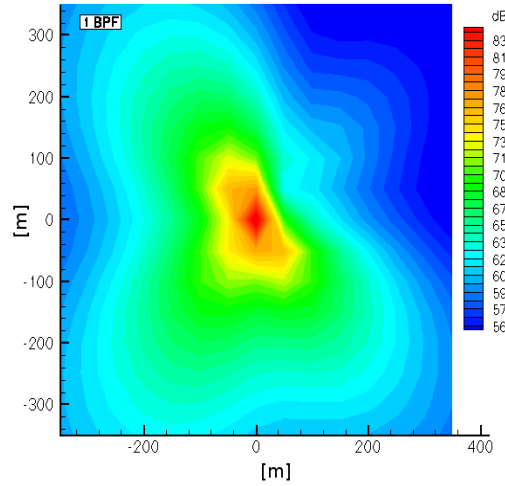
Figure 4.25: 1st *BPF scattered field.*

whereas Fig. 4.24 (right) shows the results from the application of the scattering formulation (the helicopter travels from the right to the left). Both concern the 1st BPF of the signal which, in this simple case, is the only one to be not negligible. The two predictions are in good agreement, with a small discrepancy appearing in the rear region at the right hand side, as seen from the helicopter. This confirms the capabilities of the present scattering approach to capture with satisfactory accuracy the effects of the fuselage presence on the noise field emitted by the fuselage/main-rotor configuration.
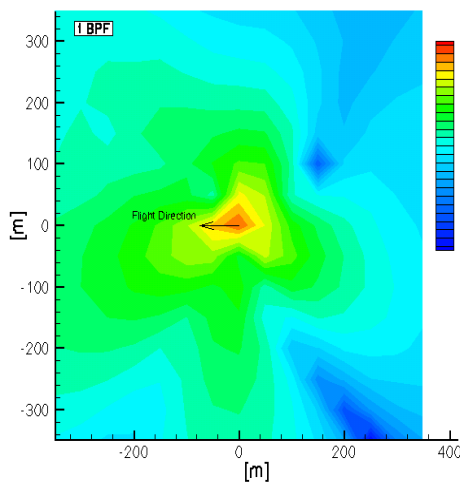
Figure 4.26: 1st *BPF total field.*
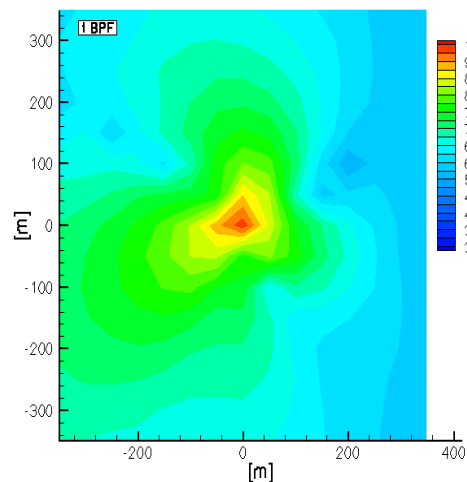
Figure 4.27: 1st *BPF isolated rotor field.*

Next, we examine the prediction of fuselage scattering effects in the realistic descent flight

condition described above. In this case, the noise emitted by the fuselage/main-rotor configuration has a much higher harmonics frequency content because of the impulsive loads produced on the rotor blades by BVI occurrence. Considering the 1st BPF, Fig. 4.25 shows the SPL contour levels of the noise scattered by the fuselage. This figure reveals that the scattered noise rapidly decreases moving far from the fuselage and has a quite uniform distribution around the helicopter, with three directions where it is prominent and one (the rear region at the right hand side of the rotorcraft) where it is attenuated. The corresponding total noise field is depicted in Fig. 4.26, while Fig. 4.27
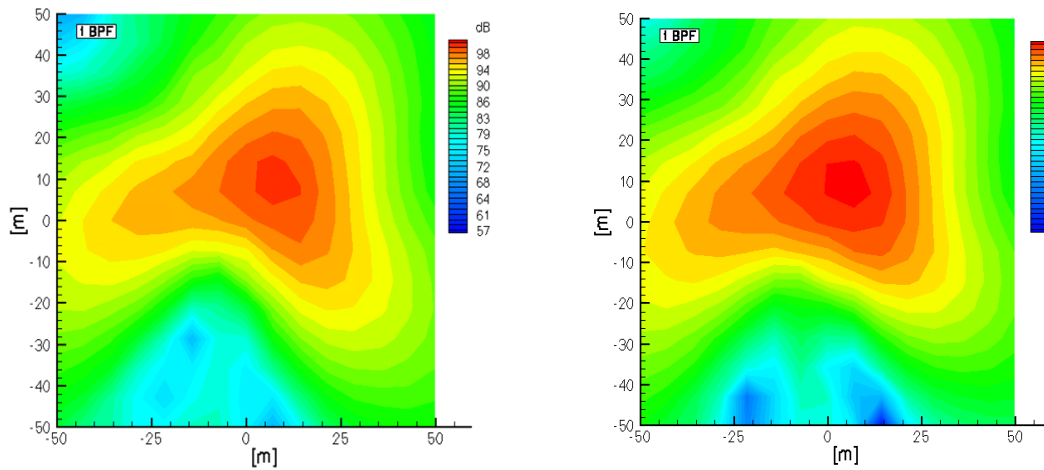
Figure 4.28: *Left: 1st BPF total field (close view); right: 1st BPF isolated rotor field (close view).*
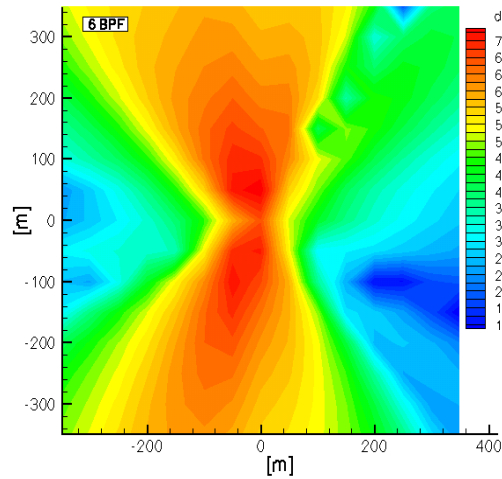
Figure 4.29: *6th BPF scattered field.*

shows the acoustic field radiated by the isolated rotor for comparison. These results demonstrate that the presence of the fuselage seems to yield a shielding effect in the rear part of the area examined, particularly at the left hand side of the rotorcraft. In addition, it attenuates the very-near field noise and re-distributes it in left-hand-side and front right-hand-side regions. A close view of the noise levels in the near field is given in Fig. 4.28, respectively for the total noise

(left) and for the noise from the isolated rotor (right). They show that the highest noise levels are uniformly attenuated by the fuselage presence and that an increase of noise at the left hand side of the rotorcraft is present starting from the region 40m distant from the rotor.

In order to correlate Fig. 4.25 with Figs. 4.26–4.28, it is worth noting that a high level noise region in the scattering field not necessarily implies that there the total noise is higher than the noise field not affected by scattering. Indeed, a high level of scattering means that its effect is significant, but it may cause an increase or a decrease of noise depending on the phase shift that the scattered signal has with respect to the incident field.
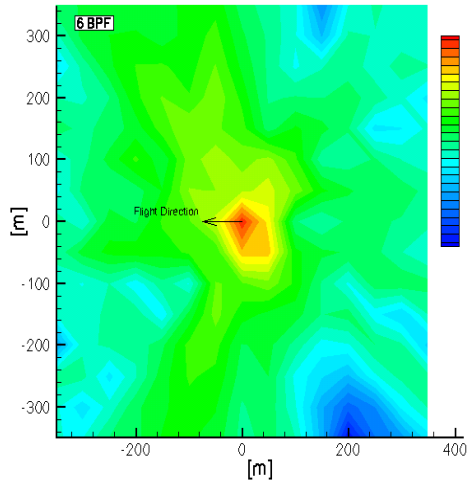
Figure 4.30: 6th *BPF total field.*
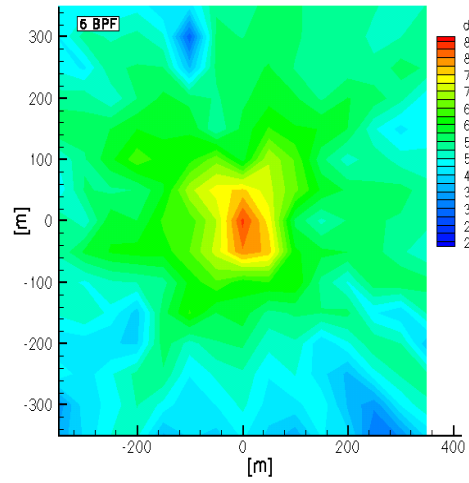
Figure 4.31: 6th *BPF isolated rotor field.*
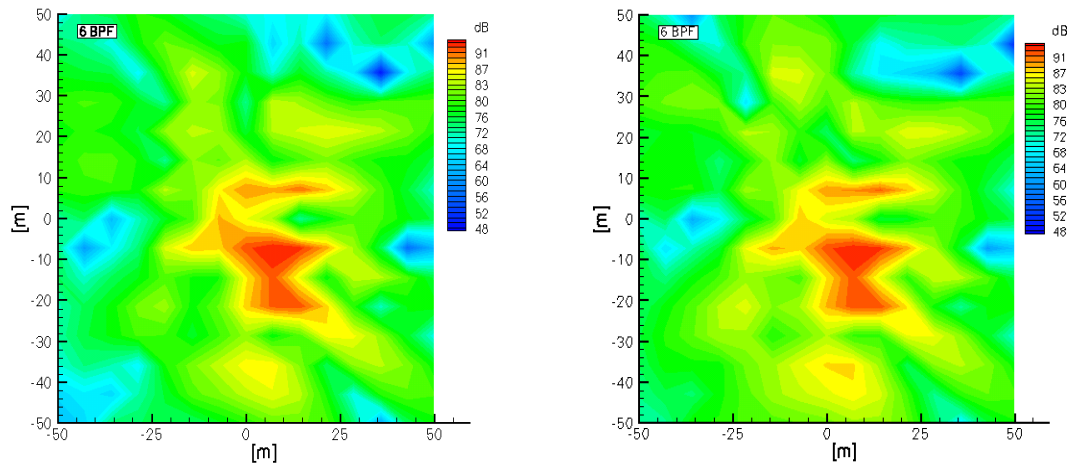
Figure 4.32: *Left:* 6th *BPF total field (close view); right:* 6th *BPF isolated rotor field (close view).*

Note that the 1st BPF that has been examined in Figs. 4.25–4.28 corresponds to a wavelength of about 13.5m, which is comparable with the length of the fuselage, but is much higher than the characteristic dimension of its cross section (about 1.8m). A different pattern of the scattered noise contour levels is predicted when higher harmonics of the noise are examined, such that their

wavelengths are comparable with or smaller than the characteristic dimension of fuselage cross section. This particularly occurs starting from the 5th BPF of the signal ($\lambda \approx 2.2m$). For instance, Fig. 4.29 shows the SPL contour levels of the 6th BPF of the noise scattered by the fuselage. Differently from what observed for the 1st BPF, this scattering field shows a clear directivity in the direction normal to the longitudinal axis of the fuselage. Moreover, in this direction it slowly decreases, thus remaining significant also in the far field. Concerning the effects of the scattering field on the total noise, these are observed by comparing Fig. 4.30 and Fig. 4.31 that depict the contour plots of the SPL related to the total noise and to the noise from the isolated main rotor, respectively. Also in this case the effect of the scattering field seems to attenuate the very-near field noise, while the acoustic disturbance is increased along the direction orthogonal to the fuselage, especially at the right hand side of it. Furthermore, it is notable the shielding effect at the rear part, particularly at the left side of the cabin. Close views of the near field 6th BPF noise levels are given in Fig. 4.32, respectively for the total noise (left) and the isolated-rotor field (right). In this case, the local slight noise alleviation due to the fuselage is not uniformly distributed around the rotorcraft, but is rather focused at its right-hand-side and left-hand-side regions.

A similar behaviour is observed at higher BPF: Fig. 4.33 shows the scattered field of the 8th BPF whereas Fig. 4.34 and 4.35 depict the contour plots of the SPL related to the total noise and to the noise from the isolated main rotor, respectively. Note that a particular increase of noise at the right hand side of the helicopter has been observed for all the higher BPF's examined: this could be explained by the fact that strongest BVI occurs at the advancing side of the blade that, in this case, corresponds to the right hand side of the rotorcraft.
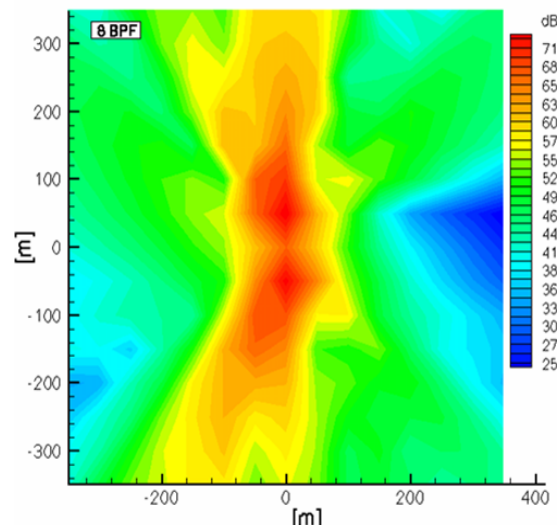
Figure 4.33: 8st *BPF scattered field.*

The shielding effect caused by the presence of the cabin is shown in Fig. 4.36; here, the difference between the SPL due to main rotor noise–cabin scattering effect and the SPL due to the isolated rotor is plotted. The zones where the difference is negative indicate the noise shield effect induced by the fuselage.

In conclusion, the results have demonstrated that the impact of the fuselage strongly depends on the noise harmonic examined. Indeed, the lowest BPF's of the acoustic signal show an influence of the fuselage that is localized around the helicopter and has moderate azimuthal differences. For higher harmonics such that their wavelengths are comparable with or smaller than the characteristic dimension of fuselage cross section, the scattered field is characterized by a strong directivity in the direction orthogonal to the fuselage longitudinal axis and a slow decrease moving far from
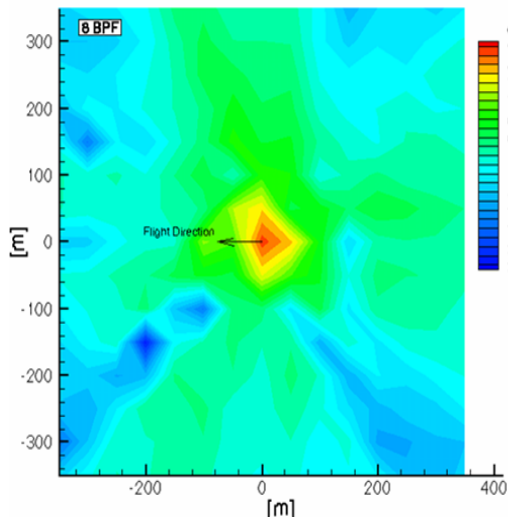
Figure 4.34: 8th *BPF total field.*
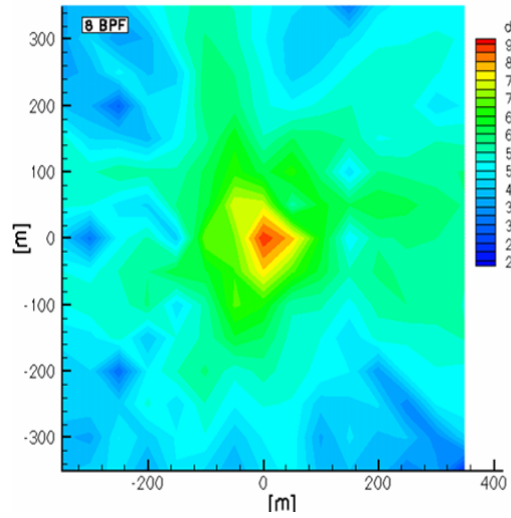
Figure 4.35: 8th *BPF isolated rotor field.*
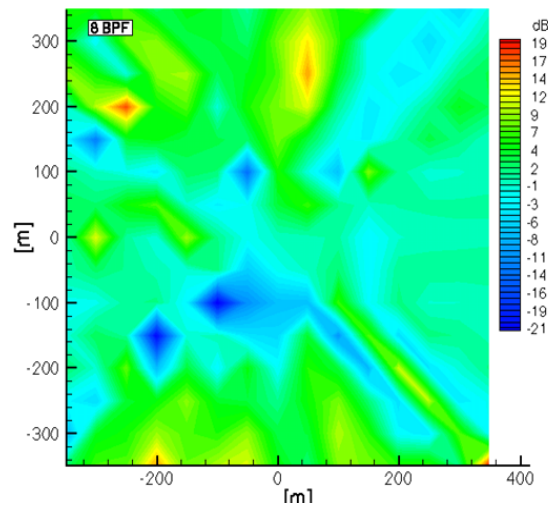
Figure 4.36: $\Delta\ SPL$ *between main rotor in the presence of the cabin and isolated main rotor.*

the rotorcraft. In both cases, the effect of the scatterer is to alleviate the noise in the very-near field and to increase it in the far-field regions at the left-hand-side and at the right-hand-side of the rotorcraft.

4.4.5   Concluding Remarks

The formulation presented yields a unified approach for the prediction of surface pressure perturbations and sound radiation generated by pressure waves impinging moving, elastic bodies. The proposed formulation is able to include surface vibration effects, and thus can be applied to vibroacoustic/acoustoelastic problems. The numerical investigation demonstrates that it gives very accurate predictions of near-field and far-field pressure scattered by stationary rigid spheres, both for low-frequency and mid-frequency incident waves. Very accurate numerical predictions are obtained also for scattering problems concerning stationary elastic surfaces, both in terms of resulting elastic deformations and in terms of radiated sound. Note that the problem of the presence of spurious frequency in the integral operator is successfully solved by the widely-used CHIEF regularization technique.

When the present integral formulation is applied to scattering and vibrating surfaces in uniform motion, the assumption of neglecting the nonlinear terms related to the quadrupole contribution may be not reasonable as the Mach number increases. As a matter of fact, the comparison with the results given by a linearized velocity potential formulation shows that discrepancies grow together with the body Mach number. An explanation of this behaviour is that the nonlinear terms (not included in both approaches) yield a quantitative different influence in the two formulations. In particular, in the present approach the quadrupole term might become relevant when the observer is on the body, unless the Lighthill tensor is very small. This is an open problem whose investigation is beyond the scope of the present thesis.

Chapter 5

Conclusions and Recommendations

5.1 Conclusions

The present work has dealt with the prediction of the noise field emitted by propeller and helicopter rotors in unbounded space, or in the presence of solids boundaries, for aeronautical and marine applications based on the Ffowcs Williams and Hawkings equation (FWHE). The attention has been focused on those problems where transonic effects may be neglected, along with the quadrupole term in the noise prediction.

Noise Radiation

Noise radiation from marine propeller blades, operating in non–cavitating condition, has been first addressed. The interest in doing such investigation arises from the fact that the hydroacoustic community typically performs noise calculations using the Bernoulli equation. Taking into account that, after 40 years of applications, the FWHE has been proven to be a very efficient aeroacoustic solver for aeronautical subsonic and supersonic configurations where the sound generated aerodynamically plays a significant role, and considering that air and water propeller have much in common from the theoretical modeling point of view[1], such behaviour is quite surprising. Hence, in order to highlight the capabilities of the FWHE in studying marine propeller, a comparison with the Bernoulli-based methodology has been here proposed. As shown in chapter 2, the most important remark arising from this comparison is that:

- The Ffowcs Williams and Hawkings equation has been shown to be notably more *robust* for noise prediction respect to the Bernoulli–based method. In the framework of potential flows, it yields noise signature predictions not directly affected by the presence of the potential wake. In fact the presence of the wake influences the pressure distribution on the blade(s), hence the noise related to the blade; however, for a given operating condition, the noise signature predicted by the FWH approach does not exhibit a strong sensitivity to the shape of the wake used in the hydrodynamic analysis, apart from slight differences due to the differences in the blade loads. On the contrary, in the Bernoulli approach, noise predictions deeply depend on the wake modeling adopted; by considering a prescribed-wake modeling, different wakes (in terms of pitch) produce notable differences in the waveform of the resulting noise signal. The reasons for this behaviour of the numerical solution are twofolds: 1) the need of computing the velocity potential in the flow–field by performing an integral on the wake surface; 2) any prescribed wake modeling does not represent a material surface hence behaves as a numerical source of loading noise.

---

[1]Particularly if one's attention is restricted to air propellers operating at low Mach numbers and to water propellers operating without cavitation.

The use of the FWHE filters such problems because the potential wake contribution to the noise signal (in terms of thickness and loading noise) is exactly zero; the acoustics effects of the potential wake are modeled by the quadrupole term and become relevant when the non linear terms associated to the the flow velocity are not negligible. From a theoretical standpoint the use of a free-wake, that is a wake locally aligned with the fluid velocity, should overcome this limitation associated to the Bernoulli approach. However, the use of the free-wake algorithm does not yield the expected improvement. The reason is more a hydrodynamic issue than a hydroacoustic one; in fact, the rate of convergence of the computed flow velocities is significantly slower than the rate of convergence associated with the prescribed wake. The same converged solution could be obtained at price of unacceptable computational efforts because of the too much fine grid to be used. Hence, the guideline derived from the numerical comparison between the FWHE and the Bernoulli method is that the physically consistent approach for hydroacoustic purposes is the FWHE because of the proven influence of the wake modeling on acoustic pressure computed through the Bernoulli equation. Apart from the problem of the shape of the potential wake, the evaluation of the pressure loads on the blade needs an amount of wake, in terms of number of spirals, that is considerably less than the wake length ensuring a converged aero/hydro–acoustic solution (for a given observer positions). Therefore, the FWHE is more efficient in terms of computational effort with respect to the Bernoulli solver.

Cavitating Propellers

After having applied the FWHE to predict the noise field radiated by non–cavitating propellers, the study of cavitation noise has been addressed. Cavitation, _i.e.,_ vaporization occurring in high–speed flow regions, is a typical phenomenon affecting marine propellers in many different operating conditions. The evaluation of the noise due to the cyclic growth and collapse of the cavity on the surface of a propeller in a non–uniform onset flow, has been performed through a novel application of the permeable FWHE combined with a suitable hydrodynamic model describing the unsteady cavitation pattern (Transpiration Velocity Model, TVM). The main remarks can be summarized as follows:

- The Transpiration Velocity Modeling, based on the permeable FWHE, simulates the presence of the transient sheet cavitation through the difference between the normal component of the body velocity and the fluid velocity wherever cavitation occurs. Noise produced by the cyclic growth and collapse of the cavity is mainly due to the time history of the acceleration during a blade revolution. Akin to the application of the FWHE to non–cavitating propellers, a hydrodynamic solver has to provide the pressure distribution on the blade to compute the loading noise term; however when cavitation occurs, further hydrodynamic data are needed: velocity and acceleration distribution on the blade surface and thickness of the cavity. The numerical results provided by the TVM model have been successfully compared with those provided by the Equivalent Blade Modeling (EBM) based on a different strategy to include the presence of the cavity inside the FWHE. Numerical applications of the two methodologies reveal that noise prediction, using TVM and EBM, are in agreement. Nevertheless, some discrepancies in noise prediction arise from the different sensibility of the two FWH–based approaches respect to the hydrodynamic data describing the cavitation pattern. As a matter of fact, the TVM is more sensible to the accuracy of the hydrodynamic input because of the need to compute time derivatives of the function describing cavity thickness distribution on the blade surface, whereas the EBM requires integration over a variable shape blade to account for the presence of the unsteady pocket of vapor. For both TVM and EBM, problems in describing unsteady sheet cavitation noise arise when the frequency of the cavitation phenomenon increases; in fact the TVM is affected by the inaccuracy due to

the cavity thickness derivatives that, for highly impulsive signals, may become very difficult to be computed whereas the EBM is conditioned by the step-by step strategy in computing the presence of the cavity that makes it a *quasi–steady* approach, with a limited capability to correctly describe rapidly changing flow conditions.

Scattering

In order to appreciate the sound field change when solid surfaces are present in the flow field and to allow the prediction of the noise produced by those aeronautical and marine configurations where one single body may be identified as the main noise source (with the pressure on it approximately independent on the presence of the other bodies), the problem of the scattering has been investigated through a novel integral formulation based on the FWHE. When applicable, a scattering model allows to study the acoustic behaviour of whole configurations as fuselage–propeller, fuselage-main/tail–rotor and hull-propeller, without invoking the interactional aero–hydro–dynamics to calculate the scattered pressure field on the boundary of the scatterer. Differently from noise radiation problems where the FWHE is used as an integral representation, in this problem the integral solution of the FWHE is used as an integral equation to determine the scattered pressure distribution upon the scattering body. The main remarks are drawn in the following:

- The proposed FWH formulation yields a unified solver able to radiate sound and to evaluate the acoustic disturbance over moving surfaces. It may be applied to those aeronautical or naval multi–body configurations where the sources of noise may be considered aerodynamically or hydrodynamically independent on the presence of the rest of the configuration. For some operating conditions, propeller–driven aircraft, rotorcrafts and ships fall in this category. The evaluation of the sound field produced by the impingement of the pressure disturbance(s) on the scatterer(s) requires a prior analysis of the isolated source(s), to identify the incident pressure field(s). The formulation herein proposed is flexible in that allows to study scattering problems concerning rigid as well as elastic bodies, moving or at rest.

- Numerical results show that, for stationary rigid or vibrating scattering bodies, the proposed methodology yields excellent results. Dealing with moving scatterers, the issue of the quadrupole term must be pointed out. In fact, when the FWHE is applied to face problems where acoustic waves impinge on solid boundaries (scattering problems), the assumption to ignore the quadrupole term in the FWHE may become too much restrictive. The opportunity of neglecting the quadrupole term depends on the advancing speed of the scatterer and on its shape. For some configurations and advancing speed, the contribution arising from the Lighthill tensor on the body surface might be comparable with the perturbation velocity itself and the inclusion of the quadrupole term in the FWHE would be required.
  Obviously, the inclusion of volume terms in the FWHE to determine the scattered pressure on the scatterer would require the knowledge of the aerodynamic field around the scatterer itself, in presence of the source of noise. Apart from the complexity due to the inclusion of volume terms, any aerodynamic solver able to furnish such an input is in principle able to calculate the pressure distribution on the scatterer accounting also for the interactional effects; therefore, the scattering modeling could be completely useless. Hence, the analysis of moving scatterers has to be addressed carefully because the Lighthill tensor would give raise to perturbation terms which might become relevant when the integral formulation is used as an integral equation.

5.2   Recommendations

Basing on the above conclusions, the following recommendations are given for further development and improvement of the present work.

- Investigation on the importance of the quadrupole term should be done in the future. Emphasis should be put on the Lighthill tensor in order to include the quadrupole term into the solution of the boundary integral equation aimed to determine the scattered pressure field.

- The capability of the scattering formulation to solve acoustoelastic problems has been analysed considering an elastic sphere impinged by a plane wave; validation of numerical results addressing more complex configurations, in terms of geometry and load, as real airplanes or helicopter fuselages or hull ships should be considered. In particular the acoustoelastic behaviour of a *real* configuration impinged by the acoustic disturbance generated by propeller or rotor blades should be investigated. In this case the aero(hydro)–acoustic methodology should be coupled with a structural finite element analysis (FEM) to model the acoustoelasticity of the scatterer.

- For scattering problems dealing with moving bodies, further careful analysis of the theory is needed to well justify the disagreement of the results of the present thesis with those shown in [76].

- For underwater cavitating propellers, validation of numerical noise predictions (in unbounded space or in the presence of free-surface) against experimental flow data, is not possible because of the lack of quantitative data covering a useful spectrum of flow conditions. This point may be considered as one of the most urgent hydroacousticians's need. Hence, suitable experimental investigations should be carried out to assess a rich cavitating and non–cavitating flow database.

- Further investigation on the numerical behaviour of the TVM, at high frequencies, should be carried out. Furthermore, the use of two phase flow models combined with the solution of the Navier-Stokes equations, in principle, allows the description of the inhomogeneous cavitating flow around the propeller blades; therefore, it is possible to model the spatial gradients of the speed of sound that deeply affect the noise radiation when cavitation occurs. By using the permeable KFWH formulation and providing the required hydrodynamic data on the *control surface* by a viscous two-phase CFD code, the resulting noise signals should be compared with experimental data or with those obtained by the use of CAA.

- Apart from cavitating propellers, different types of aero–hydrodynamic models aimed to provide the required input to the KFWH formulation should be considered. In fact, the use of aero–hydrodynamic models based on the theory of potential flows allows to well describe the interaction between solid bodies and an onset flow characterized by negligible turbulence of the incoming flow, and is physically consistent when the effects of viscosity are confined within the boundary layer attached to the body surface and flow separation does not occur. Nevertheless, in many operating conditions these assumptions do not hold. Hence, the use of CFD data is suitable to analyse the behaviour of a rotating propulsive systems in more realistic operating conditions.

Appendix A

A Boundary Integral Formulation for Aerodynamics and Aeroacoustics of Moving Bodies

A.1 The Differential Aeroacoustic Problem

There, the general form of the Ffowcs Williams and Hawkings equation is derived. For the sake of simplicity, it is convenient to introduce a set of orthogonal coordinates (O, x_1, x_2, x_3) related to an air frame of reference (frame fixed to the medium) denoted by unit vectors $\mathbf{i}_1\, \mathbf{i}_2\, \mathbf{i}_3$. In the following, the indicial notation is adopted, for which $f_{,j} = \dfrac{\partial f}{\partial x_j}$ and $f_j = \mathbf{f} \cdot \mathbf{i}_j$.

Let us assume that the fluid is compressible and undergoes transformations with negligible entropy changes; by combining the continuity equation and the Navier–Stokes equations

$$\dot{\rho} + (\rho u_j)_{,j} = 0$$
$$(\rho \dot{u}_j) + (\rho u_j u_k)_{,k} = -p_j + V_{jk,k} \tag{A.1}$$

the following equation, known as Lighthill's equation, is easily obtained

$$\Box^2 p' = \frac{1}{c_0^2}\frac{\partial^2 p'}{\partial t^2} - \nabla^2 p' = T_{jk,jk} \tag{A.2}$$

where c_0 represents the sound speed in quiescent medium, $p' = c_0^2(\rho - \rho_0)$ denotes the aeroacoustic pressure, $T_{jk} = \{[(p - p_0) - c_0^2(\rho - \rho_0)]\delta_{jk} + \rho u_j u_k - V_{jk}\}$ are the components of Lighthill stress tensor, V_{jk} are the viscous stress tensor components and p_0 the pressure field in the undisturbed medium.

Next, let us consider a moving permeable surface S enclosing both the noise sources and solid surfaces (*i.e.* the bodies surfaces) in a volume $\mathcal{V}$, and introduce the domain function $E(\mathbf{x}, t)$

$$E(\mathbf{x}, t) = \begin{cases} 1 & \text{if } \mathbf{x} \in \Re^3 \setminus \mathcal{V} \\ 0 & \text{if } \mathbf{x} \in \mathcal{V} \end{cases} \tag{A.3}$$

such that

$$\hat{p}'(\mathbf{x}, t) = E(\mathbf{x}, t)p'(\mathbf{x}, t) \tag{A.4}$$

Combining Eq. (A.2) with Eq. (A.4) the following infinite–space problem is obtained

$$\Box^2 \hat{p}' = E T_{jk,jk} - p'_{,j} E_{,j} - (p' E_j)_{,j} + \frac{1}{c_0^2}\left[\dot{p}' \dot{E} + (p' \dot{E})\right]^{\cdot} \tag{A.5}$$

111

Noting that

$$(ET_{jk})_{,jk} = ET_{jk,jk} + T_{jk,k}E_{,j} + (T_{jk}E_{,k})_{,j} \tag{A.6}$$

recalling that $p' = c_0^2(\rho - \rho_0)$ and using the Navier–Stokes equations and the continuity equation Eq. (A.5) becomes

$$\begin{aligned}
\square^2 \hat{p}' &= (ET_{jk})_{,jk} - (P_{jk}E_{,k})_{,j} + \dot{u}_j \rho E_{,j} + 2\dot{\rho}u_j E_{,j} + \\
&\quad - \rho u_j(u_k E_{,k})_{,j} + 2\dot{\rho}\dot{E} + \rho\ddot{E} - \rho_0\ddot{E}
\end{aligned} \tag{A.7}$$

where $P_{jk} = [(p - p_0)\delta_{jk} - V_{jk}]$ is the compressive stress tensor.

Note that the material derivative $\dfrac{DE}{Dt}$, following a fluid point, is given by

$$\frac{DE}{Dt} = \dot{E} + u_j E_{,j} \tag{A.8}$$

and therefore

$$(\frac{\dot{DE}}{Dt}) = \ddot{E} + \dot{u}_j E_{,j} + u_j \dot{E}_{,j} \tag{A.9}$$

Hence the following relation is obtained

$$2\dot{\rho}(\dot{E} + u_j E_{,j}) + \rho[\ddot{E} + \dot{u}_j E_{,j} - u_j(u_k E_{,k})_{,j}] = 2\frac{\partial}{\partial t}(\rho\frac{DE}{Dt}) - \rho\frac{D^2 E}{Dt^2} \tag{A.10}$$

through which Eq. (A.7) is recast into the following form

$$\square^2 \hat{p}' = (ET_{jk})_{,jk} - \rho_0\ddot{E} - (P_{jk}E_{,k})_{,j} + 2\frac{\partial}{\partial t}(\rho\frac{DE}{Dt}) - \rho\frac{D^2 E}{Dt^2} \tag{A.11}$$

that represents the Ffowcs Williams and Hawkings equation for permeable surfaces, governing the aeroacoustic field around a volume $\mathcal{V}$ moving in arbitrary motion with respect to the air space.

In order to re-write the FWHE in a more suitable mathematical form, let the boundary of S be mathematically defined by $f(\mathbf{x}, t) = 0$, with $f > 0$ outside S and such that $\nabla f = \mathbf{n}$, where $\mathbf{n}$ is the outward unit normal vector. Observing that $E(\mathbf{x}, t) = H[f(\mathbf{x}, t)]$, where H denotes the Heaviside function, the following relations hold

$$\nabla E = \frac{dH}{df}\nabla f = \delta(f)\,\mathbf{n} \tag{A.12}$$

$$\frac{DE}{Dt} = \frac{dH}{df}\frac{Df}{Dt} = \delta(f)\frac{Df}{Dt} \tag{A.13}$$

The material time derivative, following a fluid particle, is given by $\dfrac{Df}{Dt} = \dfrac{\partial f}{\partial t} + \mathbf{u}\cdot\nabla f$ where $\dfrac{\partial f}{\partial t}$ indicates the eulerian derivative; furthermore, following a material point on the surface S that moves with velocity $\mathbf{v}$, the time derivative of $f(\mathbf{x}, t)$ is equal to $\dfrac{Df}{Dt} = \dfrac{\partial f}{\partial t} + \mathbf{v}\cdot\nabla f = 0$. It results that following a fluid particle, the material derivative may be written as

$$\frac{Df}{Dt} = (\mathbf{u} - \mathbf{v})\cdot\mathbf{n} \tag{A.14}$$

Thus, accounting for Eqs. (A.12), (A.13) and (A.14), the material derivative $\dfrac{DE}{Dt}$ may be written as

$$\frac{DE}{Dt} = (\mathbf{u} - \mathbf{v}) \cdot \nabla E \tag{A.15}$$

from which the following equations may be obtained

$$-\rho \frac{D^2 E}{Dt^2} = -\frac{\partial}{\partial t}[\rho(u_j - v_j)E_{,j}] - [\rho u_j(u_k - v_k)E_{,k}]_{,j} \tag{A.16}$$

$$2\frac{\partial}{\partial t}(\rho \frac{DE}{Dt}) = 2\frac{\partial}{\partial t}[\rho(u_j - v_j)E_{,j}] \tag{A.17}$$

Combining Eqs. (A.16), (A.17) with Eq. (A.11), the FWHE transforms into

$$\begin{aligned}
\square^2 \hat{p}' &= (ET_{jk})_{,jk} - \rho_0 \ddot{E} - (P_{jk}E_{,k})_{,j} + \frac{\partial}{\partial t}[\rho(u_j - v_j)E_{,j}] + \\
&- [\rho u_j(u_k - v_k)E_{,k}]_{,j}
\end{aligned} \tag{A.18}$$

that, in terms of invariants becomes

$$\begin{aligned}
\square^2 \hat{p}' &= \nabla \cdot \nabla \cdot (E\mathbf{T}) - \frac{\partial}{\partial t}(\rho_0 \frac{\partial E}{\partial t}) - \nabla \cdot (\mathbf{P}\nabla E) + \frac{\partial}{\partial t}[\rho(\mathbf{u} - \mathbf{v}) \cdot \nabla E] + \\
&- \nabla \cdot [\rho \mathbf{u} \otimes (\mathbf{u} - \mathbf{v})\nabla E)] \quad \forall \mathbf{x} \in \Re^3
\end{aligned} \tag{A.19}$$

where $\mathbf{P} = [(p - p_0)\mathbf{I} + \mathbf{V}]$ and $\mathbf{T} = [\rho(\mathbf{u} \otimes \mathbf{u}) + (p - p_0)\mathbf{I} - c_0^2(\rho - \rho_0)\mathbf{I} + \mathbf{V}]$. Accounting for Eqs. (A.8), (A.12) and (A.15), it comes out that $\dot{E} = -\mathbf{v} \cdot \mathbf{n}\,\delta(f)$ and hence

$$-\rho_0 \ddot{E} = \frac{\partial}{\partial t}\left[-\rho_0 \frac{\partial E}{\partial t}\right] = \frac{\partial}{\partial t}[\rho_0\,\mathbf{v} \cdot \mathbf{n}\,\delta(f)] \tag{A.20}$$

Thus substituting Eq. (A.20) in Eq. (A.19) and accounting for Eq. (A.12) the following form of the FWHE is obtained

$$\begin{aligned}
\square^2 p' &= \frac{\overline{\partial}}{\partial t}[\rho_0\,\mathbf{v} \cdot \nabla f\,\delta(f)] + \frac{\overline{\partial}}{\partial t}[\rho\,(\mathbf{u} - \mathbf{v}) \cdot \nabla f\,\delta(f)] \\
&- \overline{\nabla} \cdot [\mathbf{P}\,\nabla f\,\delta(f)] - \overline{\nabla} \cdot [\rho\,\mathbf{u} \otimes (\mathbf{u} - \mathbf{v})\,\nabla f\,\delta(f)] \\
&+ \overline{\nabla} \cdot \left\{\overline{\nabla} \cdot [\mathbf{T}\,H(f)]\right\} \quad \forall \mathbf{x} \in \Re^3
\end{aligned} \tag{A.21}$$

where the bar over the derivative symbol denotes generalized differentiation. Equation (A.21) is written by using the typical notation for the FWHE.

If the surface S, moving with velocity $\mathbf{v}$, is impermeable, $\dfrac{DE}{Dt} = 0$ and Eq. (A.18) reduces to

$$\square^2 \hat{p}' = (ET_{jk})_{,jk} - \rho_0 \ddot{E} - (P_{jk}E_{,k})_{,j} \tag{A.22}$$

that in invariant form is

$$\begin{aligned}
\square^2 p' &= \frac{\overline{\partial}}{\partial t}[\rho_0\,\mathbf{v} \cdot \nabla f\,\delta(f)] - \overline{\nabla} \cdot [\mathbf{P}\,\nabla f\,\delta(f)] + \\
&+ \overline{\nabla} \cdot \left\{\overline{\nabla} \cdot [\mathbf{T}\,H(f)]\right\} \quad\quad\quad \forall \mathbf{x} \in \Re^3
\end{aligned} \tag{A.23}$$

A.2   The Differential Aerodynamic Problem

For an inviscid, non–conducting, shock–free, initially isentropic and initially irrotational (initially at rest and in thermodynamic equilibrium) flow, the velocity field may be described by means of a velocity potential function $\phi(\mathbf{x}, t)$ such that $\mathbf{u} = \nabla\phi$.

Similarly to the pressure disturbance, the velocity potential is governed by the following non–homogeneous wave equation [22]

$$-\Box^2\phi = \sigma \tag{A.24}$$

where $\sigma = \left[(c^2 - c_0^2)\nabla^2\phi + 2\mathbf{u}\cdot\dot{\mathbf{u}} + \mathbf{u}\cdot\dfrac{\nabla u^2}{2}\right]/c^2$ denotes all the non–linear terms.

The problem is completed by the boundary conditions. In the air frame of reference, the boundary condition at infinity is given by $\phi = 0$ (fluid at rest). Then, the surface $\mathcal{S}$ of the body is assumed to impermeable; hence $(\mathbf{u} - \mathbf{v})\cdot\mathbf{n} = 0$ yields $\dfrac{\partial\phi}{\partial n} = \mathbf{v}\cdot\mathbf{n}$, where $\mathbf{v}$ is the velocity of the points of the surface. In addition for lifting flows the issue of the wake has to be addressed. A detailed analysis is given in Ref. [22] and Ref. [81]. Here, it is sufficient to note that an inviscid isentropic initially–irrotational flow remains irrotational at all times except for those points that come in contact with the surface of the body, because Kelvin's theorem is not applicable in this case. These points form a surface on which the flow is not necessarily potential. This surface, called the wake, is a surface of discontinuity for the potential. From the application of the conservation of mass and linear momentum across a surface of discontinuity, it results that the fluid does not penetrate it (the wake is a material surface) and hence $\Delta(\dfrac{\partial\phi}{\partial n}) = 0$, and in addition the pressure is continuous across it. Furthermore, the Bernoulli theorem yields that the potential jump across the wake, $\Delta\phi$, remains constant following a wake point and equal to the value it had when it left the trailing edge. Following the same procedure used in the previous section to extend to the whole space the potential governing equation, here the domain function $E(\mathbf{x}, t)$ defined as

$$E(\mathbf{x}, t) = \begin{cases} 1 & \text{if } \mathbf{x} \in \Re^3 \setminus \mathcal{V} \\ 0 & \text{if } \mathbf{x} \in \mathcal{V} \end{cases} \tag{A.25}$$

is introduced, and the extended function $\hat{\phi}(\mathbf{x}, t) = E(\mathbf{x}, t)\,\phi(\mathbf{x}, t)$ is defined. Then using the mathematical relations

$$\nabla^2\left[E\phi\right] = E\nabla^2\phi + \nabla E\cdot\nabla\phi + \nabla\cdot(\phi\nabla E) \tag{A.26}$$

and

$$\frac{\partial^2\hat{\phi}}{\partial t^2} = (\phi\dot{E})^{\cdot} + \ddot{\phi}E + \dot{\phi}\dot{E} \tag{A.27}$$

the equation governing the velocity potential is recast in the following form

$$-\Box^2\hat{\phi} \;\; = \;\; E\,\sigma + \nabla E\cdot\nabla\phi + \nabla\cdot(\phi\nabla E) - \frac{1}{c_0^2}\left[\dot{\phi}\dot{E} + (\phi\dot{E})^{\cdot}\right] \tag{A.28}$$

that is valid $\forall\mathbf{x} \in \Re^3$.

Observing that $E(\mathbf{x}, t) = H[f(\mathbf{x}, t)]$ and recalling Eq. (A.12), Eq. (A.28) may be written as

$$
\begin{aligned}
-\Box^2\hat{\phi} \;\; = \;\; & \sigma\,H(f) + \nabla\phi\cdot\mathbf{n}\,\delta(f) + \nabla\cdot[\phi\,\mathbf{n}\,\delta(f)] + \\
& - \frac{1}{c_0^2}\left\{\dot{\phi}\dot{H}(f) + \left[\phi\dot{H}(f)\right]^{\cdot}\right\} \quad \forall\mathbf{x} \in \Re^3
\end{aligned} \tag{A.29}
$$

Accounting that $\dot{H}(f) = -\mathbf{v} \cdot \nabla H = -\mathbf{v} \cdot \mathbf{n}\,\delta(f)$ one obtains

$$
\begin{aligned}
-\Box^2 \hat{\phi} \;=\;& \sigma\, H(f) + \nabla\phi \cdot \mathbf{n}\,\delta(f) + \nabla \cdot [\phi\,\mathbf{n}\,\delta(f)] + \\
& -\; \frac{1}{c_0^2}\Big\{ -\dot{\phi}\,\mathbf{v}\cdot\mathbf{n}\,\delta(f) + [-\phi\,\mathbf{v}\cdot\mathbf{n}\,\delta(f)]^{\cdot} \Big\} \quad \forall \mathbf{x} \in \Re^3 \qquad \text{(A.30)}
\end{aligned}
$$

A.3 A General Form of Integral Solution

Dealing with compressible flows, sections A.1 and A.2 show that the structure of the differential equation governing the propagation of the pressure disturbance or the propagation of the velocity potential in the flow–field when a contour surface $\mathcal{S}$ moves respect to the air space (SRA), is described by an inhomogeneous wave equation forced by source terms distributed both over $\mathcal{S}$ in addition to those present in the fluid.

Here, in order to derive an integral solution that is applicable to both aeroacoustic and aerodynamic problems, the following general inhomogeneous wave equation is considered

$$
\begin{aligned}
-\Box^2 \hat{u} \;=\;& \chi + \mathbf{z} \cdot \nabla E + \nabla \cdot (\mathbf{Z}\nabla E) + \frac{\partial}{\partial t}\Big(k_2 \frac{\partial E}{\partial t}\Big) + k_1 \frac{\partial E}{\partial t} + \\
& -\; \frac{\partial}{\partial t}(\mathbf{z}_1 \cdot \nabla E) + \nabla \cdot (\mathbf{Z}_1 \nabla E) \qquad\qquad\qquad\qquad \text{(A.31)}
\end{aligned}
$$

from which Eqs. (A.19) and (A.28) may be derived as particular cases. In Eq. (A.31), $\hat{u}$ represents the generic variable to be propagated, whereas the forcing terms at the right–hand–side are expressed through generic vectorial and tensorial fields. In deriving a boundary integral solution for the above equation, for the sake of simplicity, the surface $\mathcal{S}$ is assumed to move in rigid–body motion so that E is time independent in the frame fixed to the body. In addition boundary conditions at infinity, as well as the initial conditions, are homogeneous for all the perturbative quantities involved.

The application of the Green function method that combines Eq. (A.31) with the fundamental wave equation problem

$$
\begin{aligned}
-\Box^2 G &= \delta(\mathbf{x}-\mathbf{x}^*, t - t^*) \\
G &= 0 \qquad \forall \mathbf{x} \in \infty \\
G &= 0 \qquad t = \infty \\
\frac{\partial G}{\partial t} &= 0 \qquad t = \infty \qquad\qquad\qquad \text{(A.32)}
\end{aligned}
$$

yields the following integral solution of the Eq. (A.31) in the SRA

$$
\begin{aligned}
E(\mathbf{x}^*, t^*)u(\mathbf{x}^*, t^*) \;=\;& \int_0^\infty \int_{\Re^3} G\,\chi\,\mathrm{d}V\,dt + \int_0^\infty \int_{\Re^3} \nabla \cdot (\mathbf{Z}\nabla E)\,G\,\mathrm{d}V\,dt + \\
& +\; \int_0^\infty \int_{\Re^3} \frac{\partial}{\partial t}\Big(k_2 \frac{\partial E}{\partial t}\Big) G\,\mathrm{d}V\,dt + \\
& -\; \int_0^\infty \int_{\Re^3} \frac{\partial}{\partial t}(\mathbf{z}_1 \cdot \nabla E)\,G\,\mathrm{d}V\,dt + \\
& +\; \int_0^\infty \int_{\Re^3} \nabla \cdot (\mathbf{Z}_1 \nabla E)\,G\,\mathrm{d}V\,dt + \\
& +\; \int_0^\infty \int_{\Re^3} k_1 \frac{\partial E}{\partial t}\,\mathrm{d}V\,dt + \\
& +\; \int_0^\infty \int_{\Re^3} \mathbf{z} \cdot \nabla E\,G\,\mathrm{d}V\,dt \qquad\qquad \text{(A.33)}
\end{aligned}
$$

where

$$G(\mathbf{x}^* - \mathbf{x}, t - t^*) = \frac{-1}{4\pi r}\delta(t - t^* + \frac{r}{c_0}) \qquad (A.34)$$

with $r = |\mathbf{x}^* - \mathbf{x}|$, for $\mathbf{x}$ and $\mathbf{x}^*$ representing the source and the observer positions in the air frame of reference, respectively, while t^* represents the time of observation and t the time of emission of the signal. At this stage it is worthy noting that two Dirac delta functions appear in the integrals in Eq. (A.33), one arising from the derivatives of E, and the other from the Eq. (A.34).

As mentioned above, E is time–independent in the body space; hence it is convenient to transform the air–space solution (A.33) into one expressed in the body space. In order to distinguish the air–space and the body–space, in the following we use $(\mathbf{x}, t)$ to indicate an event in the air space and $(\mathbf{y}, \bar{t})$ to indicate an event in the body space. To accomplish this transformation, the following relation relating the two spaces is introduced

$$\mathbf{x}(\mathbf{y}, \bar{t}) = \mathbf{x}_0(\bar{t}) + \mathbf{R}(\bar{t})\mathbf{y} \qquad (A.35)$$

where $\mathbf{x}_0$ denotes the air–space image of the body point $\mathbf{y} = 0$ and $\mathbf{R}$ is an orthogonal tensor representing a rigid–body rotation around $\mathbf{x}_0$. The Jacobian of the rigid–body transformation is equal to one. In addition, by defining $\mathbf{v}_y = \mathbf{R}^T\frac{\partial\mathbf{x}}{\partial\bar{t}}$ as the body–space vector of the velocity of $\mathbf{y}$ relative to the air space, the time derivatives between the two spaces are related by[1]

$$\frac{\partial}{\partial t} = \frac{\partial}{\partial\bar{t}} - \mathbf{v}_y \cdot \nabla_y \qquad (A.36)$$

where ∇_y denotes the body–space gradient operator given by $\nabla_y = \mathbf{R}^T\nabla$.

For the next mathematical manipulations it is useful to recall that for any function $h(\bar{t})$ and $g(\bar{t})$,

$$\int_0^\infty h(\bar{t})\delta[g(\bar{t})]d\bar{t} = \sum_k \int_0^\infty \frac{h(\bar{t})}{\dot{g}(\bar{t})}\delta(\bar{t} - \bar{t}_k)d\bar{t} \qquad (A.37)$$

where $\bar{t}_k$ are the roots of $g(\bar{t}) = 0$. Making reference to the body–space, it results that $g = (\bar{t} - \bar{t}^* + \frac{|\mathbf{r}_y|}{c_0})$ with $\mathbf{r}_y = \mathbf{R}^T[\mathbf{x}(\mathbf{y}^*, \bar{t}^*) - \mathbf{x}(\mathbf{y}, \bar{t})]$ and thus $\dot{g} = 1 - \mathbf{r}_y \cdot \frac{\mathbf{v}_y}{c_0|\mathbf{r}_y|}$. Throughout the thesis, we limit ourselves to the case in which the local Mach number is less than one; this implies that the equation $g(\bar{t}) = 0$ has only a root, denoted with $(\bar{t}^* - \vartheta)$. By combining the above relations with Eq. (A.33) and performing an integration by parts (with the condition $u = 0$ at infinity) on the right side of Eq. (A.33), one obtains the following integral solution in the body–space

$$
\begin{aligned}
E(\mathbf{y}^*)u(\mathbf{y}^*, t^*) =& \int_0^\infty \int_{\Re^3} \check{G}\,\chi\,dV d\bar{t} + \\
& -\int_0^\infty \int_{\Re^3} (\mathbf{Z}_y\nabla_y E)\,\nabla_y\check{G}dV d\bar{t} + \\
& -\int_0^\infty \int_{\Re^3} k_2\frac{d_B E}{d\bar{t}}(\frac{d_B\check{G}}{d\bar{t}})dV d\bar{t} + \\
& +\int_0^\infty \int_{\Re^3} (\mathbf{z}_{1y} \cdot \nabla_y E)\,\frac{d_B\check{G}}{d\bar{t}}dV d\bar{t} + \\
& -\int_0^\infty \int_{\Re^3} (\mathbf{Z}_{1y}\nabla_y E)\,\check{G}dV d\bar{t} + \\
& +\int_0^\infty \int_{\Re^3} k_1\frac{d_B E}{d\bar{t}}\,\check{G}dV d\bar{t} + \\
& +\int_0^\infty \int_{\Re^3} (\mathbf{z}_y \cdot \nabla_y E)\,\check{G}dV d\bar{t} \qquad (A.38)
\end{aligned}
$$

---

[1]For the sake of clarity, in the following, the pedix y indicates tensorial and vectorial quantities whose images are referred to the body–space.

where the invariants and mathematical operators with the suffix y have their image in the body–space; in particular, $\mathbf{z}_y = \mathbf{R}^T \mathbf{z}$ and $\mathbf{Z}_y = \mathbf{R}^T \mathbf{Z} \mathbf{R}$.

The eulerian time derivative $\dfrac{d_B}{d\bar{t}}$ is expressed by

$$\frac{d_B}{d\bar{t}} = \frac{\partial}{\partial \bar{t}} - \mathbf{v}_y \cdot \nabla_y \tag{A.39}$$

where $\dfrac{\partial}{\partial \bar{t}}$ denotes the material derivative (following a body point); accounting for (A.37), it results that $\check{G}(\mathbf{y} - \mathbf{y}^*, \bar{t} - \bar{t}^*) = \hat{G}\,\delta(\bar{t} - \bar{t}^* + \vartheta)$ with

$$\hat{G} = \left[\left| 1 - \frac{\mathbf{r}_y \cdot \mathbf{v}_y}{c_0 |\mathbf{r}_y|} \right|^{-1} \frac{-1}{4\pi |\mathbf{r}_y|} \right]_\vartheta \tag{A.40}$$

In order to transform the integral solution (A.38) into a more suitable expression, let us note that $\nabla_y E = \delta(f)\mathbf{n}_y |\nabla_y f|$; hence, for any body–space vector $\mathbf{a}(\mathbf{y}, t)$ we have

$$\int_0^\infty \int_{\Re^3} \mathbf{a} \cdot \nabla_y E\,\delta(\bar{t} - \bar{t}^* + \vartheta)\,\mathrm{d}V d\bar{t} = \int_S [\mathbf{a} \cdot \mathbf{n}_y]_\vartheta\,\mathrm{d}S \tag{A.41}$$

where $[...]_\vartheta = [...]_{\bar{t}^* - \vartheta}$ denotes that the kernel of the integral is evaluated at the emission time. Moreover, $\dfrac{\partial E}{\partial \bar{t}} = 0$ implies $\dfrac{d_B E}{d\bar{t}} = -\mathbf{v}_y \cdot \nabla_y E$; hence, Eq. (A.41) yields, for any $f(\mathbf{y}, \bar{t})$

$$\int_0^\infty \int_{\Re^3} f \frac{d_B E}{d\bar{t}}\,\delta(\bar{t} - \bar{t}^* + \vartheta)\,\mathrm{d}V\,d\bar{t} = -\int_S [f\,\mathbf{v}_y \cdot \mathbf{n}_y]_\vartheta\,\mathrm{d}S \tag{A.42}$$

Next, using the relation $\nabla_y \check{G} = \nabla_y \hat{G}\,\delta + \hat{G}\,\nabla_y \delta$ and noting that $\vartheta = \vartheta(\mathbf{y}, \mathbf{y}^*, \bar{t}^*)$ we have that

$$\nabla_y \check{G} = \nabla_y \hat{G}\,\delta(\bar{t} - \bar{t}^* + \vartheta) + \hat{G}\,\dot{\delta}(\bar{t} - \bar{t}^* + \vartheta)\nabla_y \vartheta \tag{A.43}$$

Furthermore, $\dfrac{d_B \check{G}}{d\bar{t}} = \hat{G}\,\dot{\delta} - \mathbf{v}_y \cdot \nabla_y \check{G}$ and hence recalling that $\displaystyle\int_{-\infty}^\infty f\dot{\delta}d\bar{t} = -\dot{f}(0)$ we obtain the following expressions for the integrals appearing in Eq. (A.38)

$$\begin{aligned}
I_1 &= \int_0^\infty \int_{\Re^3} (\mathbf{Z}_y \nabla_y E)\,\nabla_y \check{G}\mathrm{d}V d\bar{t} = \\
&= \int_S \left[(\mathbf{Z}_y \mathbf{n}_y) \cdot \nabla_y \hat{G} - (\dot{\mathbf{Z}}_y \mathbf{n}_y) \cdot \nabla_y \vartheta\,\hat{G} \right]_\vartheta\,\mathrm{d}S
\end{aligned}$$

$$\begin{aligned}
I_2 &= \int_0^\infty \int_{\Re^3} k_2 \frac{d_B E}{d\bar{t}} \left(\frac{d_B \check{G}}{d\bar{t}} \right) \mathrm{d}V d\bar{t} = \\
&= \int_S \left\{ k_2\,\mathbf{v}_y \cdot \mathbf{n}_y \mathbf{v}_y \cdot \nabla_y \hat{G} + [k_2\,\mathbf{v}_y \cdot \mathbf{n}_y (1 - \mathbf{v}_y \cdot \nabla_y \vartheta)]\dot{\,}\,\hat{G} \right\}_\vartheta\,\mathrm{d}S
\end{aligned}$$

$$\begin{aligned}
I_3 &= \int_0^\infty \int_{\Re^3} (\mathbf{z}_{1y} \cdot \nabla_y E) \frac{d_B \check{G}}{d\bar{t}}\,\mathrm{d}V d\bar{t} = \\
&= -\int_S \left\{ [\mathbf{z}_{1y} \cdot \mathbf{n}_y (1 - \mathbf{v}_y \cdot \nabla_y \vartheta)]\dot{\,}\,\hat{G} + \mathbf{z}_{1y} \cdot \mathbf{n}_y \mathbf{v}_y \cdot \nabla_y \hat{G} \right\}_\vartheta\,\mathrm{d}S
\end{aligned}$$

$$
\begin{aligned}
I_4 &= \int_0^\infty \int_{\Re^3} \left(\mathbf{Z}_{1y}\nabla_y E\right)\nabla_y \check{G}\,\mathrm{d}V\,d\bar{t} = \\
&= \int_S \left[\left(\mathbf{Z}_{1y}\mathbf{n}_y\right)\cdot\nabla_y\hat{G} - \left(\dot{\mathbf{Z}}_{1y}\mathbf{n}_y\right)\cdot\nabla_y\vartheta\,\hat{G}\right]_\vartheta\,\mathrm{d}S
\end{aligned}
$$

$$
I_5 = \int_0^\infty \int_{\Re^3} k_1 \frac{d_B E}{d\bar{t}}\check{G}\,\mathrm{d}V\,d\bar{t} = -\int_S \hat{G}\left[k_1\,\mathbf{v}_y\cdot\mathbf{n}_y\right]_\vartheta\,\mathrm{d}S
$$

$$
I_6 = \int_0^\infty \int_{\Re^3} \left(\mathbf{z}_y\cdot\nabla_y E\right)\check{G}\,\mathrm{d}V\,d\bar{t} = \int_S \left[\mathbf{z}_y\cdot\mathbf{n}_y\hat{G}\right]_\vartheta\,\mathrm{d}S
$$

where all the time derivatives are performed in the body–space. Finally, combining the above equations, one obtains the desired boundary integral representation of the solution of Eq. (A.31) for the field around a volume $\Re^3 \setminus \mathcal{V}$ moving in arbitrary rigid motion

$$
E(\mathbf{y}^*)u(\mathbf{y}^*,t^*) = \int_0^\infty \int_{\Re^3} \check{G}\,\chi\,\mathrm{d}V\,d\bar{t} - I_1 - I_2 + I_3 - I_4 + I_5 + I_6 \tag{A.44}
$$

Application to Aeroacoustics

For aeroacoustics applications the variable to be propagated is the pressure disturbance p' governed by Eq. (A.21) which is represented by Eq. (A.31) for $\hat{u} = \hat{p}'$, $\mathbf{Z} = \mathbf{P}$, $\chi = -\nabla \cdot \nabla \cdot (E\mathbf{T})$, $k_2 = \rho_0$, $\mathbf{z}_1 = \rho(\mathbf{u} - \mathbf{v})$, $\mathbf{Z}_1 = \rho\mathbf{u} \otimes (\mathbf{u} - \mathbf{v})$, $k_1 = 0$ and $\mathbf{z} = 0$. Thus $I_5 = I_6 = 0$ and observing that $(\mathbf{a} \otimes \mathbf{b})\mathbf{c} = (\mathbf{b} \cdot \mathbf{c})\mathbf{a}$ and for $\mathbf{u}^- = (\mathbf{u} - \mathbf{v})$ and $\mathbf{u}^+ = (\mathbf{u} + \mathbf{v})$ the integral solution for the permeable FWHE, written in the space rigidly moving with the body, reads

$$
\begin{aligned}
E(\mathbf{y}^*)p'(\mathbf{y}^*, t^*) &= \int_0^\infty \int_{\Re^3} \check{G}\, \chi \,\mathrm{d}V\, d\bar{t} \\
&\quad - \int_S \left[(\mathbf{P}_y \mathbf{n}_y) \cdot \nabla_y \hat{G} - (\dot{\mathbf{P}}_y \mathbf{n}_y) \cdot \nabla_y \vartheta\, \hat{G} \right]_\vartheta \,\mathrm{d}S \\
&\quad - \rho_0 \int_S \left\{ \mathbf{v}_y \cdot \mathbf{n}_y \mathbf{v}_y \cdot \nabla_y \hat{G} + [\mathbf{v}_y \cdot \mathbf{n}_y (1 - \mathbf{v}_y \cdot \nabla_y \vartheta)]\, \hat{G} \right\}_\vartheta \,\mathrm{d}S \\
&\quad - \int_S \left\{ \rho\mathbf{u}^- \cdot \mathbf{n}_y\, \mathbf{u}^+ \cdot \nabla_y \hat{G} \right\}_\vartheta \,\mathrm{d}S \\
&\quad + \int_S \left\{ [\rho\mathbf{u}^- \cdot \mathbf{n}_y (1 - \mathbf{u}^+ \cdot \nabla_y \vartheta)]\dot{}\, \hat{G} \right\}_\vartheta \,\mathrm{d}S
\end{aligned}
\tag{A.45}
$$

In appendix A.4 it is shown that the above integral solution is fully equivalent to the Farassat formulation 1A.

Application to Potential Aerodynamics

Concerning the aerodynamic problem, the velocity potential is governed by Eq. (A.28) which is represented by Eq. (A.31) for $\hat{u} = \hat{\phi}$, $\chi = E\sigma$, $\mathbf{z} = \nabla\phi$, $\mathbf{Z} = \mathbf{I}\phi$, $k_1 = -\dot{\phi}/c^2$, $k_2 = -\phi/c^2$, $\mathbf{z}_1 = 0$ and $\mathbf{Z}_1 = 0$.

In this case it results that $I_3 = I_4 = 0$ and the following boundary integral representation in the body space is obtained for the velocity potential

$$
\begin{aligned}
E(\mathbf{y}^*, t^*)\phi(\mathbf{y}^*, t^*) &= \int_V \hat{G}\, [\sigma]_\vartheta \,\mathrm{d}V + \int_S \left[\frac{\partial\phi}{\partial\tilde{n}}\hat{G} - \phi\frac{\partial\hat{G}}{\partial\tilde{n}} \right]_\vartheta \,\mathrm{d}S + \\
&\quad + \int_S \left[\hat{G}\frac{\partial\phi}{\partial\bar{t}} \left(\frac{\partial\vartheta}{\partial\tilde{n}} + 2\frac{\mathbf{v}_y \cdot \mathbf{n}_y}{c_0^2} \right) \right]_\vartheta \\
&\quad + \frac{1}{c_0^2} \int_S \left[\phi\, \hat{G}\frac{\partial}{\partial\bar{t}}[\mathbf{v}_y \cdot \mathbf{n}_y(1 - \mathbf{v}_y \cdot \nabla_y\vartheta)] \right]_\vartheta \,\mathrm{d}S
\end{aligned}
\tag{A.46}
$$

where $\dfrac{\partial}{\partial\tilde{n}} = \dfrac{\partial}{\partial n} - \dfrac{1}{c_0^2}(\mathbf{v}_y \cdot \mathbf{n}_y)(\mathbf{v}_y \cdot \nabla_y)$.

A.4   Equivalence with Farassat 1A Formulation for Aeroacoustic Applications

Equation (A.45) is the integral solution of the permeable Ffowcs Williams and Hawkings equation, written in the body space of reference; in this section, the equivalence with the Farassat 1A formulation is demonstrated for impermeable body surfaces. According to Farassat 1A formulation the thickness noise and the loading noise contributions are, respectively, given by

$$
\begin{aligned}
4\pi p_T{}'(\mathbf{x}^*, t^*) &= \int_S \left[\frac{\rho_0(\dot{v}_n + v_{\dot{n}})}{r|1 - M_r|^2} \right]_\vartheta \, \mathrm{d}S(\mathbf{y}) \\
&\quad + \int_S \left[\frac{\rho_0 v_n (r\dot{M}_r + c_0 M_r - c_0 M^2)}{r^2 |1 - M_r|^3} \right]_\vartheta \, \mathrm{d}S(\mathbf{y})
\end{aligned}
\tag{A.47}
$$

$$
\begin{aligned}
4\pi p_L{}'(\mathbf{x}^*, t^*) &= \frac{1}{c_0} \int_{S=0} \left[\frac{\dot{\hat{p}}\, cos\theta + \hat{p}\, \dot{n}_j \hat{r}_j}{r|1 - M_r|^2} \right]_\vartheta \, \mathrm{d}S(\mathbf{y}) \\
&\quad + \int_S \left[\frac{\hat{p}\, cos\theta - \hat{p}\, M_n}{r^2 |1 - M_r|^2} \right]_\vartheta \, \mathrm{d}S(\mathbf{y}) \\
&\quad + \frac{1}{c_0} \int_S \left[\frac{\hat{p}\, cos\theta\, (r\dot{M}_r + c_0 M_r - c_0 M^2)}{r^2 |1 - M_r|^3} \right]_\vartheta \, \mathrm{d}S(\mathbf{y})
\end{aligned}
\tag{A.48}
$$

where $r = |\mathbf{x}^* - \mathbf{x}|$ is the magnitude of the vector $\mathbf{r}$ representing the distance source–observer, M_r represents the Mach number, at the $\mathbf{x}$ source point, computed along the source–observer direction identified by $\hat{\mathbf{r}}$, $v_n = \mathbf{v} \cdot \mathbf{n}$, $\dot{v}_n = \dot{\mathbf{v}} \cdot \mathbf{n}$, $v_{\dot{n}} = \mathbf{v} \cdot \dot{\mathbf{n}}$, $\dot{M}_r = \dot{\mathbf{M}} \cdot \hat{\mathbf{r}}$, $M_n = \mathbf{M} \cdot \mathbf{n}$ and $cos\theta = \mathbf{n} \cdot \hat{\mathbf{r}}$. The time derivatives $(\dot{\ })$ are performed in the air-space.

   In order to show the equivalence between the above formulation and that proposed by Morino and Gennaretti, the first step is to express $\nabla_y \hat{G}$ and $\nabla_y \vartheta$. To this purpose, let us first note that the time derivative of a retarded function $f_\vartheta = f(\mathbf{y}, \bar{t}^* - \vartheta(\mathbf{y}, \mathbf{y}^*, t^*))$ may be expressed as

$$
\frac{\partial f_\vartheta}{\partial \mathbf{y}} = \frac{\partial f}{\partial \mathbf{y}}\Big|_{ret} + \frac{\partial f}{\partial \bar{t}}\Big|_\mathbf{y} \frac{\partial \bar{t}}{\partial \vartheta}\Big|_{ret} \frac{\partial \vartheta}{\partial \mathbf{y}}
\tag{A.49}
$$

where $\bar{t} = \bar{t}^* - \vartheta$. By exploiting the above relation and observing that the time delay satisfies the following equation

$$
c_0 \vartheta = |\mathbf{x}^*(\mathbf{y}^*, \bar{t}^*) - \mathbf{x}(\mathbf{y}, \bar{t}^* - \vartheta)|
\tag{A.50}
$$

$\nabla_y \vartheta$ may be written as

$$
\nabla_y \vartheta = -\frac{\hat{\mathbf{r}}_y}{c_0 (1 - M_r)}\Big|_\vartheta
\tag{A.51}
$$

where $\hat{\mathbf{r}}_y$ is the unit vector in the direction observer–source. Next, let us consider the retarded Green function

$$
\hat{G} = \left[-\frac{1}{4\pi|\mathbf{r}_y|} \left(\frac{1}{1 - M_r} \right) \right]_\vartheta
\tag{A.52}
$$

where $(M_r = \dfrac{\mathbf{v}_y}{c_0} \cdot \hat{\mathbf{r}}_y)$ Thus, from (A.49) and (A.52) and observing that, for any vector $\mathbf{c}$, $\mathbf{d}$, one has $\nabla(\mathbf{c} \cdot \mathbf{d}) = [\nabla \mathbf{c}]^T \mathbf{d} + [\nabla \mathbf{d}]^T \mathbf{c}$, it follows that

$$
\nabla_y \hat{G}_\vartheta = \nabla_y \hat{G}\Big|_\vartheta - \dot{\hat{G}}\Big|_\vartheta \nabla_y \vartheta
\tag{A.53}
$$

120

with

$$\nabla_y \hat{G} = \frac{-1}{4\pi} \nabla_y \left(\frac{1}{|\mathbf{r}_y|} \right) \left(\frac{1}{1 - M_r} \right) - \frac{1}{4\pi |\mathbf{r}_y|} \nabla_y \left(\frac{1}{1 - M_r} \right) \tag{A.54}$$

and

$$\nabla_y \frac{1}{|\mathbf{r}_y|} = \frac{\hat{\mathbf{r}}_y}{|\mathbf{r}_y|^2}$$

$$\nabla_y \left(\frac{1}{1 - M_r} \right) = -\frac{1}{c_0 (1 - M_r)^2} \nabla_y (\mathbf{v}_y \cdot \hat{\mathbf{r}}_y) = \frac{[\nabla_y \mathbf{v}_y]^T \hat{\mathbf{r}}_y + [\nabla_y \hat{\mathbf{r}}_y]^T \mathbf{v}_y}{c_0 (1 - M_r)^2}$$

The tensor quantities $\nabla_y \mathbf{v}_y$ and $\nabla_y \hat{\mathbf{r}}_y$ come from the relations describing the body motion. To this aim, by denoting with $\boldsymbol{\omega}$ the body angular velocity, we introduce an skew tensor $\boldsymbol{\Omega}$ such that, for any vector $\mathbf{c}$, $\boldsymbol{\omega} \wedge \mathbf{c} = \boldsymbol{\Omega} \mathbf{c}$.

Thus, the air–space derivative of $\mathbf{R}$ is $\dot{\mathbf{R}} = \mathbf{R}\boldsymbol{\Omega}_y = \boldsymbol{\Omega}\mathbf{R}$. By recalling that the air–space image of $\mathbf{y}$ is

$$\mathbf{x}(\mathbf{y}, \bar{t}) = \mathbf{x}_0(\bar{t}) + \mathbf{R}(\bar{t})\mathbf{y} \tag{A.55}$$

the body–space image of the velocity of $\mathbf{y}$ (relative to the air–space) results

$$\mathbf{v}_y = \mathbf{R}^T \mathbf{v}_0 + \mathbf{R}^T \dot{\mathbf{R}} \mathbf{y} = \mathbf{R}^T \mathbf{v}_0 + \boldsymbol{\Omega}_y \mathbf{y} \tag{A.56}$$

Thus, being

$$\mathbf{r}_y = \mathbf{R}^T [\mathbf{x}(\mathbf{y}^*, \bar{t}^*) - \mathbf{x}(\mathbf{y}, \bar{t})] \tag{A.57}$$

one obtains

$$\nabla_y \mathbf{v}_y = \boldsymbol{\Omega}_y$$

and

$$\nabla_y \hat{\mathbf{r}}_y = -\frac{\mathbf{I}}{|\mathbf{r}_y|} + \frac{\hat{\mathbf{r}}_y \otimes \hat{\mathbf{r}}_y}{|\mathbf{r}_y|}$$

The time derivative of $\hat{G}$ may be written as

$$\dot{\hat{G}} = -\frac{\dot{M}_r}{4\pi |\mathbf{r}_y| (1 - M_r)^2} + \frac{(|\mathbf{r}_y|)^{\cdot}}{4\pi (1 - M_r) |\mathbf{r}_y|^2} \tag{A.58}$$

The rate of change of the local velocity, as viewed by the body–space is

$$\mathbf{R}^T \dot{\mathbf{v}} = \dot{\mathbf{v}}_y + \boldsymbol{\Omega}_y \mathbf{v}_y \tag{A.59}$$

in which $\dot{\mathbf{v}}$ represents the air–space image of the time derivative of the velocity of $\mathbf{y}$. Furthermore, observing that $\dot{\mathbf{r}}_y = -\boldsymbol{\Omega}\mathbf{r}_y - \mathbf{v}_y$, the rate of change of the distance $|\mathbf{r}_y|$ as viewed by the body–space is coincident with the component of the local velocity along the direction observer–source, that is

$$(|\mathbf{r}_y|)^{\cdot} = \dot{\mathbf{r}}_y \cdot \hat{\mathbf{r}}_y = -v_r \tag{A.60}$$

Basing on the above relations, some mathematical manipulations show the excepted equivalence between formulations.

Thickness Noise Term

By combining the following expressions

$$\left[\mathbf{v}_y \cdot \mathbf{n}_y (1 - \mathbf{v}_y \cdot \nabla_y \vartheta)\right]^{\cdot} \hat{G} \;=\; -\frac{\dot{v_n}}{4\pi |\mathbf{r}_y|\,(1 - M_r)} - \frac{\dot{v_n}\mathbf{v}_y \cdot \hat{\mathbf{r}}_y}{4\pi c_0 |\mathbf{r}_y|\,(1 - M_r)^2}$$

$$+\; v_n \frac{\mathbf{\Omega}_y \mathbf{v}_y \cdot \hat{\mathbf{r}}_y}{4\pi c_0 |\mathbf{r}_y|\,(1 - M_r)^2}$$

$$-\; v_n \frac{\mathbf{R}^T \dot{\mathbf{v}} \cdot \hat{\mathbf{r}}_y}{4\pi c_0 |\mathbf{r}_y|\,(1 - M_r)^2} \tag{A.61}$$

$$\mathbf{v}_y \cdot \mathbf{n}_y \, \mathbf{v}_y \cdot \nabla_y G \;=\; \frac{v_n}{4\pi} \left[-\frac{\hat{\mathbf{r}}_y \cdot \mathbf{v}_y}{|\mathbf{r}_y|^2\,(1 - M_r)} - \frac{\mathbf{\Omega}_y \hat{\mathbf{r}}_y \cdot \mathbf{v}_y}{c_0 |\mathbf{r}_y|\,(1 - M_r)^2} \right]$$

$$+\; \frac{v_n}{4\pi} \left[\frac{\mathbf{v}_y - v_r \hat{\mathbf{r}}_y}{c_0 |\mathbf{r}_y|^2\,(1 - M_r)^2} \cdot \mathbf{v}_y - \frac{\frac{v_r}{|\mathbf{r}_y|}\hat{\mathbf{r}}_y \cdot \mathbf{v}_y}{c_0 |\mathbf{r}_y|\,(1 - M_r)^2} \right]$$

$$-\; \frac{v_n}{4\pi} \left[\frac{\mathbf{R}^T \dot{\mathbf{v}} \cdot \hat{\mathbf{r}}_y - \frac{v^2 - v_r^2}{|\mathbf{r}_y|}\hat{\mathbf{r}}_y \cdot \mathbf{v}_y}{c_0^2 |\mathbf{r}_y|\,(1 - M_r)^3} \right] \tag{A.62}$$

in which $\dot{\mathbf{v}}$ is the air–space image of the time derivative of the air–space velocity of $\mathbf{y}$, $\dot{v_n} = \dot{\mathbf{v}}_y \cdot \mathbf{n}_y$, $v_r = \mathbf{v}_y \cdot \hat{\mathbf{r}}_y$, $v^2 = \mathbf{v} \cdot \mathbf{v}$ and by noting that $(\mathbf{\Omega}_y \mathbf{v}_y \cdot \hat{\mathbf{r}}_y) = -\mathbf{\Omega}_y \hat{\mathbf{r}}_y \cdot \mathbf{v}_y$, one obtains the following expression for the kernel of the thickness noise integral

$$-\rho_0 \left\{ \mathbf{v}_y \cdot \mathbf{n}_y \, \mathbf{v}_y \cdot \nabla_y G + \left[\mathbf{v}_y \cdot \mathbf{n}_y (1 - \mathbf{v}_y \cdot \nabla_y \vartheta)\right]^{\cdot} \hat{G} \right\} =$$

$$\rho_0 \left\{ -v_n \frac{c_0\,M^2 - c_0\,M_r - \dot{\mathbf{M}} \cdot \mathbf{r}}{4\pi |\mathbf{r}_y|^2\,(1 - M_r)^3} + \frac{\dot{v_n}}{4\pi |\mathbf{r}_y|\,(1 - M_r)^2} \right\} \tag{A.63}$$

where $\dot{\mathbf{M}}$ denotes the air–space derivative of the local Mach number whereas $\mathbf{r}$ indicates the air–space image of the distance between the observer position and the source point. Let us note that $[\mathbf{v} \cdot \mathbf{n}]^{\cdot} = [\mathbf{v}_y \cdot \mathbf{n}_y]^{\cdot} = \dot{\mathbf{v}} \cdot \mathbf{n} + \mathbf{v} \cdot \dot{\mathbf{n}} = \dot{\mathbf{v}}_y \cdot \mathbf{n}_y$ because, in the body–space, $\dot{\mathbf{n}}_y = 0$; hence, the equivalence with the kernel of the Eq. (A.47) is shown.

Loading Noise Term

In order to show the equivalence between $-\left[(\mathbf{P}_y \mathbf{n}_y) \cdot \nabla_y \hat{G} - (\dot{\mathbf{P}}_y \mathbf{n}_y) \cdot \nabla_y \vartheta \, \hat{G}\right]$ and the kernel of the Eq. (A.48), let us observe that (see equations above)

$$\nabla_y G \cdot \hat{\mathbf{n}}_y \;=\; \frac{1}{4\pi} \left[-\frac{cos\theta}{|\mathbf{r}_y|^2\,(1 - M_r)} + \frac{\mathbf{\Omega}_y \hat{\mathbf{r}}_y \cdot \hat{\mathbf{n}}_y}{c_0 |\mathbf{r}_y|\,(1 - M_r)^2} \right]$$

$$+\; \frac{1}{4\pi} \left[\frac{v_n - v_r\,cos\theta}{c_0 |\mathbf{r}_y|^2\,(1 - M_r)^2} - \frac{v_r\,cos\theta}{c_0 |\mathbf{r}_y|^2\,(1 - M_r)^2} \right]$$

$$-\; \frac{1}{4\pi} \left[\frac{\mathbf{R}^T \dot{\mathbf{v}} \cdot \hat{\mathbf{r}}_y + \frac{v^2 - v_r^2}{|\mathbf{r}_y|}}{c_0^2 |\mathbf{r}_y|\,(1 - M_r)^3} \right] cos\theta \tag{A.64}$$

Furthermore

$$\mathbf{R}^T \dot{\mathbf{n}} = \dot{\hat{\mathbf{n}}}_y + \mathbf{\Omega}_y \hat{\mathbf{n}}_y \tag{A.65}$$

Hence, since $\dot{\hat{\mathbf{n}}}_y = 0$

$$\dot{\hat{\mathbf{n}}} \cdot \hat{\mathbf{r}} = \mathbf{R}\,\boldsymbol{\Omega}_y\,\mathbf{n}_y \cdot \hat{\mathbf{r}} = \boldsymbol{\Omega}_y \mathbf{n}_y \cdot \hat{\mathbf{r}}_y \qquad (A.66)$$

Observing that $(-\boldsymbol{\Omega}_y \hat{\mathbf{r}}_y \cdot \hat{\mathbf{n}}_y) = \boldsymbol{\Omega}_y \hat{\mathbf{n}}_y \cdot \hat{\mathbf{r}}_y$, from the above relation one obtains

$$(-\boldsymbol{\Omega}_y \hat{\mathbf{r}}_y \cdot \hat{\mathbf{n}}_y) = \dot{\hat{\mathbf{n}}} \cdot \hat{\mathbf{r}} \qquad (A.67)$$

Similarly, $\mathbf{R}^T \dot{\mathbf{M}} \cdot \hat{\mathbf{r}}_y = \dot{\mathbf{M}} \cdot \hat{\mathbf{r}}$; it results that

$$
\begin{aligned}
\nabla_y G \cdot \hat{\mathbf{n}}_y &= \frac{1}{4\pi}\left[-\frac{cos\theta}{|\mathbf{r}_y|^2\,(1-M_r)^2} - \frac{M_r\,cos\theta}{|\mathbf{r}_y|^2\,(1-M_r)^3}\right] \\
&+ \frac{1}{4\pi}\left[-\frac{\dot{\hat{\mathbf{n}}}\cdot\hat{\mathbf{r}}}{c_0|\mathbf{r}_y|\,(1-M_r)^2} + \frac{M_n}{|\mathbf{r}_y|^2\,(1-M_r)^2}\right] \\
&- \frac{1}{4\pi}\left[\frac{\dot{\mathbf{M}}\cdot\hat{\mathbf{r}}\,cos\theta}{c_0|\mathbf{r}_y|\,(1-M_r)^3} - \frac{M^2\,cos\theta}{|\mathbf{r}_y|^2\,(1-M_r)^3}\right]
\end{aligned}
\qquad (A.68)
$$

Furthermore, relations (A.51) and (A.52) yield

$$\nabla_y \vartheta \cdot \mathbf{n}_y\,\hat{G}_\vartheta = \frac{cos\theta}{4\pi\,c_0|\mathbf{r}_y|\,(1-M_r)^2} \qquad (A.69)$$

Finally it results that

$$
\begin{aligned}
-\mathbf{P}_y \mathbf{n}_y \cdot \nabla_y \hat{G} &= \frac{p\,cos\theta\,(c_0\,M_r + \dot{\mathbf{M}}\cdot\mathbf{r} - c_0\,M^2)}{4\pi\,c_0|\mathbf{r}_y|^2\,(1-M_r)^3} \\
&- \left[\frac{-p\,cos\theta + pM_n}{4\pi\,|\mathbf{r}_y|^2\,(1-M_r)^2} - \frac{p\dot{\hat{\mathbf{n}}}\cdot\hat{\mathbf{r}}}{4\pi\,c_0|\mathbf{r}_y|\,(1-M_r)^2}\right]
\end{aligned}
\qquad (A.70)
$$

and

$$\dot{\mathbf{P}}_y \mathbf{n}_y \cdot \nabla_y \vartheta\,\hat{G} = \frac{\dot{p}\,cos\theta}{4\pi\,c_0|\mathbf{r}_y|\,(1-M_r)^2} \qquad (A.71)$$

Combining Eqs. (A.70) and (A.71) one obtains the following expression for the kernel of the loading noise term

$$
\begin{aligned}
-\Big[(\mathbf{P}_y\mathbf{n}_y)\cdot\nabla_y\hat{G} &- (\dot{\mathbf{P}}_y\mathbf{n}_y)\cdot\nabla_y\vartheta\,\hat{G}\Big] = \\
&= \frac{p\,cos\theta\,(c_0\,M_r + \dot{\mathbf{M}}\cdot\mathbf{r} - c_0\,M^2)}{4\pi\,c_0|\mathbf{r}_y|^2\,(1-M_r)^3} + \\
&- \left[\frac{-p\,cos\theta + pM_n}{4\pi\,|\mathbf{r}_y|^2\,(1-M_r)^2} - \frac{p\dot{\hat{\mathbf{n}}}\cdot\hat{\mathbf{r}}}{4\pi\,c_0|\mathbf{r}_y|\,(1-M_r)^2}\right] + \\
&+ \frac{\dot{p}\,cos\theta}{4\pi\,c_0|\mathbf{r}_y|\,(1-M_r)^2}
\end{aligned}
\qquad (A.72)
$$

that is equivalent to Eq. (A.48).

Appendix B

Hydrodynamics of Cavitating Propellers

B.1   Statement of the Problem

The hydrodynamic model discussed here is based on a potential flow formulation; this approach combines a boundary integral formulation for the velocity potential with a cavitation model aimed to study the time dependent sheet cavity, typically occurring on propeller blades in the wake of the hull. Since the cavity surface is not known a priori (its location is part of the solution to the boundary value problem) and the boundary conditions on it are non linear, the resulting problem is fully non linear. The main features of the cavitation model is that it does not describe the two-phase flow inside the bubble but it considers the cavity as a homogeneous bubble bounded by an unknown surface. Moreover, for the scope of the present work, the effects induced by the viscosity on the detachment point are not considered; the cavity detachment point is assumed to be located at the blade leading edge[1].

The proposed model is valid to study a single propeller subject to a spatially non-uniform onset flow (hereafter referred to as *behind-hull* condition). This configuration is used to simulate a propeller in the wake of a ship hull through a simplified model where hull-propeller interactions are limited to consider a prescribed hull wake flow incoming to an isolated propeller in unbounded fluid domain. Such a configuration may be conveniently studied introducing two Cartesian frames
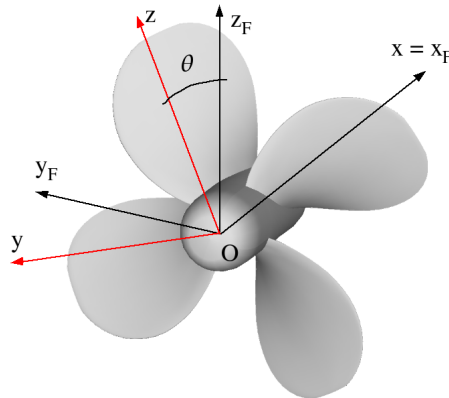
Figure B.1: *Definition of rotating and fixed frames of reference: righthanded propeller observed from front–side.*

of reference. One is fixed to the hull, $(Oxy_F z_F)$ (fixed frame of reference, FFR), whereas the other

---

[1]Under the assumption that the viscosity effects are confined inside the boundary layer, the present model might be coupled with the integral equation of the boundary layer to consider a more realistic prevision of the cavity detachment point. Details on this aspect are shown in Ref. [30]

is rigidly connected to the rotating propeller, $(Oxyz)$ (rotating frame of reference, RFR). The two frames have common origin and x axis, parallel to the propeller axis and pointing downstream (see Fig. B.1). Conversion of tensor quantities from FFR to RFR is obtained through a rotation tensor $\mathbf{A}_{RF} = \mathbf{A}_{RF}(\theta)$, where $\theta = 2\pi n t$ is the angle spanned by the z-axis of the RFR, t is time and n is the propeller rotational speed (rps). At time t = 0, the two frames of reference coincide. The inflow $\mathbf{v}_A$ to the propeller is written as the sum of two contributions

$$\mathbf{v}_A = -\mathbf{v}_0 + \mathbf{v}_w \tag{B.1}$$

where $\mathbf{v}_0$ denotes the ship speed[2] and $\mathbf{v}_w = \mathbf{v}_w(y_F, z_F)$ is the velocity defect due to the hull boundary layer. In the present model, it is assumed that quantity $\mathbf{v}_w$ is constant along x- axis (*frozen incoming wake* assumption).

Denoting by $\mathbf{u}$ the propeller-induced perturbation velocity, the total velocity relative to the body reads

$$\mathbf{q} = \mathbf{q}_0 + \mathbf{q}_w + \mathbf{u} \tag{B.2}$$

where

$$\mathbf{q}_0 = -\mathbf{v}_0 - \mathbf{\Omega r} \tag{B.3}$$

and

$$\mathbf{q}_w = \mathbf{A}_{RF}\mathbf{v}_w \tag{B.4}$$

The tensor $\mathbf{\Omega}$ represents the rotation tensor associated to the propeller rotational speed. It should be observed that quantity $\mathbf{q}_w$ is time-dependent due to conversion from FFR to RFR.

Basic assumption of the present formulation is that only the velocity perturbation associated to inviscid, irrotational flow effects is considered. Thus, it is possible to recast the perturbation velocity $\mathbf{u}$ in terms of the gradient of a scalar potential as $\mathbf{u} = \nabla\phi$. Being the incompressible flow assumption fully adequate to describe the hydrodynamic behaviour of the blade, the Laplace equation

$$\nabla^2\phi = 0 \tag{B.5}$$

holds everywhere except for a zero thickness layer where the vorticity related to the lift/thrust generation mechanism is shed downstream the body. This surface, labelled as the trailing wake, represents a discontinuity surface for the velocity potential. Equation (B.5) must be completed with suitable boundary conditions on the wetted body surface $\mathcal{S}_{WB}$ and on the hub surface $\mathcal{S}_H$, on the potential wake $\mathcal{S}_W$ and on the cavity. To this purpose, the following relations must be satisfied:

$\underline{BC_s}$ on wetted area

$$\mathbf{q} \cdot \mathbf{n} = 0 \tag{B.6}$$

that, denoting with $\mathbf{n}$ the outward unit normal vector, transforms into

$$\chi = \frac{\partial\phi}{\partial n} = -(\mathbf{q}_0 + \mathbf{q}_w) \cdot \mathbf{n} \qquad\qquad \forall \mathbf{x} \in \mathcal{S}_{WB} \cup \mathcal{S}_H \tag{B.7}$$

$\underline{BC_s}$ on the wake

$$\begin{cases} \Delta\left(\dfrac{\partial\phi}{\partial n}\right) = 0 \\[2mm] \Delta p = 0 \end{cases} \qquad\qquad \forall \mathbf{x} \in \mathcal{S}_W \tag{B.8}$$

---

[2]A ship advancing with a time independent forward speed $\mathbf{v}_0$ is considered.

In order to derive the boundary conditions on the cavity, the cavitation model is outlined in the following sections. More details are presented in Ref. [82]. The approach, adapted from a formulation proposed by Kinnas and Fine [83], is limited to address vaporization phenomena on lifting surfaces in which the cavity originates in the leading edge region and is attached to the solid surface (partial cavitation) or extends downstream the lifting surface trailing edge (supercavitation). The resulting methodology is valid to study sheet cavitation on propeller blades, whereas no attempt to model cavity two-phase flow features like re-entrant jet, cloud formation and vortex cavitation (at blade tip or at propeller hub) is done. In the cavitation model here presented, a closed homogeneous surface $\mathcal{S}_C$ enclosing the vapor region (the cavity) is introduced; this surface represents a boundary surface of the computational domain and no attempt to investigate the gaseous phase inside the volume surrounded by $\mathcal{S}_C$ is done.

B.2   Sheet Cavitation Modeling

Metrics

Let us introduce a right–handed system of material coordinates, *i.e.,*a system of curvilinear coordinates that moves with the propeller blade; specifically, s ed u are chordwise and spanwise curvilinear abscissae on propeller blade surface[3], respectively, whereas n is normal to the surface. Denoting with $\xi^\alpha, (\alpha = 1, 2, 3)$ the material coordinates and with $\mathbf{x}$ the location of a material particle identified by $\mathbf{x} = \hat{\mathbf{x}}(\xi^\alpha, t)$, the definition of material covariant base vectors $\mathbf{g}_\alpha = \dfrac{\partial \mathbf{x}}{\partial \xi^\alpha}$ allows to identify the following unit vectors tangent to the s, u and n line

$$\hat{\mathbf{s}} = \left(\frac{\partial x}{\partial s}\mathbf{i} + \frac{\partial y}{\partial s}\mathbf{j} + \frac{\partial z}{\partial s}\mathbf{k} \right) \Big/ \sqrt{\left(\frac{\partial x}{\partial s}\right)^2 + \left(\frac{\partial y}{\partial s}\right)^2 + \left(\frac{\partial z}{\partial s}\right)^2}$$

$$\hat{\mathbf{u}} = \left(\frac{\partial x}{\partial u}\mathbf{i} + \frac{\partial y}{\partial u}\mathbf{j} + \frac{\partial z}{\partial u}\mathbf{k} \right) \Big/ \sqrt{\left(\frac{\partial x}{\partial u}\right)^2 + \left(\frac{\partial y}{\partial u}\right)^2 + \left(\frac{\partial z}{\partial u}\right)^2}$$

$$\mathbf{n} = \hat{\mathbf{s}} \times \hat{\mathbf{u}} / \|\hat{\mathbf{s}} \times \hat{\mathbf{u}}\|$$

where $\mathbf{i}$, $\mathbf{j}$, $\mathbf{k}$ are the base vectors of a orthonormal Cartesian system and x, y, z represents the Cartesian components of the location of a material point ξ^α on the body surface $\mathcal{S}_B$ or on the wake. The surface of the cavity $\mathcal{S}_C$, introduced at the end of section (B.1), may be conveniently expressed as

$$\hat{S}_C (s, u, n, t) = 0 \tag{B.9}$$

or equivalently as

$$\zeta - h_c(s, u, t) = 0 \tag{B.10}$$

where ζ represents the coordinate of a material particle on the cavity surface in the n direction and h_c denotes the thickness of the bubble. The normal vector at any point on the cavity is defined by

$$\mathbf{n}_c = \nabla \mathcal{S}_C \tag{B.11}$$

By using Eq. (B.10), and the expression of the gradient in curvilinear coordinates

$$\nabla \mathcal{S}_C = \frac{\partial \mathcal{S}_C}{\partial \xi^\alpha} \mathbf{g}^\alpha \tag{B.12}$$

in which $\mathbf{g}^\alpha$ are the contravariant base vectors, the following relation may be derived

$$\mathbf{n}_c = -\frac{\partial h_c}{\partial s}\check{\mathbf{s}} - \frac{\partial h_c}{\partial u}\check{\mathbf{u}} + \mathbf{n} \tag{B.13}$$

---

[3]On the wake, s is in the flow direction and u is transversal.

where š and ǔ are the contravariant base vectors associated to the s and u directions. By exploiting the following relations relating covariant and contravariant bases

$$\check{\mathbf{s}} = \frac{1}{sin^2\theta}(\hat{\mathbf{s}} - cos\theta\ \hat{\mathbf{u}})$$

$$\check{\mathbf{u}} = \frac{1}{sin^2\theta}(\hat{\mathbf{u}} - cos\theta\ \hat{\mathbf{s}})$$

$$\check{\mathbf{n}} = \mathbf{n}$$

where θ is the local angle between s and u lines, Eq. (B.13) may be written as

$$\mathbf{n}_c = -\frac{1}{\sin^2\theta}\left[\left(\frac{\partial h_c}{\partial s} - \frac{\partial h_c}{\partial u}\cos\theta\right)\hat{\mathbf{s}} + \left(\frac{\partial h_c}{\partial u} - \frac{\partial h_c}{\partial s}\cos\theta\right)\hat{\mathbf{u}}\right] + \mathbf{n} \qquad (B.14)$$

stating that the for any point of the cavity, the difference between $\mathbf{n}_c$ and the normal $\mathbf{n}$ to the blade surface is related to contributions of $O(h_c)$ in s and u directions. Furthermore, one obtains that

$$\|\mathbf{n}_c\|^2 = \frac{1}{\sin^2\theta}\left[\left(\frac{\partial h_c}{\partial s}\right)^2 + \left(\frac{\partial h_c}{\partial u}\right)^2 - 2\frac{\partial h_c}{\partial s}\frac{\partial h_c}{\partial u}\cos\theta + \sin^2\theta\right]$$

that is

$$\|\mathbf{n}_c\| = \sqrt{1 + \mathcal{O}\left(h_c^2\right)} \qquad (B.15)$$

stating that the amplitude of the vector $\mathbf{n}_c$ is different from unity because of quantities $\mathcal{O}\left(h_c^2\right)$. Within the approximation of the proposed model, such differences may be neglected.

Geometry of the Cavitation Bubble

Let $\mathcal{V}_C$ be the region characterized by the cavitation bubble[4], $\mathcal{S}_{WB}$ the non–cavitating portion of the blade surface, $\mathcal{S}_H$ the hub surface[5], $\mathcal{S}_W$ the wake surface, $\mathcal{S}_{CB}$ the cavitating portion of the body surface and $\mathcal{S}_{CW}$ the cavitating portion of the potential wake.

The cavity thickness h_c is defined as the distance between surfaces $\mathcal{S}_C$ and $\mathcal{S}_{CB}$. Recalling constant-pressure and impermeability conditions, $\mathcal{S}_C$ is a material surface and an evolution equation for h_c may be derived. To this aim, the physical condition

$$\frac{D}{Dt}\hat{\mathcal{S}}_C(s, u, n, t) = 0 \qquad (B.16)$$

with $D/Dt = \partial/\partial t + \mathbf{q}\cdot\nabla$, may be suitable re–written by using Eq. (B.10); this yields

$$-\frac{\partial h_c}{\partial t} + \mathbf{q}\cdot\left(\mathbf{n} - \frac{\partial h_c}{\partial s}\check{\mathbf{s}} - \frac{\partial h_c}{\partial u}\check{\mathbf{u}}\right) = 0 \qquad (B.17)$$

that is equal to

$$-\frac{\partial h_c}{\partial t} + \mathbf{q}\cdot\mathbf{n}_c = 0 \qquad (B.18)$$

or

$$\frac{\partial\phi}{\partial n} = -\mathbf{v}_I\cdot\mathbf{n} + \chi_c \qquad\qquad \forall\mathbf{x}\in\mathcal{S}_{CB} \qquad (B.19)$$

---

[4]Dealing with attached cavitation, it is reasonable to identify the cavity surface $\mathcal{S}_C$ with its projection $\mathcal{S}_{CB}$ and $\mathcal{S}_{CW}$ on the blade and wake surfaces.

[5]We assume that on the hub surface, cavitation does not occur.

in terms of velocity potential, being $\chi_c = \mathbf{q} \cdot \nabla_s h_c + \dfrac{\partial h_c}{\partial t}$ and $\mathbf{v}_I = \mathbf{q}_0 + \mathbf{q}_w$.

Note that ∇_s is the gradient operator acting on the surface. Equation (B.19) yields a condition for the normal derivative of the potential velocity at any point of $\mathcal{S}_{CB}$.

The governing equation for the dynamics of the cavity may be derived by combining Eqs. (B.18) and (B.13) such to obtain

$$
\begin{aligned}
C_s\,(s,u)\,\frac{\partial h_c}{\partial s} \quad &+ \quad C_u\,(s,u)\,\frac{\partial h_c}{\partial u} + \\
&+ \quad C_t\,(s,u)\,\frac{\partial h_c}{\partial t} = -\left(v_{I_n} + \frac{\partial \phi}{\partial n}\right) \quad \forall \mathbf{x} \in \mathcal{S}_{CB}
\end{aligned} \tag{B.20}
$$

where the coefficients C_s, C_u e C_t are given by

$$
\begin{aligned}
C_s\,(s,u) &= \frac{1}{\sin^2\theta}\left[\left(v_{I_u} + \frac{\partial \phi}{\partial u}\right)\cos\theta - \left(v_{I_s} + \frac{\partial \phi}{\partial s}\right)\right] \\
C_u\,(s,u) &= \frac{1}{\sin^2\theta}\left[\left(v_{I_s} + \frac{\partial \phi}{\partial s}\right)\cos\theta - \left(v_{I_u} + \frac{\partial \phi}{\partial u}\right)\right] \\
&\qquad\qquad\qquad\qquad\qquad C_t\,(s,u) = -1
\end{aligned}
$$

The solution of Eq. (B.20) provides the thickness of the bubble h_c.

A similar equation may be obtained to describe cavities extending downstream the blade trailing edge (supercavitating-flow conditions). Denoting with $\mathcal{S}_C^+$ e con $\mathcal{S}_C^-$ the upper and lower sides of the supercavitation region, Eq. (B.16) yields

$$
\begin{aligned}
\frac{D^+}{Dt}\hat{\mathcal{S}}_C^+\,(s,u,n,t) = 0 &\Leftrightarrow \left(\frac{\partial}{\partial t} + \mathbf{q}^+ \cdot \nabla\right)[\zeta - h_c^+\,(s,u,t)] = 0 \;\; \forall \mathbf{x} \in \mathcal{S}_C^+ \\
&\\
\frac{D^-}{Dt}\hat{\mathcal{S}}_C^-\,(s,u,n,t) = 0 &\Leftrightarrow \left(\frac{\partial}{\partial t} + \mathbf{q}^- \cdot \nabla\right)[\zeta - h_c^-\,(s,u,t)] = 0 \;\; \forall \mathbf{x} \in \mathcal{S}_C^-
\end{aligned} \tag{B.21}
$$

Manipulating one obtains

$$
\begin{aligned}
-\;\frac{\partial h_c^+}{\partial t} + \mathbf{q}^+ \cdot \left(\mathbf{n}_W - \frac{\partial h_c^+}{\partial s}\check{\mathbf{s}} - \frac{\partial h_c^+}{\partial u}\check{\mathbf{u}}\right) &= 0 \\
-\;\frac{\partial h_c^-}{\partial t} + \mathbf{q}^- \cdot \left(\mathbf{n}_W - \frac{\partial h_c^-}{\partial s}\check{\mathbf{s}} - \frac{\partial h_c^-}{\partial u}\check{\mathbf{u}}\right) &= 0
\end{aligned} \tag{B.22}
$$

where $\mathbf{n}_W = \mathbf{n}$ indicates the normal vector to the wake surface $\mathcal{S}_W$ oriented from the lower side to the upper one. After algebraic manipulations, the following relation is derived

$$
\begin{aligned}
-2\frac{\partial h_{cw}}{\partial t} + \left(\frac{\partial \phi^+}{\partial n} - \frac{\partial \phi^-}{\partial n}\right) \quad &- \quad 2\left(\frac{\partial h_{cw}}{\partial s}\mathbf{q}^+ \cdot \check{\mathbf{s}} - \frac{\partial h_{cw}}{\partial u}\mathbf{q}^+ \cdot \check{\mathbf{u}}\right) + \\
&- \quad (\mathbf{q}^+ - \mathbf{q}^-) \cdot \left(\check{\mathbf{s}}\frac{\partial h_c^-}{\partial s} + \check{\mathbf{u}}\frac{\partial h_c^-}{\partial u}\right) = 0
\end{aligned}
$$

where h_{cw} and h_{cm}, allowing to describe the shape of $\mathcal{S}_C^+$ and $\mathcal{S}_C^-$, are defined by

$$
h_{cw} = \frac{1}{2}\left(h_c^+ - h_c^-\right)
$$

$$
h_{cm} = \frac{1}{2}\left(h_c^+ + h_c^-\right) \tag{B.23}
$$

In particular h_{cm} identifies the distance between the wake and the average surface of the bubble while h_{cw} is the semi–thickness of the supercavitating bubble measured from the average surface.

By assuming the supercavitating surface $\mathcal{S}_C$ equal to its projection $\mathcal{S}_{CW}$ on the wake, without loss of generality we assume $h_c^- = 0$; thus, h_{cw} coincides with h_{cm} and assumes the same role of h_c on the blade where $h_c = 2\,h_{cw}$ at the trailing edge. Such assumption yields

$$2\frac{\partial h_{cw}}{\partial t} + 2\frac{\partial h_{cw}}{\partial s}\mathbf{q}^+ \cdot \check{\mathbf{s}} + 2\frac{\partial h_{cw}}{\partial u}\mathbf{q}^+ \cdot \check{\mathbf{u}} = \Delta(\frac{\partial \phi}{\partial n}) \tag{B.24}$$

that, once manipulated, provides the governing equation for the dynamic behaviour of the cavity downstream the blade trailing edge. It results

$$C_s^+(s,u)\,\frac{\partial 2h_{cw}}{\partial s} + C_u^+(s,u)\,\frac{\partial 2h_{cw}}{\partial u} + C_t^+(s,u)\,\frac{\partial 2h_{cw}}{\partial t} = -\chi_w \quad \forall \mathbf{x} \in \mathcal{S}_{CW} \tag{B.25}$$

where

$$C_s^+(s,u) = \frac{1}{\sin^2\theta}\left[\left(v_{I_u} + \frac{\partial \phi^+}{\partial u}\right)\cos\theta - \left(v_{I_s} + \frac{\partial \phi^+}{\partial s}\right)\right]$$

$$C_u^+(s,u) = \frac{1}{\sin^2\theta}\left[\left(v_{I_s} + \frac{\partial \phi^+}{\partial s}\right)\cos\theta - \left(v_{I_u} + \frac{\partial \phi^+}{\partial u}\right)\right]$$

$$C_t^+(s,u) = 1 \tag{B.26}$$

and

$$\chi_w = \Delta\left(\frac{\partial \phi}{\partial n}\right) \tag{B.27}$$

More details may be found in Ref. [83].

B.3   Boundary Conditions on the Cavitation Bubble

A surface tracking approach is followed in which the vapor/water interface is determined as a physical boundary of the liquid domain. Basic assumptions are that the cavity outer edge $\mathcal{S}_C$ is characterized by a constant pressure condition $p = p_v$, where p_v is the vapor pressure, whereas $\mathcal{S}_C$ is impermeable. Imposing $p = p_v$, the Bernoulli theorem [23], referred to the RFR, reads

$$\frac{\partial \phi}{\partial t} + \frac{1}{2}q^2 + \frac{p_v}{\rho_0} + g\,z_0 = \frac{1}{2}\|\mathbf{v}_I\|^2 + \frac{p_a}{\rho_0} \qquad \forall \mathbf{x} \in \mathcal{S}_C \tag{B.28}$$

where $q = \|\mathbf{q}\|$, $\mathbf{v}_I = \mathbf{q}_0 + \mathbf{q}_w$, whereas gz_0 is the hydrostatic head term. The Bernoulli equation yields a direct relationship between the cavitation number $\sigma_n = (p_a - p_v)/\frac{1}{2}\rho(nD_P)^2$ and the total velocity at an arbitrary point on the cavity surface, that is

$$q = \sqrt{(nD)^2\,\sigma - 2\left(\frac{\partial \phi}{\partial t} + gz_0\right) + \|\mathbf{v}_I\|^2} \qquad \forall \mathbf{x} \in \mathcal{S}_C \tag{B.29}$$

Recalling Eq. (B.2) with $\mathbf{u} = \nabla\phi$ and separating $\nabla\phi$ components, Eq. (B.29) can be manipulated to obtain a Dirichlet-type condition; to this aim, the fluid velocity at any point of the cavity may be written in terms of the local contravariant base vectors as

$$\mathbf{q} = q_s\check{\mathbf{s}} + q_u\check{\mathbf{u}} + q_n\mathbf{n} \tag{B.30}$$

whose module is given by

$$q^2 = \frac{1}{\sin^2\theta}\left(q_s^2 + q_u^2 - 2\,q_sq_u\cos\theta + \sin^2\theta q_n^2\right). \tag{B.31}$$

The relation B.31 may be interpreted as an algebraic equation for q_s

$$q_s = q_u \cos\theta \mp |\sin\theta|\sqrt{q^2 - q_u^2 - q_n^2}. \tag{B.32}$$

where the solution with the sign $+$ is the only physically consistent one. By expressing the inflow velocity on the cavity as

$$\mathbf{v}_I = v_{I_s}\check{\mathbf{s}} + v_{I_u}\check{\mathbf{u}} + v_{I_n}\mathbf{n} \tag{B.33}$$

and by observing that

$$q_s = v_{I_s} + \frac{\partial\phi}{\partial s}$$

$$q_u = v_{I_u} + \frac{\partial\phi}{\partial u} \tag{B.34}$$

$$q_n = v_{I_n} + \frac{\partial\phi}{\partial n}$$

the combination of Eqs. (B.29) and (B.31) yields a nonlinear partial differential equation for the velocity potential on the cavity

$$\frac{\partial\phi}{\partial s} = -v_{I_s} + \left(v_{I_u} + \frac{\partial\phi}{\partial u}\right)\cos\theta \tag{B.35}$$
$$+ |\sin\theta|\sqrt{\Xi} \quad \forall\mathbf{x} \in \mathcal{S}_{CB}$$

where,

$$\Xi = (nD)^2\sigma - 2\left(\frac{\partial\phi}{\partial t} + gz_0\right) + \|\mathbf{v}_I\|^2 - \left(v_{I_u} + \frac{\partial\phi}{\partial u}\right)^2 - \left(v_{I_n} + \frac{\partial\phi}{\partial n}\right)^2$$

that requires suitable boundary conditions and initial conditions to be solved. By integrating Eq. (B.35) along s, one has

$$\phi(s,u) = \phi(s_{CLE}, u) + \int_{s_{CLE}}^{s}\left[\left(v_{I_u} + \frac{\partial\phi}{\partial u}\right)\cos\theta - v_{I_s}\right. \tag{B.36}$$
$$+ |\sin\theta|\sqrt{\Xi}\Big]\mathrm{d}\xi$$

or, in compact form

$$\phi(s,u) = \phi(s_{CLE}, u) + \int_{s_{CLE}}^{s}\mathcal{F}\mathrm{d}\xi \qquad\qquad \forall\mathbf{x} \in \mathcal{S}_{CB} \tag{B.37}$$

where s_{CLE} is the cavity leading edge abscissa in chordwise direction, whereas

$$\mathcal{F} = -(\mathbf{q}_0 + \mathbf{q}_w)\cdot\hat{\mathbf{s}} + q_u\cos\theta + |\sin\theta|\sqrt{q^2 - q_u^2 - q_n^2}$$

Equation (B.37) yields a nonlinear boundary condition on the cavitating portion of the body surface. Such a condition is also known as Dynamic Boundary Condition (DBC).
The derivation of Eq. (B.37) differs from an approach proposed in Ref. [83] by including quantity q_n at the right hand side of Eq. (B.32).
Equation (B.37) is formally valid also to describe cavities extending downstream the blade trailing edge (supercavitating-flow conditions). In this case, the cavity is assumed to be the continuation

of the cavity present on one side of the blade surface and the cavity thickness is defined with re-
spect to the wake surface. Making reference to the upper side of the cavitating wake, the potential
function may be written as

$$
\begin{aligned}
\phi^+ (s, u) \;=\;& \phi^+ (s_{TE}, u) + \\
& + \int_{s_{TE}}^{s} \left[\left(v_{I_u} + \frac{\partial \phi^+}{\partial u} \right) \cos \theta - v_{Is} + |\sin \theta| \sqrt{\Pi} \right] \mathrm{d}\xi \qquad \forall \mathbf{x} \in \mathcal{S}_{CW}
\end{aligned}
$$

where

$$
\begin{aligned}
\Pi \;=\;& (nD)^2 \sigma - 2 \left(\frac{\partial \phi^+}{\partial t} + g z_0 \right) + \|\mathbf{v}_I\|^2 + \\
& - \left(v_{I_u} + \frac{\partial \phi^+}{\partial u} \right)^2 - \left(v_{I_n} + \frac{\partial \phi^+}{\partial n} \right)^2
\end{aligned} \tag{B.38}
$$

and s_{TE} is the cavity trailing edge abscissa in chordwise direction. In compact form, one obtains

$$
\phi^+ (s, u) = \phi^+ (s_{TE}, u) + \int_{s_{TE}}^{s} \hat{\mathcal{F}} \mathrm{d}\xi \qquad \forall \mathbf{x} \in \mathcal{S}_{CW} \tag{B.39}
$$

where

$$
\hat{\mathcal{F}} = q_u^+ \cos \theta - (\mathbf{q}_0 + \mathbf{q}_w) \cdot \hat{\mathbf{s}} + |\sin \theta| \sqrt{\Pi} \tag{B.40}
$$

whereas

$$
\Pi = \sqrt{q^{+2} - q_u^{+2} - q_n^{+2}}
$$

The potential velocity ϕ^- at the lower side of the cavitating wake is then easily derived from the
knowledge of ϕ^+ and $\delta\phi$.

Finally, a further condition is required to overcome a local singularity at the cavity trailing
edge, where both the Dirichlet–type condition given by Eq. (B.37) and the Neumann–type condi-
tion $\mathbf{q} \cdot \mathbf{n}_c = 0$ should be imposed. The cavity closure region, also called cavity wake, is the most
difficult phenomenon to address within potential flow models because viscous effects dominate the
flow in this area. Therefore, within potential flows theory, some simplifications have to be intro-
duced. Potential flow models for partial cavitation may be classified in two major categories [84]:
open models and closed models. In the former, the cavity surface is an open surface, that is, there
exists a prescribed non–zero thickness at the trailing edge of the bubble; in the latter the cavity
surface meets the blade surface. Here, a closed model has been adopted[6] Therefore, it is numeri-
cally convenient to impose an automatic recovery law from the constant pressure to the pressure
downstream of the cavity [30]. Specifically, pressure is forced to vary smoothly from $p = p_v$ at the
cavity trailing edge to wetted flow conditions downstream the cavity, by the Bernoulli theorem.[7]
The procedure is based on modifying the cavitation number from σ_n to σ_n^* for the dynamic bound-
ary conditions. In detail, by allowing for 0th and 1st order continuity of the pressure between the
cavity and the downstream regions, the σ_n value in Eq. (B.29) may be replaced with a third-order
Hermitian polynomial

$$
\sigma_n^* = \sigma_n \, h_1(\xi) + \frac{\partial \sigma_n}{\partial \xi} \, h_2(\xi) - cp_l \, h_3(\xi) - \frac{\partial cp_l}{\partial \xi} \, h_4(\xi) \tag{B.41}
$$

---

[6]Differently from 2D flows, in 3D flows the reattachment point of the cavity is not a stagnation point because of the
effects induced by the cross flow.

[7]This model only needs the size of the recovery zone to be prescribed and allows to avoid instabilities of the
numerical solution of the problem.

where $h_k(\xi)$ $(k = 1, 2, 3, 4)$ are cubic interpolation polynomials, $cp = -\sigma_n$ and the abscissa $\xi = (s - s_t)/(s_l - s_t)$ varies from 0 to 1 in the transition zone. The curvilinear abscissa s_t denotes the starting point of the transition region whereas s_l identifies the end–point of the cavity. Immediately after the end of the cavity, cp_l and $\dfrac{\partial cp_l}{\partial \xi}$ are determined through an iterative procedure using the values of downstream part of the cavity. In case of supercavitation, since the pressure at the end of the super–cavity is though not to influence the loading on the blade, no pressure recovery scheme is used.

B.4 Integral Solution

The flowfield around the propeller is determined here through a boundary integral formulation for the velocity potential ϕ. As shown in Ref. [85], at any time t the following integral representation yields the potential at any point $\mathbf{x}$ immersed into the fluid

$$
\begin{aligned}
E(\mathbf{x})\phi(\mathbf{x}) \;=\; & \int_{\mathcal{S}_B \cup \mathcal{S}_H} \left(G\,\chi - \phi\frac{\partial G}{\partial n} \right) \mathrm{d}S(\mathbf{y}) - \int_{\mathcal{S}_W} \Delta\phi\frac{\partial G}{\partial n}\,\mathrm{d}S(\mathbf{y}) + \\
& + \int_{\mathcal{S}_{CW}} \Delta\left(\frac{\partial\phi}{\partial n}\right) G\,\mathrm{d}S(\mathbf{y}) \qquad\qquad \forall\mathbf{x}\in\mathcal{V}
\end{aligned} \tag{B.42}
$$

where $G = \dfrac{-1}{4\,\pi|\mathbf{x} - \mathbf{y}|}$ is the unit source in the unbounded three-dimensional space. A boundary integral equation is obtained by taking the limit of the representation B.42 as $\mathbf{x}$ tends to $\mathcal{S}_B \cup \mathcal{S}_H$, and imposing the boundary conditions previously described. The result of this operation is[8]

$$
\begin{aligned}
\frac{1}{2}\phi(\mathbf{x}) \;=\; & \int_{\mathcal{S}_B \cup \mathcal{S}_H} \left(G\,\chi - \phi\frac{\partial G}{\partial n} \right) \mathrm{d}S(\mathbf{y}) - \int_{\mathcal{S}_W} \Delta\phi\frac{\partial G}{\partial n}\,\mathrm{d}S(\mathbf{y}) + \\
& + \int_{\mathcal{S}_{CW}} \Delta\left(\frac{\partial\phi}{\partial n}\right) G\,\mathrm{d}S(\mathbf{y}) \qquad\qquad \forall\mathbf{x}\in\mathcal{S}_B \cup \mathcal{S}_H
\end{aligned} \tag{B.43}
$$

A similar integral equation is obtained for the cavitating portion of the wake; by considering two points $\mathbf{x}^+$ and $\mathbf{x}^-$ close to the upper and lower side of the cavitating wake respectively and by taking the limit of Eq. (B.42) as $\mathbf{x}^+$ and $\mathbf{x}^-$ tends to $\mathcal{S}_{CW}^+$ and $\mathcal{S}_{CW}^-$ one obtains

$$
\begin{aligned}
\frac{1}{2}\left[\phi^+(\mathbf{x}) + \phi^-(\mathbf{x})\right] \;=\; & \frac{1}{2}\Delta\phi(\mathbf{x}_W) + \\
& + \int_{\mathcal{S}_B \cup \mathcal{S}_H} \left(G\,\chi - \phi\frac{\partial G}{\partial n} \right) \mathrm{d}S(\mathbf{y}) + \\
& - \int_{\mathcal{S}_W} \Delta\phi\frac{\partial G}{\partial n}\,\mathrm{d}S(\mathbf{y}) + \\
& + \int_{\mathcal{S}_{CW}} \Delta\left(\frac{\partial\phi}{\partial n}\right) G\,\mathrm{d}S(\mathbf{y}) \qquad \forall\mathbf{x}\in\mathcal{S}_{CW}
\end{aligned} \tag{B.44}
$$

where $\mathbf{x}_W$ represents a generic point located on the wake.
Observing that $\phi^+ + \phi^- = 2\phi^+ - \Delta\phi$ the above integral equation transforms into

$$
\begin{aligned}
\phi^+(\mathbf{x}) \;=\; & \frac{1}{2}\Delta\phi(\mathbf{x}_W) + \int_{\mathcal{S}_B \cup \mathcal{S}_H} \left(G\,\chi - \phi\frac{\partial G}{\partial n} \right) \mathrm{d}S(\mathbf{y}) + \\
& - \int_{\mathcal{S}_W} \Delta\phi\frac{\partial G}{\partial n}\,\mathrm{d}S(\mathbf{y}) + \int_{\mathcal{S}_{CW}} \Delta\left(\frac{\partial\phi}{\partial n}\right) G\,\mathrm{d}S(\mathbf{y}) \quad \forall\mathbf{x}\in\mathcal{S}_{CW}
\end{aligned} \tag{B.45}
$$

---

[8]Here, we assume that $\mathbf{x}$ is a regular point of $\mathcal{S}_B \cup \mathcal{S}_H$.

It is worthy observing that Eqs. (B.43), (B.45) yield a mixed Neumann-Dirichlet problem, where ϕ and ϕ^+ on $\mathcal{S}_{CB}$ and $\mathcal{S}_{CW}$ are known from pressure-based conditions (B.37), (B.39) and $\partial\phi/\partial n$ as well as $\Delta(\partial\phi/\partial n)$, are unknown on $\mathcal{S}_{CB}$ and $\mathcal{S}_{CW}$, respectively. On the wetted body portion $\mathcal{S}_{WB} \cup \mathcal{S}_{H}$, $\partial\phi/\partial n$ is known from the impermeability condition (B.7), and ϕ is unknown. The closure of the problem is obtained by observing that

$$\lim_{\mathbf{x}_W \to \mathbf{x}_{TE}} \Delta\phi(\mathbf{x}_W, t) = \phi_u(t) - \phi_l(t) \tag{B.46}$$

and

$$\Delta\phi(\mathbf{x}_W, t) = \Delta\phi(\mathbf{x}_{TE}, t - \tau) \tag{B.47}$$

where ϕ_u and ϕ_l are the potential at the upper and lower side of the wake, $\mathbf{x}_{TE}$ denotes a wake point located at the blade trailing edge and τ the convection time between wake points $\mathbf{x}_w$ and $\mathbf{x}_{TE}$. The numerical solution of Eqs. (B.43), (B.45) and (B.46) is complicated in that the location of the cavity surface $\mathcal{S}_{CB}$ and $\mathcal{S}_{CW}$ is unknown, and the boundary condition (B.37) and eventually (B.39) is nonlinear with respect to ϕ.

Numerical solutions are determined through a boundary element method. Body and wake surfaces are discretized into hyperboloidal quadrilateral elements and flow quantities are kept piecewise constant on each surface element (zero-th order discretization). Source G and dipole $\partial G/\partial n$ integral contributions are evaluated by general analytical formulas derived in Ref. [25]. Details of the computational methodology may be found in Ref. [85] for non-cavitating flow, and in Ref. [86] for cavitating flow applications.

For the sake of completeness, the computational algorithm to simulate cavitating propeller flows is briefly reviewed.

B.5   Hydrodynamic Solution Procedure

After discretizing Eqs. (B.43), (B.45), (B.46) and corresponding boundary conditions, an iterative procedure is used, at each time step, to reduce the problem to the solution of a linear algebraic set of equations. First[9], an initial guess of the cavity planform $\mathcal{S}_{C_0}^{(1)}$ is assigned, and zero cavity thickness is assumed. Solving discretized Eqs. (B.43), (B.45), (B.46) a first guess of ϕ and $\partial\phi/\partial n$ is obtained. The nonlinear boundary condition given by Eq. (B.37) and Eq. (B.39) is linearized assuming flow quantities in the right-hand side known from solution at the previous iterative step. A first guess of the cavity thickness h_c is then determined from Eq. (B.20) and Eq. (B.25). These partial differential equations for h_c are numerically solved through a strip-wise approach from blade root to blade tip and from leading edge to trailing edge. Spatial and time derivatives are discretized by a upwind first-order scheme.

Once an estimate of the cavity thickness is determined, a zero thickness condition is applied to determine the cavity trailing edge. An extrapolation procedure in case the condition $h_c = 0$ is not fulfilled within the guessed cavity planform $\mathcal{S}_{C_0}^{(1)}$ is applied. Then, an update of the cavity planform $\mathcal{S}_{C_0}^{(2)}$ is obtained and discretized Eqs. (B.43), (B.45) and (B.46) are solved again. This process is iterated at each time step until convergence of the cavity planform and of the cavity volume are reached.

The thickness of the cavity is neglected when numerically solving the boundary integral equations for ϕ and for $\nabla\phi$. Thus, source and dipole terms on the cavitating surface are evaluated on $\mathcal{S}_{C_0}$ instead on $\mathcal{S}_C$. The approximation is justified in the limit as the present formulation is valid only for thin cavities, and a robust computational scheme that is solved at reduced computational burden is obtained.

---

[9]For compactness, in the following $\mathcal{S}_{C_0}$ indicates $\mathcal{S}_{CB} \cup \mathcal{S}_{CW}$.

Finally, hydrodynamic loads can be determined by integrating pressure and viscous friction[10] over the propeller surfaces. Pressure is then determined from the Bernoulli theorem

$$\frac{\partial \phi}{\partial t} + \frac{1}{2}q^2 + \frac{p}{\rho_0} + g\,z_0 = \frac{1}{2}\|\mathbf{v}_I\|^2 + \frac{p_a}{\rho_0} \qquad (B.48)$$

---

[10]An approximated estimation of the friction coefficient could be derived through semi-empirical formulas for a flat plate in turbulent flow (see Ref. [87]).

Bibliography

[1] J.E. Ffowcs Williams, D. L. Hawkings, Sound Generation by Turbulence and Surfaces in Arbitrary Motion, *Philosophical Transactions of the Royal Society* 264 A 1151 (1969) 321–342.

[2] A.D. Pierce, R. N. Thurston, *Physical Acoustics: High Frequency and Pulse Scattering*, vol. 21, Academic Press, 1992.

[3] E. Manoha, S. Redonnet, M. Terracol, R. Guenanff, Numerical Simulation of Aerodynamic Noise, *European Congress on Computational Methods in Applied Sciences and Engineering* (2004) Jyvaskyla (Finlande).

[4] M.J. Lighthill, On Sound Generated Aerodynamically, I: General Theory, *Proc. of the Royal Society* A211 (1952) 564-587.

[5] F. Farassat, M.K. Myers, Extension of Kirchhoff's Formula to Radiation From Moving Surfaces, *Journal of Sound and Vibration* 123, 3 (1998) 451–461.

[6] K.S. Brentner, F. Farassat, An Analytical Comparison of the Acoustic Analogy and Kirchhoff Formulation for Moving Surfaces, *AIAA Journal* 36, 8 (1998) 1379–1386.

[7] R. Kinns, N. Peake, O.R. Spivack, Hull Vibration Excitation by Propeller Sources: a link between Hydrodynamics and Marine Acoustics, $24^t h$ *Symp.on Naval Hydrodynamics* 2003.

[8] O.R. Spivack, R. Kinns, N. Peake, Hull Excitation by Fluctuating and Rotating Acoustic Sources at the Propeller, *25th Symposium on Naval Hydrodynamics*, St. John's Newfoundland, Canada 2004.

[9] H. Seol, B. Jung, J. C. Suh, S. Lee, Prediction Of Non–Cavitating Underwater Propeller Noise, *Journal of Sound and Vibration* 257, 1 (2002), 131–156.

[10] A.S. Morgan, S.A. Karabasov, A.P. Dowling, T.P., Hynes, Transonic Helicopter Noise, *AIAA Journal* 43, 7 (2005) 1512–1524.

[11] F. Farassat, Introduction to Generalized Functions With Applications in Aerodynamics and Aeroacoustics, NASA Technical Paper 3428, 1994 (Corrected April 1996).

[12] K.S. Brentner, Modeling Aerodynamically Generated Sound: Recent Advances in Rotor Noise Prediction, *AIAA Paper 2000-0345, 38th Aerospace Sciences Meeting and Exhibit*, Reno, NV, January 2000.

[13] P. Di Francescantonio, A New Boundary Integral Formulation for the Prediction of Sound Radiation, *Journal of Sound and Vibration* 202, 4 (1997) 491–509.

[14] D,B. Hanson, M.R. Fink, The Importance of Quadrupole Sources in Prediction of Transonic Tip Speed Propeller Noise, *Journal of Sound and Vibration* 62, 1 (1979) 19–38.

[15] F.H. Schmitz, Y.H. Yu, Helicopter Impulsive Noise: Theoretical and Experimental Status, *Journal of Sound and Vibration* 109, 3 (1986) 361–427.

[16] F. Farassat, H. Tadghighi, Can Shock Waves on Helicopter Rotors Generate Noise? A Study of Quadrupole Source, *Annual Forum Proc., American Helicopter Society* 1, (1990) 323–346.

[17] S. Ianniello, An Algorithm to Integrate the FW-H Equation on a Supersonic Rotating Domain, *AIAA Journal* 37, 9 (1999) 1040–1047.

[18] S. Ianniello, New Perspectives in the Use of the Ffowcs Williams-Hawkings Equation for Aeroacoustic Analysis of Rotating Blades, *accepted for publication on the Journal of Fluid Mechanics*

[19] K.S. Brentner, Prediction of helicopter rotor discrete frequency noise, NASA TM-87721, 1986.

[20] F. Farassat, Derivation of Formulations 1 and 1A of Farassat, by Farassat, NASA TM-2007-214853, March 2007.

[21] K.S. Brentner, F. Farassat, Modeling Aerodynamically Generated Sound of Helicopter Rotors, *Progress in Aerospace Sciences* 39, 2–3 (2003) 83–120.

[22] L. Morino, M. Gennaretti, Boundary Integral Equation Methods for Aerodynamics, *Computational Nonlinear Mechanics in Aerospace Engineering*, edited by S.N. Atluri, Progress in Aeronautics & Astronautics, 146, AIAA, Washington, DC, 1992, pp. 279-320.

[23] M. Gennaretti, L. Luceri, L. Morino, A Unified Boundary Integral Methodology for Aerodynamics and Aeroacoustics of Rotors, *Journal of Sound and Vibration* 200, 4 (1997) 461–489.

[24] A.P. Dowling, J.E. Ffocws Williams, *Sound and Sources of Sound*, Ellis Horwood Limited, West Sussex - England, 1983.

[25] L. Morino, L.T. Chen, E. Suciu, Steady and Oscillatory Subsonic and Supersonic Aerodynamics Around Complex Configurations, *AIAA Journal* 13 (1975) 368–374.

[26] Y.Z. Kehr, J. H. Kao, Numerical Prediction of the Blade Rate Noise Induced by Marine Propellers, *Journal of Ship Research* 48, 1 (2004) 1–14.

[27] S. Ianniello, Quadrupole Noise Predictions Through the Ffowcs Williams-Hawkings Equation, *AIAA Journal* 37, 9 (1999) 1048–1054.

[28] J.E. Kerwin, Marine Propellers, *Ann. Rev. Fluid Mech.* 18 (1986), 367–403

[29] F. Salvatore, P. Esposito, An Improved Boundary Element Analysis of Cavitating Three–Dimensional Hydrofoils, *Proc. of 4th International Symp. on Cavitation* B1.006, Pasadena, CA (USA) 2001.

[30] F. Salvatore, C. Testa, L. Greco, A Viscous/Inviscid Coupled Formulation for Unsteady Sheet Cavitation Modelling of Marine Propellers, *CAV 2003 Symp.* Osaka, Japan, November 2003.

[31] F. Pereira, F. Salvatore, F. Di Felice, Measurement and Modeling of Propeller Cavitation in Uniform Inflow, *Journal of Fluids Engineering* 126, (2004) 671–679.

[32] S. Ianniello, E. De Bernardis, G. Guj, M. Gennaretti, Validation of a New Code for the Prediction of Noise Generated by Helicopter Rotor, *Proc. of XIX European Rotorcraft Forum* (1993) 14–16 Como, Italy.

[33] K.S. Brentner, Prediction of Helicopter Rotor Discrete Frequency Noise, *NASA Technical Report* 87721, 1986.

[34] W.R. Splettstoesser, B. Junker, K.J. Schultz, W. Wanger, W. Weitemeyer, A. Protopsaltis, D. Fertis, The HELINOISE Aeroacoustic Rotor Test In The DNW - Test Documentation and Representative Results *DLR Technical Report* DLR-Mitt. 93-09, 1993.

[35] L. Greco, F. Salvatore, F. Di Felice, Validation of a Quasi-Potential Flow Model for the Analysis of Marine Propellers Wake, *25th Symposium on Naval Hydrodynamics* St. John's Newfoundland, Canada 2004.

[36] J.P. Breslin and P. Andersen, *Hydrodynamics of Ship Propellers*, Cambridge University Press, 1994.

[37] F. Salvatore, S. Ianniello, Preliminary Results on Acoustic Modelling of Cavitating Propellers, *Journal of Computational Mechanics*, 32 (2003) 291–300.

[38] J.P. Franc, J.M. Michel, *Fundamentals of Cavitation*. Kluwer Academic Press, 2004.

[39] R.T. Knapp, J.W. Daily, F.G. Hammitt, *Cavitation*. McGrawHill Book Company, 1970.

[40] J. Dang, Numerical Simulation of Unsteady Partial Cavity Flows, *PhD thesis*, Chinese MSc diploma in Naval Hydrodynamics, December 2000.

[41] E.M. Gates, The Influence of Freestream Turbulence, Freestream Nuclei Population and Drag–Reducing Polymer on Cavitation Inception on Two Axissymmetric Bodies, *Report No. Eng* 183–2, 1977.

[42] F.G.J. Blake, The Tensile Strenght of Liquids, Harward Acoustics Research Laboratory, *A review of literatures* TM9, 1949.

[43] J.S. Carlton, *Marine Propellers and Propulsion*. Butterworth Heinemann, 1994.

[44] N.V.B. Vaz Guilherme, Modelling of Sheet Cavitation on Hydrofoils and Marine Propollers using Boundary Element Methods, *PhD thesis*, Universidade Tećnica de Lisboa, Instituto Superior Tećnico, November 2005.

[45] Y.F. Ronald, *Cavitation*. McGraw–Hill Book Company, 1989.

[46] D.F. De Lange, Observation and Modelling of Cloud Formation Behind a Sheet Cavity, *PhD thesis*, University of Twente, January 1996.

[47] R.A. Furness, S.P. Hutton, Experimental and Theoretical Studies of Two–Dimensional Fixed Cavities, *Journal of Fluids Engineering* (1975) 515–522.

[48] C.E. Brennen, *Cavitation and Bubble Dynamics*. Oxford Univerity Press, New York, 1995.

[49] F. Pereira, F. Avellan, P. Dupont, Prediction of Cavitation Erosion: An Energy Approach, *J. of Eng.* 120–4 (1998) 719–727.

[50] F. Pereira, F. Salvatore, F. Di Felice, M. Elefante, Experimental and Numerical Investigation of the Cavitation Pattern on a Marine Propeller, *Proc. 24th Symp. on Naval Hydrodynamics*, 3 (2002) 236–251, , Office of Naval Research, Fukuoka, Japan.

[51] F. Pereira, F. Salvatore, F. Di Felice, M. Soave, Experimental Investigation of a Cavitating Propeller in Non–Uniform Inflow, *Proc. 25th Symp. on Naval Hydrodynamics*, (2004) St. John's, Newfoundland, Canada.

[52] F. Salvatore, C. Testa, S. Ianniello, F. Pereira, Theoretical Modelling of Unsteady Cavitation And Induced Noise, *Proc. 6th International Symp. on Cavitation*, (2006) Wageningen, The Netherlands.

[53] F. Salvatore, The INSEAN E779A Database on Propeller Flow Experimental Investigations, *INSEAN Technical Report* 99, 2006.

[54] U. Iemma, M. Gennaretti, Integrated Aeroacoustoelastic Modeling for the Analysis of the Propeller-Driven Cabin Noise, *AIAA Paper 99-1919, 5th AIAA/CEAS Aeroacoustic Conference*, Bellevue, Washington, May, 1999.

[55] M. Gennaretti, U. Iemma, C. Testa, Prediction of Sound Scattered by Moving Bodies with Applications to Propeller-Driven Airplanes, *AIAA Paper 2006-2475, 12th AIAA/CEAS Aeroacoustic Conference*, Cambridge, Massachusetts, May, 2006.

[56] D. Colton, R. Kress, *Integral Equation Methods in Scattering Theory*, John Wiley & Sons, New York, 1983.

[57] M. Gennaretti, U. Iemma, Aeroacoustoelasticity in State-Space Format Using CHIEF Regularization, *Journal of Fluids and Structures* 17 (2003) 983-999.

[58] J.E. Ffowcs Williams, D.L. Hawkings, Sound Generated by Turbulence and Surfaces in Arbitrary Motion, *Philosophical Transactions of the Royal Society* A 264 (1969) 321-342.

[59] M. Gennaretti, C. Testa, A Boundary Integral Formulation for Sound Scattered by Moving Bodies, accepted for publication in the *Journal of Sound and Vibration*.

[60] L.N. Long, The Compressible Aerodynamics of Rotating Blades Based on an Acoustic Formulation, NASA TP-2197, 1983.

[61] F. Farassat, Quadrupole Source in Prediction of the Noise of Rotating Blades - A new Source Description, *AIAA Paper 87-2675, 11th AIAA Aeroacoustics Conference*, Sunnyvale, California, October, 1987.

[62] F. Farassat, K.S. Brentner, The Uses and Abuses of the Acoustic Analogy in Helicopter Rotor Noise Prediction, *Journal of the American Helicopter Society* 33 (1988) 29-36.

[63] S. Lee, K. Brentner, F. Farassat, Analytic Formulation and Numerical Implementation of an Acoustic Pressure Gradient Prediction, *AIAA Paper 2007-3710, 13th AIAA Aeroacoustics Conference*, Rome, Italy, May, 2007.

[64] T.Q. Wang, S. Zhou, Investigation on Sound Field Model of Propeller Aircraft–The Effect of Vibrating Fuselage Boundary, *Journal of Sound and Vibration* 209(2) (1998) 299–316.

[65] F. Farassat, M.K. Myers, Further Comments on the Paper by Zinoviev and Bies, "On Acoustic Radiation by a Rigid Object in a Fluid Flow," *Journal of Sound and Vibration* 290 (2006) 538-547.

[66] P.M. Morse, K.U. Ingard, *Theoretical Acoustics*, Mc Graw-Hill, New York, 1968.

[67] G.C. Gaunaurd, Elastic and Acoustic Resonance Wave Scattering, *Applied Mechanics Reviews* 42 (1989) 143-192.

[68] H.A. Schenck, Improved Integral Formulation for Acoustic Radiation Problems, *Journal of the Acoustical Society of America* 44 (1968) 41-58.

[69] A.D. Pierce, *Acoustics: An Introduction to Its Physical Principles and Applications*, Acoustical Society of America, New York, 1989.

[70] A. Zinoviev, D.A. Bies, Author's reply, *Journal of Sound and Vibration* 290 (2006) 548-554.

[71] A. Zinoviev, D.A. Bies, On Acoustic Radiation by a Rigid Object in a Fluid Flow, *Journal of Sound and Vibration* 269 (2004) 535-548.

[72] W.E. Baker, Axisymmetric Modes of Vibration of Thin Spherical Shell, *Journal of Acoustical Society of America* 33 (1961) 1749-1758.

[73] M.C. Junger, Sound Scattering by Thin Elastic Shells, *Journal of Acoustical Society of America* 24 (1951) 366-373.

[74] M.K. Myers, J.S. Hausmann, Computation of Acoustic Scattering from a Moving Rigid Surface, *Journal of the Acoustical Society of America* 91 (1992) 2594-2605.

[75] L. Morino, M. Gennaretti, Toward an Integration of Aerodynamics and Aeroacoustics of Rotors, *AIAA Paper 92-02003, DGLR/AIAA 14th Aeroacoustic Conference*, Aachen, Germany, May, 1992.

[76] X. Wu, A. Akay, Sound Radiation from Vibrating Bodies in Motion, *Journal of Acoustical Society of America* 91 (1992) 2544-2555.

[77] Testa C., Bernardini G., Gennaretti M., Ianniello S. Sound Scattered by Helicopter Fuselages in Descent Flight Conditions, *13th AIAA/CEAS Aeroacoustics Conference*, Roma-Italy, Maggio 2007.

[78] M. Gennaretti, G. Bernardini, A Novel Potential-Flow Boundary Integral Formulation for Helicopter Rotors in BVI Conditions, *AIAA Paper 2005-2924, 11th AIAA/CEAS Aeroacoustics Conference*, Monterey, California, 2005.

[79] M. Gennaretti, G. Bernardini, A Novel Boundary Integral Formulation for BVI Aerodynamics of Helicopter Rotors, accepted for publication in the *AIAA Journal*.

[80] L. Morino, A General Theory of Unsteady Compressible Potential Aerodynamics, NASA CR-2464, 1974.

[81] L. Morino, K. Tseng, A General Theory of Unsteady Compressible Potential Flows With Applications to Airplanes and Rotors, *eds.: P.K.BANERJEE and L. Morino, Development in Boundary Element Method* vol.6 : Non Linear Problems of Fluid Dynamics, Elsevier Applied Sciences Publishers, Barking, UK, 1990.

[82] F. Salvatore, C. Testa, Theoretical Modelling of Marine Propeller Cavitation in Unsteady High–Reynolds Number Flow, *INSEAN Report* 0077, 2002.

[83] S.A. Kinnas, N.E. Fine, A Nonlinear Boundary Element Method for the Analysis of Unsteady Sheet Cavitation, *Proc. of the $20^t h$ ONR Symposium on Naval Hydrodynamics*, 1992, 717–737, Seoul (Korea).

[84] C. Pellone, T. Maitre, L. Briancon–Marjollet, Partially Cavitating Hydrofoils: Experimental and Numerical Analysis, *Journal of Ship Research* 44, 1 40-58, March 2000.

[85] L. Morino, Boundary Integral Equations in Aerodynamics, *Applied Mechanics Reviews*, 46(8) (1993) 445–466.

[86] F. Salvatore, Theoretical and Computational Modelling of Cavitation on Marine Propellers in Non Uniform Flow, *INSEAN Technical Report* 1999-43, 1999 (In Italian).

[87] S.A. Harvald, Resistence and Propulsion of Ships, *Wiley Interscience Publication*, New York (USA) 1992.